



HAL
open science

Electronic Structure of SrTiO₃ Thin Films Doped with 3d Transition Metal Elements

Fatima Alarab

► **To cite this version:**

Fatima Alarab. Electronic Structure of SrTiO₃ Thin Films Doped with 3d Transition Metal Elements. Materials Science [cond-mat.mtrl-sci]. CY Cergy Paris Université, 2020. English. NNT : 2020CYUN1076 . tel-03270718

HAL Id: tel-03270718

<https://theses.hal.science/tel-03270718v1>

Submitted on 25 Jun 2021

HAL is a multi-disciplinary open access archive for the deposit and dissemination of scientific research documents, whether they are published or not. The documents may come from teaching and research institutions in France or abroad, or from public or private research centers.

L'archive ouverte pluridisciplinaire **HAL**, est destinée au dépôt et à la diffusion de documents scientifiques de niveau recherche, publiés ou non, émanant des établissements d'enseignement et de recherche français ou étrangers, des laboratoires publics ou privés.

CY Cergy Paris Université
Ecole Doctorale Sciences et Ingénierie
Laboratoire de Physique des Matériaux et de Surfaces

Electronic Structure of SrTiO₃ Thin Films Doped with *3d* Transition Metal Elements

Fatima Alarab

Defence held the 12th of October 2020

Members of the jury:

President	Prof. Andreas Honecker	CY Cergy Paris Université, Neuville, France
Referees	Dr. Rémi Lazzari	Sorbonne Université, Paris, France
	Dr. Andrés Santander-Syro	Université Paris-Saclay, Orsay, France
Supervisors	Prof. Christine Richter	CY Cergy Paris Université, Neuville, France
	Prof. Ján Minár	University of West Bohemia, Plzeň, Czech Republic
	Prof. Karol Hricovini	CY Cergy Paris Université, Neuville, France
Examinators	Dr. Véronique Brouet	Université Paris-Saclay, Saint-Aubin, France
	Doc. Šimon Kos, Ph.D.	University of West Bohemia, Plzeň, Czech Republic
	Dr. Ondřej Šipr	Institute of Physics ASCR, Prague, Czech Republic

Abstract

The various physical properties of transition metal oxides make them good candidates toward possible new industrial applications, and more precisely in the novel photovoltaic productions. In fact, the rich fundamental electronic properties of transition metal oxides essentially arise from strong Coulomb interactions within the electrons of the system. Understanding of such correlation effects continues to be challenging for modern solid state physics, which makes the combination of experimental and theoretical data essential for further progress in the field.

Spectroscopic investigations of the prototypical correlated SrTiO₃ thin films doped with several transition metal (TM) ions (TM=Ni, Fe and Cr) are the main settings of this thesis. With the combination of core-level photoelectron spectroscopy (XPS), angle-resolved photoelectron spectroscopy (ARPES) and photoelectron diffraction (XPD) on one side, and of first-principles calculations by means of multiple scattering theory on the other side, a good understanding of the doping on the structural and electronic properties has been here achieved.

In SrTiO₃ polycrystalline thin films, grown by magnetron sputtering, the mean size of the crystallites increases with TM-doping content. This finding was the motivation to start further studies and get a better conception of the fundamental electronic band structure of SrTiO₃ films. For this reason, high quality ordered pristine and Ni/Fe/Cr-doped SrTiO₃ films were epitaxially prepared by pulsed laser deposition (PLD).

The electronic band structure calculations for the ground state, as well as one-step model of photoemission calculations, which were obtained by means of Korringa-Kohn-Rostoker (KKR) Greens's function (GF) method, predicted the formation of localised *3d*-impurity bands in the band gap of SrTiO₃ close to the valence band maxima. The measured band dispersion and valence bands at the Ni L-edge resonance confirmed these findings.

The two-dimensional electron gas (2DEG), observed at the surface of SrTiO₃ doped with Ni, by means of resonant-ARPES, can be indirectly controlled by the Ni content in the films. Ni doping seems to be affecting the tetragonal distortion of the TiO₆ octahedron and results in changes of the structure symmetry and the energy splitting of the Ti *3d* surface localized bands.

The XPD measurements confirmed the 4-fold symmetry of Ni-doped SrTiO₃ film's structure, and a change in the lattice parameter compared to pure SrTiO₃ films was detected. Ni impurity atoms incorporate the hosting system by substituting the Ti sites.

Abstract

Les diverses propriétés physiques des oxydes de métaux de transition font d'eux de bons candidats pour de potentielles nouvelles applications industrielles, et plus précisément dans de nouvelles productions photovoltaïques.

Concrètement, les riches propriétés électroniques fondamentales proviennent de fortes interactions de Coulomb au sein des électrons du système. La compréhension de tels effets de corrélation continue d'être un défi pour la physique du solide moderne, ce qui signifie qu'une combinaison de recherches expérimentales et théoriques est essentielle pour progresser dans ce domaine. Les études spectroscopiques de prototypes des couches minces corrélées de SrTiO_3 dopées avec divers ions de métaux de transition (MT) (e.g. Ni, Fe ou Cr) sont la colonne vertébrale de cette thèse.

Avec la combinaison de la spectroscopie de photoélectrons des niveaux de cœur, la photoémission résolue en angle (ARPES) et la photodiffraction (XPD) d'une part, et les calculs de premier principe par la théorie de la diffusion multiple d'autre part, une bonne compréhension du dopage de la structure et des propriétés électroniques a été obtenue ici.

Dans les couches minces polycristallines de SrTiO_3 , préparées par pulvérisation magnétron, la taille moyenne des cristaux augmente avec le dopage aux MT. Cette découverte était une motivation pour étudier et approfondir la connaissance des structures de bandes électroniques fondamentales du SrTiO_3 dopé aux MT. Pour cette raison, des couches minces monocristallines de haute qualité de SrTiO_3 pur et dopé avec Ni, Fe et Cr ont été préparées par ablation laser pulsé (PLD).

Les calculs des structures de bandes électroniques des états fondamentaux, aussi que les calculs de photoémission par la méthode Korring-Kohn-Rostoker (KKR), ont prédit la formation d'états localisés $3d$ liés aux impuretés dans le gap du SrTiO_3 et proches du maximum de la bande de valence. Les mesures de la dispersion des bandes électroniques et des bandes de valences à la résonance du Ni confirment ces résultats.

Le gaz bidimensionnel (2DEG), observé à la surface du SrTiO_3 dopé au Ni, par ARPES résonant, peut être indirectement contrôlé par le dopage et sa concentration dans les couches. Le dopage au Ni semble modifier la distortion de l'octaèdre TiO_6 , ce qui aboutit à des changements dans la symétrie de la structure et la partition des bandes Ti $3d$ localisées à la surface.

Les mesures XPD confirment la symétrie d'ordre quatre de la structure des couches minces de SrTiO_3 dopé au Ni, et un changement du paramètre de maille par rapport à celui de SrTiO_3 pur a été détecté. Les atomes Ni intègrent le système de base en se substituant aux sites Ti.

Contents

Introduction	1
Outline	2
1 State-of-the-art	3
1.1 Transition Metal Perovskites	3
1.1.1 Bulk structure	3
1.1.2 Electronic structure	4
1.2 Material of Interest: Strontium Titanate	5
1.2.1 SrTiO ₃	5
1.2.2 SrTiO ₃ (001) surface states	6
1.2.3 TM-doping in SrTiO ₃	6
SrTiO ₃ :Ni	8
SrTiO ₃ :Fe	11
SrTiO ₃ :Cr	12
1.3 NiO	12
1.3.1 Electronic structure	13
2 Experimental Methods	17
2.1 Photoelectron Spectroscopy	17
Three-step model	18
2.2 Resonant Photoemission Spectroscopy	21
2.3 Photoelectron Diffraction	24
2.4 Synchrotron Measurements	25
2.4.1 High-Resolution Angle-Resolved Photoelectron Spectroscopy	25
2.4.2 Soft X-ray Angle-Resolved Photoelectron Spectroscopy	25
2.4.3 Angle-Resolved Photoelectron Diffraction	26
2.5 Sample Growth	27
2.5.1 Radio Frequency Magnetron Sputter Deposition	27
2.5.2 Pulsed Laser Deposition	27
2.6 Electron Diffraction Methods	28
2.6.1 Reflection high-energy electron diffraction and low-energy electron diffraction	28

2.6.2	X-ray Diffraction	30
3	Theoretical Approach	33
3.1	Density Functional Theory	33
3.1.1	Derivation and formalism	34
3.1.2	Exchange-correlation functionals	36
3.2	Korringa-Khon-Rostoker (KKR) Method	36
3.2.1	Multiple-scattering theory for ordered systems	37
3.2.2	Multiple-scattering theory for disordered systems	39
	Virtual crystal approximation	39
	Average t -matrix approximation (ATA)	39
	Coherent potential approximation (CPA)	40
3.3	One-Step Model of Photoemission	40
4	Polycrystalline Ni-Doped SrTiO₃	45
4.1	Magnetron Sputtered SrTiO ₃ Thin Films	45
4.2	Ni-doped SrTiO ₃ Thin Films	47
4.2.1	Atomic structure	47
4.2.2	Characterization by XPS	48
4.3	Conclusion	50
5	Monocrystalline TM-Doped Thin SrTiO₃ Films	53
5.1	Elaboration of Ni-doped SrTiO ₃ (100) Thin Films	53
5.2	Fe and Cr-doped SrTiO ₃ Films	58
5.3	Impact of TM-doping on the Electronic Structure of SrTiO ₃ Films	60
5.3.1	Role of TM-doping in the modification of the SrTiO ₃ band gap	60
5.3.2	Resonant behaviour of TM-doped SrTiO ₃	64
	STO:Ni _{0.06} and STO:Ni _{0.12}	66
	STO:Fe _{0.05}	70
	STO:Cr _{0.05}	70
5.4	Conclusion	70
6	ARPES Studies of Pristine and TM-doped SrTiO₃ Films	73
6.1	Band Structure of the TM-doped SrTiO ₃ Films	74
6.1.1	Photon energy scan	75
6.1.2	Measurements along ZA	76
6.2	2D Metallic States	78
6.2.1	SrTiO ₃ (100) thin films	78
6.2.2	SrTiO ₃ :Ni(100) thin films	80
	Photon energy dependency	80
	Time dependency	82
	Ni concentration dependency	83
6.3	New Metallic State on SrTiO ₃ :Ni _{0.12} Films	85
6.4	Conclusion	87

7	X-Ray Photoelectron Diffraction of Ni-doped SrTiO₃ Films	89
7.1	Photoelectron Diffraction Measurements	90
7.2	Photoelectron Diffraction Simulations: Multiple Scattering Method	92
7.2.1	Multiple scattering series expansion	92
7.2.2	Matrix inversion method	93
7.3	Results	94
7.3.1	High kinetic energy	94
7.3.2	Low kinetic energy	96
	STO(100)	96
	STO:Ni _{0.12} (100)	98
7.4	Conclusion	101
8	Summary	103
	Bibliography	109

Introduction

Ecological and durable solar energy is considered now as one of the most safe and desired energy sources to replace fuel based supplies [1]. The development of photovoltaic technologies has advanced quickly after the discovery of the photoelectric effect [2]. Perovskite-type TM-oxide compounds have been used intensively in the last generation of photovoltaic cells due to their lower cost in terms of materials and fabrication compared to the conventional silicon solar panels [3] and their higher power conversion efficiency [4, 5]. Note also that these materials exhibit a wide variety of physical properties extending from superconductivity to ferromagnetism and ferroelectricity [6–11].

The ferroelectric photovoltaic effect was discovered about half a century ago in a variety of ferroelectric materials without inversion symmetry in which a photovoltaic response can be generated along the polarization direction [7]. One of the key challenges for solar energy conversion strategies is the minimization of charge recombination losses following light absorption [7]. One strategy is based on the use of piezoelectric and ferroelectric materials, due to the potential for the internal electric fields present in such materials to aid the spatial separation of charge carriers [6]. Recent studies showed for example, that the internal fields in a ferroelectric single crystal BaTiO_3 (BTO) inhibit electron/hole recombination resulting in long-lived carriers in the absence of externally applied electric potential [12].

The major constraint in most of the commonly used ferroelectric materials is their large band gap (≥ 3 eV), thus they can only harvest sunlight in the UV range. To match their absorption spectra to the solar radiation spectrum they can be doped with TM-elements [13, 14].

Prototypical perovskite-structured complex oxide strontium titanate ($\text{SrTiO}_3/\text{STO}$) has been a subject of intensive discussion in recent years both experimentally as well as theoretically. Fundamental physical aspects, as for example the presence of a 2DEG on the surface of STO [15, 16], its magnetism, correlation effects and proposed superconductivity [17] meet at the same time with an extensive interest in the development of new materials for solar energy conversion [18]. For instance, STO doped with $3d$ -impurities, such as Mn, Co, Fe, and Ni, seems to be a promising material from the viewpoint of the effective sunlight absorption [19–21]. However, STO is a quantum paraelectric material because at low temperature, where quantum statistics dominates, the ferroelectric ordering is suppressed and the rising of dielectric permittivity saturates [22, 23].

So, in this material, the advantage of the internal electric field which would inhibit electron-hole recombination is lost. Yet, STO with BTO forms a continuous series of solid solutions $\text{Ba}_{1-x}\text{Sr}_x\text{TiO}_3$ in which STO is an incipient ferroelectric [24]. The ferroelectricity in thin STO films can as well be induced at RT by strain [22] or by incorporating them in BTO/STO multilayers [25].

The information about the electronic states in the valence band, the oxidation state and the structural location of TMs in STO is still very controversial. From first-principles calculations of the structure, the electronic and magnetic properties of STO doped with Cr, Mn, Fe, Co, and Ni indicate that Ti can be substituted by TM ions [26]. The band structures show a variety of electronic (half metals, metals, semiconductors) and magnetic (ferro-, antiferro- and non-magnetic) properties [26]. Density of states (DOS) calculations [20,26] show an impurity band in the forbidden band gap of STO and the doping slightly decreases the band gap and increases the width of the valence band. Experimentally the ferromagnetic responses were observed in Ni and Co-doped STO polycrystalline materials even at RT [27].

In this thesis we aim to combine experimental data with KKR one-step photoemission calculations [28] to study the localised $3d$ -states of TMs, which are strongly affected by the local correlations and will lead to in-gap states [29].

Outline

In chapter 1 of this manuscript, an introduction to transition metal oxides, the materials of interest and their properties is given. We discuss the bulk structure and the orbital ordering of the Ti $3d$ derived conduction band. The properties of STO surfaces are also presented.

In chapter 2, we give an overview of the experimental methods used in this work, as well as the basic concepts of ARPES and XPD, followed by a description of the principle of magnetron sputtering method and PLD growth we used to prepare our samples. In the last part, the structural characterization techniques, x-ray diffraction (XRD), reflection high-energy electron diffraction (RHEED) and low energy electron diffraction (LEED) will be also introduced.

In chapter 3, we present an overview of the density functional theory (DFT) and of the KKR-GF method. The coherent potential approximation (CPA) we used to study the disorder in the hosting material will be introduced. Ground state electronic band calculations, as well as ARPES calculations within the one-step model of photoemission will be discussed.

The chapters 4, 5, 6 and 7, are dedicated to present our results. In chapter 4, film growth of pristine and Ni-doped STO polycrystalline samples by magnetron sputtering is presented, and Ni-doping effect on the structure of STO films is discussed. In chapter 5, film growth of pristine and Ni/Fe/Cr- doped STO(001) films by PLD, as well as their structure, chemical properties and electronic properties are demonstrated and analysed. The data will be compared to the corresponding DFT calculations. ARPES results of the PLD grown films are performed and compared to computational data in chapter 6. Photoelectron diffraction measurements on pure STO and Ni-doped STO(001) films combined with XPD simulations within multiple scattering theory will be described and discussed in chapter 7.

State-of-the-art

1.1 Transition Metal Perovskites

1.1.1 Bulk structure

Transition metal oxides comprise a wide class of compounds with properties covering almost all aspects of material science and solid state physics. These compounds belong to different structural families which depend on their bonding characteristics (covalent or highly ionic); they can be metals, semi-conductors or insulators [30, 31]. Perovskites are a large family of oxide compounds having the chemical formula of ABX_3 , which can be described as consisting of corner sharing $[BX_6]$ octahedral with the A cation occupying the 12-fold coordination site formed in the middle of the cube of eight such octahedrals (see Fig. 1.1). The positively charged A site is usually occupied by an alkaline earth. B is a $3d$, $4d$, or $5d$ TM element cation and the X-site is often occupied by oxygen anions. In this material, the A and B cations (A^{2+} , B^{4+}) donate 2 and 4 electrons respectively to the three oxygen anions (O^{2-}) with two electrons each, making ABO_3 neutral. The (100) plane is either a BO_2 plane or a AO plane.

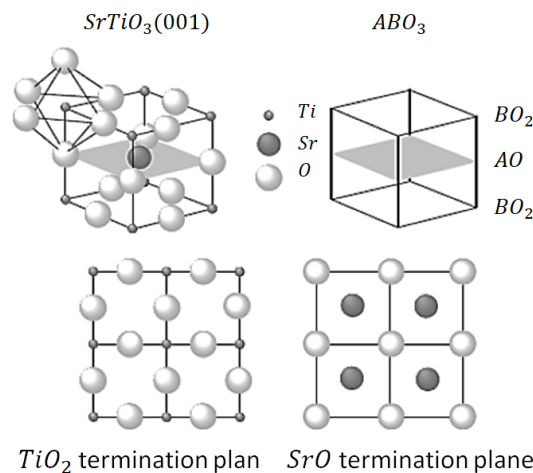


Figure 1.1: Cubic crystal structure of the ABO_3 perovskites and possible terminating planes of a (001) surface.

1.1.2 Electronic structure

Due to the six-fold coordination of Ti ions by surrounding O ions, a crystal field splitting of the degenerated Ti 3d states appears. These separated states are called t_{2g} consisting of d_{xy} , d_{xz} and d_{yz} orbitals, and e_g states with $d_{x^2-y^2}$ and d_{z^2} orbitals (see Fig. 1.2 (a,b)). The O 2p states also split into the p_σ and the p_π . Figure. 1.2 (d) shows the schematic electronic structure of STO where the Ti cation has d^0 electronic configuration. In the band picture, the valence band is formed by the O 2p bands, hybridized with the Ti 3d states, and the conduction band is mainly formed by the empty Ti 3d states.

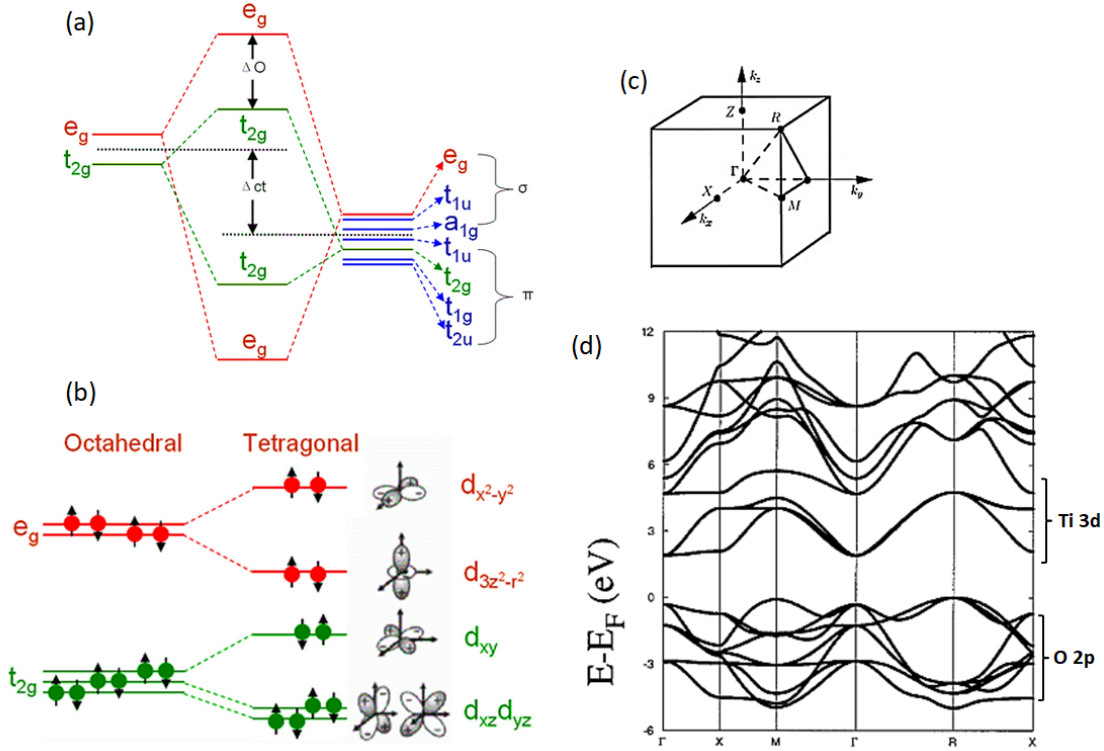


Figure 1.2: (a) Molecular-orbital energy diagram for TiO_6 octahedron (from [32]). (b) Splitting of d -orbitals in an octahedral ligand field (from [32]). (c) Three-dimensional scheme of the first Brillouin zone of a simple cubic system showing the high symmetric points. (d) Band structure of STO calculated in the local density approximation (from [33]).

The stability and structural distortions of perovskite crystal structures are usually discussed in terms of Goldschmidt's tolerance factor t , which depends on the ionic radius of the A, B and X ions [35]. Most of the perovskite oxides are not in the cubic structure; $t = 1$ represents the perfect cubic condition, the case of an ideal STO at RT. Different distorted structural variants are formed for $0.75 < t < 1$, which is the range of stability of the perovskite structure (see Fig. 1.3). This high chemical and structural flexibility combined with the distribution of the partially filled d states lead to the coexistence of several physical interactions (spin, charge, lattice and orbital), which are all active together and give rise to a wide range of physical properties and functionalities such as colossal magnetoresistance [36, 37], ferroelectricity [38], ferromagnetism [39], superconductivity [40], charge ordering [34], and spin dependent transport [41, 42]. These properties make perovskites good candidates in different fields of application, including optoelectronics [43, 44], spintronics [45, 46], catalysis [47], and piezoelectric devices [48]. Moreover, the last few years have witnessed a rapid emergence of a new class of solar cells based

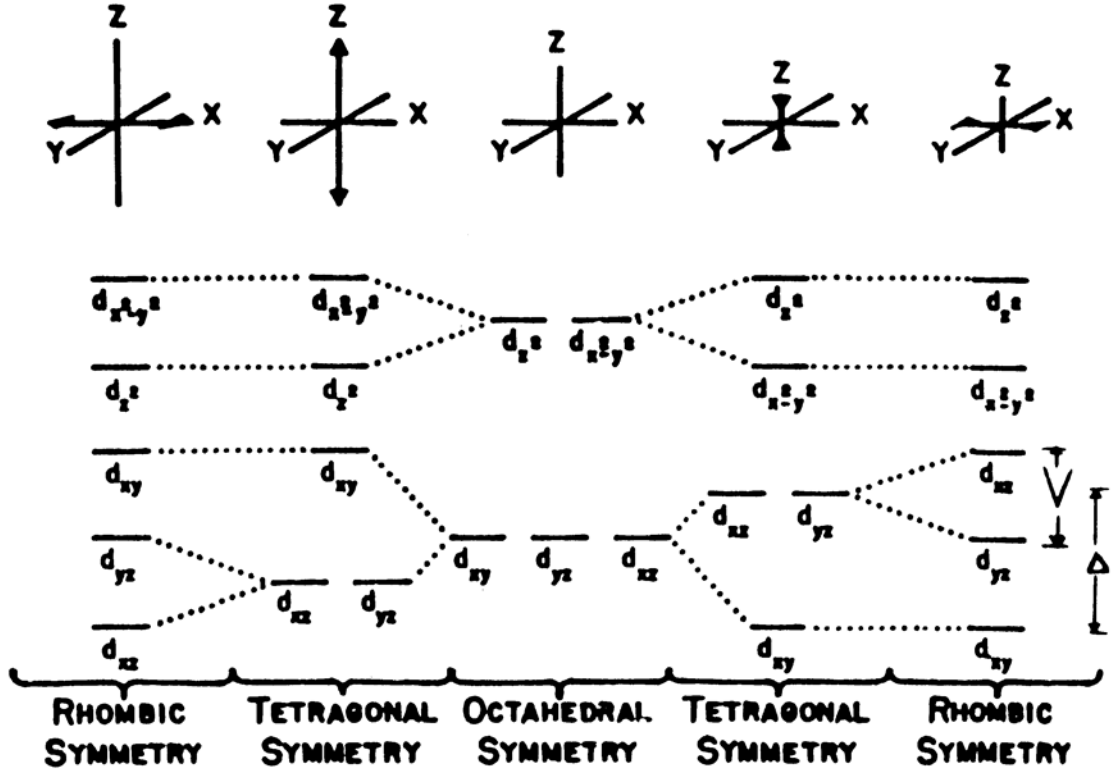


Figure 1.3: Different distortion of the TiO_6 octahedron and their effect on the splitting of the t_{2g} and e_g orbitals (from [34]).

on perovskites that are revolutionizing the field of solar technologies [49, 50]. Transition metal oxides also have a wide variety of surface structures which affect the surface energy of these compounds and influence their physical and chemical properties [51]. The bulk properties of most of them are pretty well understood. However, little is known about their surface properties of even the simplest ones.

1.2 Material of Interest: Strontium Titanate

1.2.1 SrTiO_3

At room temperature (RT), STO crystallizes in the cubic perovskite structure (space group $\text{Pm}\bar{3}\text{m}$) with a lattice parameter of 3.905 \AA [52]. In its stoichiometric form, STO is a good insulator with an indirect band gap of 3.2 eV and a direct gap of 3.75 eV [53]. STO has three phase transitions upon cooling. STO bulk crystals are considered to be tetragonal with $a=b$ and $c_{max}=3.9 \text{ \AA}$ (space group I4/mcm) between $110 \text{ K} - 65 \text{ K}$, due to the opposite rotation of neighbouring oxygen octahedral, orthorhombic in the range $55 \text{ K} - 35 \text{ K}$ and possibly rhombohedral below 10 K as X-ray diffraction studies suggest [54, 55]. Synthetic STO is a paraelectric material and has a very large dielectric constant at RT. It has a ferroelectric phase transition at low temperatures [56]. STO can exhibit ferroelectric properties upon small distortion of its lattice by exchange doping of the A-site or by applying an interface strain during films deposition with a tunable transition temperature [57]. Experimental studies done by Rice *et al.* show that local magnetic moments are induced upon irradiation of visible light in oxygen deficient STO samples at 18 K [58].

Rao *et al.* demonstrated the presence of magnetic properties by irradiation with UV light up to 400 K, which can be suppressed by annealing in oxygen [59]. These experiments indicate that magnetic moments are related to free electrons originating from oxygen vacancies which are either created by light or pre-existing in the bulk due to doping. These free electrons lead to unpaired spins that are responsible for a magnetic moment.

1.2.2 SrTiO₃(001) surface states

In general, the presence of intrinsic defects, such as vacancies, and the presence of extrinsic defects, like dopants, lead to modifications of the electronic structure and the electronic conductivity of the material. STO has shown the possibility to create a 2DEG system on its surface [15,16]. The 2D metallic state at the surface of STO and the role of oxygen vacancies in this matter have been studied intensively both experimentally and theoretically [8,15–17,60–63]. Using angle-resolved photoemission spectroscopy, it has been shown that a highly metallic 2DEG can form at the vacuum cleaved surface of STO(001) (see Fig. 1.4). The electron density of the 2DEG can be controlled through exposure of the surface to intense irradiation. Its fundamental electronic structure consists of multiple heavy and light sub-bands, resulting from the confinement of electrons near the surface of STO. The surface charge carrier density of the 2D state was found to increase under synchrotron irradiation and to saturate at a value of $n_e = 8 \times 10^{13} \text{ cm}^{-2}$ [16]. The presence of the 2DEG is accompanied by the formation of an in-gap state at a binding energy of 1.2 eV which also increases in intensity with irradiation. The authors attribute the formation of the 2D system to a surface band bending caused by oxygen vacancies, consisting of an orbitally polarized row of quantum confined t_{2g} electrons that are highly mobile in the surface plane. In fact, by creating a large number of oxygen vacancies by surface cleavage or irradiation, this will lead to two dopant electrons per created vacancy, and these electrons will delocalize within the potential generated by the positively charged layer of surface vacancies.

Plumb *et al.* [64] also investigated the mixed dimensionality of the 2DEG at the surface of STO(001) wafers with TiO₂ termination, using ARPES and XPS under irradiation (see Fig. 1.5). Their results reveal that the d_{xy} bands have a 2D dispersions with weak k_z dependence, and the $d_{xz/yz}$ bands show 3D dispersions different from bulk expectations. They demonstrated that electrons which are associated with those orbitals result from the surface region, and despite sample preparation, the characteristics of the 2DEG at the Fermi surface are the same and called "universal". This means that the formation of the metallic state at the surface of STO and other similar oxides goes beyond the chemical doping scenario and is affected by profound changes in the initial states and/or spatial distribution of electrons near the Fermi level in the surface region [64].

1.2.3 TM-doping in SrTiO₃

Chemical doping or alloying is an effective approach to manipulate the fundamental properties of materials. The lattice defects from different types of atoms and doping sites are able to modify in various ways the properties of the hosting system. For example, TM-doping into perovskite oxides is one of the effective strategies to absorb visible light. This is due to the dopant-dependent

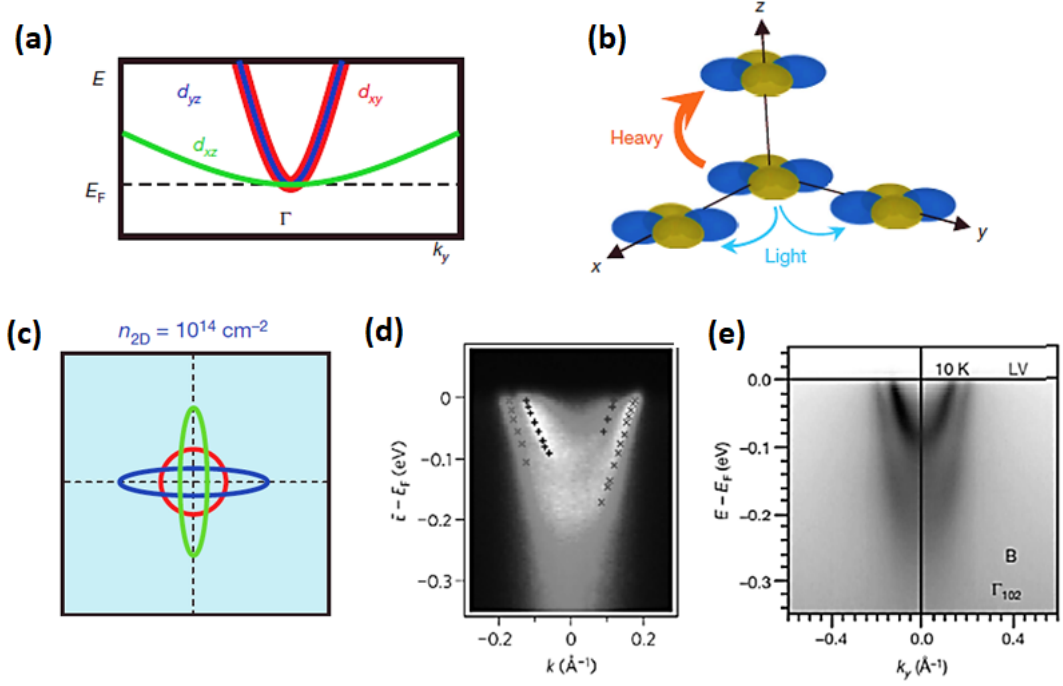


Figure 1.4: (a) Bulk conduction band of STO along k_y , consisting of a heavy d_{xz} band and a doublet of light d_{xy}/d_{yz} bands. (b) The bands in (a) result from the small and large overlaps of the Ti 3d orbitals along the y direction, depicted here for the case of $3d_{xy}$ orbitals. (c) Resulting 3D Fermi surface for a given bulk doping, deduced from a tight-binding model (from [15]). 2DEG at the surface of STO: (d) Results from Meevasana *et al.* (from [16]) and (e) results of Santander *et al.* (from [15]).

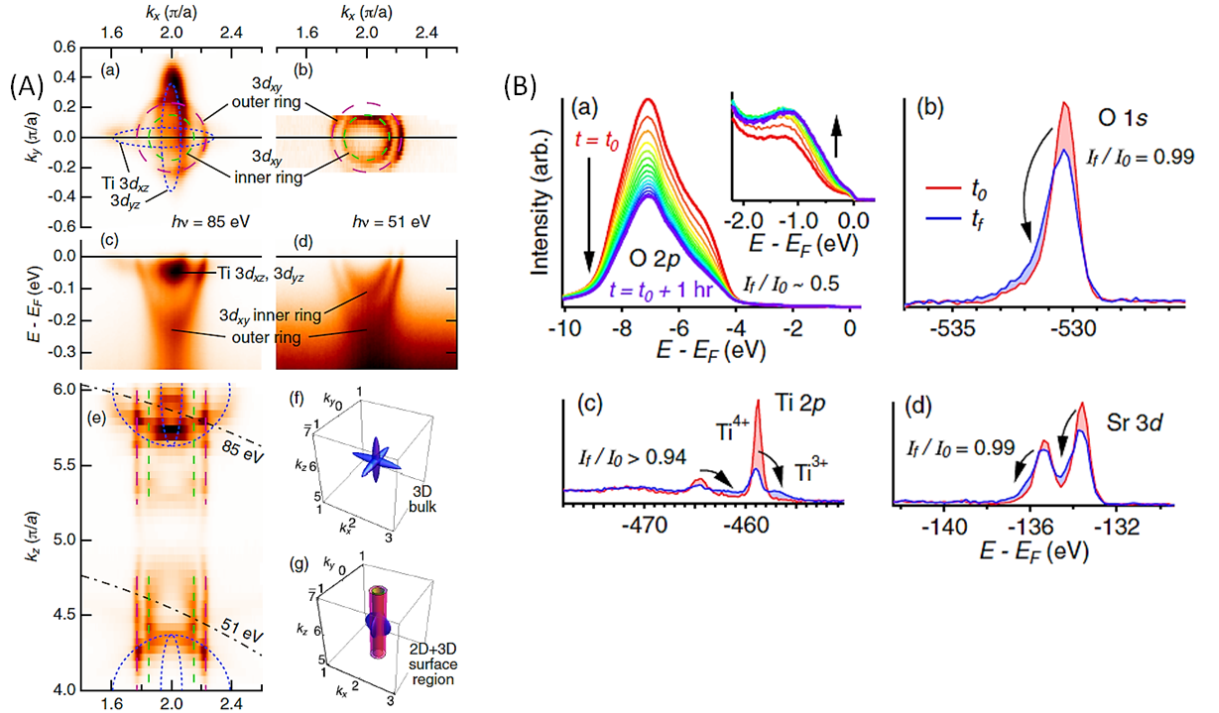


Figure 1.5: (A) Three-dimensional view of the near- E_F electronic structure of the metallic surface region on STO: (a) Fermi surface map measured at $h\nu=85$ eV and (b) at $h\nu=51$ eV. (c,d) Band dispersion along k_x at $k_y=0$. (e) k_z scan. The dot-dashed lines indicate the curvature of Fermi surface cuts in (a) and (b). (f) Expected shape of the 3D Fermi surface in the bulk. (g) Representation of the mixed quasi-2D and 3D Fermi surface sheets at the STO surface. (B) Spectral evolution of the sample as a function of irradiation time: (a) Decrease of the O 2p valence band spectral intensity during irradiation. (b) XPS spectra of the O 1s measured at t_0 and $t_f=1$ hr. (c,d) Analogous spectra for the Ti 2p and Sr 3d core levels (from [64]).

spectral characteristics in which the unique d -band configurations modify mainly the valence band and/or the conduction band and form new energy levels in the band gap [19–21]. The radius of the B-ion is about half that of the A-ion. Therefore, size considerations lead to the expectation that the TM-ions with radii ranging from 0.5 to 0.7 Å are incorporated at B sites, and those of the rare-earth series with $r \sim 1$ Å at A sites. In addition, the calculated formation energies indicate that when STO is doped with TM-ions, they are more likely favourable to replace the tetravalent Ti ions at the centre of the oxygen octahedron rather than Sr ions [20, 26]. TM-ions are not only found in cubic sites. Since the valency of TM-ions is frequently less than that of the Ti^{4+} they replace, they induce vacancies on the oxygen lattice as charge compensation [65]. In the following we are going to state some of the previous experimental and theoretical studies on $3d$ TM-doping of STO and the role of impurity energy levels in the conductivity of the doped systems.

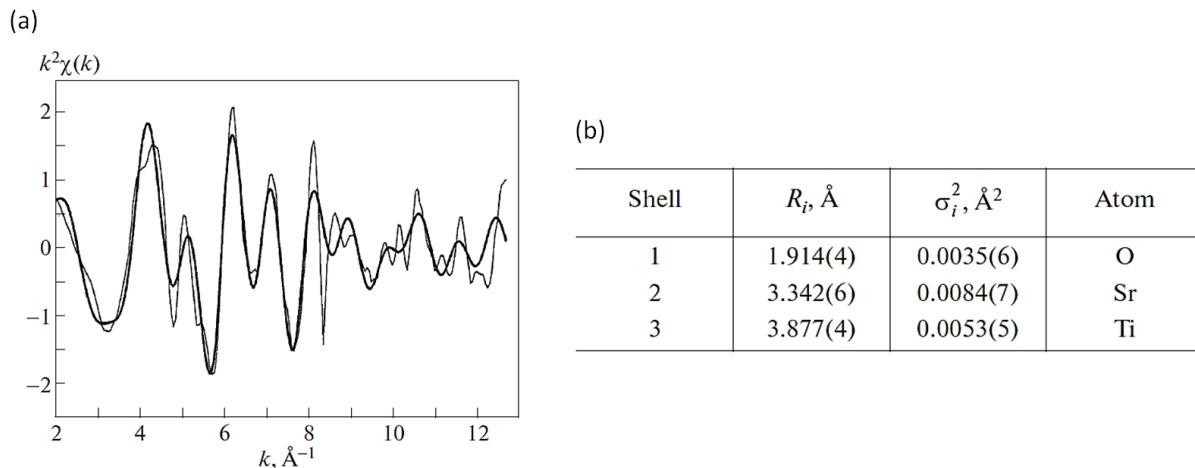


Figure 1.6: (a) EXAFS spectrum obtained at the Ti K -edge at 300 K for the $\text{SrTi}_{0.97}\text{Ni}_{0.03}\text{O}_3$ sample annealed at 1500°C (thin line) and its best theoretical fit (thick line). The theoretical fit takes into account multiple-scattering effects. (b) Table showing the interatomic distances (R_i) and Debye-Waller factors (σ_i^2) for three nearest shells in the $\text{SrTi}_{0.97}\text{Ni}_{0.03}\text{O}_3$ sample (from [66]).

SrTiO₃:Ni

Recent studies on STO doped with several $3d$ -impurities have shown that Ni is one of the most promising dopants from the point of view of the effective sunlight absorption [66]. In [65, 67, 68], the photochromic behaviour of STO:Ni grown by the fusion flame technique was investigated. The electron paramagnetic resonance (EPR) spectra showed that features related to $\text{Ni}^{3+}-V_o$ pair centres which are observed when the oxygen vacancy is empty, and to $\text{Ni}^{3+}-V_o(-2e)$ pairs created when two electrons are trapped near or at the vacancy, were systematically detected [68]. Both result from the association of a Ni^{3+} impurity with a nearest-neighbour oxygen vacancy V_o . Faughnan [69] also studied the photochromic properties of STO:Ni. He demonstrated from the EPR spectra that 80% of the observable Ni are present in the form of Ni^{2+} in cubic sites and are substitutional on Ti^{4+} sites. The presence of $\text{Ni}^{3+}-V_o(e)$ was also predicted. In the case of oxidized samples, the EPR data show the spectra related to cubic Ni^{3+} and axial $\text{Ni}^{3+}-V_o$.

Sluchinskaya *et al.* [66] presented a study of Ni-doped STO using XRD and EXAFS (extended

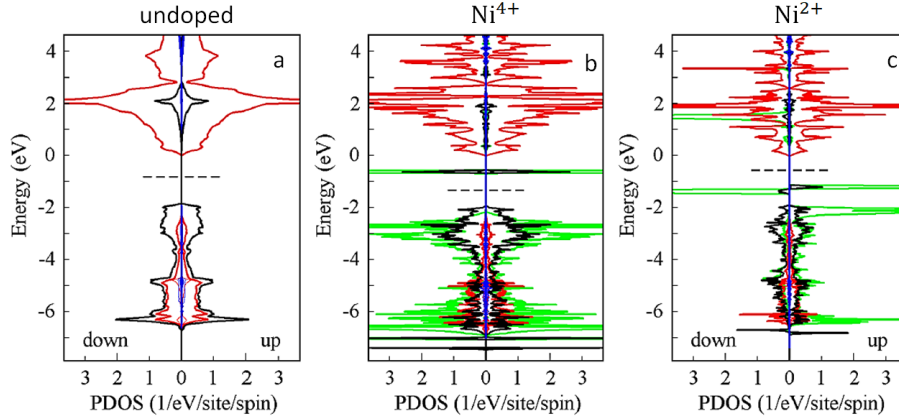


Figure 1.7: Site-projected partial density of states for undoped and Ni-doped STO samples with 6.5% and 12.5% of Ni respectively (from [70]). Ti 3d states are traced in red, Ni 3d states in green, O 2p states in black and Sr 4d states in blue. The dashed black line is set for Fermi level.

x-ray absorption fine structure) spectroscopy. The samples were prepared by solid-state reaction method with the impurity concentration of 2-3 % and various deviations from stoichiometry. Their results show that, independently of the preparation conditions, the most stable phases in the samples are the single phase $\text{SrTi}_{1-x}\text{Ni}_x\text{O}_3$ solid solution and NiTiO_3 which can coexist. From EXAFS data (see Fig. 1.6 (a)), they deduced that Ni atoms substitute the Ti atoms in the centre of the cube, in the single phase $\text{SrTi}_{1-x}\text{Ni}_x\text{O}_3$ sample. The table presented Fig. 1.6 (b) shows the small Debye-Waller factors for three nearest shells in this sample. The small Debye-Waller factors for the first and second shells, which are typical for the thermal vibrations in perovskites at 300 K, lead to the deduction that Ni atoms are located in the centre of the perovskite cube and that oxygen vacancies are not present near the impurity atoms.

The interpretation of the data on the Ni charge state in STO seems to be different from one reference to another. For example in [71], Beale *et al.* also studied STO:Ni samples (grown by hydrothermal synthesis at 150°C) by XAFS (x-ray absorption fine structure) spectroscopy. XANES (x-ray absorption near edge structure) and EXAFS spectra they obtained were qualitatively different from the results reported in [66]. The absorption edge shift in STO:Ni with respect to NiO was only 1.1 eV in [71], whereas in [66] it was 2.5 eV. Dissimilarity was also present in the samples colour (beige in [71] and almost black in [66]). Müller *et al.* [68] came to the conclusion that Ni has a 3+ valency state substituting the Ti sites in STO:Ni, while in [66] it is close to 4+. These differences in sample properties can be mainly related to different methods of growth and experimental conditions used such as temperature, pressure, and chemical reactions.

Experimental data on the electronic structure of STO:Ni and the formation of impurity bands are rare. Yet, theoretical investigations are frequently available in literature. Lebedev *et al.* [70] presented electronic structure calculations of the system within first-principles density functional theory (the Ni concentration was 6.5% and 12.5%). The results of the site-projected partial density of states (PDOS) calculations are presented in Fig. 1.7. At low doping level, Ni is in a tetravalent state and the ground-state structure is diamagnetic ($S = 0$). A Ni impurity band is formed in the band gap and slightly shifted toward the conduction band. When the impurity concentration increases, Ni is found to be in a divalent state and the ground-state structure is

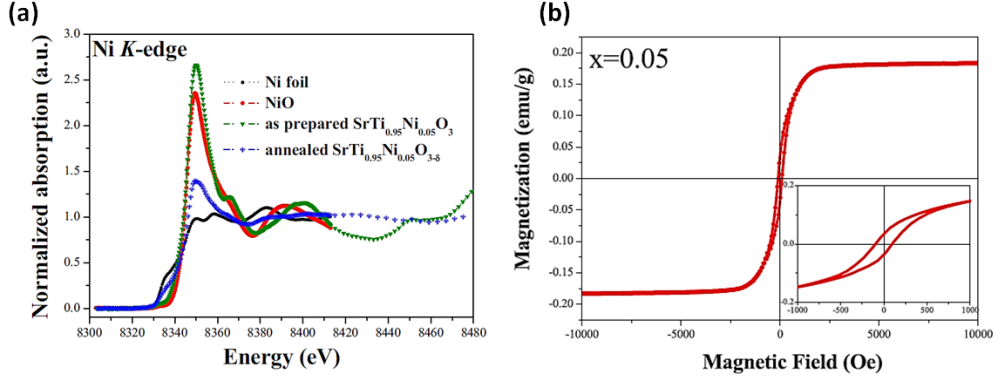


Figure 1.8: (a) XANES spectra of the standards Ni metal, as-prepared and annealed $\text{SrTi}_{0.95}\text{Ni}_{0.05}\text{O}_3$ samples. (b) Room temperature M-H curves of the annealed $\text{SrTi}_{0.95}\text{Ni}_{0.05}\text{O}_3$ samples (from [72]).

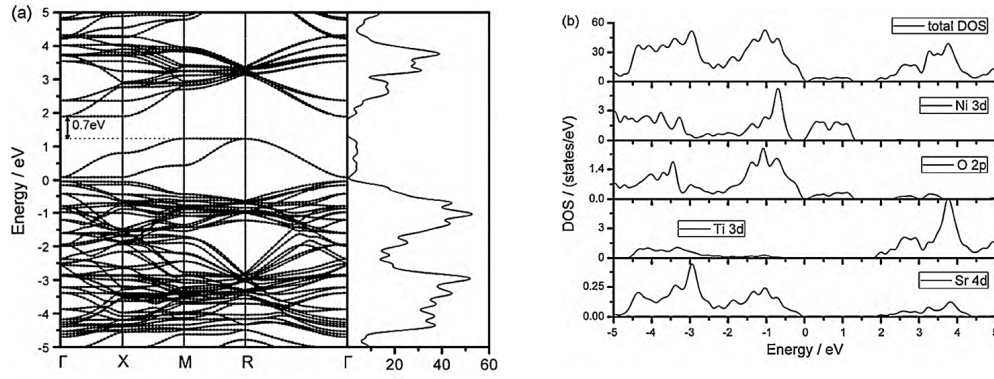


Figure 1.9: (a) Band structure of Ni-doped SrTiO_3 . (b) Corresponding total DOS and PDOS (from [20]). The zero energy locates at the Fermi level.

paramagnetic ($S = 1$). Because of the magnetic moment, the energy position of the Ni spin-up and spin-down $3d$ states is different: the spin-up states are pushed down below the Fermi level, and the spin-down states are shifted up and are located in the conduction band. The Ni impurity band in this case is shifted toward the valence band, and the Fermi level is located between the fully occupied spin-up states and the conduction band edge.

In [72] is presented a characterization of the structural and magnetic properties of $\text{SrTi}_{1-x}\text{Ni}_x\text{O}_3$ nanoparticles prepared by a hydrothermal method. The samples were annealed at 800°C for three hours. They observed that the average particle sizes decreases from 136.8 to 126 nm upon Ni doping. XANES results indicate the existence of Ni metal in annealed $\text{SrTi}_{0.95}\text{Ni}_{0.05}\text{O}_3$ sample, which also exhibits a ferromagnetic behaviour at RT (see Fig. 1.8).

A first-principles study of the electronic structure of Ni-doped STO (Ni concentration is 12%) was also carried out by Dong *et al.* and Li *et al.* [20,26]. As it is observed in Fig. 1.9 (a), the band structure of STO doped with Ni, where Ni atoms substitute Ti atoms, shows the formation of new states in the middle of the gap, and the indirect band gap is reduced to 0.7 eV (the calculated band gap of the pure STO is 1.9 eV) [20]. The defect bands are close to the valence band, which indicates that Ni impurities are acceptors, leading to an increase of oxygen vacancies and hole concentration. The corresponding O total DOS and the PDOS of the doped system are

presented in Fig. 1.9 (b). A wide isolated defect peak appears in the middle of the band gap, close to the valence band. It is purely related to Ni 3d states and O 2p states. Ni 3d states contribute to the whole valence band but not to the conduction band.

SrTiO₃:Fe

Fe-doped STO represents another model of an acceptor doped large band-gap electroceramics [73]. The mixed valence (Fe³⁺/Fe⁴⁺) character of the dopant produces a charge imbalance with respect to the lattice which is usually compensated by oxygen vacancies [74]. Several theoretical approaches to Fe doping effects in STO have shown a formation of electronic in-gap states (see Fig 1.10). Their degree of localization and bandwidth can be different because they strongly depend on the doping level, the Fe valence state and the method used for the calculations [75–77].

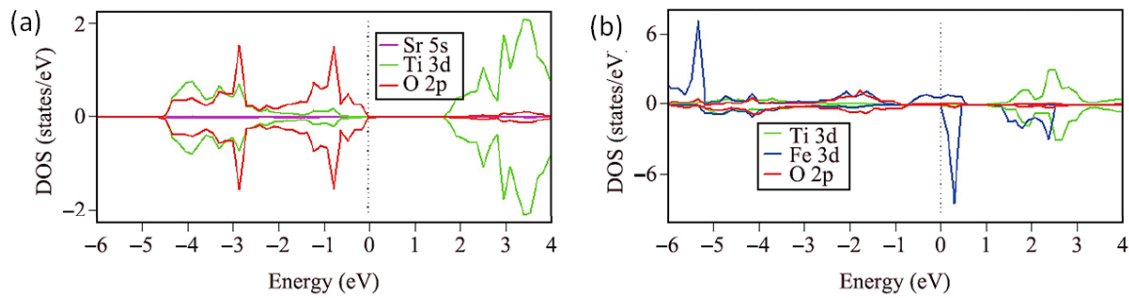


Figure 1.10: PDOS for (a) pure STO and (b) Fe-doped STO showing the formation of new states in the band gap of the doped system. These states purely belong to Fe impurity bands (from [26]).

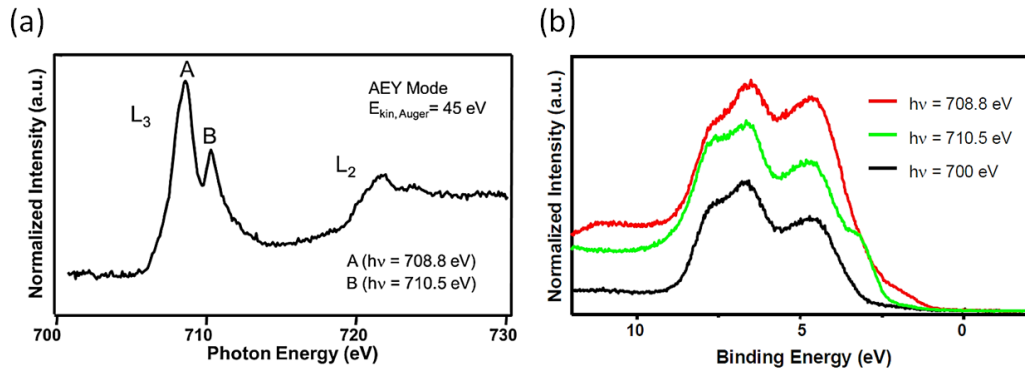


Figure 1.11: (a) Fe *L*-edge x-ray absorption spectrum obtained in the Auger electron yield mode for the STO film doped with 2% Fe. Peaks A and B can be attributed to mostly divalent and trivalent Fe ions. (b) Selected valence band photoemission spectra for the same system, obtained for photon energies on- and off-resonance. Photon energies of 708.8 eV and 710.5 eV correspond to the positions of the peaks in the XAS spectrum. 700 eV is the off-resonance photon energy (from [78]).

Recent experimental studies demonstrated that STO:Fe thin films exhibit no significant Fe⁴⁺ contribution, even when the growth is performed at high oxygen pressure [79]. Analysis of the Fe 2p core level in single crystalline STO films showed that for doping concentrations less than 2%, the valency of Fe is rather a combination of 2+ and 3+ with a divalent contribution situated mostly on the surface [80]. X-ray absorption spectroscopy (XAS) measurements confirmed the mixed valence state of Fe independently from the doping concentration (see Fig. 1.11). This study also shows that annealing the samples increases the relative Fe²⁺ signal ratio [78].

SrTiO₃:Cr

Several recent experimental and theoretical studies showed an enhancement of optical properties of Cr-doped STO [81, 82]. Alvarado *et al.* reported that the electroluminescence spectra of Cr-doped STO arises due to positioning of Cr³⁺ in an octahedral ligand field which influences the resistive switching process by involving trapping and detrapping of electrons at the Cr site [83]. Jing *et al.* reported that Cr dopant exists as Cr³⁺ and Cr⁶⁺ ions in STO [82], the latter usually behaving the trapping centre for the photoinduced electrons. By applying a hydrogen treatment on the Cr doped STO samples, it is possible to reduce Cr⁶⁺ to Cr³⁺ and therefore increase the concentration of the charge carriers. Similar results on Cr oxidation states in STO were also presented by Lacz *et al.* [84] for SrTi_{1-x}Cr_xO₃ samples obtained by sol-gel method. In addition to the contribution of Cr⁶⁺ and Cr³⁺, they found that the Cr³⁺/Cr⁶⁺ ratio strongly affects the electrical properties of the material. Wan *et al.* [85] reported that Cr doped STO exhibits low resistance with noticeable reversible hysteretic loops observed when a low voltage is applied. To explain this behaviour, they believe that the migration of oxygen vacancies resulting from the substitution of Cr³⁺ at the Ti⁴⁺ sites, is responsible for the resistance switching. Cr doping induces a transition from insulator to metal [86, 87], as well as a significant modification of the electronic properties and band structure of the hosting system [88, 89].

Other 3d TM-ions were also used for doping, such as Co, Mn, V, Mo to study the effects of each element on the fundamental properties of STO [20, 26, 65, 69, 90].

1.3 NiO

One of the main systems we are going to study is STO doped with Ni in which Ni atoms substitute Ti sites. This doping results in a chemical environment for Ni ions similar or close to the one for Ni in NiO. Therefore, using NiO as a reference to understand the fundamental physics behind the structure of the Ni 2p core level and other features is necessary.

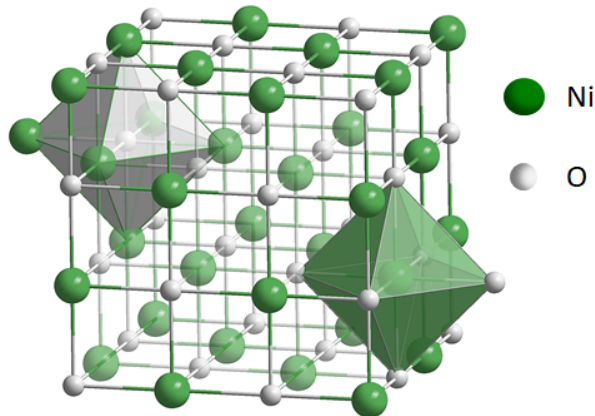


Figure 1.12: Crystal structure of NiO.

NiO is the more stable oxide form of nickel classified as a basic metal oxide [91]. It has a cubic structure with octahedral Ni²⁺ and O²⁻ sites as it is shown in Fig. 1.12. The understanding of its electronic structure is a long-standing problem and has been a subject of many experiments and

discussions over years due to the strong electronic correlation. To simply illustrate the problem, NiO has a partially filled d band as the Ni atom has eight $3d$ electrons. Its valence band is composed of O $2p$ band and localized Ni $3d$ electrons with Ni^{2+} ($3d^8$) ionic configuration [92], and therefore would be expected to be metal according to the one-electron band structure theories. However, the strong Coulomb repulsion between the d electrons leads instead to a wide band gap (~ 4 eV from experiments) [92,93]. NiO is therefore defined as a charge-transfer-type insulator at RT.

1.3.1 Electronic structure

Veenendaal *et al.* [94] and Tanaka *et al.* [95] gave a theoretical description of core levels in NiO in which they related the shape of the $2p$ photoemission spectra to the presence of neighbouring other Ni atoms. In fact the core level is a mixture of two processes happening: the first is due to screening electrons coming from the surrounding ligands and the second is due to the electrons coming from ligands around a neighbouring Ni ion. These two processes explain the double peaked main line of NiO (see Fig. 1.13 (a))

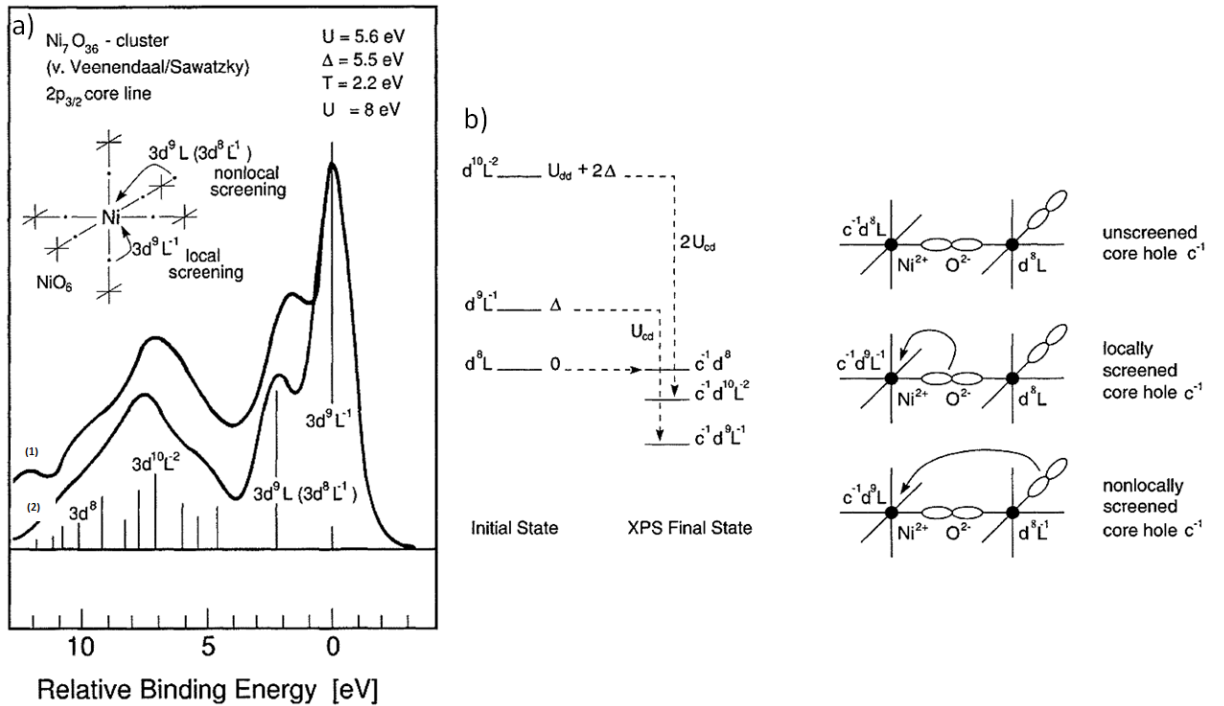


Figure 1.13: (a) Photoemission spectrum of the $2p_{3/2}$ core line in NiO (1) and the calculated spectrum in the non-local screening approximation (2). The inset shows the sketch of the mechanism of the local and the non-local screening processes; the splitting of the main line is due to two screening channels, a local one (d^9L^{-1}) and the non-local one $3d^9L(3d^8L^{-1})$. (b) Energy level diagram for the initial and final state photoemission of a Ni core line in NiO. In addition, the processes leading to an unscreened core hole $c^{-1}d^8L$, a locally screened core hole $c^{-1}d^9L^{-1}$, and a non-locally screened core hole $c^{-1}d^9L(d^8L^{-1})$ are shown. (data and caption from [94,96]).

Uhlenbrock *et al.* [97] measured the Ni $2p$ and O $1s$ core level spectra of NiO single crystal with XPS using monochromatic Al K_{α} radiation, as a function of ion bombardment. Some of the results are depicted in Fig. 1.14. They came to the conclusion that Ni^{3+} defects can be produced in NiO by sputtering but not during the growth or cleavage. However, the feature at 855.6 eV on the freshly cleaved perfect surface is related to correlation effects (see Fig. 1.14 (a)).

In these references [98,99], the surface and interface effects in the Ni $2p$ XPS spectra of NiO were reported. As presented in Fig. 1.15 (a), the Ni $2p_{3/2}$ surface-enhanced XPS shows a relative enhancement of the intensity of the well-known satellite at 1.5 eV higher binding energy from the main line, indicating a significant surface contribution of this satellite. The theoretical cluster calculations (Fig. 1.15 (b)) show that for surface Ni atoms having a pyramidal symmetry, the main line of the spectrum is shifted by 1 eV towards higher binding energy, and therefore, considerably contributing to the intensity of the satellite at 856 eV. Yet, other effects like non-local screening have also to be taken into account as they are located at the same binding energies and overlap with the surface compounds related.

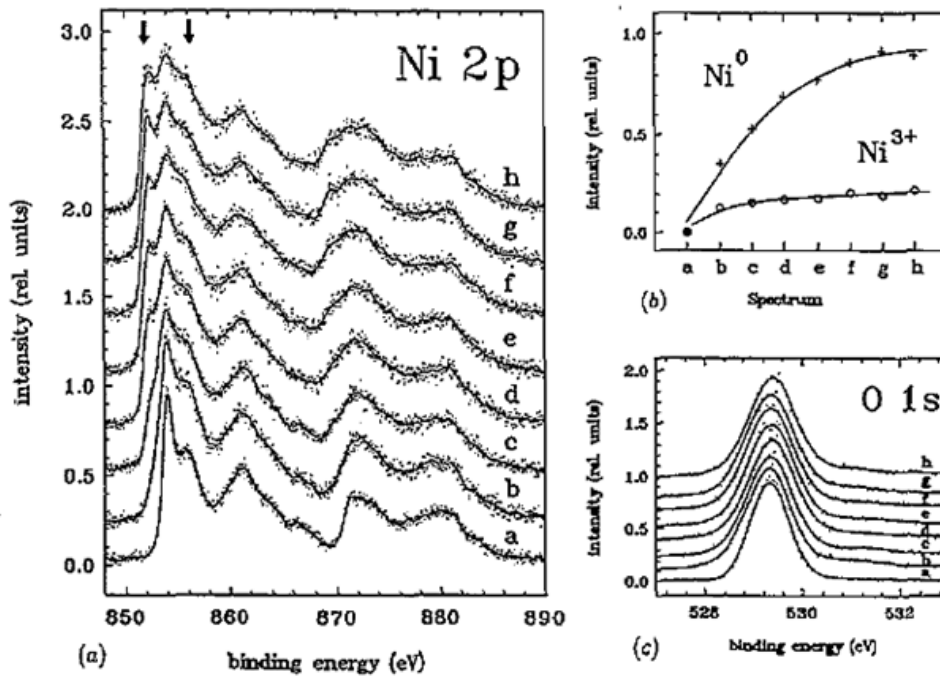


Figure 1.14: (a) Ni $2p$ XPS of a NiO(100) single crystal after successive sputter cycles. Sputter conditions: a, freshly cleaved in vacuum; b, 1 min/0.5 keV; c, 1 min/0.5 keV; d, 5 min/0.5 keV; e, 5 min/1 keV; f, 5 min/1.5 keV; g, 5 min/2 keV; h, 10 min/4.5 keV. (b) Intensity plot of the Ni 0 and Ni $^{3+}$ intensities from the Ni $2p_{3/2}$ spectra of pane (a). (c) O $1s$ XPS corresponding to the Ni $2p$ XPS of panel (a) (from [97]).

Resonance photoemission spectroscopy studies have been also performed on NiO valence band at photon energies in the vicinity of Ni $2p$ absorption threshold [100–102]. The Ni L -edge absorption spectrum of NiO is presented in Fig. 1.16 (b). It shows a spin-orbit splitting of the L_2 ($2p_{1/2}$) and L_3 ($2p_{3/2}$) edges. The different features observed are the main lines (labelled 2 and 13 in the spectrum), the multiplet structure located at 1.5 eV higher photon energy from the main line, and the satellite structure located at 6 eV higher photon energy from the main line. The multiplet structure is related to a multiplet splitting of the $2p^53d^9$ state which results from Coulomb interaction, exchange interaction, and crystal field effects [102,103].

The spectral intensity of the valence band as a function of the binding energy and photon energy around the Ni L_3 absorption edge is presented in Fig. 1.16 (a) from [101]. At the resonance with photon energy corresponding to the main XAS line, the valence band shows a very strong enhancement in intensity mainly at binding energies of 3.5 eV, 5 eV and 9.5 eV, and they related them to the resonance of the main Ni $3d$ states, multiplet structure and the satellites, respectively.

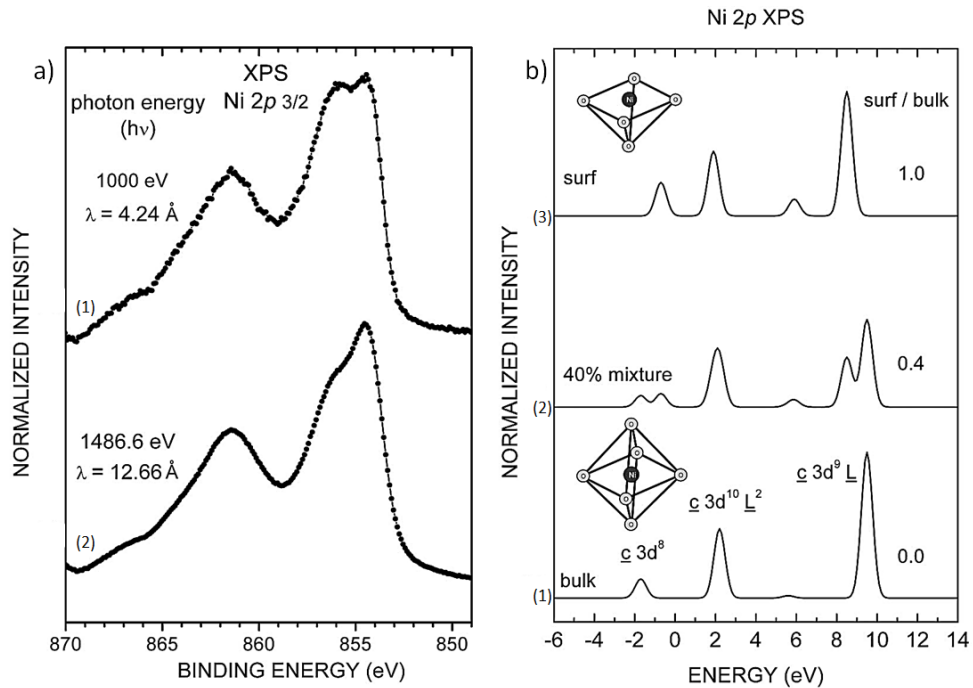


Figure 1.15: (a) Experimental XPS spectra of a NiO thin film measured at (1) 1486.6 eV and (2) 1000 eV photon energies. (b) Results of the cluster calculations performed in (1) octahedral symmetry, (2) a combination of a 60% octahedral and 40% pyramidal symmetries, and (3) pyramidal symmetry (from [98]).

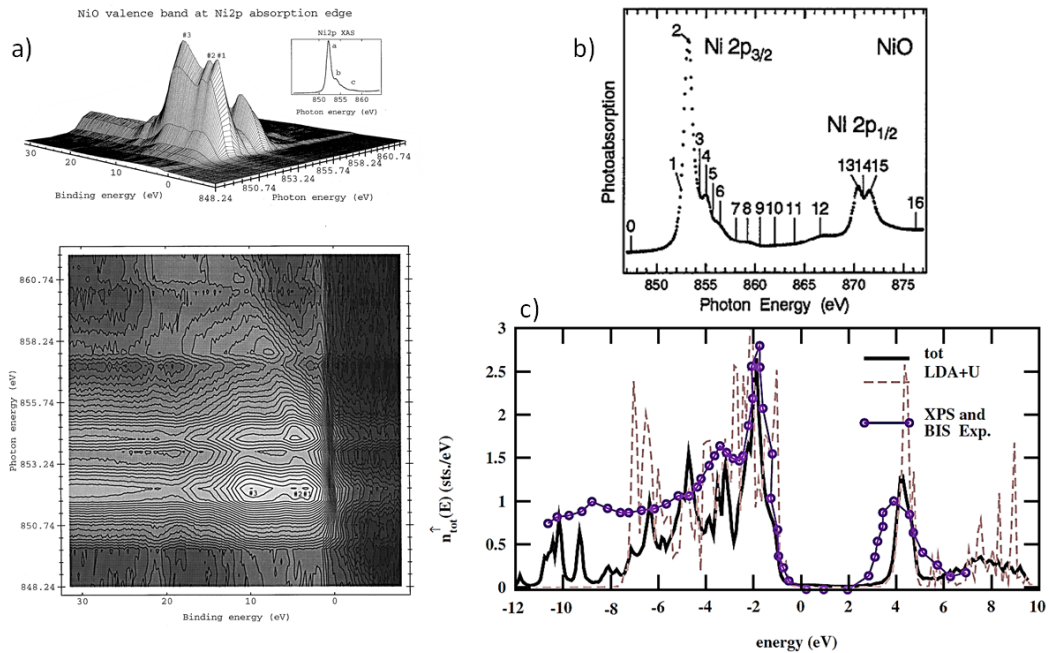


Figure 1.16: (a) Angle-integrated photoemission spectra of the NiO valence band at photon energies corresponding to the Ni 2p absorption edge (from [101]). (b) Ni 2p absorption spectrum of NiO [102]. (c) The total density of states of NiO compared with the experimental angle-integrated photoemission and inverse photoemission (from [104, 105]).

All previous studies on NiO and its electronic structure revealed the strongly correlated character of NiO. Theoretically, NiO is a typical example of the failure of DFT within the local density approximation (LDA) to produce the electronic ground state as it underestimate the Coulomb

interaction of the system. Minár *et al.* [106] calculated the total density of states of NiO by means of the full-potential KKR method and used $U = 8$ eV and $J = 1$ eV as parameters for the Coulomb interaction in the $3d$ shell (LSDA+U) and found that this approximation is sufficient for the band gap to match the experimental data as it is shown in Fig. 1.16 (c). However, it does not describe properly the several features seen at high binding energies in the valence band, in particular the satellite structure at a binding energy of about -10 eV. The use of LDA with the dynamical mean-field theory (DMFT) gave better match with the experiments in which all features were successfully reproduced (see Fig. 1.16 (b) the solid black line).

Experimental Methods

Spectroscopical methods are important tools in fundamental research as well as in applications where determination of the electronic structure, elementary composition and local atomic structure of a material are of interest. In the following, photoelectron spectroscopy and other x-ray based electron spectroscopies we used to perform our experiments are presented.

The samples we studied are pristine and transition metal doped STO thin films grown by magnetron sputtering and pulsed laser deposition. To optimize the growth process, the atomic structures of the films was characterized by high and low energy electron diffraction, and X-ray diffraction.

2.1 Photoelectron Spectroscopy

Photoelectron spectroscopy (PES) is considered as one of the most powerful techniques to study the electronic structure of solids and surfaces. It has significantly contributed to the understanding of fundamental principles in solid state physics. Historically, the first experiments that revealed the interaction between light and solids, known today as the photoelectric effect (PE), were performed by Heinrich Hertz in 1887 [107]. In 1905, Albert Einstein presented a theoretical explanation based on the quantum concept of Max Planck [108]. The PE is the phenomenon in which the absorption of light (photon) by a surface induces the emission of electrons from the surface. When the electron absorbs one of these photons, it uses part of the energy from the photon to escape from the surface. This energy is known as the work function ϕ_0 of the material. The remaining energy of the photon goes into kinetic energy E_{kin} of the electron. Thus, we can write

$$E_{kin} = \hbar\nu - \phi_0. \quad (2.1)$$

PES is non-destructive probe to examine the chemical composition (core level spectra) of a solid by XPS and its electronic structure (valence band) with ARPES. Figure. 2.1 shows the sketch of a photoelectron experiment and its fundamental principle. Photons from a monochromatized light source are directed on a sample and the photoelectrons, generated by the photoelectric effect, are analysed with respect to emission angle and kinetic energy by an electrostatic analyser. The sample and the detector are kept in an ultra-high vacuum (UHV) chamber in order to minimize surface contamination. The light source used for these measurements is either a synchrotron

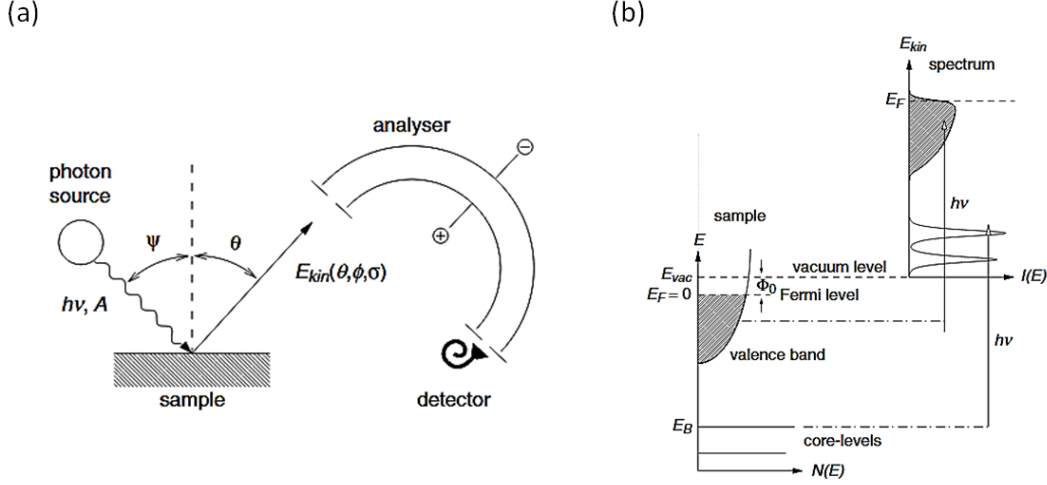


Figure 2.1: a) Principle of a photoelectron spectrometer. b) Schematic view of the photoelectron process in the single-particle picture. Electrons with binding energy E_B can be excited above the vacuum level E_{vac} by photons with energy $h\nu > E_B + \phi_0$. The photoelectron distribution can be measured by the analyser and is -in first order- an image of the occupied density of electronic states $N(E_B)$ in the sample (from [96]).

radiation, a discharge in a rare gas, an X-ray tube or a laser. By measuring the intensity of the emitted photoelectrons as a function of their kinetic energy and their emission angles, one can determine the binding energy E_B of the electrons in the solid and their momentum p , respectively, from the following equations:

$$E_{kin} = \hbar\nu - \phi_0 - E_B, \quad (2.2)$$

$$p = (2mE_{kin})^{1/2}. \quad (2.3)$$

Three-step model

A very successful model which is used in photoemission and well known in literature to simplify the photoemission process, is the three-step model (see Fig. 2.2) [109]. The steps are described as follows:

1. Excitation of an electron in the solid by absorption of a photon ;
2. Propagation of the photoexcited electron to the surface ;
3. Escape of the electron from the solid into the vacuum.

In the first step, by applying a small perturbation Δ , the transition probability w per unit time between the initial state Ψ_i and the final state Ψ_f of N -electrons is calculated by Fermi's Golden Rule:

$$w_{i \rightarrow f} = \frac{2\pi}{\hbar} |\langle \Psi_f | \Delta | \Psi_i \rangle|^2 \delta(E_f - E_i - \hbar\omega), \quad (2.4)$$

and the general expression of the photoemission intensity at a given energy E and momentum \mathbf{k} is expressed by:

$$I(\mathbf{k}, E) \sim |\langle \psi_f | \mathbf{A} \cdot \mathbf{p} | \psi_i \rangle|^2 f(E) A(\mathbf{k}, E). \quad (2.5)$$

The matrix element $\langle \psi_f | \mathbf{A} \cdot \mathbf{p} | \psi_i \rangle$ describes the excitation of the photoelectron from the solid and involves the electron-photon interaction to the photoemission intensity. It can be described in the

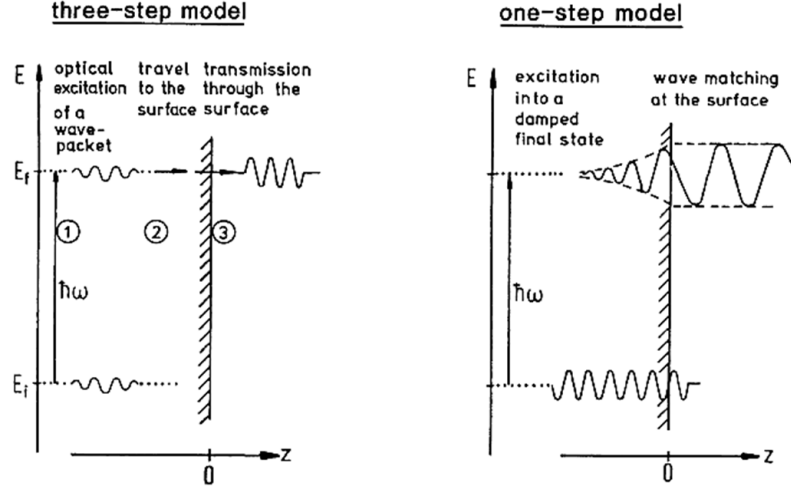


Figure 2.2: Illustration of the three-step and the one-step model in PES. The threestep model consists of (1) photoexcitation of an electron, (2) its travel to the surface and (3) its transmission through the surface into the vacuum. In the one-step model a Bloch wave electron is excited into a wave that propagates freely in the vacuum but decays away from the surface into the solid (from [96]).

framework of the *sudden-approximation* where the many-body interactions and the relaxation processes of the system are not included. Therefore, the initial system is described as a $N - 1$ body state with a single electron state with wavefunction ψ_i , and the final system consists of $N - 1$ particles and an electron final state with wavefunction ψ_f . \mathbf{p} stands for the electron momentum operator and \mathbf{A} for the electromagnetic vector potential of the photon radiation that depends on the light polarization and the photon energy [96].

$A(\mathbf{k}, E)$ is the spectral function and $f(E)$ the Fermi-Dirac distribution. The spectral function $A(\mathbf{k}, E)$ describes the probability with which an electron can be removed or added from an electron system in its ground state, modified by many-body interaction like electron-electron, electron-spin or electron-phonon interactions. This many-body interaction can be taken into account in the energy by adding to the single-particle electron energy $E^0(\mathbf{k})$, a so-called self-energy $\Sigma(\mathbf{k}, E)$:

$$\Sigma(\mathbf{k}, E) = Re\Sigma + iIm\Sigma, \quad (2.6)$$

and the spectral function can be written as

$$A(\mathbf{k}, E) = \frac{1}{\pi} \frac{Im\Sigma}{(E - E^0(\mathbf{k}) - Re\Sigma)^2 + (Im\Sigma)^2}. \quad (2.7)$$

In the independent particle approximation in which there no interactions are present, the self-energy is equal to zero and the spectral function becomes a delta function. In an interacting system with a finite self-energy, the initial band structure $E^0(\mathbf{k})$ is broadened by the imaginary part of the self-energy $Im\Sigma$ and shifted by the real part $Re\Sigma$ [96]. The measured spectra therefore contain information about the many-body interactions that occur in the solid after the photoemission process.

In the second step, one dominant mechanism that reduces the number of photoexcited electrons reaching the surface is the electron-electron interaction [110]. The intensity of the primary

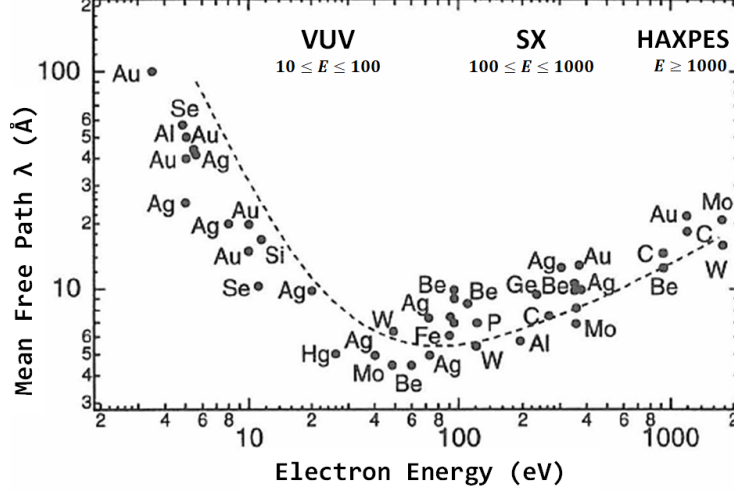


Figure 2.3: The electron energy dependent values of the inelastic mean free path λ in various materials exhibit a general trend that is highlighted by the dashed line (data taken from [111]). The different spectral ranges of radiations are shown in the graph.

photoelectrons, I_0 , is damped as a function of the distance d in the solid. The intensity decay can be expressed as followed:

$$I(d) = I_0 \exp - \left(\frac{d}{\lambda(E)} \right), \quad (2.8)$$

where $I(d)$ is the intensity after the primary photoelectrons have travelled the distance d in the solid. The parameter $\lambda(E)$, termed the inelastic mean free path, is defined as the distance an electron beam can travel before its intensity decays to $1/e$ of its initial value. Assuming that the scattering frequency $1/\tau$ ($\tau =$ lifetime) is isotropic and depends only on E , therefore, the $\lambda(E, k)$ is given by

$$\lambda(E, k) = (\tau/\hbar)dE/dk. \quad (2.9)$$

$\lambda(E)$ is described by the so-called universal curve (see Fig. 2.3). It indicates the surface sensitivity of the ARPES measurements. In UV-PES, the mean free path of an electron excited by a photon energy $\hbar\nu = 20 - 100$ eV is between $5 - 7$ Å, resulting in a sensitivity to the surface layer of the probed material. If the photon energy increases to 1000 eV, the mean free path is around 20 Å.

In the last step, the electron escapes the solid into the vacuum, where it is detected by an electron analyser. The escaping electrons are those for which the component of the kinetic energy normal to the surface is sufficient to overcome the surface potential barrier; the other electrons are totally reflected back into the bulk.

Definition of k and momentum conservation: Band structures are usually plotted in the reduced zone scheme. The bands outside the first Brillouin zone are folded back into the first Brillouin zone by adding the appropriate reciprocal lattice vector \mathbf{G} . Therefore, the wave vector of the photoexcited electron within the crystal is $\mathbf{K} = \mathbf{k} + \mathbf{G}$, where \mathbf{k} is the quantum number that defines the electron states. In the crystal, the wave vector of the photoelectron can be divided into a component parallel and a component orthogonal to the surface. For the wave vector parallel to the surface \mathbf{K}_{\parallel} , one has

$$\mathbf{p}_{\parallel}/\hbar = \mathbf{K}_{\parallel} = \mathbf{k}_{\parallel} + \mathbf{G}_{\parallel}. \quad (2.10)$$

Due to the translation symmetry along the surface, the momentum component parallel to the surface is conserved, which is Snell's law,

$$\mathbf{k}_{\parallel} = [(2m/\hbar^2)E_{kin}]^{1/2} \sin \theta. \quad (2.11)$$

The component orthogonal to the sample surface K_{\perp} (or k_{\perp}) is not conserved in the emission process because of the broken inversion symmetry along the crystal normal. The out-of-plane component can be obtained by the assumption of a free electron final state in the vacuum, with a dispersion. The kinetic energy outside the crystal is determined by [96]

$$E_{kin} = \hbar^2/2m[\mathbf{K}_{\parallel} + (p_{\perp}/\hbar)^2] = E_f(\mathbf{k}) - E_v, \quad (2.12)$$

where E_v (< 0) is the energy of the bottom of the valence band and p_{\perp}/\hbar is the perpendicular component of the electron wave vector in the vacuum. The out-of-plane component k_{\perp} is therefore given by [112]

$$k_{\perp} = 1/\hbar \sqrt{2m_e(E_{kin} \cos^2 \theta + V_0 + \phi_A)}, \quad (2.13)$$

where V_0 is the inner potential and ϕ_A is the work-function of the analyser.

In practice the dispersion with k_{\perp} is obtained by scanning the photon energy. For 2-dimensional states, k_{\perp} does not disperse due to the finite extension of the states in out-of-plane direction. Yet, 3-dimensional states show a distinct dispersion with k_{\perp} . In this case, the unknown inner potential V_0 can be determined experimentally, based on the periodicity of the 3-dimensional states with the out-of-plane momentum according to the Brillouin zone size of the material.

While the three-step model makes the photoemission process quite comprehensible and easy to discuss, it is no more than a useful approximation. In order to theoretically treat the process correctly the true final state has to be introduced into equation (2.4) in addition to the initial Bloch state. The three-step model and its relation to the correct one-step model are sketched in Fig. 2.2. In the one-step model one considers the excitation from an initial state (Bloch wave in the crystal) into a damped final state near the surface, the damping taking care of the short mean free path of the electrons in the solid. More details will be presented in the next chapter, section 3.3.

2.2 Resonant Photoemission Spectroscopy

Resonant photoemission is the photoelectron emission process that occurs in the vicinity of an X-ray absorption edge, that is with a photon energy around the binding energy of a core level. This phenomenon leads to pronounced effects for strongly correlated electron systems with transition metals where there is a huge enhancement in the photoemission cross section at resonance. The resonant photoemission process is most prominent for systems where the electrons of partially filled valence shells retain some of their atomic-like properties while at the same time they may or may not contribute to the solid state bonding.

Here, we will focus on resonant photoemission from the valence states. In the direct photoemission

process, a photon is absorbed causing the transition of one electron from a valence state into the continuum and detected at some energy ϵ_p . The process can be written as

$$|\psi_g\rangle + \hbar\omega \rightarrow |\psi_f(\underline{v}), \phi_p\rangle, \quad (2.14)$$

where ψ_g is the N -electron ground state with energy E_g , $\psi_f(\underline{v})$ a $N - 1$ -electron final state with a valence hole (\underline{v}) and energy E_f , and ϕ_p the photoelectron wave function. From energy conservation we have $\epsilon_p = \hbar\omega - E_f + E_g$ and the spectral intensity is given by

$$I(\epsilon_p, \omega) = \sum_f |\langle \psi_g | T(\omega) | \psi_f(\underline{v}), \phi_p \rangle|^2 \delta(\hbar\omega - \epsilon_p - E_f + E_g). \quad (2.15)$$

In non-resonant photoemission, there is only the direct process where the transition operator $T(\omega)$ corresponds to the interaction of the electrons with the photon field $V_{rad} \equiv -\frac{e}{mc} \mathbf{A} \cdot \mathbf{p}$. Here, \mathbf{A} is the vector potential of the light, \mathbf{p} is the electron momentum and V_{rad} does not explicitly depend on the photon energy ω .

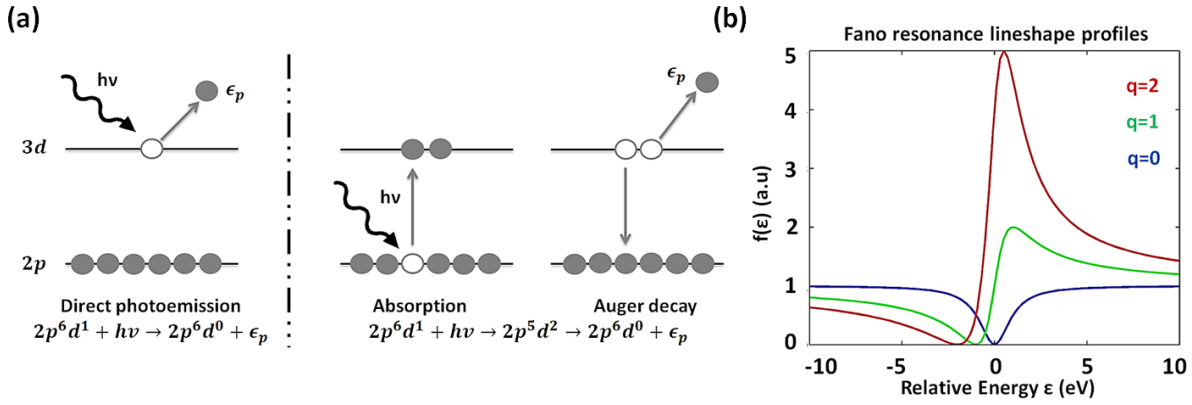


Figure 2.4: (a) Processes involved in resonant photoemission measurement at an L absorption threshold. The left diagram shows direct photoemission from $3d$ states. On the right, the two step process of absorption followed by a coherent Auger decay. In both cases the initial and final state are identical. (b) Characteristic Fano profiles for different q -values.

For photon energies around the absorption threshold, a new transition channel opens up, its the photoabsorption from a core-level followed by the decay of the core-excited state through auto-ionization. In the latter process the excited electron and one valence electron scatter by Coulomb interaction such that one electron fills the core hole and the other one is ejected as the photoelectron (see Fig. 2.4 (a) for transitions involved in an L -edge resonant photoemission experiment). The core-excitation and auto-ionization have to be considered as a coherent (one-step) process which leads to the same final state as the direct photoemission process. The resonant process is

$$|\psi_g\rangle + \hbar\omega \rightarrow |\psi_m(\underline{c}, k)\rangle \rightarrow |\psi_f(\underline{v}), \phi_p\rangle, \quad (2.16)$$

where ψ_m denotes a N -electron intermediate state with one core-hole (\underline{c}) and one electron in an excited state (k). When the resonant process is included, the transition operator becomes [95, 113]

$$T(\omega) = V_{rad} + V_C \sum_m \frac{|\psi_m\rangle \langle \psi_m|}{\hbar\omega + E_g - E_m + i\Gamma_m/2} V_{rad}. \quad (2.17)$$

Here, $V_C = e^2/r_{12}$ is the electron-electron Coulomb interaction responsible for the auto-ionization process, E_m is the energy of the intermediate state and Γ_m the life-time width of the core-excited

state. We note that if the coherence is lost in the intermediate state $|\psi_m(\underline{c}, k)\rangle$, the final states of the two channels differ and an incoherent Auger decay occurs, which does not interfere with the direct photoemission channel.

A simple description of resonant photoemission was first provided by the Fano theory [114]. It was first used in 1961 by Fano to describe the absorption spectrum of helium which is influenced by interference between the auto-ionizing resonances and the direct process. In this model, the Hamiltonian is diagonalized into a subspace which consists of one discrete core-excited ϕ with energy E_ϕ and one continuum Ψ_E with states of energy E . The non-diagonal matrix elements V_E are between the discrete state and the continuum. In the resonant photoemission process, ϕ is the core-excited intermediate state and V_E is the Auger matrix element for the decay step. The eigenfunctions of the continuum states Ψ_E can be expressed as

$$\Psi_E = a_E \phi + \int dE' b_{EE'} \Psi_{E'}, \quad (2.18)$$

where a_E and $b_{EE'}$ are wave function coefficients. The transition matrix element T to excite the state Ψ_E from the ground state Φ_g can then be written as

$$\langle \Psi_E | T | \Phi_g \rangle = a_E^* \langle \phi | T | \Phi_g \rangle + \int dE' b_{EE'}^* \langle \Psi_{E'} | T | \Phi_g \rangle. \quad (2.19)$$

The ratio f between the transition probability $|\langle \Psi_E | T | \Phi_g \rangle|^2$ and the probability of the transition to the unperturbed continuum $|\langle \Psi_E | T | \phi_g \rangle|^2$ gives the Fano resonance lineshape curves

$$f(\epsilon) = \frac{(q + \epsilon)^2}{\epsilon^2 + 1}. \quad (2.20)$$

The variable ϵ represents a reduced energy for which the resonance energy is located at 0 and q is the asymmetry strength parameter that determines the shape of the resonance. The Fano resonance lineshape curves $f(\epsilon)$ are plotted in Fig. 2.4 (b) for different values of q . At the limit $\epsilon \rightarrow \pm\infty$, i.e. far away from resonance, the discrete state has no influence and f is close to 1. The maximal enhancement is given by $q^2 + 1$ and is located at positive ϵ close to $\epsilon = 0$.

Back to equations (2.15) and (2.17), the photocurrent in resonant photoemission can be expressed as [115]

$$I(\omega, \epsilon_p) = \sum_v |\langle \phi_p | V_{rad} | \phi_v \rangle + \sum_{c,k} \frac{\langle \phi_p \phi_c | V_C | \phi_v \phi_k \rangle - [v \leftrightarrow k]}{\hbar\omega + \epsilon_c - \epsilon_k + i\Gamma_{ck}/2} \langle \phi_k | V_{rad} | \phi_c \rangle|^2 \delta(\hbar\omega - \epsilon_p + \epsilon_v), \quad (2.21)$$

where $[v \leftrightarrow k]$ denotes the exchange term and all other notation is obvious from the foregoing. The first term in equation (2.21) represents the direct photoemission, whereas the second term considers the Auger decay channel. The sum goes over several intermediate states between the two channels inducing the interference.

In the Fano model with one core-hole excitation, the photoemission intensity can be written as

$$I(\omega, \epsilon_p) \equiv |\langle \phi_p | V_{rad} | \phi_v \rangle|^2 \cdot \frac{(q + \epsilon)^2}{(1 + \epsilon^2)}, \quad (2.22)$$

where the reduced energy ϵ is equal to $(\frac{\hbar\nu - \hbar\nu_0}{\pi V_E^2})$, with $\hbar\nu_0$ the resonance energy and V_E the matrix element for the Auger decay. The parameter q is also connected to the matrix elements

of the involved processes. In case of resonant photoemission at the L -edge (see figure (2.4(a))), one can write [116]

$$q = \frac{\langle 3d|V_{rad}|2p\rangle}{\pi V_E \langle \epsilon_p|V_{rad}|3d\rangle}. \quad (2.23)$$

Here, the numerator contains the matrix elements for the X-ray absorption process whereas the denominator carries both Auger decay (V_E) and direct photoemission processes.

2.3 Photoelectron Diffraction

XPD is a method for the analysis of surface atomic structure including morphology and chemical composition. It is a scattering technique based on electron scattering that thus provides local structural information [117]. The physics of this technique can be explained as follows: by sending an incident beam of monochromatic X-rays, photoelectrons from a core level of a near-surface atom of a solid will be emitted (the emitter). Elements of the outgoing photoelectron wavefield are elastically scattered by atoms neighbouring the emitter which result in interference of the different scattered elements with the directly emitted part of the wavefield (see Fig. 2.5). Depending on the photoelectron wavelength and the scattering path-length differences, constructive or destructive interferences will happen. That requests to adjust the detected intensity in specific directions as a function of photoelectron energy (angle-scanned mode) or at fixed energy as a function of emission direction (energy-scanned mode). These adjustments are therefore typical properties of the local scattering geometry and the local structure.

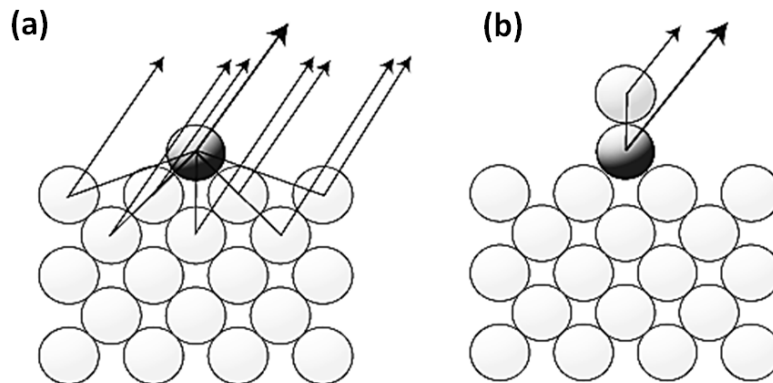


Figure 2.5: Schematic diagram showing the main scattering paths which contribute to the photoelectron diffraction process in the case of: (a) an adsorbate structure determination using backscattering; (b) a molecular orientation determination using forward scattering (from [118]).

Two different electron energy ranges describe distinguishable applications of the technique. The first one is expressed by the use of relatively low electron energies (less than 500 eV), in which backward scattering effects are reasonably strong. If the emitter stands in the most external layer of the surface, scattering from the layers below gives information on the record of these overlayer atoms (Fig. 2.5 (a)). This is powerful and suitable to study the local distribution of different elemental specificities on surfaces. In this backscattering mode of the technique, the scanned-energy mode of data collection as well as the angle-scan experiments are appropriate. The second case sketched in Fig 2.5 (b) consists in using higher electron energies. Then, the

electron elastic scattering cross-section of the atoms tops out strongly in the forward direction around 0° scattering. The photoelectron diffraction peak related to this forward scattering is in the zero order since it does not include a scattering path-length difference and its angular location is independent of the energy. This obviously means that only angle-scan experiments are convenient at high photoelectron energies. In addition, the emitter should not be at the outer atomic layer. Still, the final state given by the interference between the direct and the coherently scattered components of the photoelectron signal, as we mentioned above, depends strongly on the electron kinetic energy, the detector geometry and the position of the emitter atom relative to the scatterers. The variation of all these parameters results in a change in the interference conditions and thus can be used to extract geometrical information. More details about XPD and its applications can be found in the references [119–123].

2.4 Synchrotron Measurements

The majority of the data presented in this thesis have been measured at PEARL, ADDRESS and CASSIOPEE beamlines of the SLS and SOLEIL synchrotrons.

2.4.1 High-Resolution Angle-Resolved Photoelectron Spectroscopy

The ARPES measurements presented here were performed at the high-resolution angle-resolved photoemission spectroscopy (HR-ARPES) endstation at the CASSIOPEE beamline of SOLEIL. The photoelectron analyzer in use is a Scienta R4000 hemispherical analyzer. Its angular acceptance was set to 30° for the present experiments. The sample can be moved by a motorized 6-axis manipulator $(x, y, z, \theta, \psi, \phi)$, and cooled down to 90 K with liquid nitrogen cryostat. The combination of an angular acceptance of 30° and the rotation θ makes it possible to scan a large area of the reciprocal space. The CASSIOPEE beamline uses two undulators that provide linearly (vertical or horizontal) or circularly (right or left) polarized photons in the 8 – 1500 eV energy range with best working conditions regarding the intensity in the range from 20 eV to 800 eV. In order to transform the emission angle θ and ϕ in the geometry of the HR-ARPES setup to the momentum of the electrons, we used the following equations (see eq. 2.11 and eq. 2.13):

$$k_{\parallel}^x = 1/\hbar\sqrt{2m_e E_{kin}} \sin \theta \cos \psi \quad (2.24)$$

$$k_{\parallel}^y = 1/\hbar\sqrt{2m_e E_{kin}} \sin \theta \sin \psi \quad (2.25)$$

$$k_{\perp}^z = 1/\hbar\sqrt{2m_e(E_{kin} \cos^2 \theta + V_0 + \phi_A)}. \quad (2.26)$$

2.4.2 Soft X-ray Angle-Resolved Photoelectron Spectroscopy

In chapters 5 and 6, part of the presented data (mainly resonant ARPES measurements) were collected at the soft x-ray ARPES endstation at the ADDRESS beamline of SLS. At this beamline, the photon energy range is between 300 eV and 1600 eV with linearly (left, right) and circularly (left, right) polarized light. The analysis chamber is connected to a PHOIBOS 150 hemispherical analyser having an angular acceptance of $\pm 8^\circ$. Note that the momentum resolution as well as the photoionisation cross section for valence band states are reduced at higher photon energies. To

optimize the signal, a high pass energy of the analyser is chosen, reducing the energy resolution. The special advantage of the soft x-ray ARPES in the study of oxide materials is the possibility to measure resonant photoemission at the transition metal resonances (here Ti L -edge and Ni L -edge) to get information on correlations and hybridizations.

Here, the momentum of the photon is not negligible and does contribute to the photoelectron momentum (this contribution is comparable to the size of the Brillouin zone). For this reason, a correction for the expressions of eq. 2.11 and eq. 2.13 is required as follow [124]:

$$k_{\parallel}^x = 1/\hbar\sqrt{2m_e E_{kin}} \sin(\theta_M + \theta_A) - \frac{h\nu}{\hbar c} \sin(\alpha - \theta_M) \quad (2.27)$$

$$k_{\parallel}^y = -1/\hbar\sqrt{2m_e E_{kin}} \sin(\psi_M + \psi_A) - \frac{h\nu}{\hbar c} \sin(\alpha - \theta_M) \sin \psi_M \quad (2.28)$$

$$k_{\perp}^z = 1/\hbar\sqrt{2m_e(E_{kin}\theta + V_0 + \phi_A) - k_{\parallel}^2} - \frac{h\nu}{\hbar c} \sin(\alpha - \theta_M), \quad (2.29)$$

where θ_A and ψ_A are the angles between the electron momentum and the analyser. The angles θ_M and ψ_M are for the manipulator rotation angles parallel and perpendicular to the slit, respectively (see Fig. 2.6 (c)).

2.4.3 Angle-Resolved Photoelectron Diffraction

For the characterization of local atomic structure of our thin films, we used the photoemission station connected to the PEARL beamline of SLS where the photoelectron diffraction measurements were performed. The beamline is installed at the 1.4 T bending magnet X03DA that provides mainly linearly horizontal polarized light in the energy range of 60 – 2000 eV. It is optimized for high photon flux in the range between 500 and 1000 eV where most photoelectron diffraction measurements of the lighter elements take place.

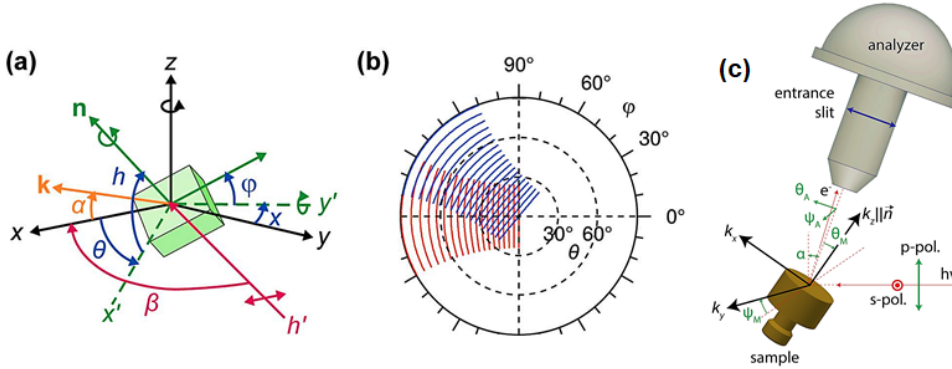


Figure 2.6: (a) Measurement geometry in the ARPES chamber at PEARL. The coordinate axes x , y and z are fixed in the laboratory frame of reference. Photoelectrons are detected in the xz plane under the acceptance angle $-30^\circ \leq \alpha \leq +30^\circ$ centered on the x axis. The synchrotron beam enters at an angle $\beta = 60^\circ$ with respect to the x axis, the polarization vector of horizontal light is in the xy plane. The sample can be moved in the x , y and z directions, and rotated about the z (polar angle θ) and y' (tilt angle ψ) axes, as well as about the surface normal \mathbf{n} (azimuthal angle ϕ). (b) Scanning scheme of angle-scanned photoelectron diffraction in the spherical coordinate system in stereographic projection. A full scan of emission angles in the hemisphere is a combination of polar (θ) and azimuthal (ψ) scans. Each of the curved lines in the plot corresponds to the angle range detected in one shot. For clarity, only a few angles are shown (from [125]). (c) Setup of the ADDRESS beamline with marked analyser angles θ_A , ψ_A and the manipulator angles θ_M , ψ_M ($\alpha=20^\circ$) (from [124,126]).

For the polar-angle-scanned XPD data presented here, a two-dimensional manipulator scan of

(θ, ϕ) was used for the measurements, and the intensity distribution $I(E, \alpha)$ at each scan position was recorded with a EW4000 electron analyser that contains a two-dimensional multi-channel plate detector (see Fig. 2.6 (a,b)). Technically, the distribution of photoelectron counts depends strongly on the polar emission angle α due to the angular dependence of the differential photoionization cross section. In addition, the cross section of the analysed volume or the escape depth can also modify the signal. These reasons made the processing of the experimental data complex and in addition a normalization procedure is required after averaging and smoothing the measured data [125]. All details about the procedures we used can be found at the following website: <https://gitlab.psi.ch/pearl-public/igor-procs>.

2.5 Sample Growth

2.5.1 Radio Frequency Magnetron Sputter Deposition

Radio frequency (RF) magnetron sputtering is a technique where argon ions are accelerated by a RF electric field to hit a target made of the material to sputter. The target is sputtered in all directions and sputtered atoms will reach the substrate placed in front of the target. When a magnetic field is used to fold ion and electron trajectories, the mean free path and sputtering yield are increased. This technique is a low-cost and easy control method for film growth, especially suitable for large-scale film deposition.

In this study, STO films were deposited by RF (13.56 MHz) magnetron sputtering using a BOC Edwards TF 600 coating system. Before sputtering, the deposition chamber was evacuated to a base pressure of 2.10^{-4} Pa. Substrates were cleaned by ion etching in argon plasma by applying RF power of 200 W for 15 minutes at 0.2 Pa. A pure target of STO was placed on a magnetron connected to the RF power supply. The deposition was kept under constant discharge RF power (400 W). The films were deposited on amorphous Si substrates at 400°C in argon atmosphere at constant pressure 0.6 Pa. The thickness of the films was in the range of 70 to 100 nm. In case of Ni-doped STO deposition, Ni pellets were placed on the deposition target.

2.5.2 Pulsed Laser Deposition

PLD has gained a great deal of attention in the past few years for its success in depositing materials of complex stoichiometry. PLD was the first technique used to successfully deposit a superconducting $\text{YBa}_2\text{Cu}_3\text{O}_7$ thin film. Since that time, many materials that are normally difficult to deposit by other methods, especially multi-element oxides, have been successfully deposited by PLD. This is a physical vapour deposition technique like RF sputtering where a high power pulsed laser beam is focused to strike a target of the desired composition. Material is then vaporised and deposited as a thin film on a substrate facing the target. This process can occur in ultra high vacuum or in the presence of a background gas, such as oxygen when depositing films of oxides [127] (see Fig. 2.7 (a,b)).

Growing oxide thin films involves a number of requirements. Often, epitaxial growth of a material is preferred and therefore the choice of the appropriate substrate material is important. Basic requirements are: a good crystallographic lattice match between film and substrate; the

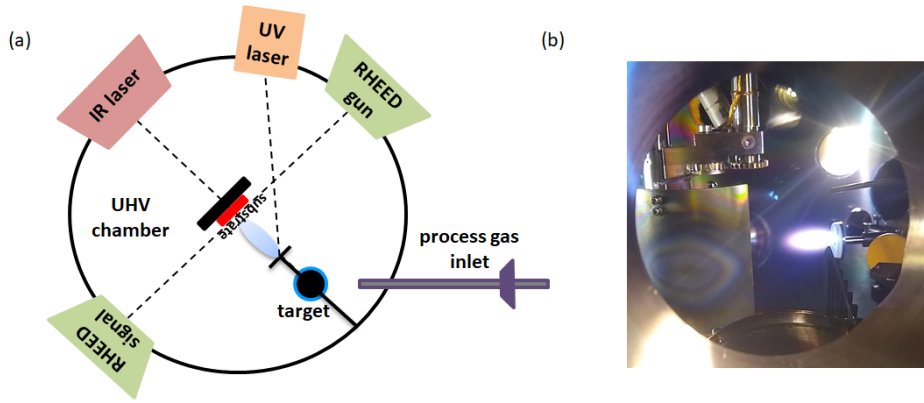


Figure 2.7: (a) Sketch of the PLD setup with the relevant components. (b) Photograph of the plasma plume taken in the setup used in Würzburg.

substrate material should be chemically compatible with the film; film and substrate should have comparable thermal expansion coefficients, and a thermodynamically and chemically stable surface. Essential for some applications is to choose selectively the chemical termination of the surface [128, 129]. Other variables in the PLD growth process should be controlled such as the laser power and repetition rate, the oxygen background pressure, the target to substrate distance and the substrate temperature. However, once the correct parameters for a type of material are found, a high-quality growth is possible.

The PLD system used for the growth of films studied in this thesis is a laser beam with a wavelength of 248 nm and an energy of approximately 62 mJ per pulse (1.8 J/cm^2). The pulses have a repetition rate of 1 Hz. As target, commercially available, pressed powder with the desired stoichiometry are used (pure SrTiO_3 , $(\text{NiO})_{0.06}:(\text{SrTiO}_3)_{0.94}$ and $(\text{NiO})_{0.12}:(\text{SrTiO}_3)_{0.88}$). The substrate has a size of $0.5 \times 5 \times 10 \text{ mm}^3$ and is clamped on top of a Nb doped STO substrate. Before and during film deposition, the substrate is heated by an infrared (IR) laser directed at the back side of the sample holder. The temperature is measured with an internal pyrometer. For the samples grown for this thesis, a temperature of approximately 700°C and oxygen pressure of 1.10^{-1} mbar were chosen. The substrates used for film growth had a (001) surface to reach a layer-by-layer growth condition. The sample as well as the target are mounted on manipulators for a precise alignment. The PLD system is furthermore equipped with a RHEED setup to monitor the growth. After the growth, the sample can be in situ transferred from the PLD growth chamber to the LEED chamber and then to the end station to do XPS experiments.

2.6 Electron Diffraction Methods

2.6.1 Reflection high-energy electron diffraction and low-energy electron diffraction

RHEED and LEED were used to characterize the sample surface regarding its crystalline quality and to identify possible reconstructions. Both techniques are based on the same principle, but are different in geometry and energy. RHEED is the standard equipment in epitaxial growth

chambers providing the opportunity to monitor the growth process. This real-time in situ method makes it possible to control the growth with atomic layer precision. In contrast, the LEED characterization is done after sample growth.

The instrumental part of LEED and RHEED consists of an electron gun and a fluorescent screen that detects the electrons diffracted by the sample under study. Since its discovery in 1927 by Davisson and Germer [130], LEED has become a widely used method for analyzing surface structures. In a typical LEED setup, the electrons are accelerated with voltage V in the $10 \sim 500$ V range. Then the de Broglie wavelength of the electrons, $\lambda_e = h/(2m_e V e)^2$, ranges from 0.5-3.8 Å. Here h is the Planck constant, m_e is electron rest mass, and e is the elementary charge. The electron beam impinges on the surface along the surface-normal direction, and the elastically backscattered electrons give an intensity pattern which visualizes (or maps) the reciprocal lattice of the surface layer. On the basis of this information about the reciprocal lattice, the real-space surface lattice can be constructed. The mathematical relation between the real lattice and reciprocal-lattice vectors can be found for example in [131,132]. The diffraction is described by the Laue condition: $\mathbf{k}_{\parallel} = \mathbf{G}$. Here \mathbf{G} is the surface reciprocal lattice vector, and \mathbf{k}_{\parallel} is the parallel component of the change ($\mathbf{k}_{out} - \mathbf{k}_{in}$) in which \mathbf{k}_{in} and \mathbf{k}_{out} are the incident and scattered wave vectors of the electron, as represented schematically in Fig. 2.8. The Laue equation also provides a physical meaning for the reciprocal vectors: every diffraction beam corresponds to the reciprocal vector. Because LEED operates in a low-energy regime, which is close to the minimum of the “universal” curve of electrons mean-free path in solids, the elastic scattering occurs mainly on the topmost layers. In RHEED, electrons are accelerated at much

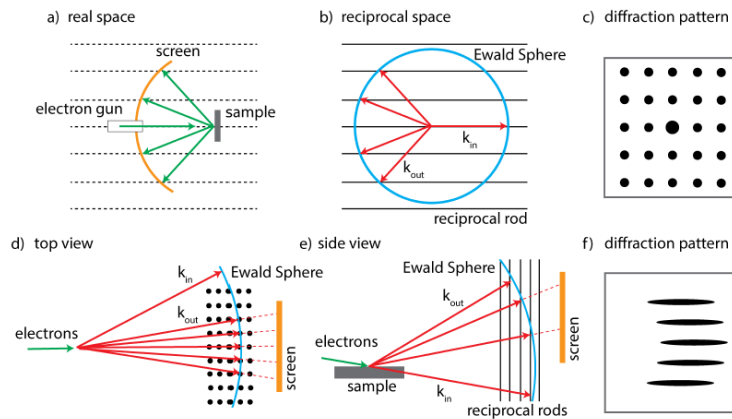


Figure 2.8: (a-c) Illustration of the LEED process. (a) Experimental setup. (b) Ewald sphere construction and (c) resulting diffraction pattern (from [126,133]). (d-f) Ewald sphere construction in the RHEED process in (d) top-view and (e) side view with (f) resulting diffraction pattern (from [126,134]).

higher voltages (i.e., from about 5 to 50 kV). For a voltage of 10 kV, the de Broglie wavelength of the electrons is 0.123 Å. The electrons hit the target at a small angle of $1^\circ - 8^\circ$ relative to the surface plane making the formation of a RHEED pattern extremely sensitive to the surface. The diffraction is described by the Laue condition as for LEED. In addition to the change in the electron momentum perpendicular to the surface, the diffraction process leads to a change of the momentum parallel to the surface. This gives rise to a set of diffracted beams on either side of the specular reflected beam. If the incident electron beam is parallel to the rows of surface

atoms that are separated by the lattice vector d_S in the direction perpendicular to the beam direction, then the diffracted electron beams contribute to constructive interference. The angle of diffracted electrons relative to the incident direction, θ , fulfils the Bragg diffraction condition: $2d_S \sin \theta = n\lambda_E$, where d_S is the interplanar distance and n is a positive integer.

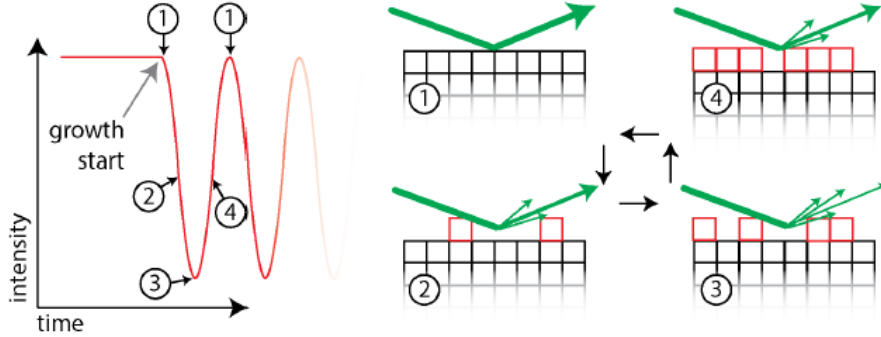


Figure 2.9: Origin of the RHEED oscillations during film growth. The diffracted electron beam (green) gets weaker due to ad-atoms at the surface. Maximal intensity is reached at the complete formation of a layer (from [126]).

In terms of application, RHEED has certain advantages over LEED: it provides an opportunity for real-time in situ monitoring of the surface structure during a layer growth, and can be used to determine the growth rate of epitaxial layers. Indeed, the intensity of the RHEED pattern gives information on the roughness of the surface and can therefore give real time information of the film growth. The intensity variation during the growth is called RHEED oscillations (see Fig. 2.9). For a perfect, well-ordered surface the RHEED intensity is high. When the deposition process starts, a partial coverage leads to a weakening of the RHEED intensity. Finally, full intensity is recovered when a complete layer is formed. Based on the RHEED oscillations the thickness of the film as well as the time to stop the deposition at the complete coverage can be determined and you can count the number of layers.

2.6.2 X-ray Diffraction

XRD is a characterization technique that provides bulk sensitive information about the crystal structure such as phase analysis, size of the crystallites, their crystallographic orientation and micro-strains. Our measurements were carried out using an automatic powder X-ray diffractometer X'Pert Pro equipped with a PIXcel ultra-fast linear semiconductor. Cu $K\alpha$ radiation ($\lambda=0.154$ nm) was used as an X-ray source. Due to the bulk sensitivity of XRD, no significant diffraction signal is obtained from ultrathin films of few unit cells thickness. Thus, only our films prepared by magnetron sputtering were characterized by XRD. Diffraction patterns were recorded mostly from 25 to 60 degrees in 2θ scales, where four strongest SrTiO₃ lines are located. The position, height, integrated intensity and full width at half maximum (FWHM) are the main four parameters that characterize the diffraction lines. For our measurements, we used the so-called asymmetric $\omega - 2\theta$ scans shown in Fig. 2.10. In this case the angle of incidence ω between x-rays and sample surface is small and fixed (usually much less than 10 degrees), whereas the detector moves by 2θ . Lattice planes where diffraction takes place are deflected in this case from the sample surface with an angle of $\theta_{hkl} - \omega$. The advantage of this geometry is

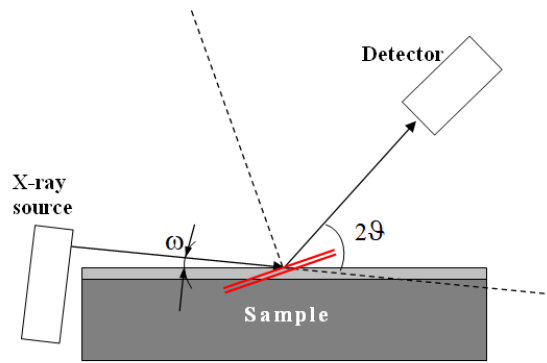


Figure 2.10: Scheme of the asymmetric $\omega - 2\theta$ geometry for XRD measurements.

that the X-ray beam does not penetrate too much into the sample when the investigated films are sufficiently thick, so we do not observe diffraction lines from the substrate material. Furthermore, the irradiated area of the sample surface is always constant during the measurement due to the fixed X-rays angle of incidence.

Theoretical Approach

This chapter is dedicated to the theoretical approach and computational method we used in this work. In the first part, we introduce the basis of density functional theory including Born-Oppenheimer approximation, Kohn-Sham equations and the exchange-correlation functionals. The second part represents more in details the Green's function Korringa-Kohn-Rostoker method based on the multiple scattering theory. The formalism of this method in case of an ordered system is presented at first. Then, we show the case of a disordered system with the most commonly applied approximations, in particular, the coherent potential approximation we used in our calculations. In the last part of this chapter, an introduction of the one-step model of photoemission and a theoretical description of the corresponding photocurrent are discussed. The author of this thesis got inspired by the following references to write this chapter [135–141].

3.1 Density Functional Theory

DFT is a computational quantum mechanical modelling used to investigate the electronic structure of many-body-electron systems. Using this theory, the properties of such systems can be determined by using functionals of the spatially dependent electron density [142, 143].

In the context of computational materials science, *ab initio* DFT calculations allow the prediction and calculation of material behaviour on the basis of quantum mechanical considerations, without requiring higher order parameters such as fundamental material properties. In DFT, the electronic structure is evaluated using a potential acting on the system's electrons. This DFT potential is constructed as the sum of external potentials, which is determined by the structure and the elemental composition of the system, and of an effective potential, which represents the interelectronic interactions. Despite recent improvements, there are still difficulties in using DFT to properly describe dopant interactions and some strongly correlated systems, as well to calculate the band gap and ferromagnetism in semiconductors [144]. For these reasons, the development of new DFT methods designed to overcome these problems, by alterations of the functional [145] or by the inclusion of additive terms [146–148], has become a current research topic.

3.1.1 Derivation and formalism

In many-body electronic structure calculations, the nuclei of the treated system are seen as fixed (Born-Oppenheimer approximation), generating an external potential V in which the electrons are moving. A stationary electronic state is then described by the many body wave function $\psi(\mathbf{r}_1, \dots, \mathbf{r}_N)$ satisfying the many-electron time-independent Schrödinger equation

$$\hat{H}\psi = [\hat{T} + \hat{V} + \hat{U}]\psi = \left[\sum_i^N \left(-\frac{\hbar^2}{2m_i} \nabla_i^2 \right) + \sum_i^N \sum_m^M V(\mathbf{r}_{im}) + \sum_{i<j}^N U(\mathbf{r}_i, \mathbf{r}_j) \right] \psi = E\psi \quad (3.1)$$

where, for the N -electron system, \hat{H} is the Hamiltonian, E is the total energy, \hat{T} is the kinetic energy, \hat{V} is the potential energy from the external field due to positively charged nuclei, \hat{U} is the electron-electron interaction energy and m_i is the electron mass. The operators \hat{T} and \hat{U} are called universal operators as they are the same for any N -electron system, while \hat{V} is system-dependent. This complicated many-particle equation is not separable into simpler single-particle equations because of the interaction term \hat{U} . By applying the Hohenberg and Kohn theorems, DFT provides a way to systematically map the many-body problem with \hat{U} , onto a single-body problem without \hat{U} [149]:

In DFT the key variable is the electron density $n(\mathbf{r})$, which for a normalized ψ is given by

$$n(\mathbf{r}) = N \int d^3r_2 \dots \int d^3r_N \psi^*(\mathbf{r}, \mathbf{r}_2, \dots, \mathbf{r}_N) \psi(\mathbf{r}, \mathbf{r}_2, \dots, \mathbf{r}_N). \quad (3.2)$$

For a given ground-state density $n_0(\mathbf{r})$ it is possible, in principle, to calculate the corresponding ground-state wavefunction $\psi_0(\mathbf{r}_1, \dots, \mathbf{r}_N)$. In other words, ψ is a unique functional of n_0 ,

$$\psi_0 = \psi[n_0], \quad (3.3)$$

and consequently the ground-state expectation value of an observable \hat{O} is also a functional of n_0

$$O[n_0] = \langle \psi[n_0] | \hat{O} | \psi[n_0] \rangle. \quad (3.4)$$

In particular, the ground-state energy is a functional of n_0

$$E_0 = E[n_0] = \langle \psi[n_0] | \hat{T} + \hat{V} + \hat{U} | \psi[n_0] \rangle, \quad (3.5)$$

where the contribution of the external potential $\langle \psi[n_0] | \hat{V} | \psi[n_0] \rangle$ can be written explicitly in terms of the ground-state density n_0

$$V[n_0] = \int V(\mathbf{r}) n(\mathbf{r}) d^3r. \quad (3.6)$$

The functionals $\hat{T}[n]$ and $\hat{U}[n]$ are called universal functionals, while $\hat{V}[n]$ is called a non-universal functional, as it depends on the system under study. The energy functional can be written as

$$E[n] = T[n] + U[n] + \int V(\mathbf{r}) n(\mathbf{r}) d^3r = F[n] + \int V(\mathbf{r}) n(\mathbf{r}) d^3r, \quad (3.7)$$

with respect to $n(\mathbf{r})$, assuming one has reliable expressions for $T[n]$ and $U[n]$. A successful minimization of the energy functional will yield the ground-state density n_0 and thus all other ground-state observables.

The different problems of minimizing the energy functional $E[n]$ can be solved by applying the Lagrange's method of undetermined multipliers. First, one considers an energy functional that does not explicitly have an electron-electron interaction energy term,

$$E_s[n] = \langle \psi_s[n] | \hat{T}_s + \hat{V}_s | \psi_s[n] \rangle, \quad (3.8)$$

where \hat{T}_s denotes the kinetic energy operator and \hat{V}_s is the external effective potential in which the particles are moving, so that

$$n_s(\mathbf{r}) = n(\mathbf{r}). \quad (3.9)$$

Of course, T_s is not equal to the true kinetic energy of the system. Kohn and Sham accounted for that by introducing the following separation of the functional $F[n]$

$$F[n] = T_s[n] + E_C[n] + E_{XC}[n], \quad (3.10)$$

where E_C is the classical Coulomb potential, and E_{XC} is the so-called exchange-correlation energy [150]. E_{XC} can be defined through eq. (3.10) as

$$E_{XC}[n] = (T[n] - T_s[n]) + (U[n] - E_C[n]). \quad (3.11)$$

The expression for the energy of the interacting system in terms of the separation described in equation (3.10) can be rewritten as

$$E[n] = T_s[n] + E_C[n] + E_{XC}[n] + \int V(\mathbf{r})n(\mathbf{r})d^3r \quad (3.12)$$

$$= T[n] + \frac{e^2}{2} \int \int \frac{n(\mathbf{r})n(\mathbf{r}')}{|\mathbf{r} - \mathbf{r}'|} d^3r d^3r' + E_{XC}[n] + \int V(\mathbf{r})n(\mathbf{r})d^3r, \quad (3.13)$$

where E_{XC} is the only term for which no explicit form can be given. Now applying the variational principle and charge conservation of a real system, one can solve the so-called Kohn-Sham equations of this auxiliary non-interacting system,

$$\left[-\frac{\hbar^2}{2m}\nabla^2 + V_s(\mathbf{r})\right]\varphi_i(\mathbf{r}) = \epsilon_i\varphi_i(\mathbf{r}), \quad (3.14)$$

which yields the orbitals φ_i that reproduce the density $n(\mathbf{r})$ of the original many-body system

$$n(\mathbf{r}) = n_s(\mathbf{r}) = \sum_i^N |\varphi_i(\mathbf{r})|^2. \quad (3.15)$$

The effective single-particle potential can be written in more detail as

$$V_s(\mathbf{r}) = V(\mathbf{r}) + \int \frac{e^2 n_s(\mathbf{r}')}{|\mathbf{r} - \mathbf{r}'|} d^3r' + V_{XC}[n_s(\mathbf{r})], \quad (3.16)$$

where the second term denotes the so-called Hartree term describing the electron-electron Coulomb repulsion, while the last term V_{XC} is called the exchange-correlation potential. Here, V_{XC} includes all the many-particle interactions. Since the Hartree term and V_{XC} depend on $n(\mathbf{r})$, which depends on the φ_i , which in turn depend on V_s , the problem of solving the Kohn-Sham equation has to be done in a self-consistent way. Usually one starts with an initial guess for $n(\mathbf{r})$, then calculates the corresponding V_s and solves the Kohn-Sham equations for the φ_i . From these one calculates a new density and starts again. This procedure is then repeated until convergence is reached.

3.1.2 Exchange-correlation functionals

The major problem in DFT is that the exact functionals for exchange and correlation are not known except for the free electron gas. However, approximations exist which permit the calculation of certain physical quantities quite accurately [151]. In physics the most widely used approximation is the local-density approximation (LDA), where the functional depends only on the density at the coordinate where the functional is evaluated. In other words, this assumes that the exchange-correlation energy at a point \mathbf{r} is simply equal to the exchange-correlation energy of a uniform electron gas that has the same density at the point \mathbf{r} . Thus we can write

$$E_{XC}^{LDA}[n] = \int \epsilon_{XC}(n)n(\mathbf{r})d^3r. \quad (3.17)$$

The local spin-density approximation (LSDA) is a straightforward generalization of the LDA to include electron spin

$$E_{XC}^{LSDA}[n_{\uparrow}, n_{\downarrow}] = \int \epsilon_{XC}(n_{\uparrow}, n_{\downarrow})n(\mathbf{r})d^3r. \quad (3.18)$$

In LDA, the exchange–correlation energy is typically separated into the exchange part and the correlation part $\epsilon_{XC} = \epsilon_X + \epsilon_C$. The exchange part is called the Dirac (or sometimes Slater) exchange which takes the form $\epsilon_X \propto n^{1/3}$. There are, however, many mathematical forms for the correlation part. Highly accurate formulae for the correlation energy density $\epsilon_C(n_{\uparrow}, n_{\downarrow})$ have been constructed from quantum Monte Carlo simulations of the jellium [152]. A simple first-principles correlation functional has been recently proposed as well [153, 154]. Although unrelated to the Monte Carlo simulation, the two variants provide comparable accuracy [155].

The LDA assumes that the density is the same everywhere. Because of this, the LDA has a tendency to underestimate the exchange energy and over-estimate the correlation energy [156]. The errors due to the exchange and correlation parts tend to compensate each other to a certain degree. To correct for this tendency, it is common to expand in terms of the gradient of the density in order to account for the non-homogeneity of the true electron density. This allows for corrections based on the changes in density away from the coordinate. These expansions are referred to as generalized gradient approximations (GGA) [157–159] and have the following form

$$E_{XC}^{GGA}[n_{\uparrow}, n_{\downarrow}] = \int \epsilon_{XC}(n_{\uparrow}, n_{\downarrow}, \Delta n_{\uparrow}, \Delta n_{\downarrow})n(\mathbf{r})d^3r. \quad (3.19)$$

Using GGA, very good results for molecular geometries and ground-state energies have been achieved.

3.2 Korrington-Kohn-Rostoker (KKR) Method

The KKR method, introduced in 1947 by Korrington [160] and in 1954 by Kohn and Rostoker [161], is one of the well known methods to calculate the electronic band structure of periodic solids. A characteristic feature of this method is the use of the multiple scattering theory for solving the Schrödinger equation. The problem is then broken into two parts. First, one solves the single scattering problem presented by a single potential in free space. Second, one solves the multiple scattering problem by demanding that the incident wave to each potential should be the sum of the outgoing waves from all other scattering centres. The resulting equations

show then a separation between potential and structural properties, characteristic for the KKR method. Later on, this method experienced a revolutionary development as a GF method. This development opened the way to deal with solids with reduced symmetry, as, for example an impurity in an otherwise ordered host crystal by means of the coherent potential approximation (KKR-CPA) [162]. It is basically the availability of the Green's function that makes this method so powerful and uniquely distinguishes it from other electronic structure methods.

A short description of the spin-polarized relativistic KKR-GF method that supplies the formal background for the SPR-KKR-package, used for the calculations we have performed, is given in the following [138, 162–165].

3.2.1 Multiple-scattering theory for ordered systems

In order to describe electrons in solid systems by applying the multiple scattering theory, one has to represent each scattering site as a potential of a finite range. In this case the crystal potential can be written as

$$V(\mathbf{r}) = \sum_n V_n(\mathbf{r}_n), \quad (3.20)$$

where $V_n(r)$ describes the individual contribution of an atom on site \mathbf{r}_n . Here we assume that the potentials of individual scatterers do not overlap and are isotropic, thus one obtains the so-called muffin-tin approximation.

The Kohn-Sham equation can be presented in terms of the Green's function as

$$[-\nabla_{\mathbf{r}} + V(\mathbf{r}) - E]G(\mathbf{r}, \mathbf{r}'; E) = -\delta(\mathbf{r} - \mathbf{r}'), \quad (3.21)$$

in which the Green function $G(\mathbf{r}, \mathbf{r}'; E)$ of a perturbed system H is connected to the Green's function $G^0(\mathbf{r}, \mathbf{r}'; E)$ of an unperturbed system H^0 by the Dyson equation

$$G(E) = G^0(E) + G^0(E)V G(E) \quad (3.22)$$

$$= G^0(E) + G(E)V G^0(E) \quad (3.23)$$

$$= G^0(E) + G^0(E)T(E)G^0(E), \quad (3.24)$$

where $V = H - H^0$ describes the perturbation potential, and T the scattering matrix defined as

$$T(E) = V + V G^0(E)T(E). \quad (3.25)$$

In the KKR method, a separation of the single-site and crystal quantities is applied, so the Green's function of the crystal potential can be constructed via a Dyson equation starting from the Green's function of an isolated potential. The Dyson equation for a single-site Green's function is therefore given as

$$G_s(\mathbf{r}, \mathbf{r}'; E) = G^0(\mathbf{r}, \mathbf{r}'; E) + \int d\mathbf{r}'' \int d\mathbf{r}''' G^0(\mathbf{r}, \mathbf{r}''; E)t(\mathbf{r}'', \mathbf{r}'''; E)G^0(\mathbf{r}''', \mathbf{r}'; E), \quad (3.26)$$

where the t -matrix describes the scattering from a single-site potential. The free-particle Green's function $G^0(\mathbf{r}, \mathbf{r}'; E)$ can be expanded in the angular momentum basis as follows

$$G^0(\mathbf{r}, \mathbf{r}'; E) = -ip \sum_L j_l(pr_{<}) h_l^+(pr_{>}) Y_L(\mathbf{r}) Y_L^*(\mathbf{r}'), \quad (3.27)$$

where $j_l(z)$ and $h_l(z)$ are the spherical Bessel and Hankel functions, respectively, and $p = \sqrt{E}$. The matrix elements of the single-scattering t -matrix are defined as

$$t_{LL'}^n(E) = \int d\mathbf{r}_n \int d\mathbf{r}'_n j_l(pr_n) t(\mathbf{r}_n, \mathbf{r}'_n; E) j_{l'}(pr'_n) Y_L(\mathbf{r}_n) Y_{L'}^*(\mathbf{r}'_n). \quad (3.28)$$

Therefore, one can write the expression for the single-scattering Green's function as

$$G_s(\mathbf{r}_n, \mathbf{r}'_n; E) = \sum_{LL'} Z_L^n(\mathbf{r}_n; E) t_{LL'}^n(E) Z_{L'}^{n\times}(\mathbf{r}'_n; E) - \sum_L Z_L^n(\mathbf{r}_{<}; E) J_L^{n\times}(\mathbf{r}_{>}; E). \quad (3.29)$$

The building blocks of this Green's function expression (eq. 3.29) are the regular $Z_L(\mathbf{r}; E)$, and irregular $J_L(\mathbf{r}; E)$, solutions of the radial Schrödinger equation at the given energy E ,

$$Z_L^n(\mathbf{r}_n; E) = \sum_{L'} Z_{LL'}^n(r_n; E) Y_{L'}(\mathbf{r}_n), \quad (3.30)$$

$$Z_L^{n\times}(\mathbf{r}_n; E) = \sum_{L'} Z_{LL'}^n(r_n; E) Y_{L'}^*(\mathbf{r}_n), \quad (3.31)$$

$$J_L^n(\mathbf{r}_n; E) = \sum_{L'} J_{LL'}^n(r_n; E) Y_{L'}(\mathbf{r}_n). \quad (3.32)$$

The radial part of $Z_L^n(\mathbf{r}_n; E)$ and $J_L^n(\mathbf{r}_n; E)$ functions are matched to spherical Bessel $j_l(z)$ and Hankel $h_l(z)$ functions outside the potential range (outgoing wave behaviour at great distances) [162]. In principle, for any assembly of atoms, the scattering operator $T(E)$ can be obtained from equations 3.20 and 3.25:

$$T(E) = \sum_n t^n(E) + \sum_{n \neq m} t^n(E) G^0(E) t^m(E) + \dots \quad (3.33)$$

This equation (3.33) is separated into partial sums which are characterized by fixed site indices n and m at the leftmost and rightmost single-site t -matrix, respectively. Thus, one can define:

$$T(E) = \sum_{nm} \tau^{nm}, \quad (3.34)$$

where $\tau^{nm}(E)$ is the scattering path operator which includes all possible scattering events between those two cells n and m . In real-space multiple scattering theory, the Green's function for any arrangement of atoms can be demonstrated in terms of the scattering path operator $\tau^{nm}(E)$ to be:

$$G(\mathbf{r}_n, \mathbf{r}'_m; E) = \sum_{LL'} Z_L^n(\mathbf{r}_n; E) \tau_{LL'}^{nm}(E) Z_{L'}^m(\mathbf{r}'_m; E) - \sum_L Z_L^n(\mathbf{r}_{<}; E) J_L^m(\mathbf{r}_{>}; E) \delta_{nm}. \quad (3.35)$$

The τ -matrix for general electronic systems is given in terms of the t -matrix and the structure constants $g(E)$ representing the free-electron Green's function and can be found as:

$$\tau(E)^{nm} = [t(E)^{-1} - g(E)]_{nm}^{-1}. \quad (3.36)$$

The equation (3.36) is the main equation of the KKR-GF method. It gives a complete separation of the potential aspects of a material, revealed in the scattering matrices, from the structural aspects, represented in the structure constants $g(E)$ of the underlying lattice. The structure constants $g(E)$ can be obtained from the equation (3.27) in real space and generalized for any

symmetric case by a corresponding Fourier transformation according to symmetry properties of the problem. In case of 3D periodic solids, the lattice Fourier transformation of the structure constants is defined as:

$$g_{LL'}^{\alpha\beta}(\mathbf{k}, E) = \frac{1}{N} \sum_{mn} g_{LL'}^{m\alpha, n\beta}(\varepsilon) e^{i\mathbf{k} \cdot \mathbf{R}_{mn}}, \quad (3.37)$$

where \mathbf{R}_m and \mathbf{R}_n are direct lattice vectors, α and β designate the unit cell. The scattering path operator in momentum space can be calculated by solving the following Dyson equation:

$$\tau^{\alpha\beta}(\mathbf{k}; E) = [t^\alpha(E)^{-1} - g^{\alpha\beta}(\mathbf{k}; E)]^{-1}_{\alpha\beta}. \quad (3.38)$$

A similar transformation can be done in case of two- or one-dimensional periodicities.

3.2.2 Multiple-scattering theory for disordered systems

If we consider an ordered three dimensional periodic system, the equation (3.36) can be easily solved for the energy E and for the \mathbf{k} vector in the first Brillouin zone of the reciprocal lattice. In this case, the KKR matrix is controlled by the size of the unit cell and angular momentum expansion that mainly accelerates the computational speed. On the other hand, systems with broken translational symmetry such as impurities and alloys can be treated by the real-space multiple scattering theory. But solving the KKR equation is limited by the size of the matrix element equation (3.36) which can be very large for realistic materials, as we previously mentioned. Yet, in many random alloys a periodic lattice can be kept, but lattice sites are randomly occupied by atoms of different species. The effective Schrödinger equation for such systems can be solved for a particular configuration which distributes the atoms of the different type over the lattice sites consistent with their concentrations, then it can be statistically averaged over all possible configurations and finally Fourier transformed. Solving this problem is still considered as a difficult task that may be simplified in some mean field approach. The most used mean field is the coherent potential approximation which in combination with the multiple scattering method provides the KKR-CPA electronic structure computational scheme for random alloys [166].

Virtual crystal approximation

In this approach, one considers a random substitutional alloy in which a material is defined by an underlying regular lattice, but all its sites are randomly occupied by other atomic species. The probability of finding one type of atoms on any lattice site is then determined by the relative concentration of that species of atoms in the hosting crystal [167]. It also includes an assumption that the site occupancies are not correlated, i.e. all correlations that may exist are neglected. In the case of weak scattering, the alloy potential can be assumed to be periodic with the same potential associated with every site and averaged over all different atomic types with concentration c_i and individual potentials V_i :

$$V_c(\mathbf{r}) = \sum_i c_i V_i(\mathbf{r}). \quad (3.39)$$

Average t -matrix approximation (ATA)

This approximation is applied on systems with low dopant concentration in which one can neglect inter-site scattering and allow only the scattering of individual scattering centres [168].

In this case, the scattering centre is defined by a single-scattering t -matrix which is averaged over individual single-site scattering t_i -matrices placed on every site of the effective ordered lattice:

$$t_{ATA}(E) = \sum_i c_i t_i(E). \quad (3.40)$$

For a very diluted alloys, the ATA provides relatively correct results due to the small inter-site correlations at low concentrations. With increasing concentration, the inter-site scattering becomes more and more important, and the accuracy of this mean field decreases even further.

Coherent potential approximation (CPA)

The coherent potential approximation is also based on multiple scattering theory and characteristic of the KKR-GF method [166,169]. In this approximation, impurities are embedded into a reference medium which consists of a system with a coherent t -matrix, t_{CPA} , and site-diagonal scattering path operator, τ_{CPA} , on each scattering site. The CPA condition to obtain the coherent medium is that, on the average, the additional scattering due to replacing a coherent t -matrix by impurity t -matrices, should vanish (see Fig. (3.1)). Considering a binary system A_xB_{1-x} for example, the CPA condition in terms of t_{CPA} and τ_{CPA} can be written as

$$\tau_{CPA} = x\tau_A + (1-x)\tau_B, \quad (3.41)$$

with,

$$\tau_A = \tau_{CPA}[1 + (t_A^{-1} - t_{CPA}^{-1})\tau_{CPA}]^{-1}. \quad (3.42)$$

Here τ_{CPA} describes scattering from the ordered range of coherent potentials, while τ_A (τ_B) describes the scattering properties of an A atom (B atom) embedded in the CPA medium, where t_A (t_B) is the single t -matrix of this component [170, 171].

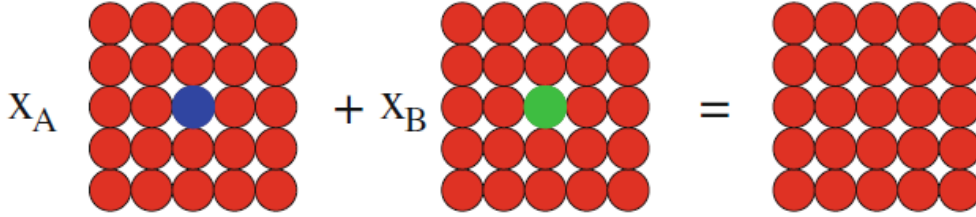


Figure 3.1: The major idea of the CPA: an auxiliary CPA medium that is meant to represent the average over all possible configurations of a disordered substitutional alloy A_xB_{1-x} is constructed by the requirement that embedding of an A or B atom does not give rise to additional scattering with respect to the CPA medium (from [170]).

The CPA equations can be solved self-consistently by means of the so-called CPA cycle. In contrast to the ATA and other single-site theories, the CPA is exact in both the weak-scattering and the narrow band limits. It has been successfully applied for electronic structure studies of bulk materials, surfaces, interfaces and clusters [29, 104, 163, 172].

3.3 One-Step Model of Photoemission

As we mentioned at the end of section 2.1, the main idea of the one-step model of photoemission is to describe the different "three steps" of the photoemission process (the electron excitation,

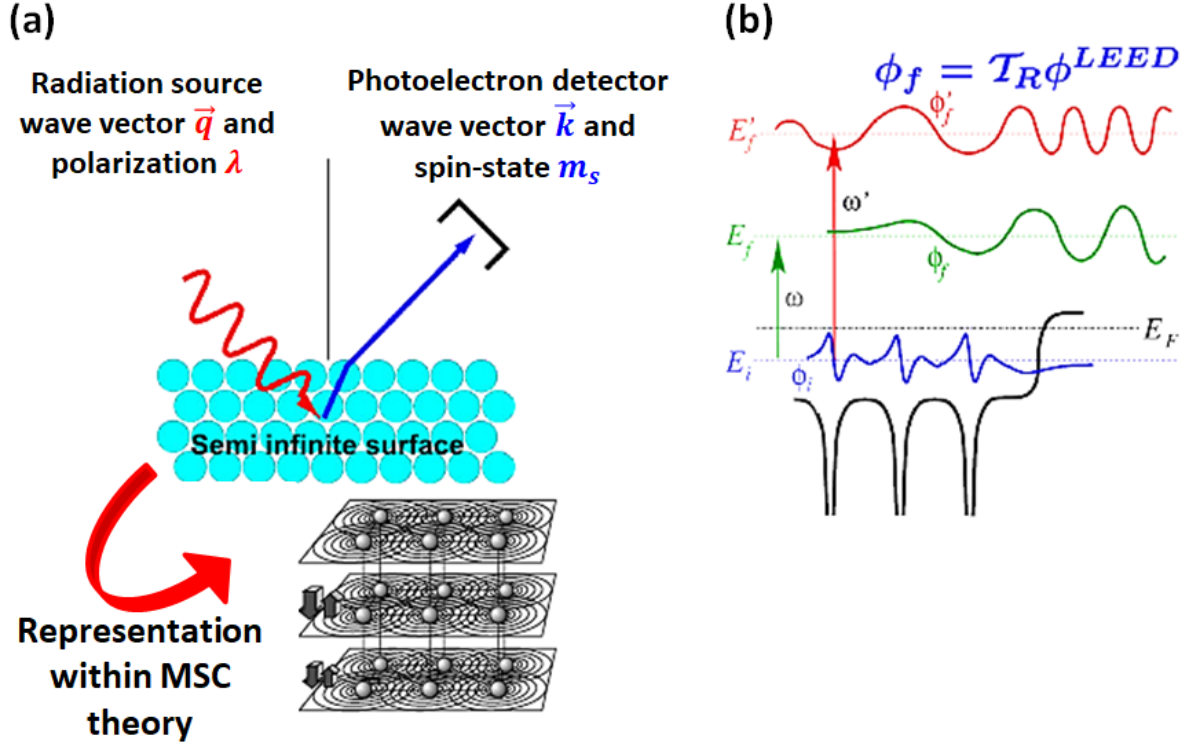


Figure 3.2: (a) Overview of the one-step model of photoemission. (b) The electron from initial state ϕ_i at energy E_i is excited to the final state ϕ_f that corresponds to the time-reversed LEED state. Meaning that the final state decays into the solid due to the inelastic processes. By increasing the mean free path of the time-reversed LEED state E'_f , the photoemission process becomes more bulk sensitive (from [173]).

the transport of the photoelectron through the solid to the surface, and its escape into the vacuum) into a single quantum-mechanically coherent process that includes all multiple-scattering events [140] (see Fig. 3.2(a)). Here, self-energy corrections are properly included in the initial and the final states, so that the photoemission intensity is rightly estimated. In fact, during the photoemission process, the outgoing electrons interact with the solid through many-body interaction, and therefore the electrons are strongly damped (see Fig. 3.2 (b)). As the KKR-GF method is based on the multiple-scattering formalism, a description of the photoemission process can be easily made using this method [174].

Let us recall equation 2.5, the general expression of the photoemission intensity which is derived from the transition probability w (see Fermi's Golden Rule in eq. 2.4). In the simple one-electron picture [175], the photocurrent becomes

$$I(\hbar\omega) = \frac{1}{\hbar} \sum_{f,i,j} \Delta_{f,i}^* A_{i,i'}(E_I) \Delta_{i',f}, \quad (3.43)$$

with

$$A_{i,i'}(E_I) = \sum_s \langle \Psi_i | a_{i'}^\dagger | \Psi_f^s \rangle \delta(E_f - E_i - \hbar\omega) \langle \Psi_f^s | a_i | \Psi_i \rangle. \quad (3.44)$$

The term $\Delta_{f,i}$ denotes for the one-particle matrix element, and a_i^\dagger (a_i) is for the creation (annihilation) operator. The initial state is then defined as $|\Psi_i\rangle = |\Psi_N^0\rangle$, and the final state $|\Psi_f\rangle = a_f^\dagger |\Psi_{N-1}^s\rangle$, where $|\Psi_N^0\rangle$ designates the ground state and $|\Psi_{N-1}^s\rangle$ the excited $N-1$ particle state of many-particle system. Here, the so-called sudden approximation is used to find an explicit

formulation of the initial state $|\Psi_i\rangle$. In this approximation, we assume that the initial state consists of a one-particle photoelectron state and the interaction with the excited $(N - 1)$ -state $|\Psi_{N-1}^s\rangle$ is completely neglected [140]. In other words, $a_f|\Psi_N^0\rangle = 0$.

The one-electron spectral intensity $A_{i,i'}$ is connected to the retarded one-electron Green's function of the interacting system by

$$A_{i,i'}(E_i) = -\frac{1}{\pi} \text{Im} G_{i,i'}(E_i). \quad (3.45)$$

Therefore, the intensity of the photocurrent in term of $G_{i,i'}$ can be written as

$$I(\hbar\omega) = -\frac{1}{\hbar\pi} \text{Im} \sum_{f,i,i'} \langle \phi_f | \Delta | \phi_i \rangle G_{i,i'}(E_i) \langle \phi_{i'} | \Delta^* | \phi_f \rangle = -\frac{1}{\hbar\pi} \text{Im} \sum_f \langle \phi_f | \Delta G(E_i) \Delta^* | \phi_f \rangle, \quad (3.46)$$

with $G(E_i) = \sum_{i,i'} |\phi_i\rangle G_{i,i'}(E_i) \langle \phi_{i'}|$ is the operator representation for $G_{i,i'}(E_i)$.

In ARPES, the final state $|\phi_f\rangle$ depends on the wavevector component parallel to the surface \mathbf{k}_{\parallel} and the single-particle energy for the final state ϵ_f . The connection to the experiment can be determined by mapping the final state $|\phi_f\rangle$ on a time-reversed-LEED state $|\mathbf{k}_{\parallel}, \epsilon_f\rangle$ [141]. By introducing the advanced Green's function G_2 that contains all scattering properties of the material at the final state, one can write

$$|\phi_f\rangle = G_2^- |\mathbf{k}_{\parallel}, \epsilon_f\rangle, \quad (3.47)$$

and

$$\langle \phi_f | = \langle \epsilon_f, \mathbf{k}_{\parallel} | G_2^+. \quad (3.48)$$

Inserting equations 3.47 and 3.48 in 3.46, the final expression for the photocurrent is

$$I(\epsilon_f, \mathbf{k}_{\parallel}) = -\frac{1}{\hbar\pi} \text{Im} \langle \epsilon_f, \mathbf{k}_{\parallel} | G_2^+ \Delta G(E_i) \Delta^* G_2^- | \mathbf{k}_{\parallel}, \epsilon_f \rangle. \quad (3.49)$$

In this equation, the initial state represented by the propagator $G(E_i)$ contains all many-body correlations due to the complex self-energy (see equation 2.6). If we consider the non-interacting limit where $\Sigma(E_i) = 0$ at $T=0$ K, equation 3.49 is related to the one-step model [141]:

$$I(\epsilon_f, \mathbf{k}_{\parallel}) = -\frac{1}{\hbar\pi} \text{Im} \langle \epsilon_f, \mathbf{k}_{\parallel} | G_2^+ \Delta G_1^+ \Delta^* G_2^- | \mathbf{k}_{\parallel}, \epsilon_f \rangle. \quad (3.50)$$

The next step is to calculate the propagators G_2^{\pm} and G_1^+ from multiple scattering theory. For this, one needs to evaluate the one-step formula of photoemission (equation 3.50) for a semi-infinite crystal decomposed into a semi-infinite stack of layers. For each layer we use the muffin-tin potentials at the atomic positions and the constant potential between the these spherically symmetric spheres [140]. Equation 3.50 can be written into the space representation as follows:

$$I(\epsilon_f, \mathbf{k}_{\parallel}) = -\frac{1}{\pi} \text{Im} \int d\mathbf{r} \int d\mathbf{r}' \Psi_f^*(\mathbf{r}) \Delta G_1^+(\mathbf{r}, \mathbf{r}') \Delta^* \Psi_f(\mathbf{r}'). \quad (3.51)$$

Therefore, the final state, so-called time-reversed LEED-state, is now written as

$$\Psi_f(\mathbf{r}) = \langle \mathbf{r} | G_2^+ | \epsilon_f, \mathbf{k}_{\parallel} \rangle. \quad (3.52)$$

Here, the wavelength for the final state $\Psi_f(\mathbf{r})$ can be deduced everywhere in the crystal, after finding the scattering properties of each layer. The unknown variable that remains is the initial

state propagator G_1^+ for the semi-infinite crystal. Note that, the intensity of the photocurrent has to be divided into four different contributions, as a consequence of multiple scattering techniques:

$$I(\epsilon_f, \mathbf{k}_{\parallel}) = I_{atom}(\epsilon_f, \mathbf{k}_{\parallel}) + I_{intra}(\epsilon_f, \mathbf{k}_{\parallel}) + I_{inter}(\epsilon_f, \mathbf{k}_{\parallel}) + I_{surf}(\epsilon_f, \mathbf{k}_{\parallel}) \quad (3.53)$$

The first term is related to the atomic contribution to the photocurrent, that results from substituting the Green's function for a single atomic site G_{1atom}^+ :

$$I_{atom}(\epsilon_f, \mathbf{k}_{\parallel}) = -\frac{1}{\pi} Im \int d\mathbf{r} \int d\mathbf{r}' \Psi_f^*(\mathbf{r}) \Delta G_{1atom}^+(\mathbf{r}, \mathbf{r}') \Delta^* \Psi_f(\mathbf{r}'). \quad (3.54)$$

Within the second term in equation 3.53, multiple scattering of the initial state inside the n th layer is written as:

$$I_{intra}(\epsilon_f, \mathbf{k}_{\parallel}) = -\frac{1}{\pi} Im \int d\mathbf{r} \Psi_f^*(\mathbf{r}) \Delta \Psi_i^{intra}(\mathbf{r}), \quad (3.55)$$

with

$$\Psi_i^{intra}(\mathbf{r}) = \int d\mathbf{r}' G_{1intra}^+(\mathbf{r}, \mathbf{r}') \Delta^* \Psi_f(\mathbf{r}'). \quad (3.56)$$

The third term in equation 3.53 contains the multiple scattering contributions of the initial state between all layers on the semi-infinite crystal:

$$I_{inter}(\epsilon_f, \mathbf{k}_{\parallel}) = -\frac{1}{\pi} Im \int d\mathbf{r} \Psi_f^*(\mathbf{r}) \Delta \Psi_i^{inter}(\mathbf{r}), \quad (3.57)$$

with

$$\Psi_i^{inter}(\mathbf{r}) = \int d\mathbf{r}' G_{1inter}^+(\mathbf{r}, \mathbf{r}') \Delta^* \Psi_f(\mathbf{r}'). \quad (3.58)$$

The last contribution to the intensity of the photocurrent comes from the surface of the semi-infinite crystal:

$$I_{surf}(\epsilon_f, \mathbf{k}_{\parallel}) = -\frac{1}{\pi} Im \int d\mathbf{r} \Psi_f^{*surf}(\mathbf{r}) \Delta \Psi_i^{surf}(\mathbf{r}), \quad (3.59)$$

with

$$\Psi_i^{surf}(\mathbf{r}) = \int d\mathbf{r}' G_{1surf}^+(\mathbf{r}, \mathbf{r}') \Delta^* \Psi_f^{surf}(\mathbf{r}'). \quad (3.60)$$

In case of z -dependent calculation, the barrier potential $V_B(z)$ at the surface in this direction must be taken into account. Consequently, the initial and final state wavefields are calculated numerically in the surface region along the z -direction that correspond to the parallel components [176]:

$$\Psi_i^{surf}(\mathbf{r}) = \sum_g \phi_{1g}(z) e^{ik_{1g\parallel}(r-c_1)_{\parallel}} \quad (3.61)$$

$$\Psi_f^{surf}(\mathbf{r}) = \sum_g \psi_{2g}(z) e^{ik_{2g\parallel}(r-c_1)_{\parallel}} \quad (3.62)$$

The two equations 3.61 and 3.62 are solved with the regular solutions of the Schrödinger equation ϕ_{1g} and ψ_{2g} to the reciprocal lattice vector \mathbf{g} for $V_B(z)$ with $-\infty < z < c_{1z}$. The value c_{1z} represents the point where the surface potential integrates smoothly into the inner potential of the bulk crystal.

Polycrystalline Ni-Doped SrTiO₃

According to most of the studies on TM-doped STO we mentioned in chapter 1, doping STO with Ni seems to be very efficient to reduce the gap and enhance light absorption. At the beginning of this project, we chose to study Ni-doping effects on STO thin films grown by magnetron sputtering. This procedure for film deposition is considered as a flexible technique, less time consuming and relatively inexpensive, because it does not require any particular growth conditions such as ultra-high vacuum and high temperature. These characteristics make it suitable for industrial applications. In this chapter, we will discuss the microstructure of pristine and Ni-doped STO films grown by magnetron sputtering (see section 2.5.1 for details) on the basis of XRD and XPS data. All as-deposited films show an amorphous-like structure, i.e. a lack of the long-range order that is characteristic of a crystal. The films were thermally investigated to record the response of a thin film structure after a sequentially heating treatment. In addition to this, the Ni-doping impacts on the microstructure of the films were investigated, as well as the chemical and structural environments of the compound elements.

4.1 Magnetron Sputtered SrTiO₃ Thin Films

The XRD patterns of the as-deposited and annealed STO films are given in Fig. 4.1 (a). For as-deposited STO samples, the sharp line belongs to the crystalline silicon substrate, and the broad lines denote the amorphous structure of the films. The term amorphous designs here the non-crystalline structure of the films that lacks the long-range order (more than few nm) of the basic structural units. In principle, even amorphous structures have a short-range order at the atomic length scale due to the nature of chemical bonding. Yet, the XRD technique shows a difficulty in resolving the crystalline structures at these length scales.

After annealing at 900°C, the broad lines changed to sharp lines that correspond to those of a cubic perovskite structure (ref. JCPDS: 35-0734). The films are showing a polycrystalline structure after a transition from non-ordered structure to an ordered structure composed of many crystallites of varying size and orientation. Movchan *et al.* developed a structure zone model to describe the micro-structure of thin films as a function of the homologous temperature T_h that is the ratio of deposition temperature over melting temperature [177]. According to this model, one condition for amorphous phases to occur is that T_h has to be smaller than 0.3; in other

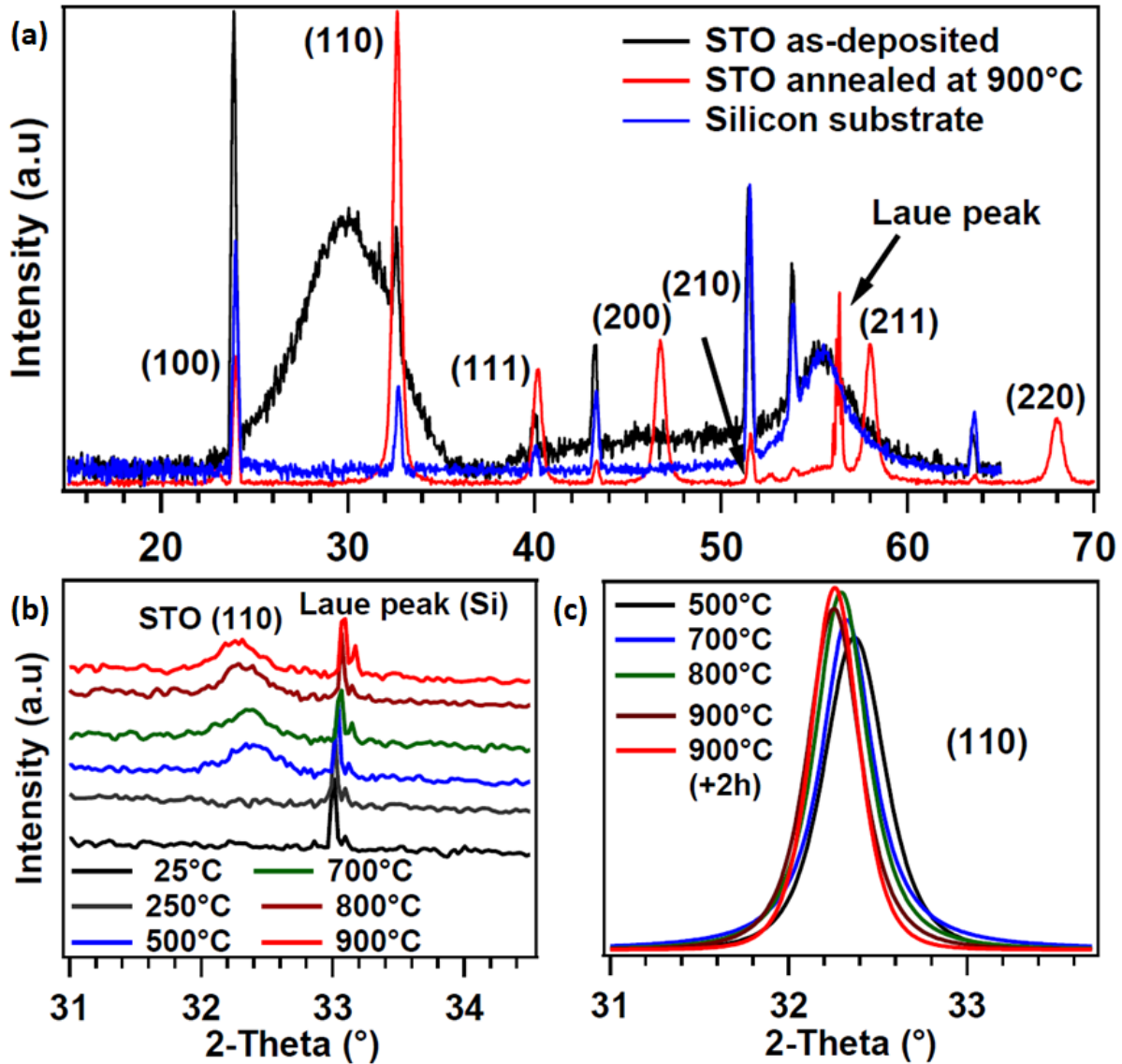


Figure 4.1: (a) XRD patterns for as-deposited (black line) and annealed at 900°C (red line) STO film. The blue line represents the patterns for the silicon substrate. (b) XRD patterns around the (110) diffraction line recorded during the heating treatment. (c) STO (110) diffraction lines obtained from fitting showing the change in the micro-structure of the material during the heating treatment.

words the deposition temperature must be below 30% of the melting temperature. For higher values, the surface diffusion of deposited atomic species allows the formation of crystallites with long-range atomic order [178]. Here, the growth was performed at RT (20°C) and STO's melting temperature is 2080°C. The value of T_h is then equal to 0.01 way smaller than 0.3 attesting the amorphous structure of the deposited films. Heating at 900°C which is equivalent to 43.3% of the melting temperature shows signs of being high enough to see the crystallinity of the films by XRD.

To follow the micro-structure changes of the as-deposited STO films as a function of temperature, we recorded the XRD patterns around the (110) diffraction line after a sequential heating treatment from 25°C to 900°C; the data are plotted in Fig. 4.1 (b). A fitting procedure [179] based on a Voigt function was used to analyse the data, and the normalized (110) diffraction

lines are presented in Fig. 4.1 (c). The estimated crystallite sizes (D_{XRD}) at each temperature are calculated from the X-ray line broadening of the (110) plane using Scherrer's equation:

$$D_{XRD} = k\lambda/(\beta\cos\theta), \quad (4.1)$$

where D_{XRD} is the mean size of the crystallite, λ is the X-ray wavelength, k is a constant (shape factor, 0.98), θ is the diffraction angle and β is the peak FWHM [180]. The data are presented in Table 4.1.

Table 4.1: Size of crystallites oriented in the (110) direction for STO films at each temperature during the heating treatment.

Temperature (°C)	2θ (°)	FWHM (°)	Crystallite size D_{XRD} (nm)
500	32.37	0.4	22.52
700	32.33	0.35	25.75
800	32.3	0.345	26.09
900	32.25	0.341	26.477
900 (+2h)	32.25	0.319	28.21

The polycrystalline phase appeared already at 500°C in which crystallites oriented in the (110) direction are formed. An improvement of the crystal structure is observed with increasing temperature sequentially through the line profile narrowing. In fact, the estimated crystallite size at 500°C was found to be 22.52 nm and this value increased to 28.21 nm after an annealing up to 900°C for two hours (the maximum limit of the experimental setup). In addition, the intensity of the (110) peak also increased by a factor of 1.15 after the heating at 900°C compared to 500°C, indicating a higher number of ordered crystallites in the films.

4.2 Ni-doped SrTiO₃ Thin Films

In this section, we present a structural characterization of STO films doped with several Ni concentrations grown by magnetron sputtering as described in section 2.5.1. All as-deposited films are annealed up to 900°C for several hours to induce crystallinity. Atomic structure and chemical characteristics of the doped films were investigated by means of XRD and XPS methods.

4.2.1 Atomic structure

The XRD Bragg reflection of pure STO and STO:Ni_x with $x=0.047$, 0.06 and 0.08 are presented in Fig. 4.2 (a). In comparison with pure STO, the doped films show a polycrystalline structure typical of a cubic STO lattice, the line positions of the patterns matching perfectly. However, the relative peak intensity of the perovskite peaks increased with Ni doping, suggesting that the films become more crystalline (number of crystallites oriented in a given direction increases with Ni-doping concentration). An additional peak positioned at $\sim 44.5^\circ$ is detected only in patterns of STO:Ni_{0.08} films. This peak results from the presence of Ni in the metallic phase in the sample (JCPDS: 04-0850). Detailed plots of the (110) diffraction lines are presented in Fig. 4.2 (b) after normalization for different Ni-doping concentrations; the corresponding mean crystallite sizes

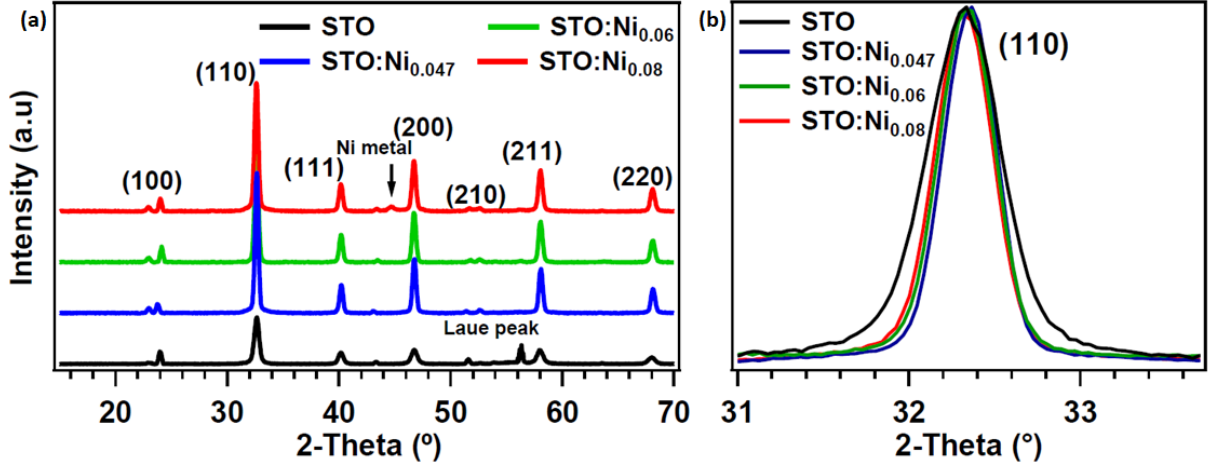


Figure 4.2: a) XRD patterns of annealed pure STO and STO:Ni_x films. b) Normalized (110) diffraction lines for STO and STO:Ni_x films with ($x=0.047, 0.06$ and 0.08).

D_{XRD} are given in Table 4.2. Surprisingly, the data shows a remarkable difference in the width of the lines of the pure and doped films in which the diffraction lines of STO:Ni_x films are sharper in comparison to pure STO films by a factor of ~ 1.2 . The mean crystallite size increased from 28.21 nm for undoped films to 34.63 nm for STO doped with 0.047% of Ni reflecting a better atomic ordering and crystallinity of the films.

Table 4.2: This table illustrates the size of crystallites oriented in the (110) direction for undoped and Ni-doped STO films.

Sample	2θ (°)	FWHM (°)	Crystallite size D_{XRD} (nm)
STO	32.25	0.319	28.21
STO:Ni _{0.047}	32.29	0.26	34.63
STO:Ni _{0.06}	32.29	0.27	33.34
STO:Ni _{0.08}	32.25	0.29	31.03

However, dopants are often added to decrease the crystallites size in materials, as they act to pin grain boundaries and therefore limit grain boundary mobility. A plausible explanation for our observations is that Ni in STO acts as an acceptor and induces the formation of oxygen vacancies that play an important role in structural mobility. If the mobility of oxygen vacancies is high enough, the interaction between the dopant and grain boundaries becomes relatively weak and larger crystallites are formed. An alternative explanation can be the different values of radii for the dopant combined with the growth conditions causing a strain field or stress that modify the grain growth process and might increase the crystallites size.

4.2.2 Characterization by XPS

XPS is a spectroscopic technique that measures the elemental composition, chemical state and electronic state of the elements within a material. Our XPS spectra for STO:Ni_x samples with ($x=0.047$ and 0.08) are obtained by irradiating the films with photon of 1253.6 eV (Mg $K\alpha$). All samples were annealed in UHV at 450°C for two hours before measurements, to clean off the surface contamination.

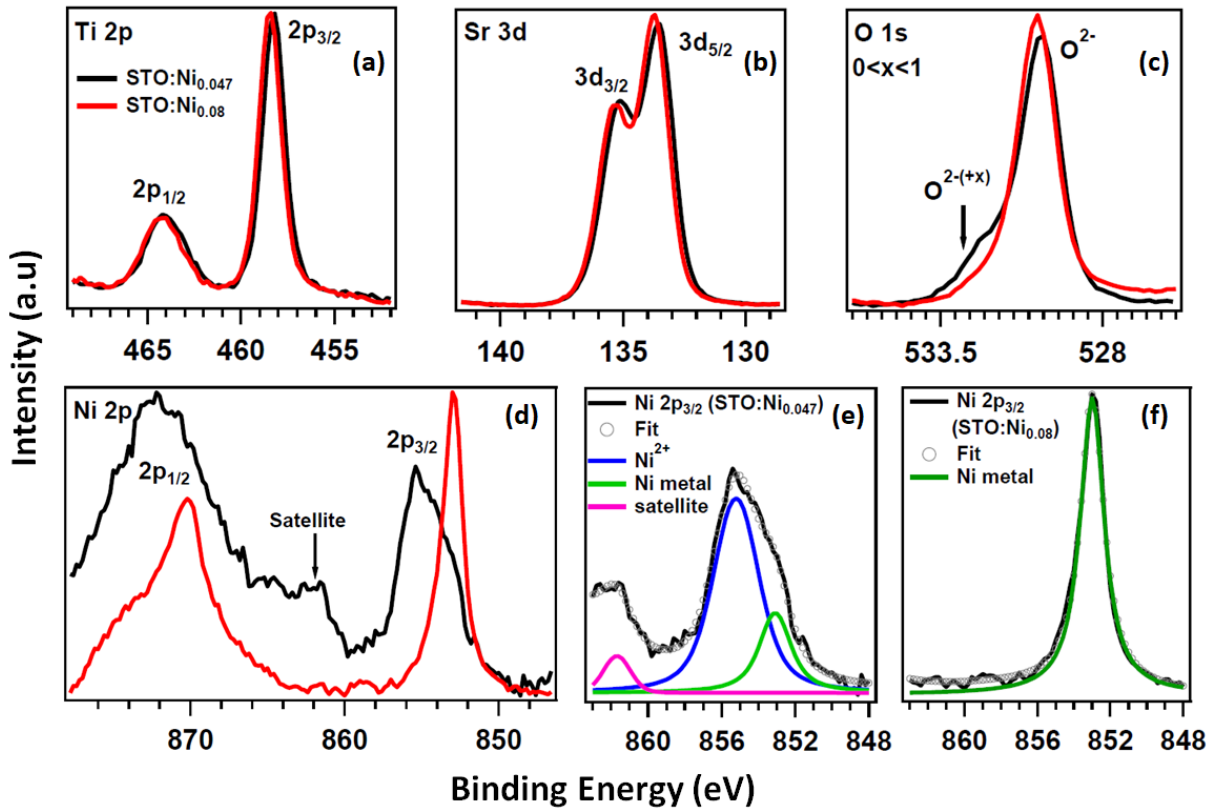


Figure 4.3: (a-d) Core level intensity obtained with $h\nu=1253.6$ eV at normal emission for STO:Ni_{0.047} and STO:Ni_{0.08} films. All spectra are normalized by the Sr 3d spectral weight. (e-f) Detailed Ni 2p_{3/2} spectra of STO:Ni_{0.047} and STO:Ni_{0.08} films. The fitting curves were obtained by subtracting a Shirley background and adding a sufficient number of Voigt curves that correspond to the chemical states indicated in the panels.

XPS spectra for the Ti 2p, Sr 3d, O 1s and Ni 2p levels of the STO:Ni_x samples, as well as the fitting of Ni 2p_{3/2} are shown in Fig. 4.3 (a-f), respectively. The Ti 2p and Sr 3d spectra are similar for both samples: the binding energy of the Sr 3d_{5/2} and Sr 3d_{3/2} signals at 133.6 eV and 135.4 eV, respectively, correspond to Sr²⁺ ions in the perovskite cubic phase of the STO structure; the binding energies of the Ti 2p_{3/2} and Ti 2p_{1/2} peaks are 458.3 eV and 464.1 eV, typical for Ti atoms in the perovskite structure of STO and correspond to Ti within a IV oxidation state [181].

For the STO:Ni_{0.047} sample, the O 1s spectrum shows two peaks. The stronger peak at 530 eV associated with O²⁻ ions in the perovskite structure of STO [181]. The peak at 531.6 eV corresponds to an intermediate oxidation state for oxygen O^{x-} with $0 < x < 2$ and might be related to defect, such as oxygen vacancies, and chemical absorption (contamination leading to the presence of C-O and C=O bonds) formed during film growth in the bulk and cannot be suppressed by applying a surface cleaning procedure (basic vacuum in the chamber of the order of $1 \cdot 10^{-6}$ mbar). STO:Ni_{0.08} sample shows only one peak for O 1s at 530.2 eV indicating the presence of O²⁻ state.

The Ni 2p XPS regions of STO:Ni_{0.047} and STO:Ni_{0.08} samples plotted in Fig. 4.3 (d), show the 2p_{3/2} and 2p_{1/2} doublet (17.1 eV splitting). In case of STO:Ni_{0.047} the spectra are shifted by 2.8 eV toward higher binding energies; the spectral weight shows a broadening and a satellite

feature at around 6 eV higher binding energy from Ni $2p_{3/2}$ peak is observed, in comparison to STO:Ni_{0.08}. We only discuss here the Ni $2p_{3/2}$ signal (Fig. 4.3 (e)) because its intensity is higher than that of the Ni $2p_{1/2}$ signal and its background can be subtracted by means of Shirley's procedure successfully. For STO:Ni_{0.047}, the Ni $2p_{3/2}$ signal has two Ni components: the first one at 855.6 eV corresponds to the presence of Ni²⁺, and the second one located at 853 eV to Ni⁰ [182]. The presence of O^{-x} states is consistent with the features seen in the Ni $2p$ spectra. We assume that Ni atoms are partially oxidized in Ni²⁺ ions that substitute Ti in the structure. For STO:Ni_{0.08} the Ni $2p_{3/2}$ peak positioned at 853 eV is related to Ni in its metallic state with no indication for oxidation [182]. The dissimilarity observed in the chemical characteristics of the STO:Ni_{0.047} and STO:Ni_{0.08} samples cannot be directly related to the difference in dopant concentrations. All parameters we used to grow these films were similar (temperature, voltage, pressure) except for the position of Ni pellets on the STO target. In practice, the distribution of the magnetic field configuration is not homogenous everywhere around the ensemble target+Ni pellets placed in the growth chamber. Therefore the position of the Ni pellets on the sputtering target can strongly affect the ionic composition of the plasma due to the non linear line of force of the magnetic field applied. This results in different atomic distributions on the substrate as well as various oxidation degrees for Ni.

4.3 Conclusion

We prepared pristine and STO:Ni_x films ($x=0, 0.047, 0.06$ and 0.08) by magnetron sputtering process. The atomic properties as well as doping effects on the structure of STO were studied by XRD and XPS:

The XRD results on STO indicate that all as-prepared samples show a non-crystalline structure and a lack of long-range ordering when the growth is performed at RT. The crystallinity is induced by annealing the films at 500°C; an enhancement in the mean crystallite size is observed with the increase of the temperature, and all samples show a cubic perovskite structure.

Ni metal is detected in annealed STO:Ni_{0.08} sample as evidenced by the XRD results. XRD data also indicates that, for Ni-doped samples, the films micro-structure is improved and the crystallite sizes increase in comparison to non-doped samples. The XPS results show that Sr and Ti ions were in the +II and +IV oxidation states respectively, for all of the Ni-doping contents. For the STO:Ni_{0.047} sample, Ni participates as a mixture of Ni⁰ and Ni²⁺ ions in the perovskite structure, which significantly increase the formation of oxygen vacancies. However, the Ni $2p$ and O $1s$ XPS spectra for the STO:Ni_{0.08} sample, indicate that Ni is purely metallic, in agreement with the XRD patterns, with no evidence of oxygen vacancies. The differences seen in the chemical and structural characteristics are mainly related to the method used for growth and the experimental conditions.

In summary, the magnetron sputtering process allows the deposition of STO thin films doped with Ni, which can be useful for industrial sectors in particular the photovoltaic applications. This technique is economic and does not require specific conditions such as high temperature for growth and UHV environment. Even though the micro-structure of the produced films is weak

and crystallites are not perfectly ordered, yet, the local atomic structure is conserved as well as the elemental properties of the material. However, the films quality is not sufficient to investigate the fundamental electronic properties by means of ARPES. For this purpose, one needs to grow epitaxially high quality ordered flat films.

Monocrystalline TM-Doped Thin SrTiO₃ Films

In order to understand better the electronic properties of materials, in particular the electronic band dispersion with ARPES, a high quality of crystalline samples is necessary. The growth of monocrystals can be achieved by PLD for film growth, as already mentioned in section 2.5.2. In practice a large number of variables can affect the properties of the films during the growth, such as laser energy, background gas pressure and substrate temperature. These variables allow the film properties to be manipulated to suit individual applications. The optimization can require a considerable amount of time and effort.

The different systems we present in the rest of this manuscript are pure STO(100), STO:Ni_{0.06}(100), STO:Ni_{0.12}(100), STO:Fe_{0.05}(100) and STO:Cr_{0.05}(100) thin films, grown by PLD. The author of this thesis assisted with the film growth of the first three systems at the university of Würzburg (collaboration with Prof. Ralph Claessen and Berengar Leikert), the last two were fabricated by Milan Radović at Paul Scherrer Institute.

In the first part of this chapter, the empirical optimization of deposition conditions for pristine and STO:Ni_{*x*} (*x*=0.06 and 0.12) films are discussed, as well as the structural and chemical characteristics of all the systems mentioned above.

In the second part, the impact of TM-doping on the electronic structure of strontium titanate, as well as the role of the 3*d*-impurity energy levels, as revealed by angle-integrated PES and resonant photoelectron spectroscopy (resPES) are presented. Measurements were performed at SLS (PEARL and ADRESS beamlines) and SOLEIL (CASSIOPEE beamline). The experimental results are supported by a theoretical investigation by DFT revealing the sites doping impurities and their influence on the electronic properties of STO.

5.1 Elaboration of Ni-doped SrTiO₃(100) Thin Films

As seen previously in section 2.5.2, PLD is well adapted for the epitaxial thin film growth of oxide materials such as STO. We therefore used this technique for the fabrication of STO and STO:Ni_{*x*} thin films with (*x*=0.06 and 0.12). One of the main challenges in the preparation

of Ni-doped films is to succeed the substitution of Ni cations in STO lattice sites. Giving the calculated formation energy (E_f) for Ni-doped STO, Ni atoms prefer to substitute Ti (Ni at Ti sites: $E_f=7.8$ eV) rather than Sr (Ni at Sr sites: $E_f=9$ eV) [26]. However, this value is relatively high because of the very low solubility of Ni in STO, which makes the substitution difficult to realize experimentally and favours the formation of metal clusters in the hosting lattice [183].

To avoid Ni clustering and induce an oxidation toward the Ni^{x+} state ($2 < x < 4$), we used an amorphous $\text{STO}_{1-x}/\text{NiO}_x$ target with $x=6$ at.%, and 12 at.%. The oxygen background during the growth as well as the substrate temperature and the laser fluence used to ablate material from the targets can strongly affect the growth process. Since the parameters may finely depend on the exact geometry of the used PLD setup or on variations in the composition and density of the target, an optimization of the film growth is required before a detailed study of the films can be performed.

All films are deposited on TiO_2 -terminated (100) surfaces of STO substrates with niobium doping (5 at.%). The preparation procedure we applied for the substrates to get TiO_2 termination is presented in [129]. Every substrate used was checked by atomic force microscopy before the growth and exhibits an atomically flat surface with terrace steps of single unit cells height. For the undoped and Ni-doped films, the optimized substrate temperature, laser energy and oxygen background gas values were found to be 700°C , 1.8 J/cm^2 and 1.10^{-1} mbar , respectively. Prior to the film growth, a preablation is performed at RT in oxygen background gas ($P_{\text{O}_2}=5.10^{-2} \text{ mbar}$); then the sample holder and substrate are heated up to 700°C for 30 min to remove adsorbates. We stopped the deposition after growing 11 unit cells on each substrate. The resulting structural characterization data obtained by RHEED and LEED for the undoped and Ni-doped STO are presented in Fig. 5.1.

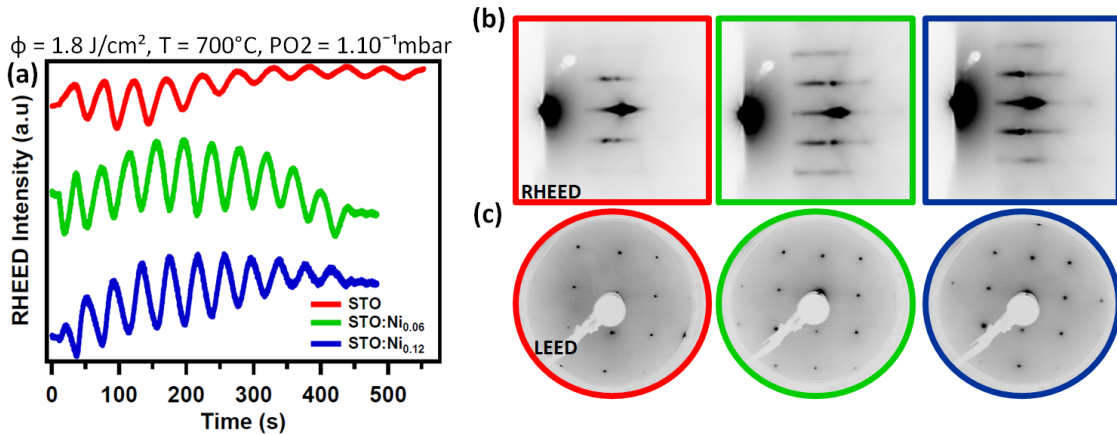


Figure 5.1: Structural characterization of thin STO and STO:Ni_x films grown on STO (100). (a) Intensity oscillations of the specular RHEED reflection. In all cases, intensity of the oscillations is regular, indicating layer-by-layer growth. (b) Corresponding post-growth RHEED patterns of the films. (c) LEED patterns of the undoped and Ni-doped STO films taken with an electron energy of 75 eV. All patterns exhibit a (1×1) reconstruction typical for the cubic perovskite (100) surface.

The RHEED intensity of the specular reflection during the growth process is plotted in Fig. 5.1 (a). In all cases, the intensity oscillations indicate a layer-by-layer growth mode. However, their evolution can be roughly distinguished between the undoped and doped films. For the

undoped STO films, the oscillations are initially strongly pronounced and then partially fade after depositing 6 unit cells ($t=300$ seconds). For the STO:Ni_x films, the oscillations and their amplitudes are more intense and stable throughout the growth. This RHEED intensity evolution can be understood by analysing the post-growth RHEED and LEED diffraction patterns presented in Fig. 5.1 (b) and (c), respectively. For the pure STO films, the diffraction patterns detected in RHEED are typical for STO (100) surface as well as the pattern observed in LEED. The intensity and contrast of the RHEED patterns clearly increase by increasing the Ni concentration in STO. This suggests that the STO:Ni_x films are better ordered than the STO films. The corresponding LEED patterns show a (1×1) surface reconstruction similar to the STO (100) films, yet the diffraction signal appears to be clearer for the doped samples.

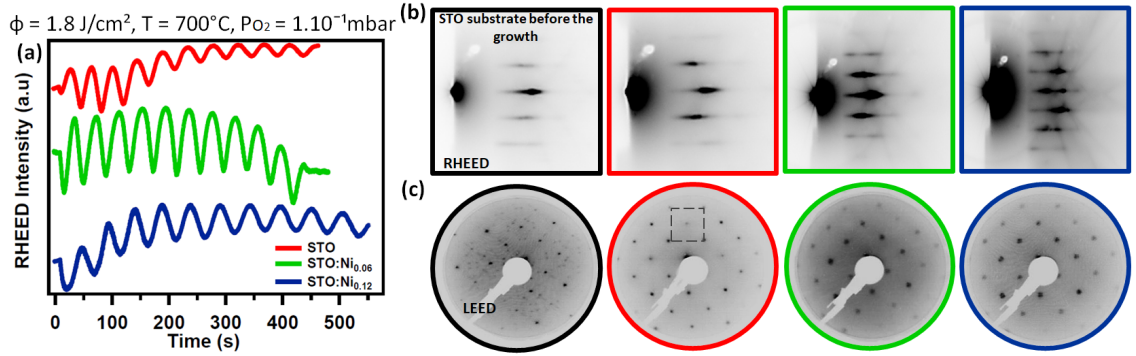


Figure 5.2: Structural characterization of STO and STO:Ni_x thin films grown on STO $c(1 \times 1)$. (a) RHEED intensity oscillations. (b) RHEED patterns of the STO substrate registered before the growth and the pristine and Ni-doped STO thin film surfaces after growth. (c) Corresponding LEED patterns, measured with an electron energy of 75 eV. All patterns exhibit a $\sqrt{2} \times \sqrt{2}$ R(45°) reconstruction with respect to the cubic perovskite unit cell of STO as marked by the dashed square. The LEED pattern of the STO substrate before growth shows additional diffraction spots resulting from oxygen vacancies at the surface.

Another set of samples was also prepared by PLD with the same growth parameters on a new set of STO substrates, and the results are presented in Fig. 5.2. The RHEED intensities of undoped and doped films displayed in Fig 5.2 (a) show the same evolution as for the previous set. However, the diffraction patterns for RHEED and LEED were not the same (see Fig. 5.2 (b) and (c)): surprisingly, the LEED patterns of all films show a $\sqrt{2} \times \sqrt{2}$ R(45°) reconstruction. Note that an optimisation procedure for $T_{\text{substrate}}$, P_{oxygen} and ϕ_{laser} was also applied to understand if this reconstruction is caused by the growth parameters we used, and we found that the LEED patterns were always showing the same surface reconstruction. The reason one can think about is the substrate structure. After the annealing procedure in the PLD chamber and before the growth, the surface structure of the substrate was checked by LEED and RHEED as displayed in Fig. 5.2 (b) and (c) (black square and black circle respectively): as expected, the LEED pattern of the substrate shows a $\sqrt{2} \times \sqrt{2}$ R(45°) reconstruction and the extra diffraction intensities indicate atomic disorder at the surface (oxygen vacancies) because of the heating at 700°C in low oxygen atmosphere before the measurements. These results are in agreement with the weak diffraction pattern detected in RHEED. Note that we used both sets of samples to perform our experiments and verify if the observed surface reconstruction has some consequences on the electronic structure of the system. The resulting data for both sets were similar and give no evidence for different features. Therefore for reasons of clarity, in the rest of this manuscript, only the data from one set of samples will be presented.

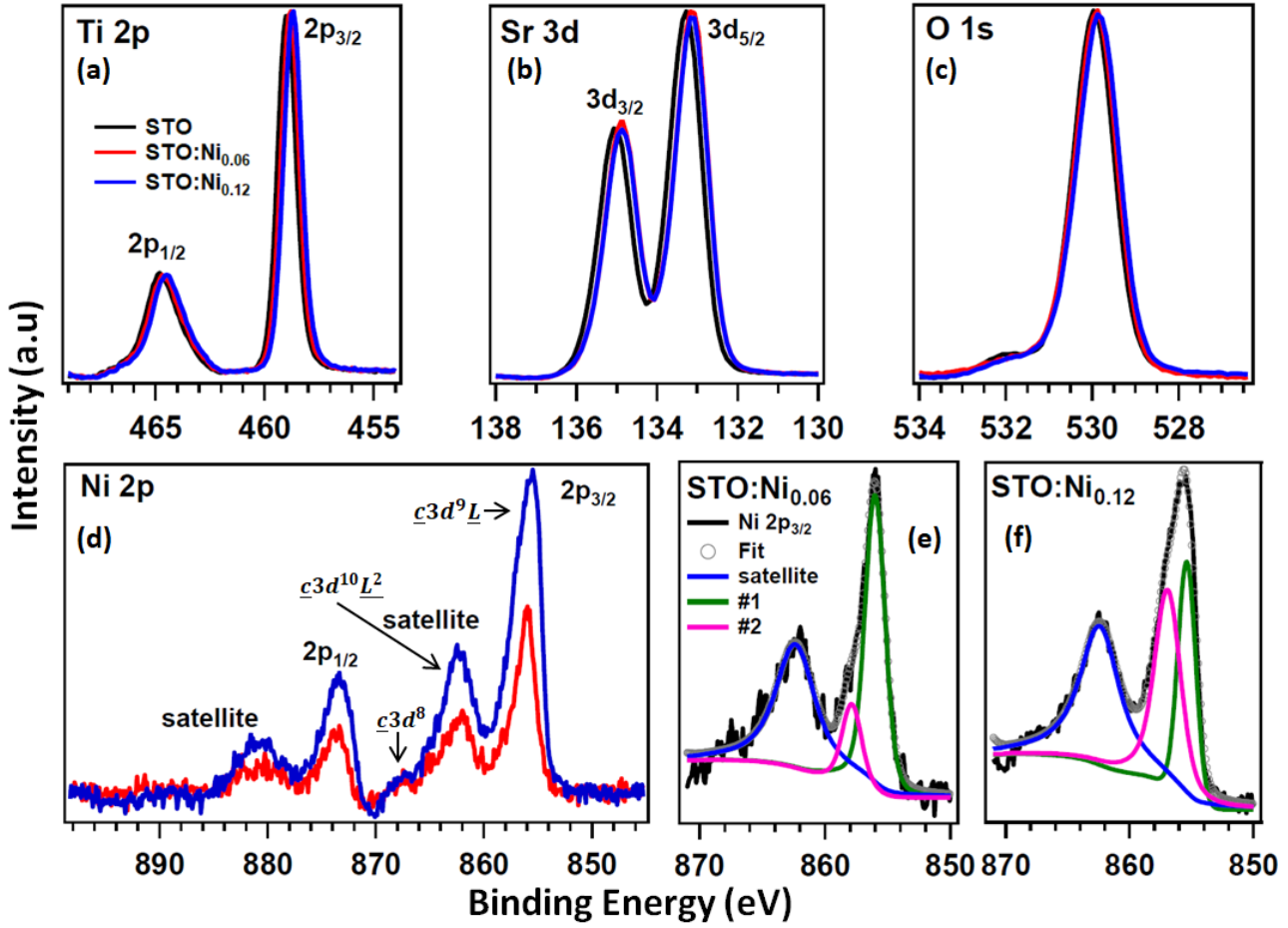


Figure 5.3: (a-d) Core level intensity obtained with $h\nu=1486.7$ eV at normal emission for STO, STO:Ni_{0.06} and STO:Ni_{0.12} films. All spectra are normalized by the Sr 3d spectral weight. (e-f) Ni 2p_{3/2} spectra of STO:Ni_{0.06} and STO:Ni_{0.12} films, respectively. The fitting curves were obtained by subtracting a Shirley background and adding a sufficient number of Voigt curves.

Having identified the optimal substrate temperature, oxygen background gas and laser energy to be 700°C, 1.10^{-1} mbar and 1.8 J/cm² as the best growth parameters, the remaining question is which type of stoichiometry is present in the samples, in particular, the Ni chemical environment. To answer this question, Sr 3d, Ti 2p, Ni 2p and O 1s core level XPS spectra for undoped and STO:Ni_x films were measured. The samples are usually kept in UHV after PLD growth and then transferred in-situ to the analysis chamber for measurements to prevent surface contamination.

The XPS spectra of the STO, STO:Ni_{0.06} and STO:Ni_{0.12} films in Fig. 5.3 (a-c), which are measured with monochromatic Al K_α x-ray source of 1486.7 eV, show the expected Sr, Ti and O core levels with no detectable contamination of the samples by C, and the spectral weights of the Sr 3d, Ti 2p and O 1s peaks are identical for all samples.

Let us now discuss the different peaks observed in the Ni 2p spectra presented in Fig. 5.3 (d): In both cases, the binding energy of the main Ni 2p-doublet lines (Ni 2p_{3/2} and Ni 2p_{1/2}) are found at 855.6 eV and 873.2 eV separated by $\Delta E=17.6$ eV. In term of orbital configuration, these peaks correspond to a Ni $\underline{c}3d^9L$ final state, where $\underline{\quad}$ denotes a hole. At around 6 eV higher binding energy from each doublet line, satellite features are visible suggesting the oxidized state of Ni atoms in STO films [184] that correspond to $\underline{c}3d^8$ and $\underline{c}3d^{10}L^2$ final states. The spectral weight

is clearly increasing by a factor of two for the STO:Ni_{0.12} sample in comparison to STO:Ni_{0.06} as expected.

For a detailed analysis of the Ni 2*p* spectra, a fitting procedure based on Voigt function (probability distribution given by the convolution of Lorentzian and Gaussian distributions) was applied and the results are depicted in Fig. 5.3 (e-f). In the following, only the Ni 2*p*_{3/2} doublet is analysed as its intensity is higher. For STO:Ni_{0.06} films, fitting of the Ni 2*p*_{3/2} line results in two peaks located at 855.8 eV and 857.7 eV ($\Delta E=1.9$ eV) labelled #1 and #2, respectively. The first one is assigned to the main line of Ni 2*p* XPS spectrum with the oxidation state Ni²⁺, while the second peak can have different explanations which we are going to discuss further in the next paragraph. Similarly for STO:Ni_{0.12} films, the double peak structure of the Ni 2*p*_{3/2} line is detected, where the main Ni 2*p* line is located at 855.4 eV (#1) and the second peak (#2) at 857 eV ($\Delta E=1.6$ eV). However, the spectral weight of the double peak structure is not the same for the different samples: In the case of STO:Ni_{0.06}, the ratio of the peaks #1/#2 is equal to 2.86, while for STO:Ni_{0.12} the contribution of peak #2 increases significantly and the ratio decreases to 1.12.

The interpretation of the extra peak (#2) located on the high binding energy side of the main Ni 2*p* line (#1) is not straightforward. Let us first assume that this peak indicates the presence of another Ni oxidation state (Ni³⁺) as result of the presence of different chemical environment in the STO lattice. Yet, the significant increase of Ni³⁺ contribution we observe in the spectra upon increasing Ni-doping from 6% to 12% cannot be totally accepted. Moreover, it is surprising that the Ni³⁺ state can be stable in STO films against reduction knowing that Ni²⁺ is the most stable oxidation state for Ni.

A most likely explanation, even though it is still controversial, was proposed to explain similar structure in the Ni 2*p* XPS spectrum in NiO [94,96,98]. Assuming that Ni has an octahedral environment with oxygen ions, the appearance of the extra peak (#2) results from a non-local screening process by an electron that does not come from the oxygen orbitals around the Ni atom with the core hole, but from a neighbouring NiO₆ unit. In this case one can define #1 peak to a locally screened core hole $c3d^9\bar{L}$ state and peak #2 to a non-locally screened core hole $c3d^9\bar{L}(3d^8\bar{L})$ state [94]. This hypothesis can be verified by the difference seen in the spectral weight of peak #2 as a function of the Ni dopant concentration in STO films. As we mentioned before, the contribution of this peak in STO:Ni_{0.06} is relatively weak and becomes more important in STO:Ni_{0.12}. According to our statement, this is expected for a Ni rich environment, where the probability of having a $d^8\bar{L}$ states available as next nearest neighbourhood to a particular Ni ion, that provides the non-local screening, is much higher. In addition, the peak #2 might also have some surface state contribution resulting from pyramidally coordinated Ni atoms located at the surface of the films and overlaps with the non-local screening peak [98,99].

In conclusion, the analysis of the Ni 2*p* core level line shapes gave us a plausible evidence of the chemical environments of Ni atoms in the doped STO films: octahedral in the bulk and pyramidal at the surface, in which Ni ions substitute the Ti ions.

5.2 Fe and Cr-doped SrTiO₃ Films

The case of STO:Fe_{0.05} and STO:Cr_{0.05} samples is slightly different. The films of 30 unit cell thickness (equivalent to 11.7 nm) were grown by PLD on TiO₂ terminated STO(100) substrates with light niobium doping (5 at.%) and the targets used for growth are crystalline STO targets, and pure Fe/Cr pellets being used for doping. The films were prepared by Milan Radovic and Marco Caputo at the Paul Scherrer Institute. Since the films were ex-situ transferred to the experimental stations, special care has to be taken to eliminate adsorbates and contamination from the surface before starting any further investigation. The main issue in oxide materials is the ease of losing oxygen atoms. So we prepare the samples under an oxygen atmosphere to prevent creating oxygen vacancies:

1. Annealing in UHV at 350°C for 40 min (or at least until the pressure in the preparation chamber drops down to 1.10^{-9} mbar). This removes most of the contamination of the top layers without inducing reduction (oxygen vacancies);
2. Add oxygen $P_{oxygen}=1.10^{-5}$ mbar and increase temperature to 600°C for 1 hour. In this step, the rest of contamination is removed and the surface is reconstructed.

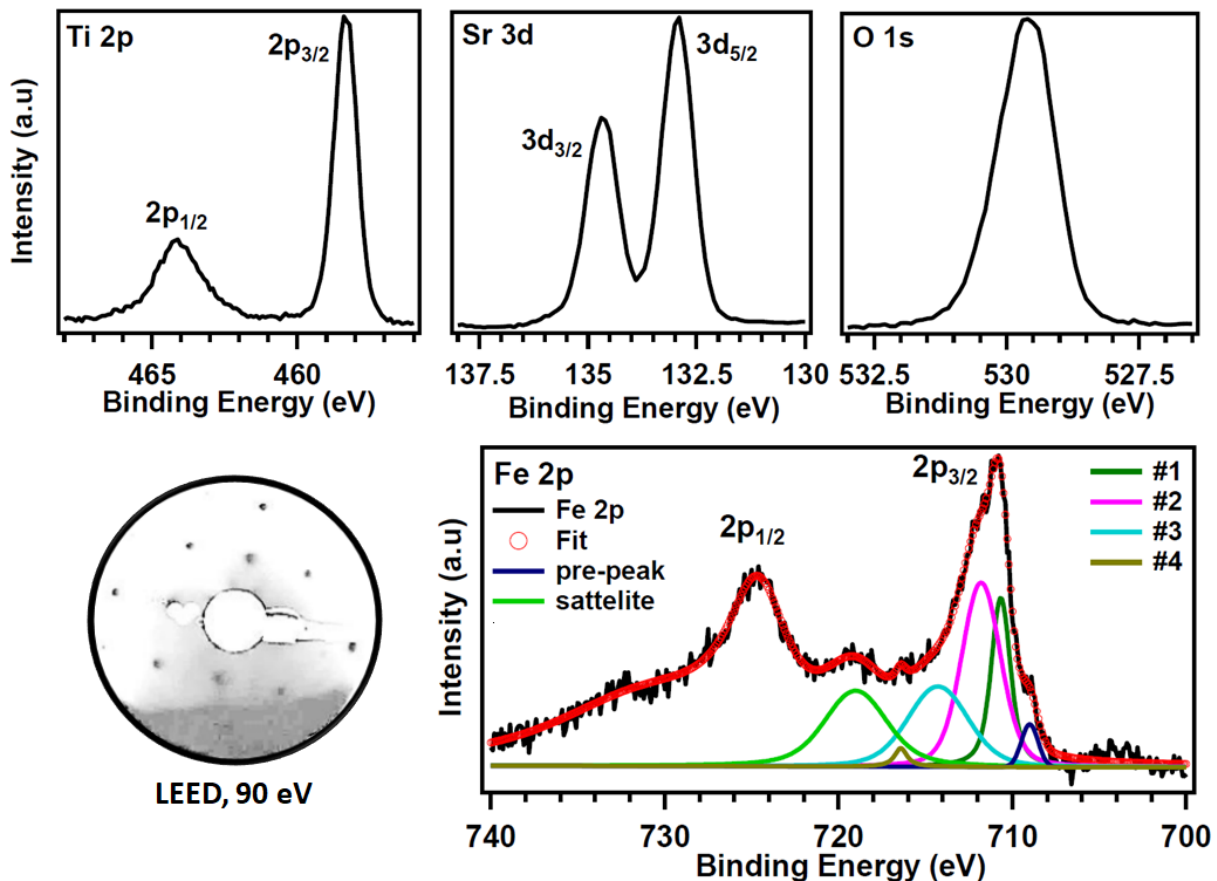


Figure 5.4: LEED pattern and XPS core level spectra obtained with $h\nu=1000$ eV at normal emission for the STO:Fe_{0.05} films. The LEED image pattern shows a (1×1) cubic Brillouin zone. The fitting curves of Fe 2p spectra were obtained by subtracting a Shirley background and adding a sufficient number of Voigt profiles.

The films structure was checked by LEED after surface preparation: the diffraction patterns of both samples show a (1×1) cubic structure with no indication of surface reconstruction (see Figs.

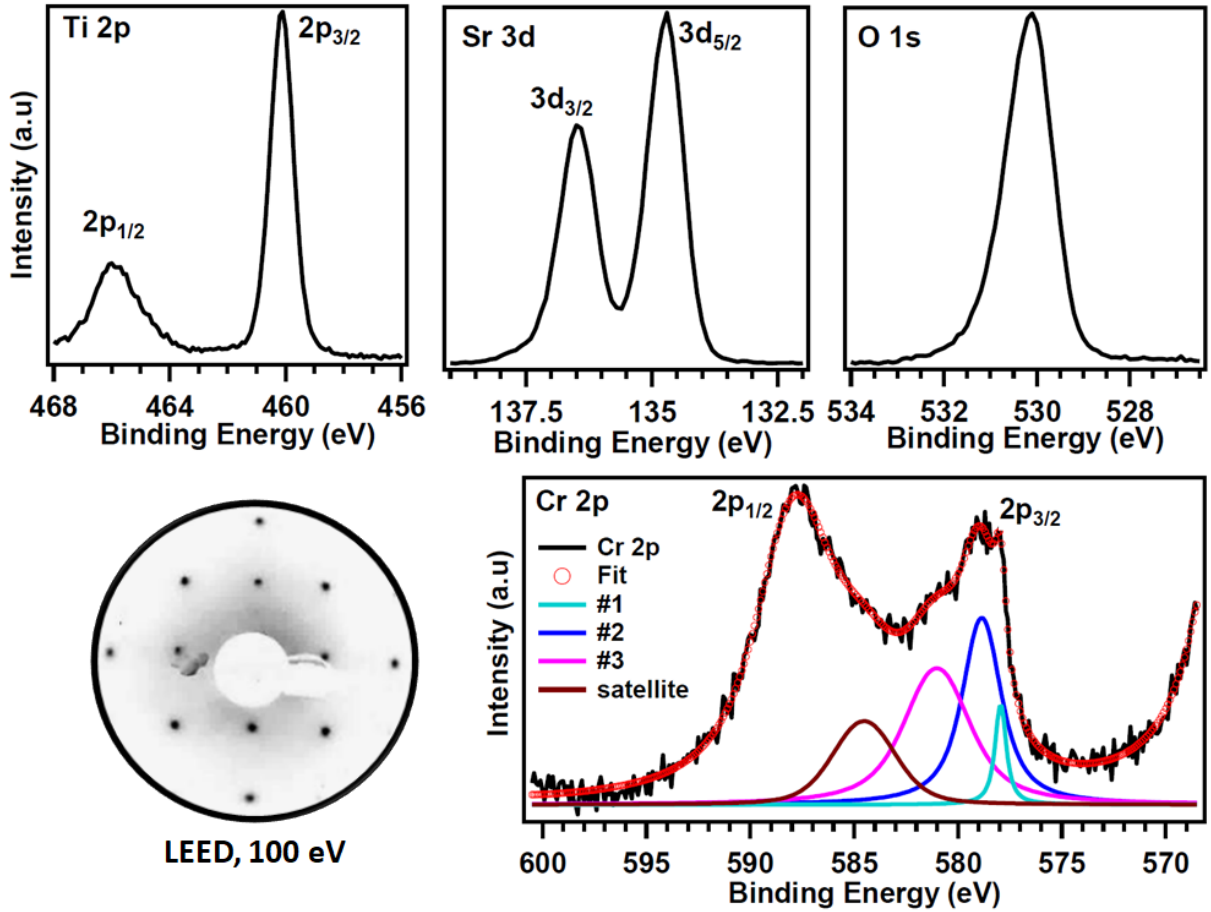


Figure 5.5: LEED pattern and XPS core level spectra obtained with $h\nu=1000$ eV at normal emission for the STO:Cr_{0.05} films. The LEED pattern shows a (1×1) cubic Brillouin zone. The fitting curves of Cr 2p spectra were obtained by subtracting a Shirley background and adding a sufficient number of Voigt profiles.

5.4 and 5.5). Then the samples were transferred under vacuum to the experimental station at the PEARL beamline of SLS where XPS spectra were recorded using linearly polarized light of $h\nu=1000$ eV at RT in UHV environment ($\sim 8.10^{-11}$ mbar). The results are displayed in Fig. 5.4 and Fig. 5.5 for STO:Fe_{0.05} and STO:Cr_{0.05} films, respectively.

Note that the same fitting procedure as that mentioned in section 5.1 is applied for the present XPS spectra. For both samples, the Sr 3d, Ti 2p and O 1s core levels attest the presence of Sr²⁺, Ti⁴⁺ and O²⁻ states. The Fe 2p XPS region (Fig. 5.4) exhibits the doublet 2p_{3/2} at 710.8 eV and 2p_{1/2} at 724.6 eV ($\Delta E=13.8$ eV). The peak at 8.4 eV higher binding energy from the 2p_{3/2} main line corresponds to the 2p_{3/2}-satellite. The "pre-peak" was required to adequately fit the spectra and the #4 peak is related to surface structures as is it located at high binding energy. Fitting of the main 2p_{3/2} spectrum gives rise to four peaks: the first three peaks (labelled #1, #2 and #3) between 710.7 eV and 714 eV correspond to the Fe³⁺ in which Fe ions substitute Ti in the STO lattice [182, 185]. According to Grosvenor *et al* and Moukassi *et al*. [186, 187], the large width of the 2p_{3/2} line that contains the multiplet structure reveals the presence of high-spin Fe³⁺ cations octahedrally coordinated.

The Cr $2p$ XPS region (Fig. 5.5) seems to be more complex. The spectrum shows the two spin-orbit split components with $\Delta E=9.1$ eV. A satellite feature of the Cr $2p_{3/2}$ peak overlaps the Cr $2p_{1/2}$ component [184]. Three main peaks are obtained after deconvolution of the Cr $2p_{3/2}$ doublet labelled #1, #2 and #3. The first two peaks located at 577.9 eV and 578.9 eV are attributed to the Cr³⁺ multiplet structure commonly observed in Cr(III) oxide compounds. Note that the Cr³⁺ oxide has many multiplet-split components which require a delicate fitting to prevent false identification of other chemical states [188]. The third peak (#3) located at 581 eV is mainly related to the higher Cr⁶⁺ oxidation state also detected in chromium oxide compounds. The quantification of the Cr⁶⁺ species is limited by the overlap with the multiplet splitting of the Cr³⁺ species [188, 189].

5.3 Impact of TM-doping on the Electronic Structure of SrTiO₃ Films

Having identified the optimal growth conditions and initiated a layer-by-layer growth mode for STO:Ni and characterized the crystal structure and chemical bonds of the STO:Ni/Fe/Cr, we now turn to analyse the electronic properties of the thin films and identify the effect of TM-doping in STO. In the following, experimental XPS data will be confronted with band structure calculations. First, we used the DFT calculations to conduct a comparative study of the band structure and the electronic properties of STO doped with Ni, Cr and Fe. Then, the resonant behaviour on all valence band XPS of all doped samples is presented.

5.3.1 Role of TM-doping in the modification of the SrTiO₃ band gap

Immediately after the growth of the Ni-doped STO thin films (samples always *in situ*), for a rough evaluation, the angle-integrated valence band (VB) of each sample was measured by XPS with monochromatic $h\nu=1486.6$ eV (Al K $_{\alpha}$). The results are given in Fig. 5.6. The common features observed in this VB series are the two bands between 3 eV and 8 eV binding energy formed by O $2p$ and Ti $3d$ states. For the doped samples, we notice the formation of an in-gap state located at a binding energy of 2-2.5 eV (indicated by the arrows). A quantitative view of the new formed states can be seen by subtracting the VB of the different doped films by that of the undoped one, as it is presented in Fig. 5.6. It is clear from these data that the intensity of the in-gap state increases with increasing the Ni content in the films assuming that this state reflects the contribution of impurity Ni $3d$ levels in the gap of STO. This observation rises the question about the effects of TM-doping on the electronic structure of STO.

To answer this question, we performed first-principles band structure calculations. All our calculations were performed within the framework of the KKR-Green's function method based on the multiple scattering theory [134, 190]. The potential energy for the STO(100) bulk system with TiO₂ termination is induced in a self-consistent way using the atomic spherical approximation (ASA). The impact of chemical disorder is handled by means of the CPA alloy theory [166, 169]: TM atoms (Ni, Fe and Cr) are randomly placed in substitution of Ti atoms and a new potential is generated. The lattice parameter used in this study is 3.905 Å. The l_{max} value was fixed to 3

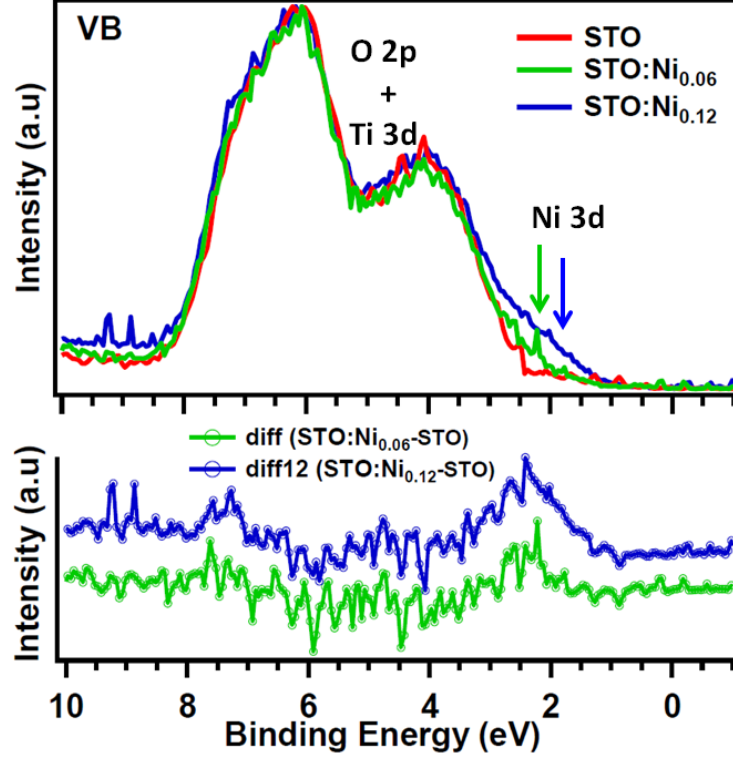


Figure 5.6: Angle integrated valence band of STO (red solid line), STO:Ni_{0.06} (green solid line) and STO:Ni_{0.12} (blue solid line) registered with monochromatic $h\nu=1486.6$ eV directly after film growth (samples in-situ). The green and blue arrows assign the formation of new in-gap states in the valence band of STO films at around 2-2.5 eV due to Ni-doping. A quantitative estimation of the new impurity states is also given by subtracting the VB of the doped films with the undoped one is shown in the bottom panel of the figure.

(f electrons) for the expansion in spherical harmonics. This will typically improve the calculated value for the band gap.

TDOS and PDOS of TM-doped STO are compared with those of undoped STO in Fig. 5.7 and 5.8. The VB of pure STO is mostly composed of the O $2p$ states and the conduction band (CB) is mainly dominated by Ti $3d$ states. For STO:Ni_{0.06}, a wide isolated distinct defect peak appears in the middle of the band gap, close to the VB. As shown by the PDOS, it corresponds to Ni $3d$ state and O $2p$ state. The relative intensity of this peak increases by a factor of two for STO:Ni_{0.12}. The Ni $3d$ states make a contribution to the whole VB and at the edge of the CB.

For STO:Fe_{0.05} and STO:Cr_{0.05}, the spin-up and spin-down states are asymmetric near the Fermi level, suggesting that these systems should be magnetic. The TDOS peaks are shifted to lower binding energy and spin splitting is induced around the Fermi level. According to PDOS, for STO:Fe_{0.05} the spin down state crosses the Fermi level, whereas the spin up band takes over the band gap around the Fermi level and contributes to the VB. For STO:Cr_{0.05}, the spin up band crosses the Fermi level, and the spin down band mainly contributes to the CB. If we look closely to the in-gap states of all TM-doped STO systems, we see that the peaks around or crossing the Fermi level are mainly due to the hybridization of TM- $3d$ and O $2p$ states. This leads to the conclusion that the localized states near the Fermi level are referable to the O $2p$ and TM- $3d$ electrons.

The ground state band structures or so-called Bloch spectral function of STO and STO:TM

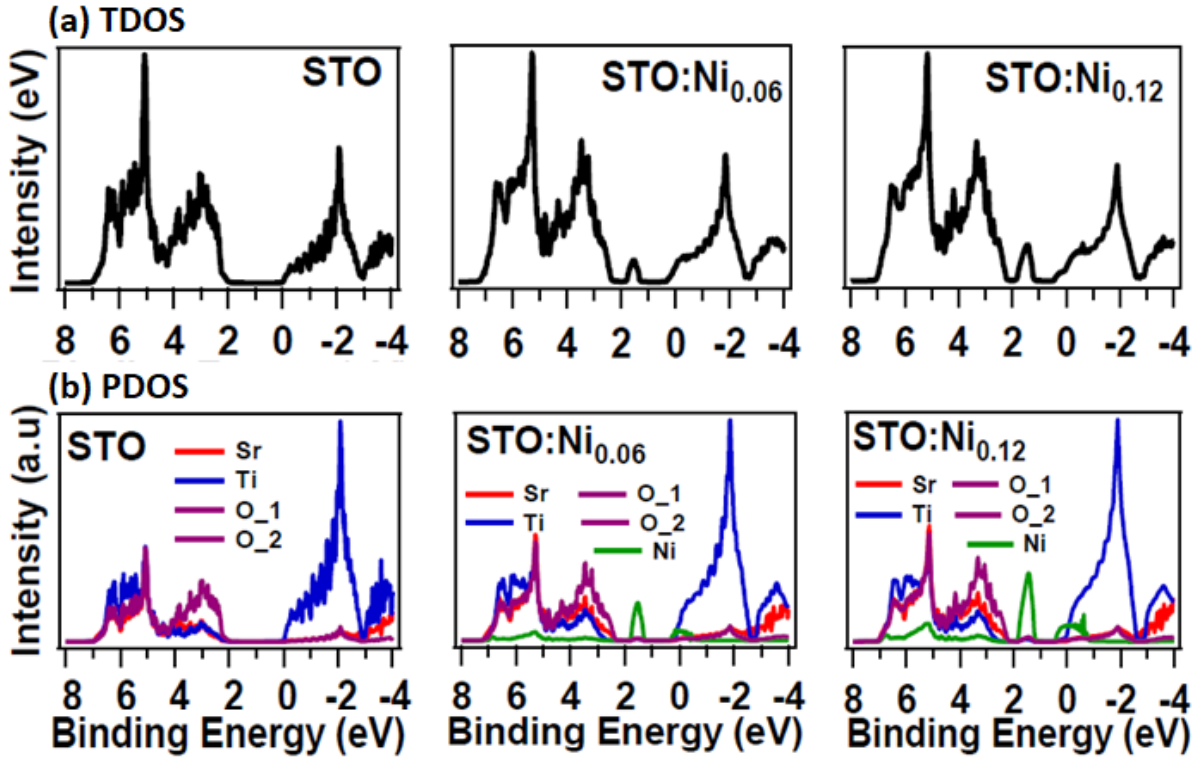


Figure 5.7: (a) Total DOS and (b) PDOS for pure STO, STO:Ni_{0.06} and STO:Ni_{0.12}. The Fermi level is set to zero.

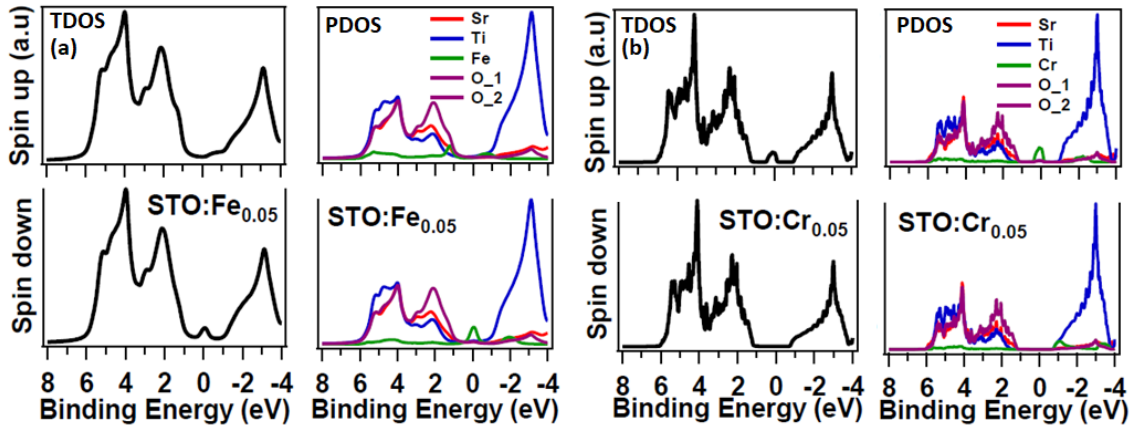


Figure 5.8: (a) Total DOS and (b) PDOS for STO:Fe_{0.05} and STO:Cr_{0.05}. The Fermi level is set to zero

Table 5.1: This table illustrates $\Delta E = \text{VBM-IEL}$ and $\Delta E = \text{IEL-CBM}$ in eV, at the Γ -point of the following systems obtained from DFT calculations.

System	VBM-IEL	IEL-CBM
STO	-	-
STO:Ni _{0.06}	0.65	1.35
STO:Ni _{0.12}	0.65	1.02
STO:Fe _{0.05}	0.84	1.06
STO:Cr _{0.05}	0.86	1.04

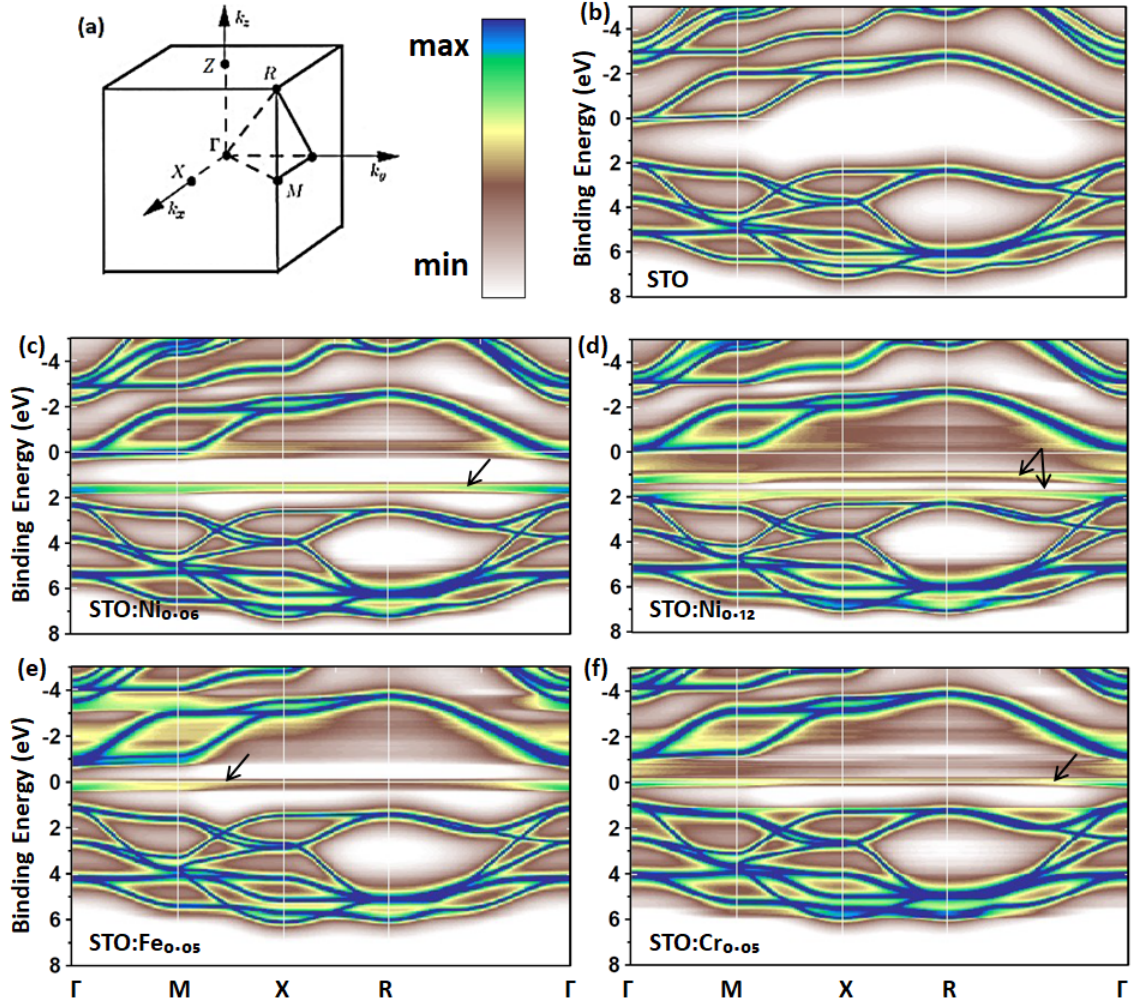


Figure 5.9: (a) Scheme of the first Brillouin zone of a simple cubic system showing the high symmetry points. Calculated ground state band structures (Bloch spectral function) of (b) STO, (c) STO:Ni_{0.06}, (d) STO:Ni_{0.12}, (e) STO:Fe_{0.05} and (f) STO:Cr_{0.05}. Black arrows are pointed to the TM 3d levels in the band gap.

(TM=Ni, Fe and Cr) are presented in Fig. 5.9. For a comparative study of the electronic structures of TM-doped STO, the same k -point mesh is chosen with respect to the high symmetry points in the first Brillouin zone of STO (see Fig. 5.9 (a)). As displayed in Fig. 5.9 (b), the band gap of undoped STO is calculated to be 2 eV, which is lower than the experimental value (~ 3.2 eV) due to the shortcoming of DFT in describing the exchange-correlation potentials using the LDA approximation (see section 3.1.2). In this part, we neglect the band gap error for all systems, so that the relative change in the band gap of doped STO (with respect to undoped STO) can provide the effect of TM-doping in STO.

Let us now discuss the modifications in the band structures of the different TM-doped STO (see plots in Fig. 5.9 (c-f)) and their band gap (see Table. 5.1): The impurity energy levels (IELs) at the conduction band minima (CBM) or valence band maxima (VBM) or insertion in between the band gap are clearly seen (marked by black arrows), attesting that 3d-TM substitution of the Ti sites induces an effective reduction in the energy gap of STO with respect to the pure one.

STO: Undoped STO is chosen as a reference for the comparative study on the doping effect in STO by $3d$ -TMs. The band gap at the Γ -point is equal to 2 eV.

STO:Ni_{0.06}: An isolated atom-like flat defect band is present through the whole the Brillouin zone and causes a considerable decrease in the band gap. The defect band is formed close to the valence band, in which the IEL is located at 0.65 eV above the VBM and at 1.35 eV below the CBM, which makes Ni dopant atoms acceptor impurities. In fact, the electronic configuration of Ni is $3d^8 4s^2$, and Ni in the Ti-site is expected to have a 3+ and/or 2+ valence state ($3d^5 4s^2$ and/or $3d^6 4s^2$) unlike the oxidation state of Ti atoms (4+). This fact leads to the increase of hole concentration and/or oxygen vacancies [89].

STO:Ni_{0.12}: By increasing twice the Ni doping concentration in STO (from 6% to 12%), all bands in the VB are shifted by 0.33 eV toward Fermi level (0 eV), and two isolated IELs are formed: The first one is located at the VBM at around 2 eV and the second one is located in the band gap at 0.65 eV above the VBM and at 1.02 eV below the CBM.

STO:Fe_{0.05} and STO:Cr_{0.05}: Doping STO with Fe or Cr results in a shift of the Fermi level by ~ 1 eV toward the VB. One single defect band is formed almost in the middle of the band gap. In case of STO:Fe_{0.05}, the IEL is located at 0.84 eV above the VBM and at 1.06 eV below the CBM. For STO:Cr_{0.05}, the IEL is positioned at 0.86 eV above the VBM and at 1.04 eV below the CBM.

In addition to the dopant bands formed in the band gap of STO, there are additional impurity bands that overlap with the VB and/or the CB. Even though they do not participate in a modification of the band gap, they contribute to the electron density of the VB and/or CB of STO.

From band structure calculations, we showed the formation of localised defect bands (non-dispersive bands) that belong to the $3d$ -TM impurities, in the band gap of STO. According to the data presented in Table. 5.1, doping with Ni seems to be the best candidate in reducing the optical band gap, and thus the optical absorption edge towards the visible light region is expanded the most.

5.3.2 Resonant behaviour of TM-doped SrTiO₃

Having identified the origin of the main valence band features of the $3d$ TM-doped STO by DFT, we now turn to investigate the correlated electronic structure of the $3d$ -TM states in our samples by resPES. As discussed in section 2.2, the resonance between direct photoemission and Auger decay channel, i.e. in this case TM $3d$ emission and LMM Auger, can strongly enhance the photoemission intensity. All measurements have been performed at the PEARL and ADDRESS beamlines of the Swiss Light Source. Since resPES is a technique that requires measurements of the photoelectron spectra for photon energies within the region of a selected absorption edge, recording of the X-ray absorption (XAS) spectrum is a first step for the resPES studies. In general, the $3d$ -TM $L_{2,3}$ -edges are sensitive to oxidation state and ligand field changes [191,192]. The Ni $L_{2,3}$, Cr $L_{2,3}$ and Fe $L_{2,3}$ XAS spectra are presented in Figs. 5.10 and 5.11.

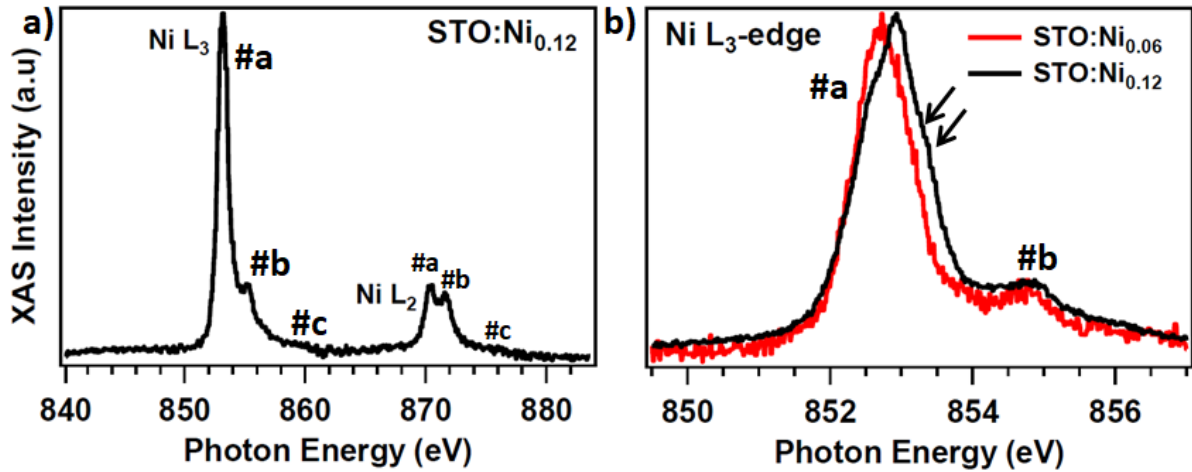


Figure 5.10: (a) Ni $L_{2,3}$ XAS spectra for STO:Ni_{0.12}. (b) Comparison of the Ni L_3 absorption spectra for STO:Ni_{0.06} and STO:Ni_{0.12} films.

For STO:Ni_{0.06} and STO:Ni_{0.12} films, the Ni XAS spectra have similar features. Thus, only one case is presented in order to define the characteristics of the spectrum (see Fig. 5.10 (a)): The $2p$ spin-orbit interaction splits the spectrum in two parts, the L_3 -edge ($2p_{3/2}$) at 853 eV and the L_2 -edge ($2p_{1/2}$) at 870.2 eV (labelled #a in the spectrum), with most of the spectral weight in the L_3 -edge. The other two features which are labelled #b and #c, lie at approximately 2 eV and 6 eV higher energy side of the edges, respectively. The first one (#b) is due to splitting of the $2p^53d^9$ state, resulting from the Coulomb interaction, exchange interaction and crystal field effects as it was reported by Laan *et al.* for NiO, and the second one (#c) is attributed to the satellite structure [103]. A quantitative comparison of the L_3 -edge for STO:Ni_{0.06} and STO:Ni_{0.12} films is presented in Fig. 5.10 (b). The main line (#a) broadens when increasing the Ni concentration, in which additional feature is formed at higher energy side of the line (tagged by the black arrows). This broadening can be mainly resulting from a non-local screening process that involves the Ni²⁺ ion and the ligand states, as it was suggested by the analysis of the XPS data in section 5.1.

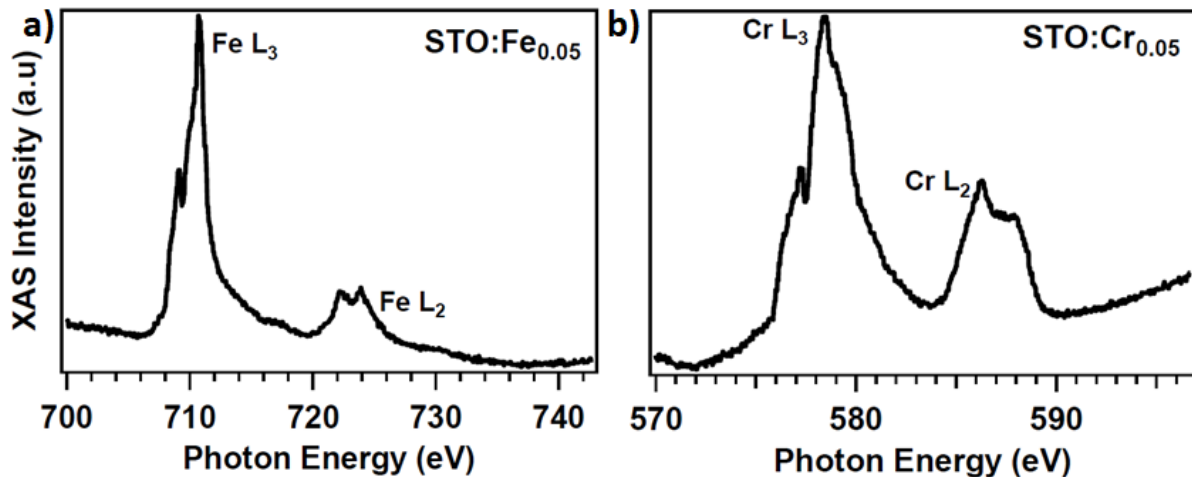


Figure 5.11: (a) Fe $L_{2,3}$ and (b) Cr $L_{2,3}$ absorption spectra for STO:Fe_{0.05} and STO:Cr_{0.05} films, respectively.

The Fe $L_{2,3}$ XAS presented in Fig. 5.11 (a) shows the spin-orbit splitting of the two main absorption lines separated by approximately 11 eV. Let us consider the L_3 -edge with the most spectral weight: It is mainly attributed to the Fe^{3+} contribution in STO. The spectrum has two maxima, at about 709 eV and 710.8 eV with are related to the e_g and t_{2g} orbitals . Another weak feature formed at 713.3 eV is due to the $2p3d$ multiplet interaction [193].

The Cr $L_{2,3}$ -edge presented in Fig. 5.11 (b) is also showing the spin-orbit splitting of the two components L_3 (578.5 eV) and L_2 (586 eV) edges. The three peaks within the L_3 spectrum which are positioned at 577.3 eV, 578.5 eV and 579.5 eV, reflect the relative strength of the atomic crystal field interactions [194–196], and the lineshape of the Cr L_3 shows a clear correlation with the octahedral Cr^{3+} [197].

To determine by resPES the $3d$ TM related parts of the VB, spectra are recorded at two photon energies: one across the $3d$ TM absorption L-edge (resON), and the second below threshold (resOFF). Since the resonance affects TM $3d$ states, only the $3d$ PDOS is left when an resOFF spectrum is subtracted from each spectrum.

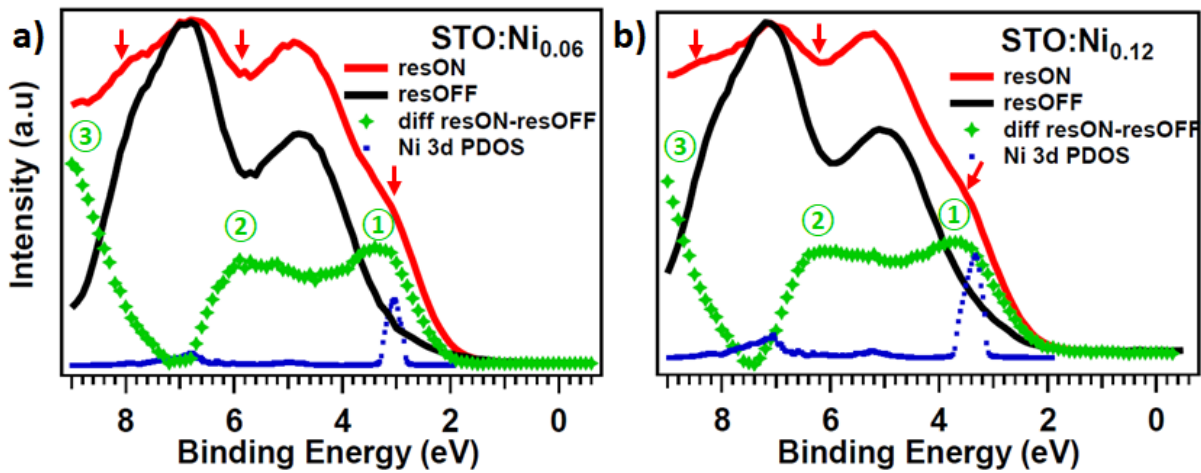


Figure 5.12: Resonant photoemission measurements for the VB of (a) $\text{STO:Ni}_{0.06}$ and (b) $\text{STO:Ni}_{0.12}$ films recorded with two photon energies. resON: Photon energy around the TM L_3 -edge absorption. resOFF: Photon energy below threshold. The difference of the valence bands resON-resOFF, as well as the $3d$ -TM PDOS of STO:TM systems are also given.

$\text{STO:Ni}_{0.06}$ and $\text{STO:Ni}_{0.12}$

For $\text{STO:Ni}_{0.06}$ and $\text{STO:Ni}_{0.12}$, the intensity of the VB features are strongly enhanced at the resonance of Ni ($2p \rightarrow 3d$) as it is presented in Fig. 5.12 (a,b) (the new features at the resonance are marked by the red arrows in the figure). The difference (resON-resOFF) (green solid line), gives a quantitative representation of the three major resonances labelled 1, 2 and 3. The maximum of each feature lies at binding energy 3.5 eV, 5.5 eV and 9 eV, respectively. The Ni $3d$ PDOS (blue solid line) shows one main peak that matches only with feature 1, yet, features 2 and 3 are not predicted by the calculations. As it fits with the Ni $3d$ PDOS, feature 1 represents the main Ni $3d$ -band that contribute in the VB of STO in this binding energy range. Features 2 and 3 are related to multiplet and satellite structures, respectively, that we are going to discuss further. In principle, the resonance of multiplet and satellite features results mainly from

electron-electron correlations. To perform our calculations, we used the LDA approximation, in which the correlation effects are not included and therefore all the structures that involve correlations cannot be obtained. Moreover, the difference in intensities and spectral weight of the Ni 3d PDOS and (resON-resOFF) curve can be related to two facts: surprisingly, it might be finite hybridization of the Ni 3d and O 2p states, described by charge transfers from the ligand to the transition metal ions, that makes the O 2p feature to resonate as well at the Ni L-absorption. The second fact, which is more general, is that the calculated density-of-states does not include all many-body effects, mainly the scattering effects which are caused by the changes in cross section with the used photon energy and lead to a serious modification in the spectral intensity.

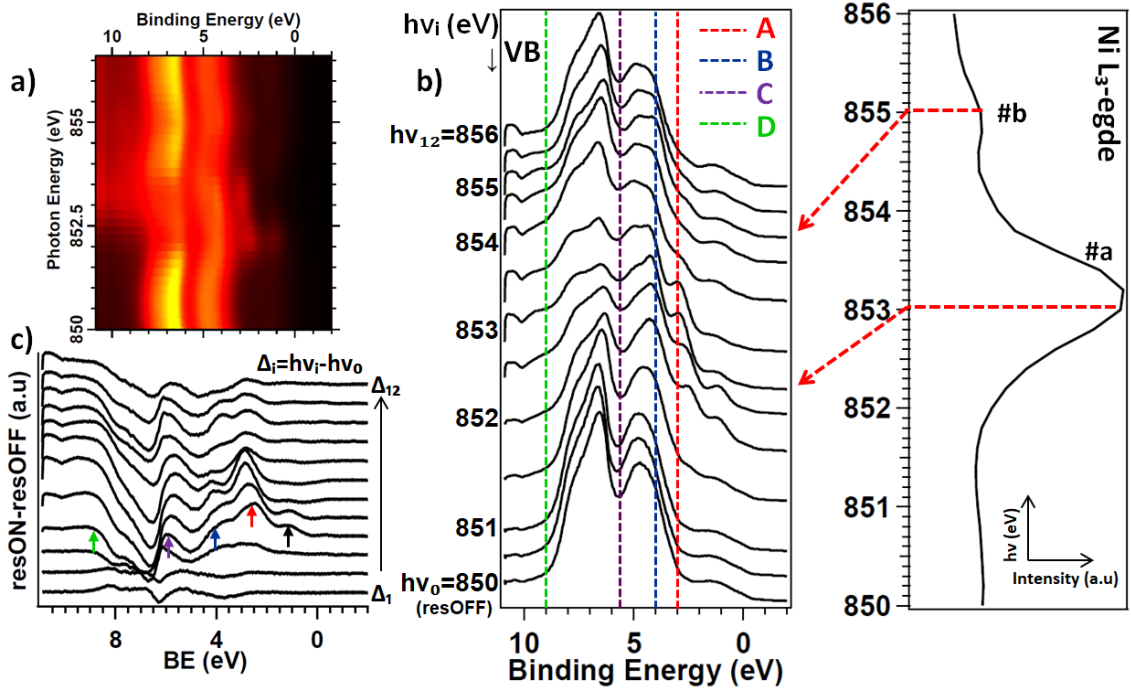


Figure 5.13: (a) Photoemission intensity map in the valence band region of STO:Ni_{0.06} films for photon energies within the Ni 2p → 3d (*L*₃) resonance. (b) Stack of angle-integrated profiles of the VB at photon energies from 850 eV to 856 eV with a 0.5 eV step, that correspond to the XAS spectrum of Ni *L*₃-edge plotted in the figure. $h\nu_0=850$ eV corresponds to OFF-resonance. The labels A, B, C and D correspond to the new features observed in the VB at the resonance. (c) Difference of the valence bands resON-resOFF ($\Delta=h\nu_i-h\nu_0$ which $i=1, 2, \dots, 12$). The arrows correspond to the features A, B, C and D according to their colours. The black arrow is related to oxygen vacancies neighbouring Ni ions.

A more detailed study of the resonant behavior in STO doped with Ni has been performed and the data are presented in Figs. 5.13 and 5.14: The STO:Ni_{0.06} and STO:Ni_{0.12} VBs were recorded with photon energies from 850 to 856 eV (with step of 0.5 eV), within the absorption edge of Ni 2p_{3/2}. To facilitate the analysis, each set of data is presented in two ways, as a photoemission intensity map and as a mesh plot of spectral intensity for different photon energies.

Let us first start with STO:Ni_{0.06} films (Fig. 5.13). We remind that the main Ni *L*₃ absorption edge is found at 853.3 eV (#a), followed by a weak feature at around 855 eV (#b) which is due to multiplet splitting of the 2p⁵3d⁹ state (see the XAS spectrum in Fig. 5.13 (b)). In the photon energy range of the Ni *L*₃ absorption edge, a clear resonance enhancement of the in-gap electronic states is observed. Surprisingly, the intensities of the valence band maxima at $E_B=4.7$ eV and 6.6 eV with photon energies before- and after-resonance are higher compared to resON case. In the photoemission spectra of the valence band presented in Fig. 5.13 (b), four

features can be observed due to Ni ($2p \rightarrow 3d$) resonance, labelled A, B, C and D. These features are quantitatively extracted by subtracting the resON and resOFF spectra, and the data are depicted in Fig. 5.13 (c). All features are dispersing at photon energies higher than 852 eV while staying almost constant at lower photon energies:

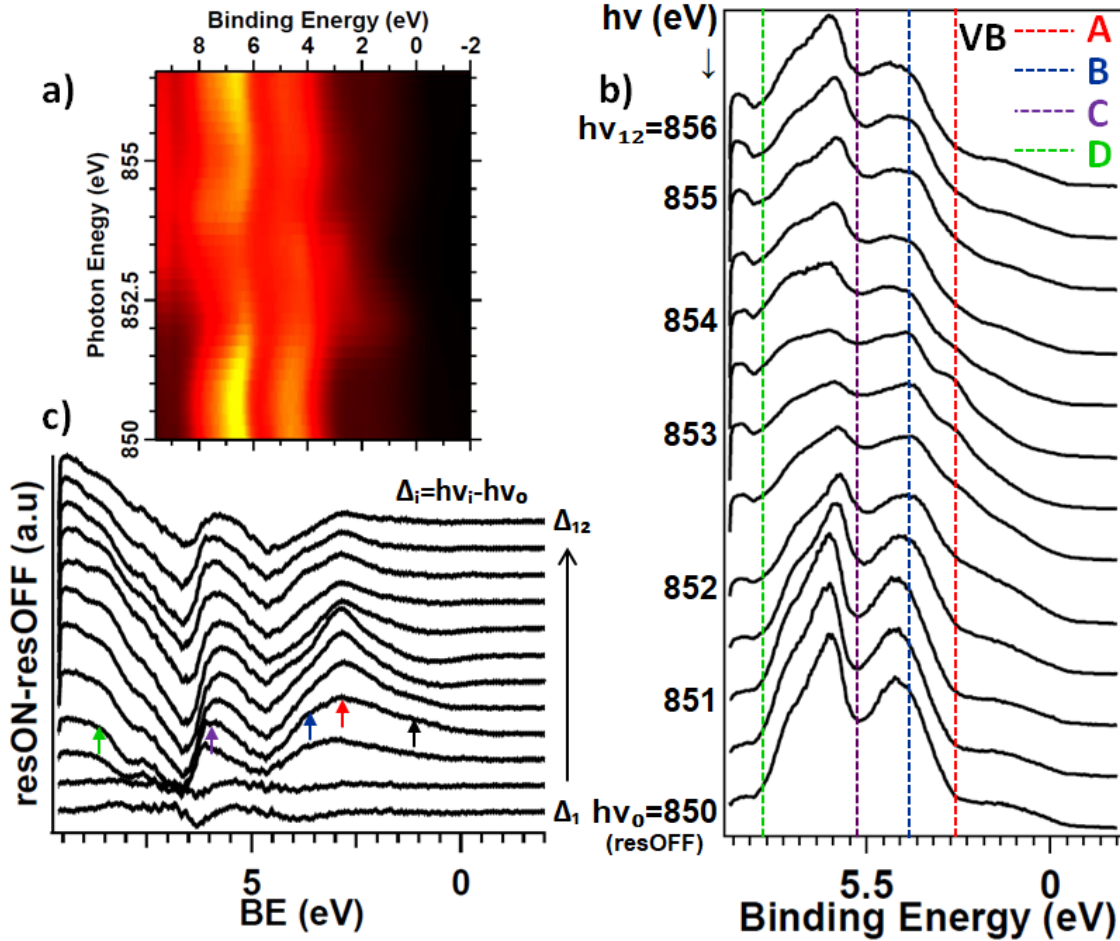


Figure 5.14: (a) Photoemission intensity map in the valence band region of STO:Ni_{0.12} films for photon energies within the Ni $2p \rightarrow 3d$ (L_3) resonance. (b) Stack of angle-integrated profiles of the valence band at photon energies from 850 eV to 856 eV with a 0.5 eV step, that correspond to the XAS spectrum of Ni L_3 -edge. $h\nu_0=850$ eV corresponds to resOFF. The labels A, B, C and D correspond to the new features observed in the valence band at the resonance. (c) Difference of the valence bands resON-resOFF ($\Delta=h\nu_i-h\nu_0$ which $i=1, 2, \dots, 12$). The arrows correspond to the features A, B, C and D according to their colours. The black arrow is related to oxygen vacancies neighbouring Ni ions.

A is related to the main Ni $3d$ band formed at $E_B=2.8$ eV. Its intensity increases and reaches its maximum amplitude at a photon energy equal to that of peak #a in the XAS (~ 853 eV) attesting that the upper part of the valence band at this binding energy level has Ni $3d$ character. At $h\nu=855$ eV, the photon energy equal to that of the peak #b, the magnitude of A decreases again, with the most intensity in features B and C. This means that B and C result from resonance of multiplet structure, reflecting the strongly-correlated nature of Ni-ions with the crystal field. While features A, B and C follow a constant binding energy lines with the increase of photon energy, feature D (at $E_B=9$ eV) keeps at a constant binding energy for photon energies around 853 eV (Raman-Auger emission) and then starts to follow a constant kinetic energy line for photon energies away from threshold. This peak is mainly related to an incoherent Auger decay not participating in the resonance photoemission process and resulting from the satellite

state located at 6 eV higher binding energy from Ni L_3 (see section 2.2 and Fig. 5.3 (d)).

Back to the description we mentioned above about the intensity of the valence band at the resonance and before/after the resonance: As we discussed, the features A, B, C and D result from resonance of the main Ni $3d$ states, Ni related multiplet structures and the satellite structure, respectively, which also result from the strongly correlated nature of Ni ions with the crystal field and the oxygen ligand. Assuming that Ni $3d$ bands are partially hybridized with O $2p$ bands, at Ni ($2p \rightarrow 3d$) resonance the electrons which are oxygen related and correlated with Ni ions will resonate as well and follow same binding energies of the Ni $3d$ resonating structures. This phenomenon reduces the spectral weight of the valence band at E_B around 4.7 eV and 6.6 eV where O $2p$ bands are located, and increases it at lower binding energies (features A and B) and higher binding energies (feature C) where Ni $3d$ related states are located.

Another last interesting feature is seen in the gap at $E_B=1.1$ eV (tagged by black arrows in Fig. 5.13 (c)). This peak overlaps with the famous in-gap state already seen in the band gap of reduced STO surfaces called oxygen polaron and is related to oxygen vacancies neighbouring Ti ions [60]. From this we can assume that these states which are resonating at photon energies around Ni L_3 threshold correspond to localized charge carriers trapped in d -orbitals of Ni ions surrounding oxygen vacancies. This statement confirms the hybridized nature of Ni $3d$ and O $2p$ bands in the VB of STO.

The same features are also seen in the VB of STO:Ni_{0.12} films at the Ni ($2p \rightarrow 3d$) resonance (see Fig. 5.14). Only feature A, which is related to the main Ni $3d$ -band is more intense and broader compared to STO:Ni_{0.06}'s case, leading to an enhancement of the Ni related in-gap state. However, B, C and D seem to be similar for both samples in which their intensities as well as their general tendencies do not show any remarkable differences.

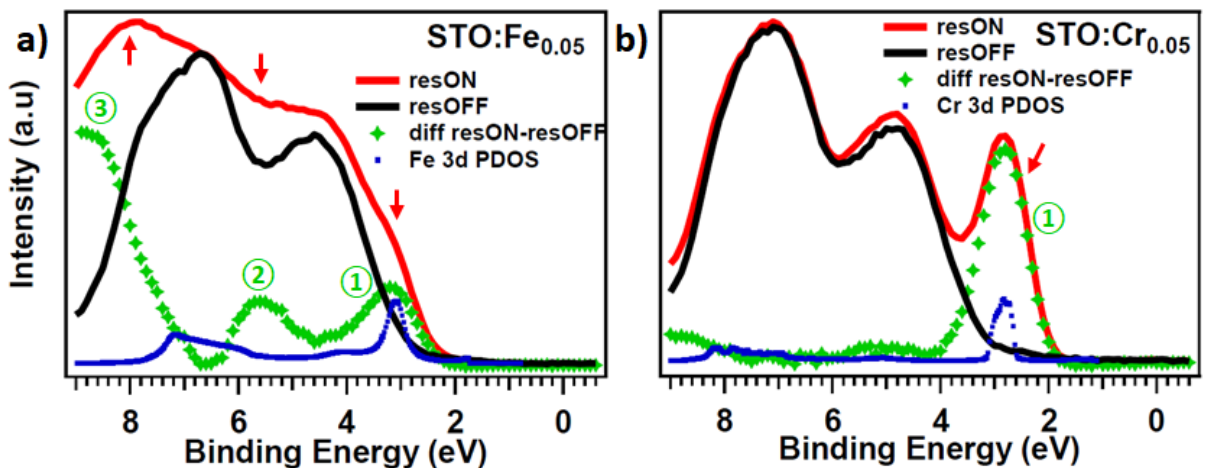


Figure 5.15: Resonant photoemission measurements for the valence band of (a) STO:Fe_{0.05} and (b) STO:Cr_{0.05} films registered with two photon energies. resON: Photon energy around the TM L_3 -edge absorption. resOFF: Photon energy away from the TM L_3 -edge absorption. The difference of the valence bands resON-resOFF, as well as the $3d$ -TM PDOS of STO:TM systems are plotted.

STO:Fe_{0.05}

Since the photon energy resolution available at the beamline used to perform the experiments on this sample is not high enough, it was not possible to realise the measurements at various photon energies across the Fe L-absorption edge in steps of hundreds meV in order to detect the different oxidation states of Fe in STO films. Therefore, to induce the resonance, we chose one photon energy across the absorption Fe L_3 -edge ($h\nu=709.7$ eV). The photoemission VB measured with photon energies at the resonance and before the resonance, the difference (resON-resOFF) curve and the Fe $3d$ PDOS are presented in Fig. 5.15 (a).

The intensity of the VB features are strongly enhanced at the resonance of Fe L_3 -edge, both in the gap at binding energies around 2.5 eV, and in the valence band at 5.5 eV (resonance of multiplet structure). The strong background observed at around 8 eV is due to an incoherent superposition of the photoemission signal with a more intense signal from Fe LMM Auger emissions. Back to the $3d$ Fe PDOS, the peak at 3 eV at the edge of the VB matches with the feature resulting from the difference of resON-resOFF curve at this energy, testifying the involvement of Fe $3d$ impurity band at the top of the VB. Yet the peaks resulting from the resonance of the multiplet structure (at 5.5 eV) and the satellite feature (at 8 eV) are not seen in the Fe $3d$ PDOS, since the calculation does not include electron-electron correlations.

STO:Cr_{0.05}

Similarly, in case of STO:Cr_{0.05} films, the VB was registered using two photon energies, at the Cr L_3 absorption edge ($h\nu=579$ eV) and away from the threshold. The experimental data are presented in Fig. ?? (b) and compared to the Cr $3d$ PDOS.

The main and almost only Cr $3d$ band contribution is present in the gap of the films at 2.6 eV and fits well with the Cr $3d$ PDOS. Surprisingly, the experimental data does not show any other features which can be related to correlation effects such as multiplet structures unlike Ni and Fe doped STO cases.

5.4 Conclusion

In this chapter, the role of $3d$ metal dopants in STO was studied using experimental and theoretical approaches. Pure STO(100) and Ni-doped STO(100) films were grown by PLD in which a detailed study having been carried out to find the optimal growth parameters. Based on the results, the parameters were found to be 700°C, 1.10^{-2} mbar and 1.8 J/cm² for substrate temperature, oxygen background gas and laser fluence, respectively. Structural characterisation analysis showed that Ni doping enhanced the quality of STO thin films. XPS data suggested that all TM atoms (Ni, Fe and Cr) were successfully incorporated in the lattice of the hosting system and mostly substituting Ti sites.

Compared to STO, the electronic structures and density of states of the $3d$ -TM doped STO show that $3d$ -TM doping leads to the formation of localized impurity energy levels in the band gap close to the VB, and can lead to the improvement of visible light absorption.

Absorption and resonant photoelectron measurements were performed in order to detect the $3d$ -TM states in the VB and in the gap of STO: According to XAS spectra, Ni, Fe and Cr L-edge show a strong multiplet splitting structures due to the Coulomb interaction (electron-electron correlations), exchange interaction and crystal field effects. The resonant photoelectron data revealed that the TM- $3d$ bands strongly contribute at the top of the VB in the gap, and a hybridization of the Ni and Fe- $3d$ bands with the O $2p$ bands is proposed.

ARPES Studies of Pristine and TM-doped SrTiO₃ Films

As shown in the previous chapters, photoemission has already yielded to a deeper understanding of the electronic structure of the investigated samples. We now go one step further and add momentum resolution to study the band structure by means of HR-ARPES.

As already discussed in chapter 1, the formation of charge carriers at the surface of STO can be induced by creating in-situ oxygen vacancies [15, 16]. The crystal arrangement of the surface layers appears to be another key reason responsible for the formation and structure of the 2DEG as it was reported in Refs. [198–200], where the results show a buckling distortion of the SrO and TiO₂ surface layers different from the bulk crystal structure

In the first part of this chapter, our studies of 3*d*-TM doped STO films are discussed. In these systems, the 3D bands dispersion in a wide binding energy range are observed, as well as the localised impurity energy levels in the band gap.

In the second part, an approach to induce the formation of the 2DEG at the surface of STO thin films is presented. Since its creation depends on both surface structure and surface preparation, despite its origin, the main goal here is to test the feasibility of this experimentation and the quality of the films. The properties of the 2DEG formed at the surface of Ni-doped STO films with Ti-resonant ARPES are also presented and discussed. The data shows that the spectral feature associated with the 2DEG increases with Ni-doping concentration.

In the last part, we present the measurements for STO:Ni_{0.12} films, in which an iso-energetic cut in the gap show a one dimensional distribution along one axis of the surface plane. We assume that these states are related to Ni impurity bands hybridized with the O 2*p* bands in the band gap of STO films.

The HR-ARPES measurements were performed at the CASSIOPEE beamline of SOLEIL synchrotron. To avoid oxidation and adsorption in air, the samples are transferred in-situ from the PLD chamber to the analysis chamber by means of an UHV suitcase. The resonant-ARPES measurements were performed at the ADRESS beamline of SLS by Dr. Vladimir Strocov and Dr. Juraj Krempasky. The author of this thesis processed and analysed the data.

6.1 Band Structure of the TM-doped SrTiO₃ Films

Substituting Ti by 3d-TM ions in STO leads to electron/hole doping and makes the system semi-conducting already for very low carrier concentrations as it was demonstrated by Koonce *et al.* for Nb-doped STO [201].

In the previous chapter, we reported the formation of in-gap states associated with the impurity ions for STO films doped with several 3d-TM ions, as well as a hybridization of the impurity energy levels with O 2p states. Indeed, the effect of electron correlation in these systems plays a key role in the modification of their electronic properties. This declaration can be verified by ARPES measurements on the correlated 3d-TM doped STO. The focus of the studies is placed on the impurity energy levels in the gap, but in addition the dispersion of the bulk bands in a wide binding energy range is also investigated and compared to the non-doped system.

The ARPES data presented here are measured at two different endstations:

1. Pristine and Ni-doped STO films were measured at the HR-ARPES endstation of the CASSIOPEE and ADRESS beamlines.
2. Fe and Cr-doped STO films were measured at the ARPES endstation of the PEARL beamline.

The experimental geometry is almost the same for the three endstations (see Fig. 6.1 (d)). The entrance slit of the hemispherical analyzer is aligned along the (100) direction of the films. The angular scanning direction (θ) is perpendicular to the alignment direction. The angular acceptance of the analyzer at CASSIOPEE (ADRESS, PEARL) is $\pm 15^\circ$ ($\pm 10^\circ$, $\pm 30^\circ$). The synchrotron beam enters at an angle of $\alpha=45^\circ$ at CASSIOPEE, 20° at ADRESS and 60° at PEARL with respect to the y -axis. Apart from changes in the relative intensities, these differences in the geometry do not affect the data.

Coming to the computational details, some theoretical specifications are given. A powerful aspect of the KKR-GF method is given by the ability to perform ARPES calculations based on the so-called one-step model of photoemission (see section 2.1) in which same experimental parameters such as measurement geometry, photon energy, binding energy and k -vector resolutions can be taken into account. However, we were not able to generate a converged surface potential within a tight-binding model, as we are dealing with thin films close to a 2-dimensional system; thus, the same bulk potential as the one used for the ground states calculations in section 5.3 is used here for each system.

This part of the chapter is structured as follows: first, a photon energy scan for the Ni-doped STO film is presented and compared to the corresponding calculations for pristine and doped STO; second, the experimental as well as the theoretical ARPES data from all samples are introduced.

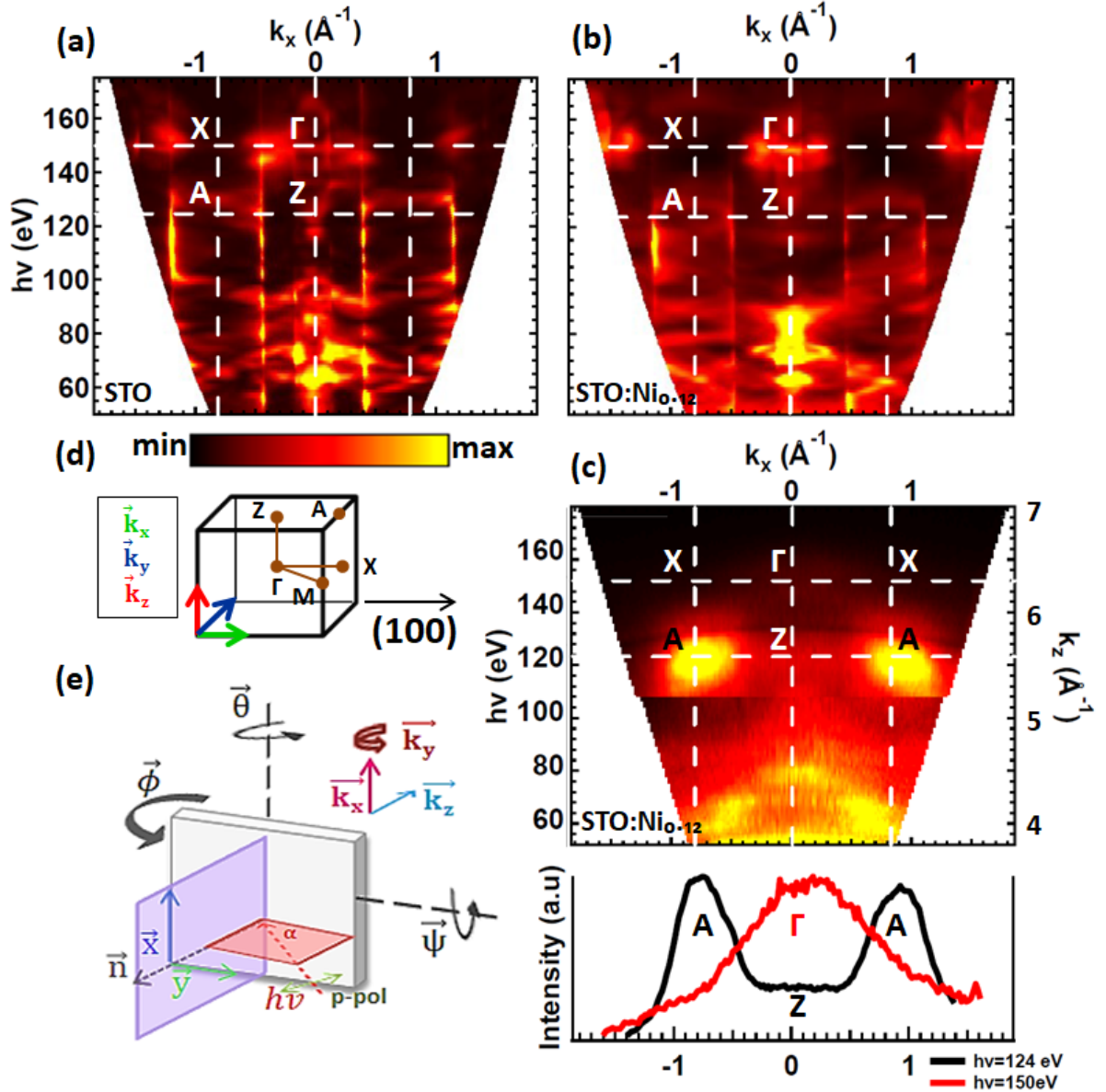


Figure 6.1: Dispersion along the k_z at BE=4 eV below Fermi energy from $h\nu=50$ eV to $h\nu=175$ eV showing the high symmetry points. The computational data from the one-step model of photoemission for bulk STO and STO:Ni_{0.12} are displayed in (a) and (b), respectively. (c) The experimental data for STO:Ni_{0.12} films. (d) Notation of the high symmetry points within the first BZ of STO. (e) Measurement geometry.

6.1.1 Photon energy scan

The ARPES calculation for bulk STO(001) and STO:Ni_{0.12}(001) and experimental data for STO:Ni_{0.12}(001) films are displayed in Fig. 6.1. The dispersion along the k_z is obtained by scanning the photon energy. The conversion from $h\nu$ to k_z is carried out within the free electron final state approximation discussed in section 2.1 and an inner potential of 14.65 eV was retrieved from the periodicity observed in the measurements. The high symmetry points at $k_x=0$ \AA^{-1} ($k_x=0.8$ \AA^{-1}) are named Γ and Z (X and A) as labelled in Fig. 6.1 (d).

The data in Fig. 6.1 are presented for a binding energy of 4 eV below the Fermi level. Let us first compare the characteristics of the theoretical data for bulk STO(001) and STO:Ni_{0.12}(001):

At first sight, the main features that correspond to the high symmetry points are the same for both cases. Yet, if we look closely at the Γ and X-points ($h\nu=150$ eV), a clear change in the spot shape is observed. Similar changes are also detected around the other symmetry points. This dissimilarities result from a slight upward binding energy shift of the bands for STO:Ni_{0.12} in comparison with STO. This shift will be discussed more in details in the next paragraph. Another remarkable difference is the intensity embodied in the background all over the k_x and k_z ranges in case of STO:Ni_{0.12}. This intensity is purely related to the localised Ni impurity bands formed at this binding energy level and more importantly, it confirms that these states are located not only around a specific symmetry point or one direction, but they are homogeneously localised in the whole volume of the Brillouin zone for a given binding energy. The experimental data displayed in Fig. 6.1 (c) for STO:Ni_{0.12}(001) films are in a good agreement with the theoretical results except for the intensity of the symmetry points at higher photon energy. The experiments show a weak intensity around the Γ -point in comparison with the A-point. The reason for this is the flux of the photon beam that reduces with the increase of $h\nu$. However, the line profile plotted for $h\nu=150$ eV confirms the position of the Γ and X-points. The Z-point is detected at $h\nu=124$ eV. These values correspond to the third Brillouin zone along the k_z -axis.

6.1.2 Measurements along ZA

Experimental band dispersion and corresponding ARPES calculations (one-step model) for the STO, STO:Ni_{0.12}, STO:Fe_{0.05} and STO:Cr_{0.05} along the ZA direction are displayed in Fig. 6.2. All data are recorded with a linearly polarized light of 200 eV at RT for a wide binding energy range (10 eV below the Fermi level).

Let us first discuss the data of the reference sample: STO(001) (see Fig. 6.2 (a)). The most significant feature is a nice dispersion of the bulk O 2*p* bands partially hybridized with Ti 3*d* bands between 4.5 eV and 10 eV below the Fermi energy, which is also shown by the angle-integrated VB profile. The shake-up peak at around 3.8 eV is a polaron mostly related to Ti/Sr vacancies as it was reported by Janotti *et al.* [202], and it is reflected by the relatively weak local intensity observed at this binding energy level in the E- k_x plot.

For the sake of clarity, only data of STO:Ni_{0.12}(001) films are presented (in Fig. 6.2 (b)). Note that no major differences between STO:Ni_{0.12}(001) and STO:Ni_{0.06}(001) are detected but only some minor intensity variations in particular when it concerns the impurity states. ARPES data on STO films doped with Ni show a different behaviour; The main bulk band between 7 eV and 9 eV, is shifted to lower binding energy level by 1 eV in comparison to pure STO films. The upper bands between 4 eV and 6 eV, are shifted by ~ 1.3 eV to lower binding energy, but also hybridized with the localized Ni 3*d*-bands formed at the top of the valence band. The angle integrated VB assigns as well the formation of an in-gap state between 2 eV and 4 eV (tagged by the blue arrow).

Note that the data of STO:Fe/Cr films were obtained with a different synchrotron light source resulting in different intensities and resolutions. Doping STO films with Fe also leads to a band shift of ~ 1 eV toward the Fermi level (see Fig. 6.2 (c)). The Fe 3*d*-bands are detected at 2 eV and strongly hybridized with O2*p* and Ti 3*d* bands. The band dispersion plot of Cr-doped STO

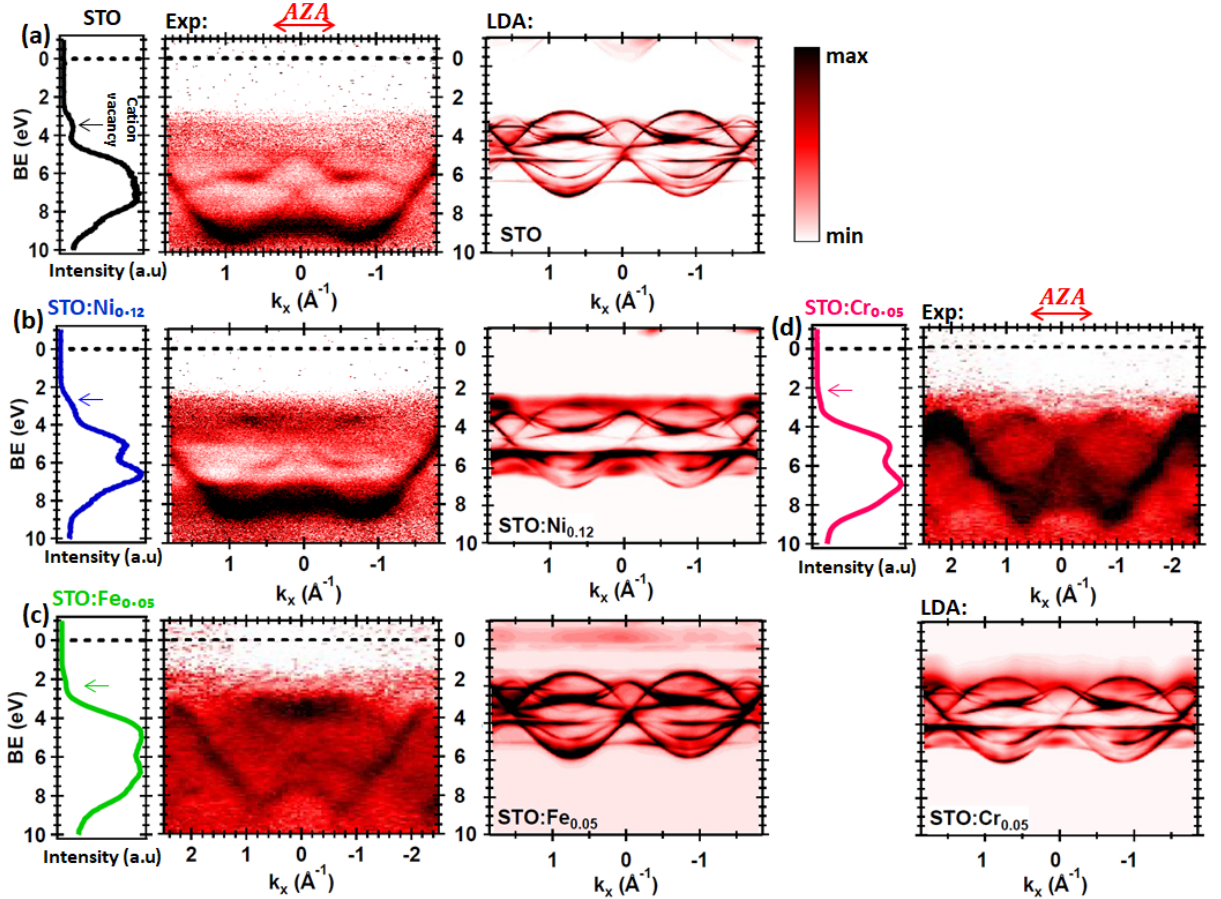


Figure 6.2: experimental band dispersion along the k_x direction for $k_y=0 \text{ \AA}^{-1}$, and corresponding ARPES calculations based on one-step model of photoemission, respectively, for (a) STO(001), (b) STO:Ni_{0.12}(001), (c) STO:Fe_{0.05}(001) and (d) STO:Cr_{0.05}(001) thin films. Data shows the bulk bands dispersion and the localized impurity bands at the top of the valence band for the 3d-TM doped STO films. Angle-integrated valence band for each system is also plotted showing the in-gap states resulting from the formation of 3d impurity bands (coloured arrows). All data are acquired with linearly polarized light of 200 eV. The measurements were performed at room temperature. Fermi level is set to zero.

films in Fig. 6.2 (d) shows the same characteristics for the bulk bands which are shifted by ~ 0.8 eV toward the Fermi level and the localized Cr 3d-bands are observed in the gap at around 2.5 eV.

Before going into the details of the ARPES calculations based on the one-step model of photoemission, let us note that we only used the LDA approximation for the exchange-correlation potential (see section 3.1.2). Such a description underestimates the short range electron correlation effects which are very important in these systems. However, it provides the basic shape of the band structure and in the case of doped STO even gives a quantitative description of the impurity bands. The impact of correlation effects on the electronic structure of the present systems will become clearer in the following.

The STO band structure consists mainly of O 2p bands partially hybridized with Ti 3d bands dispersed between 2.5 eV and 7 eV below the Fermi level (right panel in Fig. 6.2 (a)). The dispersion of the bands with respect to k -vector is in a good agreement with the experimental data. Yet the measurements show a shift of the bands compared to LDA calculations (i.e. a shift of the Fermi level). This disagreement reflects the limitations of DFT with LDA especially when

it deals with strongly correlated systems. One approach used to improve the energy band gap in STO is the DFT+Hubbard U method where U counts for the calculation of the electronic couplings [203].

Despite the position of the Fermi level, the calculated band dispersion of STO:Ni_{0.12} is closely similar to the measured one, notably the localized Ni 3*d* energy levels formed at the top of the valence band (right hand plot in Fig. 6.2 (b)). Same description is also valid in the case of STO doped with Fe and Cr (LDA calculations in Fig. 6.2 (c,d)). Another discordance is observed between the theoretical and experimental results: the measured bands show a broadening of the VB with respect to binding energy compared to the theory. This is also due to the strong electron-electron correlations occurring in these materials that lead to different matrix elements for the initial and final states which are not taken into account in our calculations.

In summary, the band dispersions for undoped and 3*d*-TM doped STO are in qualitative agreement with the one-step model calculations. The impurity bands are localized mainly at the top of the valence band forming an in-gap state at around 2-2.5 eV below the Fermi energy and most importantly hybridizing with the bulk bands of STO.

6.2 2D Metallic States

In the preceding paragraph, we have presented an ARPES study of STO(001) and TM-doped STO(001) films in a wide binding energy scale and revealed the formation of localised 3*d* impurity energy levels in the band gap. Now we investigate how conductivity can be induced at the surface of Ni-doped films by creating the two dimensional electron gas; In principle, just like it is possible to get a 2DEG at the surface of STO, it might be possible to reproduce a similar phenomenon with STO surface doped with TM-ions.

6.2.1 SrTiO₃(100) thin films

The 2DEG at the surface of pure STO films is not the aim of our studies. However, as STO is our reference sample, we performed only basic measurements which are already published previously in literature.

In order to create in-situ oxygen vacancies, a reduced STO surface is required. For this, we prepared the sample in a relatively low oxygen atmosphere of 1.10^{-7} mbar at high temperature (650-700°C). Our measurements presented in this section were all performed at T=90°C.

The XPS measurements for the reduced STO surface are presented in Fig. 6.3 (a) in black. The Ti 3*p* core level shows one peak at 38 eV that corresponds to Ti with an oxidation state of 4+ and no signature for Ti³⁺ formation. Surprisingly, the intense peak positioned at 6 eV lower binding energy from the Ti⁴⁺ is mainly related to a Ti¹⁺ state. It is not common to see the formation of Ti¹⁺ at the surface of STO; As it was demonstrated by Scheiderer [204] for LTO grown on STO substrate, the titanium valence is tentatively connected to the oxygen content in which it scales with the oxygen pressure. Here, the sample was annealed in a low oxygen atmosphere at high temperature in comparison to the optimal growth conditions used during the growth. Such environment results in an insufficient oxygen out-diffusion from the surface, and then the

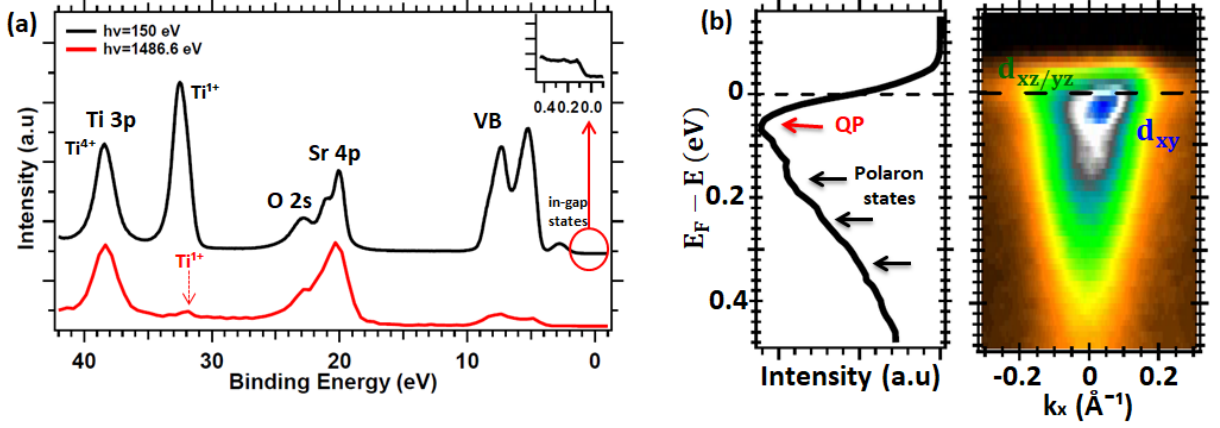


Figure 6.3: (a) XPS spectra for core levels, valence band and in-gap states of the sample measured after the growth (red line) with $h\nu=1486.6$ eV, and after annealing at $T=700^\circ\text{C}$ in partial oxygen pressure (black line) with $h\nu=150$ eV. (b) EDC close to Fermi energy of the reduced sample registered few minutes after exposure to the synchrotron beam showing the primary quasiparticle states (QP) and polaron replicas, with corresponding ARPES plot around the Γ point demonstrating the dispersion of the 2DEG. The spectra were registered with circularly polarized light of 150 eV at $T=90$ K. The Fermi level is set to zero.

present oxygen ions contribute to reach the optimal oxidation conditions for Ti ions in STO. This experimental condition favours the formation of Ti^{1+} ions rather than Ti^{3+} ions. On the other hand, the XPS spectra of the same sample measured directly after the growth with $h\nu=1486.6$ eV (red line in Fig. 6.3 (a)), where the resulting data are mostly bulk related, show a weak Ti^{1+} peak. Therefore, in comparison to the measurements at low photon energy ($h\nu=150$ eV, surface sensitive) we assume that Ti^{1+} ions are likely formed at the first top layers of the films, which explains the high intensity of the Ti^{1+} peak. This finding has been reported in literature and the present measurements are not enough to prove if it affects or not the properties of the 2DEG states. In the band gap, the formation of in-gap state at 2.8 eV is visible, originating from cation vacancies (here Ti), and can be mainly related to the Ti^{1+} peak observed [202]. However, the in-gap state at 1.2 eV related to oxygen vacancies responsible for the formation of a polaron in this range of energy (reported in [202, 205, 206]) is not detected in our measurements.

The intensity in the vicinity of the Fermi level strongly arises indicating the formation of the 2DEG (see Fig. 6.3 (b)). The first main peak in the EDC (energy distribution curve) cut, at Fermi energy demonstrates the dispersion of the primary quasiparticle (QP) bands followed by polaron replicas at higher binding energies which are separated by approximately 100 meV. The corresponding ARPES data shown in Fig. 6.3 (b) are registered with circularly polarized light of 150 eV in a small binding energy range close to Fermi level around the Γ point. The plot shows the dispersion of the d_{xy} bands and the shallower heavy band originated from the $d_{xz/yz}$ orbitals [15, 16]. The QP band followed by two polaron replicas were also resolved, each separated by approximately 100 meV accompanied progressively by a loss of intensity [207]. Back to the features we observed in the band gap and core levels, the oxygen vacancies and Ti^{3+} did not contribute here to the formation of the metallic state. This opens again the question about the origin of the 2DEG formed at the surface of STO.

As mentioned at the beginning of this paragraph, the 2DEG on STO was not our goal in this work, and therefore we did not perform more measurements on it. Its presence testifies however

the high quality of our samples.

6.2.2 SrTiO₃:Ni(100) thin films

In the present investigation, we have explored the formation of the 2DEG at the Ni-doped STO films by means of Ti-resonant ARPES. That means the measurements are performed at photon energies around the Ti L-edge absorption peaks, in order to enhance the emission from the states represented by the 2DEG, which have a high degree of Ti 3d character. In addition, a comparative study of the 2DEG properties as a function of Ni dopant concentration is also discussed.

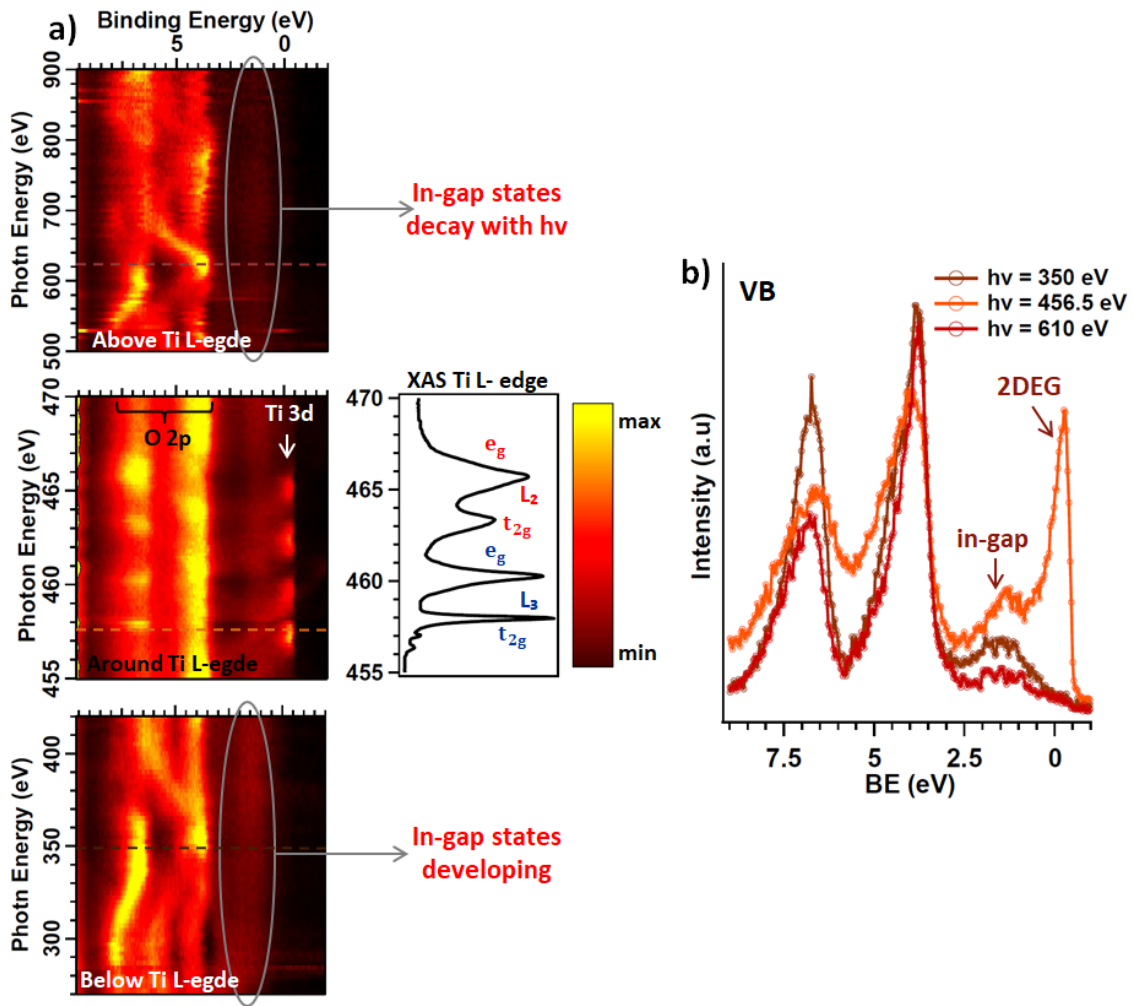


Figure 6.4: (a) Photon energy scan for $k_x = \pm 0.2 \text{ \AA}^{-1}$ (Γ point) of STO:Ni_{0.06} films. Three photon energy ranges are considered: Below Ti L-edge ($h\nu = 270\text{--}420$ eV), around Ti L-edge ($h\nu = 455\text{--}470$ eV), and above Ti L-edge ($h\nu = 500\text{--}900$ eV). The corresponding Ti L_{2,3} XAS spectra are displayed. (b) Angle-integrated valence bands for three different photon energies below, around and above the Ti L-edge, showing the in-gap states and the 2DEG development. Measurements are registered with circularly polarized light at 15 K.

Photon energy dependency

To catch the resonance of the Ti 3d related parts at the Γ -point, spectra of the VB are taken at various photon energies across the Ti L_{2,3}-absorption edge in steps of 0.2 eV for $k_x = \pm 0.2 \text{ \AA}^{-1}$. The VB spectra are also registered at photon energies below and above the Ti L-edge which

allows to probe less and more deeply into the samples, respectively (k_z dependency). The data for STO:Ni_{0.06} films are depicted in Fig. 6.4.

Let us first mention that, the inelastic mean free paths of the valence photoelectrons in STO, which represent approximately the mean depths of emission from the sample, are estimated to be 8 Å for $h\nu=270$ eV, 10 Å for $h\nu=465$ eV and 16 Å for $h\nu=900$ eV.

In Fig. 6.4 (a) the x-ray absorption spectrum of the Ti L-edge is presented, and the main features are labelled. It shows the spin-orbit splitting of the L-edge in L_2 and L_3 , as well as the crystal field splitting into t_{2g} and e_g orbitals. At photon energies below the Ti L-edge ($h\nu=270-420$ eV), the in-gap states around $E_B=1.2$ eV (oxygen vacancy state) are developing and no enhancement of the Ni-impurity states is observed (see the valence band at $h\nu=350$ eV in Fig. 6.4 (b)). At photon energies around the Ti absorption edge ($h\nu=455-470$ eV), the intensity of the VB features of O $2p$ and Ti $3d$ character are strongly enhanced (see the valence band at $h\nu=456.5$ eV in Fig. 6.4 (b)). Above the Ti L-edge ($h\nu=500-900$ eV), the in-gap states drastically decay with $h\nu$ (see the valence band at $h\nu=610$ eV in Fig. 6.4 (b)).

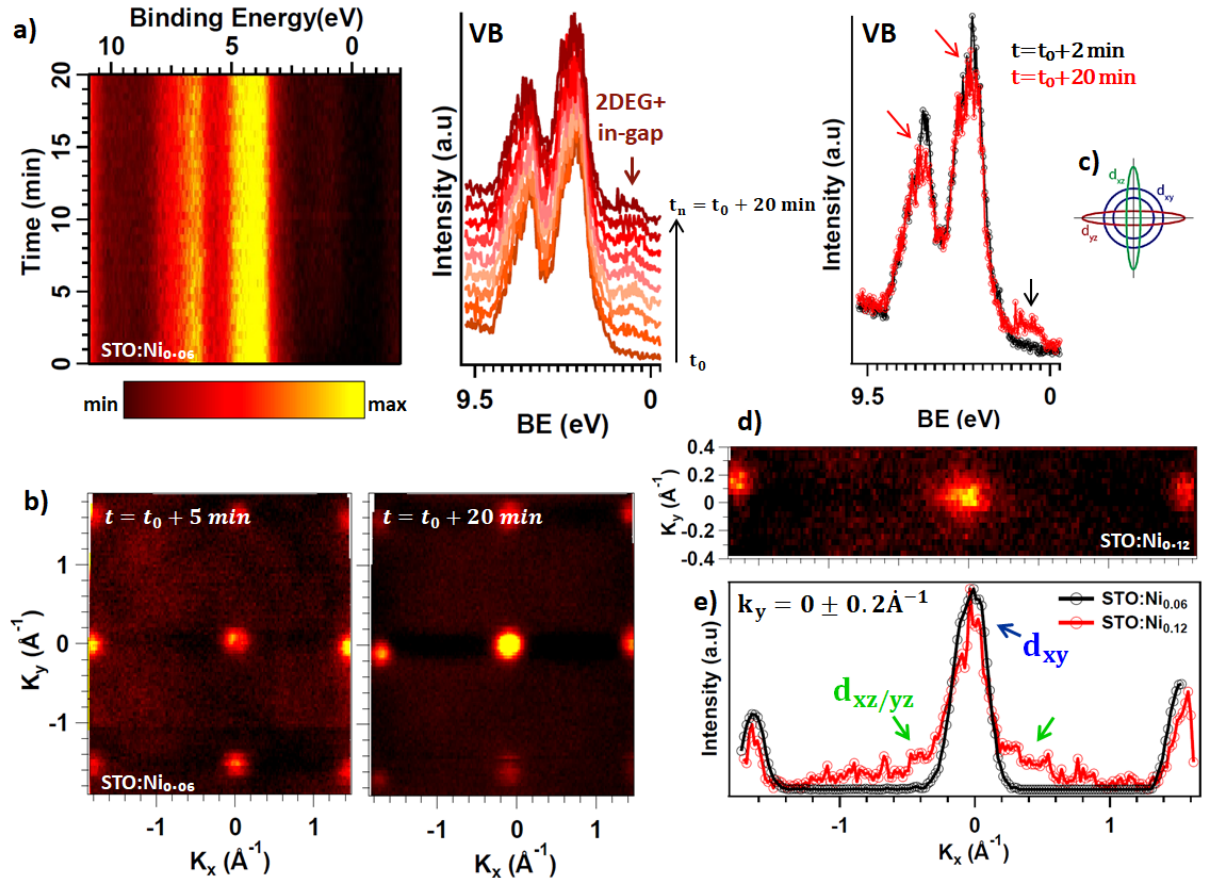


Figure 6.5: (a) Angle-integrated cut through Γ -point at $h\nu=460.5$ eV of STO:Ni_{0.06} films: in-gap states and 2DEG at Fermi level developing under irradiation over 20 min. (b) Fermi surface ($E_B=0.1$ eV) registered at $t=t_0+5$ min and $t=t_0+20$ min of irradiation showing an enhancement of the 2DEG signal. (c) Two-dimensional visualization of the Fermi surface at Γ -point together with the notation of the different Ti $3d$ t_{2g} suborbitals. (d) Fermi surface ($E_B=0.1$ eV) around Γ -point of STO:Ni_{0.12} films registered at $h\nu=460.5$ eV at $t=t_0+5$ min under irradiation. (e) Profile cut from Fermi surface map of STO:Ni_{0.06} and STO:Ni_{0.12} films, for $k_y=0 \pm 0.2 \text{ \AA}^{-1}$. The data show the presence of Ti $3d$ $d_{xz/yz}$ bands in case of STO:Ni_{0.12} films in addition to the d_{xy} band compared to STO:Ni_{0.06}. Measurements are registered with circularly polarized light at 15 K.

According to these data, the 2DEG is clearly observed only inside the Ti $2p \rightarrow 3d$ resonance, and a strong contribution of the O $2p$ states is revealed, unlike the Ni $3d$ -impurity states. In fact, the minimal photon energy used for these measurements is 270 eV and corresponds to 8 Å the mean depth of emission from the sample, which is equivalent to ~ 2 u.c in thickness. So, the absence of the 2DEG off the resonance and the decay of the in-gap states with the photon energy assign their surface localization within 1 u.c or 1.5 u.c in thickness, or more precisely in the top most film containing 2 or 3 layers of TiO_2 composition.

Time dependency

The time dependent behaviour of $\text{STO:Ni}_{0.06}$ films under UV-irradiation is presented in Fig. 6.5 (a), where angle-integrated cut through the Γ -point at 460.5 eV is recorded. The spectral intensity of the VB shows that the in-gap states and Fermi states are increasing with irradiation with time over 20 min. Moreover, the enhancement of the in-gap states is followed by a reduced intensity of the O $2p$ bands as it is showed in the valence bands at $t=t_0+2$ min and $t=t_0+20$ min under irradiation. And the Ni-impurity states localised at $E_B=2.5$ eV do not show any evolution in this time frame. Therefore, the intensity of the in-gap states seems to be directly related to the O $2p$ bands but not the Ni $3d$ states. The corresponding Fermi surface maps ($E_B=0.1$ eV) at $t=t_0+5$ min and t_0+20 min under irradiation show also an enhancement in the structure and intensity of the metallic states at Fermi level with time (see Fig. 6.5 (b)). The metallic surface states seem to have a d_{xy} character with no signature of the $d_{xz/yz}$ bands. We remind that the measurements here are performed at $T=15$ K. At this temperature, STO incurs a phase transition to a orthorhombic unit cell [55], so the lattice is arranged by altering the Ti-O-Ti bond angles between two neighbouring octahedrons. Consequently, the ordering of the Ti $3d$ t_{2g} suborbitals is affected, in which the d_{xy} and the $d_{xz/yz}$ are energetically splitted (see section 1.1.2).

The same investigation was performed for $\text{STO:Ni}_{0.12}$ films and showed similar time dependent behaviour. However, the Fermi surface map registered at $t=t_0+5$ min under irradiation with the same photon energy ($h\nu=460.5$ eV) shows different dispersion as for $\text{STO:Ni}_{0.06}$ films, in which the $d_{xz/yz}$ -cross is present in addition to the d_{xy} -circle (see Fig. 6.5 (c-e)). This observation leads to several questions:

1. How the Fermi states are developing under light within longer time frame, until saturation is reached. In particular, define if the suborbitals appear simultaneously or first the d_{xy} fills and then the $d_{xz/yz}$ for the different Ni-doping concentration.
2. If we assume that the population of the suborbitals differs from $\text{STO:Ni}_{0.06}$ and $\text{STO:Ni}_{0.12}$ due to the distortion of the TiO_6 octahedrons, the main question will be if this distortion is occurred because of the doping and if Ni $3d$ states are contributing indirectly to develop the metallic Fermi surface states.

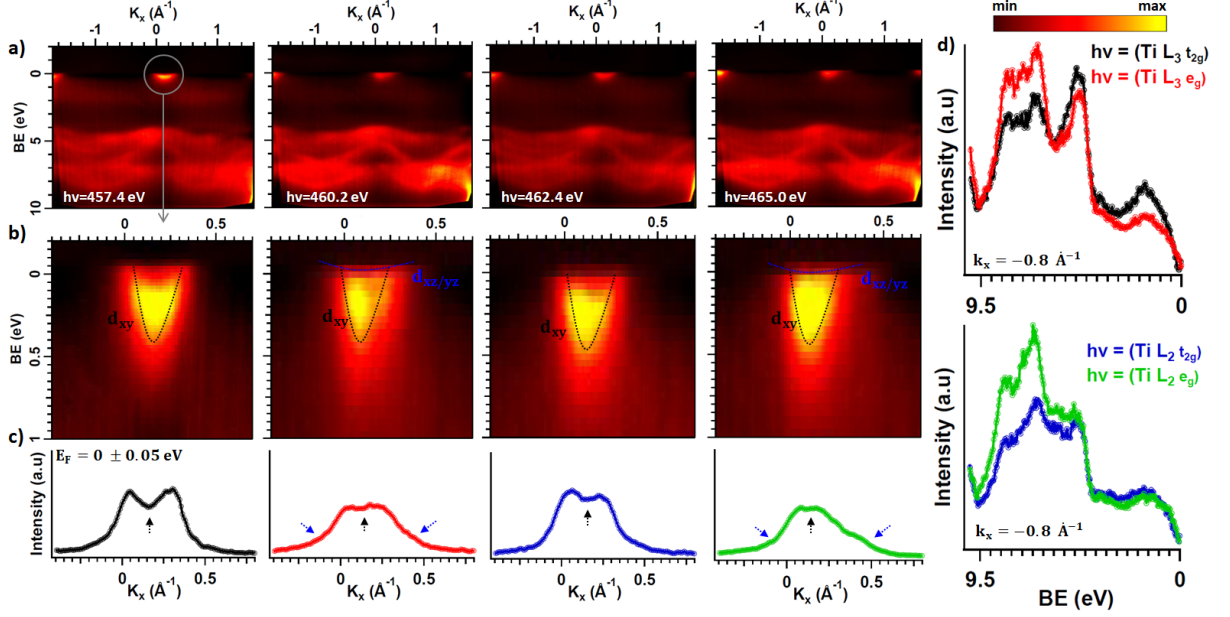


Figure 6.6: STO:Ni_{0.06} films: (a) Resonant-ARPES registered with four photon energies that correspond respectively to the absorption edge of Ti L₃(*t*_{2g}), L₃(*e*_g), L₂(*t*_{2g}) and L₂(*e*_g). Data are registered with circularly polarized light in the ΓX direction at 15 K. Fermi level is set at $E_B=0$ eV. (b) Zoom-in around Fermi level. (c) MDC at $E_F=0\pm 0.05$ eV. The black arrows and blue arrows are assigned to the *d*_{xy} bands and the *d*_{xz/yz} bands, respectively. (d) Evolution of the valence band states (O 2*p* bands) and the in-gap states at the different resonance edges as it is presented in the figure.

Ni concentration dependency

The Ti-resonant ARPES measurements in the ΓX -direction (normal emission) for STO films with the two different Ni content 6% and 12% are displayed in Fig. 6.6 and 6.7, respectively. Note that the intensity scale of the colour map used to plot the data is the same for both figures. All the measurements are performed using a circularly polarized light at $T=15$ K. Let us first describe the main features observed in the figures, and then discuss the resemblances and dissimilarities.

In Fig. 6.6 (a) and 6.7 (a) the bands are measured in a wide binding energy scale using four photon energies that correspond to the Ti L absorption edge (see Fig. 6.4). For both samples, the plots show a dispersion of the bulk bands located at binding energies between 4 eV and 9 eV (mainly O 2*p* bands), with the VBM centred at $k_x=0$ \AA^{-1} , and the 2DEG at Fermi Level formed at the Γ -point. However, in case of STO:Ni_{0.06}, the Γ -point (k_F , where F is for Fermi level) is shifted by 0.12 \AA^{-1} from the VBM and in the case of STO:Ni_{0.12} k_F is at 0.02 ± 0.02 \AA^{-1} . If we compare the resonant behaviour of the in-gap states (at $E_B=1.2$ eV) and the O 2*p* bands (at E_B around 7 eV) at the Ti L-edges (see also the valence bands in Fig. 6.6 (d) and 6.7 (d)), we find that in case of STO:Ni_{0.06}, the in-gap states are more pronounced at the L-*t*_{2g} edge, and the O 2*p* bands are more intense at the L *e*_g-edge. For STO:Ni_{0.12}, the in-gap states are more pronounced at the L_{2,3} *t*_{2g}-edges, and the O 2*p* bands are more intense at the L *e*_g-edges. Although, the average intensity of the STO:Ni_{0.12} bands is higher with more contrast compared to STO:Ni_{0.06} despite the photon energy.

Coming now to the 2DEG at Fermi surface, the data in Fig. 6.6 (b-c) and 6.7 (b-c)) show that its structure and properties are photon energy dependent: As the photon light used is circularly polarized, all orbitals are probed. Therefore the bands that might be visible in the vicinity of

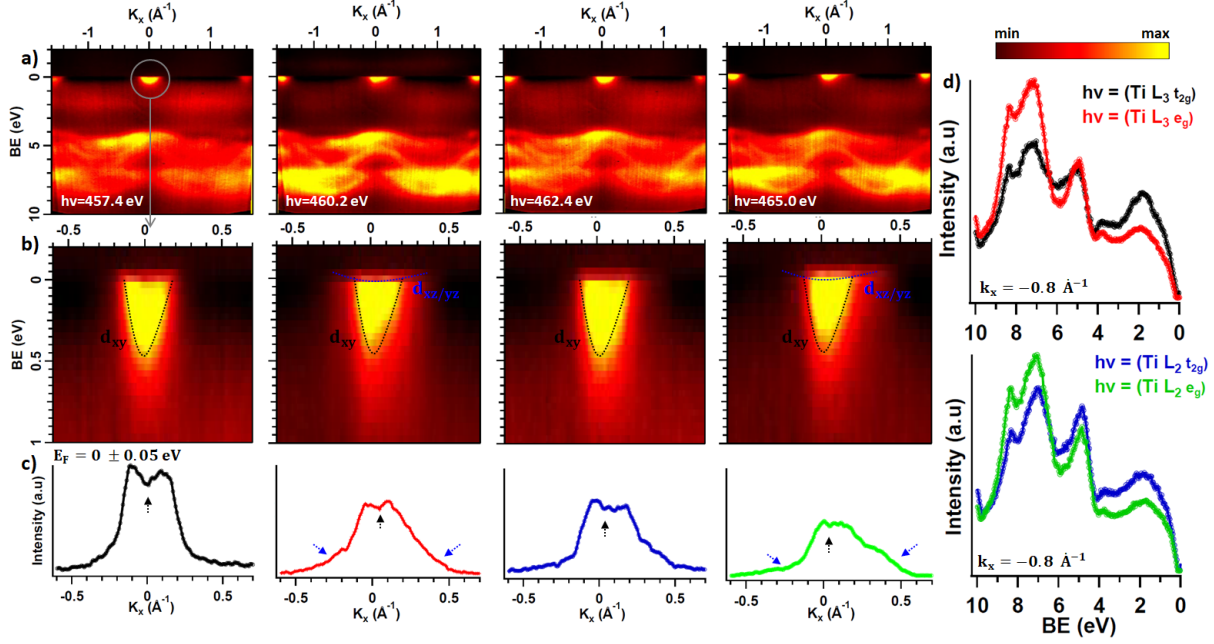


Figure 6.7: STO:Ni_{0.12} films: (a) Resonant-ARPES registered with four photon energies that correspond respectively to the absorption edge of Ti L₃(t_{2g}), L₃(e_g), L₂(t_{2g}) and L₂(e_g). Data are registered with circularly polarized light in the ΓX direction at 15 K. Fermi level is set at E_F=0 eV. (b) Zoom-in around Fermi level. (c) MDC at E_F=0±0.05 eV. The black arrows and blue arrows are assigned to the d_{xy} bands and the d_{xz/yz} bands, respectively. (d) Evolution of the valence band states (O 2p bands) and the in-gap states at the different resonance edges as it is presented in the figure.

the Γ-point are the 2D d_{xy} and the 3D d_{xz/yz}. The d_{xy} are clearly visible at all Ti threshold, and the energetic width of the d_{xy} bands are approximately 300 meV for STO:Ni_{0.06} and 400 meV for STO:Ni_{0.12}. In addition to the d_{xy} bands, at photon energies in the vicinity of Ti L_{2,3} e_g, the flat d_{xz/yz} bands are visible, with a bandwidth of few meV located at Fermi level (tagged by the blue arrows in the MDC (momentum distribution curve) plots in Fig. 6.6 (c) and 6.7 (c)). Interestingly, despite the Ni content in the films, the structure of the bands at k_F is showing a less polaronic weight (almost not visible) compared to STO (see Fig. 6.3).

Coming to the discussion; Previously, Plumb *et al.* reported on the band structure of nominally flat STO measured with circularly polarized light and found that the 2DEG band width is about 230 meV and located at k_F=0.18 Å⁻¹ [64]. Also, in [126], temperature dependent band structure measurements on STO films with 10° miscut to (001) at Γ-point showed the variation of k_F of the outer d_{xy} state for different temperatures, in which a shift of 0.12 Å⁻¹ was observed at T=20 K. They related these findings to the TiO₆ distortion occurred during the phase transition at such low temperature and the lattice arrangement at the surface. Our data showed that the Γ-point is located at k_F=0.12 Å⁻¹ for STO:Ni_{0.06} films and returns back to k_F=0.02 Å⁻¹ for STO:Ni_{0.12}. A possible explanation of the observation, is an interplay between Ni impurities, distortion of the TiO₆ octahedron and their Ti-O-Ti bond angles: The distortion of the TiO₆ octahedron at low temperature is responsible for the k_F shift in pure STO. The reduction of the k_F shift in Ni-doped STO is found to be proportional to the increase of Ni content. Assuming that Ni substitutes Ti, Ni²⁺ (6-coordinate, octahedral: r=83 pm [208]) has larger ionic radius compared to Ti⁴⁺ (6-coordinate, octahedral: r=74.5 pm [208]), implying a new lattice strength that can change the distortion of the octahedron differently. The bond angle between neighbouring octahedron is

modified, and affect the symmetry of the structure.

Distortion of the octahedron does not affect only the symmetry of the structure but also the band dispersion, in which the splitting between the d_{xy} and $d_{xz/yz}$ can differ accordingly [34]. Here, the d_{xy} bands are visible at all Ti L-edges. Moreover, the intensity of in-gap states, which are correlated with the Ti 3d states, show an impotent enhancement at the t_{2g} -edge compared to e_g -edge where the resonance has mostly an O 2p character. This means that d_{xy} bands are at the lowest energy in the CB, and therefore they have the highest probability to be filled. Additional to the light band with xy -symmetry, we observe the bottom of the flat heavy band $d_{xz/yz}$ with $h\nu=e_g$ -edge. The absence of the $d_{xz/yz}$ bands can be explained by their higher binding energy level, not enough to be reached at $h\nu=t_{2g}$ -edge.

It was reported that the bottom of the d_{xy} bands of nominally flat STO measured with circularly polarized light is in the range of 230 meV and can decrease in case of STO surface with terrace [64, 126]. Here, the size of the parabola increased to 300 meV and approximately to 400 meV when doping STO with 6% and 12% of Ni respectively. All the previous data did not show any direct contribution of the localised Ni impurity bands in the formation of the 2DEG nor signature for Ti 3d-Ni 3d correlations. Yet, Ni-ions might indirectly be contributing by enhancing the number of oxygen vacancies and the free electron density. In fact, Ni atoms substitute the Ti atoms with valence of 2+ instead of 4+, in other words, every Ni replacing one Ti leads to create two oxygen vacancies and therefore 2 trapped electrons.

As we mention in the description of the data, the polaron replicas are not visible, although the Luttinger volume (QP and polaron replicas) of the light d_{xy} subband is slightly larger compared to STO. In fact, when the carrier density is approaching a high order ($n_e=9.10^{13} \text{ cm}^{-2}$), the effective electron-phonon coupling strength decreases from $\alpha=2.8$ to $\alpha=1.3$ as it was reported by Wang *et al.* [60] in their study on the evolution of the 2DEG spectral function with carrier concentration in STO. As a result, the polaron replicas become hard to be experimentally resolved, which might explain our current findings.

6.3 New Metallic State on SrTiO₃:Ni_{0.12} Films

Here in this section, we will examine various isoenergetic (k_x - k_y) maps from different binding energy level and close to Fermi energy. The measurements were performed at RT with two photon energies $h\nu=124 \text{ eV}$ and 150 eV and for k_x (k_y) along the [100] ([010]) direction centred at $k_x=k_y=0 \text{ \AA}^{-1}$. For clarity reason, we will only show results with $h\nu=124 \text{ eV}$ that corresponds to the $\overline{Z\bar{A}}$ direction (see Fig. 6.8 (a)).

The data of STO and STO:Ni_{0.12} films are depicted in Fig. 6.8 (b). Deep in the valence band, at high binding energy levels the isoenergetic maps (first column) show a high cubic symmetry for the undoped and Ni-doped STO films with mentioning that same features were not found exactly at the same binding energies; The states are shifted to lower binding energy level by $\sim 300 \text{ meV}$ for the doped films. At the top of the valence band which corresponds to $E_B=4.5 \text{ eV}$ for STO and 4.2 eV for STO:Ni_{0.12} films, the intensity maps also show a cubic symmetry, but the

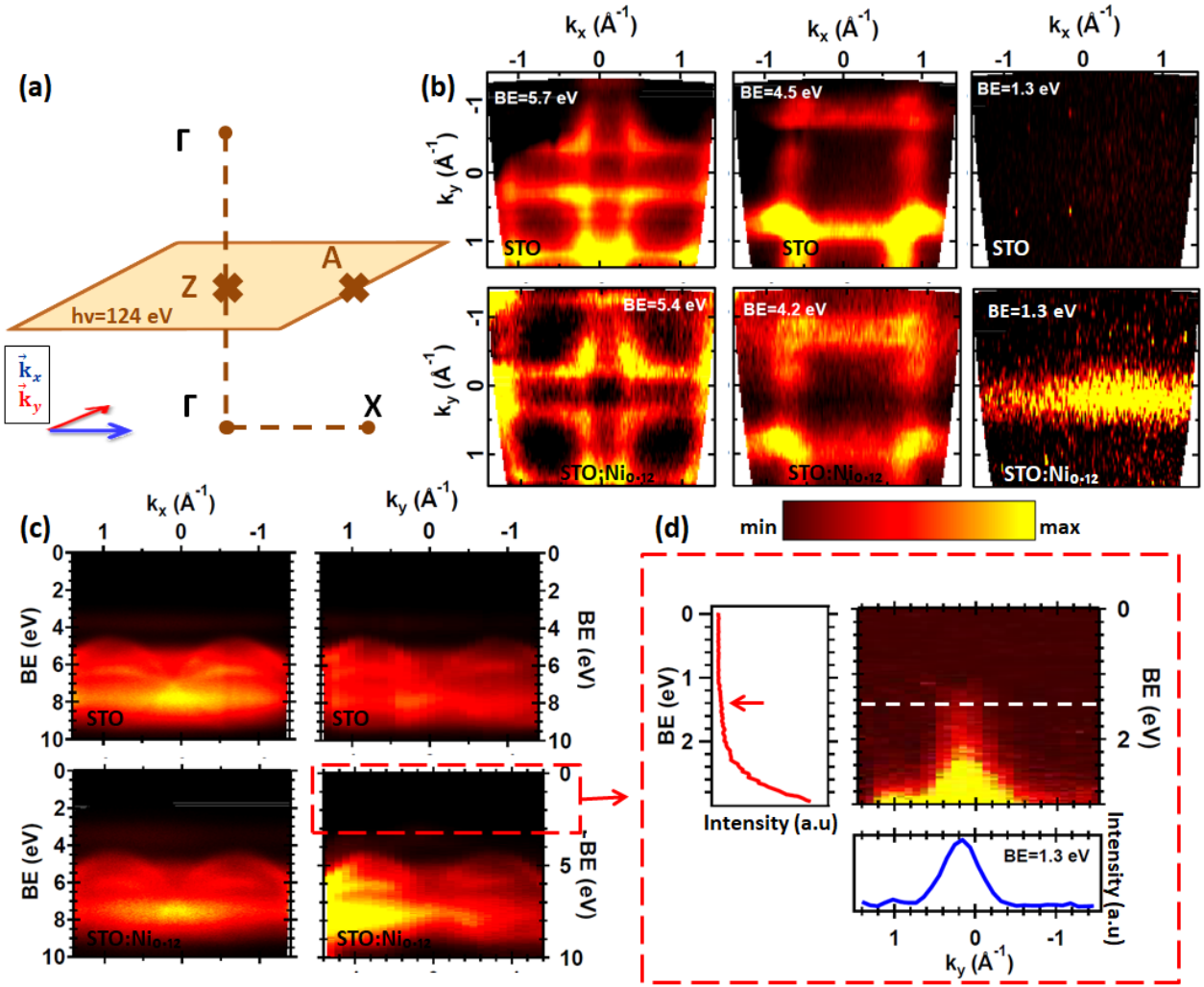


Figure 6.8: (a) Location of the high symmetry points with respect to the probed plane. (b) Intensity plots of the measured STO and STO:Ni_{0.12} k_x - k_y surfaces at different binding energy levels. (c) corresponding band dispersions in the k_x and k_y directions. (d) ARPES for STO:Ni_{0.12} films in the k_y direction close to Fermi energy with the corresponding EDC and MDC cuts as it is displayed. Data are registered with linearly polarized light of $h\nu=124$ eV at RT.

states around $(k_x=\pm 0.8 \text{ \AA}^{-1}, k_y=0 \text{ \AA}^{-1})$ for the Ni-doped films are not present. Closer to Fermi level (at $E_B=1.3$ eV), the undoped films are showing no trace for an in-gap state, as expected. For Ni-doped films, an unexpected signal is observed around $k_y=0 \text{ \AA}^{-1}$ all along k_x direction. For a better description of the data, we plot the corresponding band dispersion in the k_x and k_y direction over a wide binding energy scale, and the results are displayed in Fig 6.8 (c). In the following we are interested in the detected features within the band gap; In the k_x direction, as it was discussed previously in section 6.1.2 for STO:Ni_{0.12} films, the localised Ni $3d$ - bands are formed in the gap at around 2.5 eV without dispersing along k -vector. In the k_y direction, the impurity states seem to be dispersing around the Z-point ($k_y=0 \text{ \AA}^{-1}$). A close up of the region between 0 eV and 3 eV with the corresponding EDC and MDC at BE=1.3 eV are presented in Fig. 6.8(d). The data show clearly the intensity arising in the band gap up to 1.3 eV and confined in the centre at $k_y=0 \text{ \AA}^{-1}$. The actual measurements are not enough to have a certain interpretation for these observations. Yet, one can retrieve possible hypothesis; One plausible explanation for this behaviour is the braking of homogeneity of Ni-impurities in the films due to the exposure to the synchrotron radiation, meaning that despite the origin of these states, they

were formed during the photoelectron measurements and not the growth. In this case, multiple domains for the oxygen octahedral (centred by Ni ion) might find their stability in different preferred orientations of the axis of the Brillouin zone. However, other structural defects such as oxygen vacancies in the films could offer another alternative explanation for the present 1D dispersed in-gap state.

6.4 Conclusion

We have presented the band dispersion of STO and 3d-TM (TM=Ni, Fe and Cr) doped STO thin films in a wide binding energy range. For the doped films, the bands are shifted toward Fermi Level and localized impurity 3d-bands are observed at around 2.5 eV in the gap of STO. The one-step model computational data with LDA are in a good agreement with the experimental results when it comes to the dispersion of the bands despite the position of Fermi level and the bands width. In order to correct the position of E_F , one can use LDA+U approximation. LDA+DMFT calculations are necessary to introduce all correlation effects that affect the width of the bands, and might also modify quantitatively the electronic structure.

One approach to manipulate the 2DEG formation at the reduced surface of STO thin films was presented. The creation of oxygen vacancies and the presence of Ti^{1+} ions are mainly responsible for the filling of the Ti 3d states in the presented data.

Results on Ti-resonant ARPES for Ni-doped STO films show that the 2DEG states disperse within 1 u.c or 1.5 u.c at the surface. In general, the distortion of the TiO_6 octahedron, responsible for the splitting between the d_{xy} bands and $d_{xz/yz}$ bands, affects the filling of the Ti 3d states. Doping with Ni seems to be efficient to reduce the octahedral distortion: the Γ -point was found at 0.12 \AA^{-1} for STO:Ni_{0.06} and at approximately 0.02 \AA^{-1} for STO:Ni_{0.12} versus 0.18 \AA^{-1} for STO (from the literature). At the Ti L e_g -edge, in addition to the 2D d_{xy} bands, the 3D $d_{xz/yz}$ are present at few meV from Fermi level, and move slightly to lower binding energy with Ni-doping content. These observations indicate a change in the octahedral deformation under lattice strength due to the doping, which therefore reduces the splitting between the d_{xy} and $d_{xz/yz}$ bands, as well as the symmetry of the lattice.

At last, results of STO films doped with Ni were presented more in details and compared to pure STO films. The bands structure of the two named systems deep in the valence band are similar with a small energy shift of 300 meV lower binding energy for the doped films. Ni impurity bands are localized in the k_x direction at 2.5 eV and dispersing in the k_y direction around $k_y=0 \text{ \AA}^{-1}$ at 1.3 eV. Likely this in-gap state can be attributed to Ni impurity bands or oxygen vacancies created in the films during the measurements. However, resonant ARPES in this case would be necessary to make a conclusive statements about surface states and their evolution with experimental conditions such as temperature, photon irradiation and oxidation.

X-Ray Photoelectron Diffraction of Ni-doped SrTiO₃ Films

In the previous chapters, we showed clear hints, which are based on XPS measurements and KKR-calculations, that Ni dopants occupy substitutional position in the lattice. The main objective of this chapter is to proof this hypothesis and to study structure close to the surface by XPD.

XPD is a powerful method used to determine element-specific local atomic surface structure of materials. Shortly, photoelectrons are emitted by absorbing photons in the energy range of the x-ray regime. These electrons scatter in a coherent manner with neighbouring atoms and constitute an interference pattern with the non-scattered direct electron wave [209]. Therefore, by scanning the intensity distribution of the photoelectrons in function of θ and ϕ for an ordered crystal, a diffraction pattern can be registered that contains information about the local structure around the emitter atoms. This method is quite interesting to investigate films structures and the local environment of impurities (dopant atoms) inside the surface. A detailed introduction of the method is discussed in section 2.3.

In this chapter we present and discuss the XPD measurements of pure STO and STO:Ni_{0.12} thin films. Our experiments were performed at the ARPES endstation of the PEARL beamline at SLS. XPD data were recorded within a high and low kinetic energy ranges in order to spot the consequences of backscattering effects on the interference and outgoing waves. Measurements were also performed for energies in the vicinity of Ni $2p$ core level to get information on the position of Ni atoms in the film structure. The data are supported by photoelectron diffraction simulations based on the multiple scattering (MSC) theory. This part has been performed in collaboration with Prof. Didier Sébilleau at Rennes University. The fundamental physics behind this method as well as the structure of our simulations will be described. The scattering factor and diffraction patterns for several atomic configurations will be considered and investigated. At last, our experimental data meet with our theoretical results leading to several conclusions and hypothesis about the local atomic structure of the films.

7.1 Photoelectron Diffraction Measurements

The quality of the structural characteristics that can be extracted from XPD measurements strongly depends on the experimental instrumentation such as angular resolution, angular window covered by the detector and the sampling density, as well as on the investigated sample. In principle, one needs to use a conventional hemispherical analyser with one channeltron detector to evaluate several thousands angle settings controlled by the sample manipulator [210]. In this case, the measurement time can be of the order of tenth of hours for one full diffraction pattern. An alternative direction but less time consuming is described by the use of a two-dimensional detector instead of a conventional channeltron detector. Here the data are recorded over a long line on the hemisphere above the sample for each angle setting rather than only one point. In other words, the diffraction pattern over a large solid angle is measured in a parallel mode (see Fig. 7.1 (a)). In this way, the measurements time is reduced, as well as the number of registered points while always sustaining the same angular resolution and statistical reliability.

In the present work, a 60° line on the hemisphere above the sample is registered for each angle setting (θ, ϕ) of the manipulator. Further details about the experimental setup and measurement geometry are described in section 2.4.3.

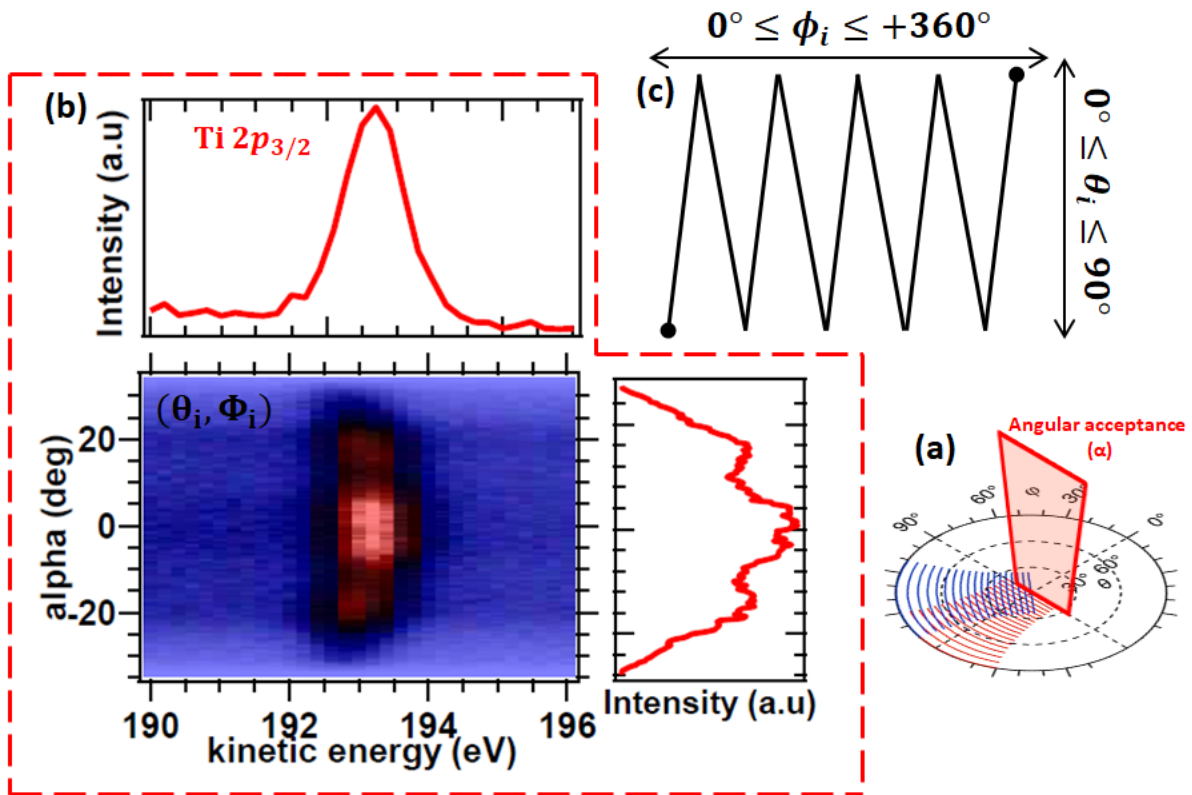


Figure 7.1: (a) Hemispherical scanning scheme of XPD. Each of the curved lines in the plot corresponds to the α interval detected in one shot. The resulting I_α measured at several polar angles θ are gathered to form a large slice from the 2π intensity distribution (adapted from [125]). (b) Measured photoelectron intensity of the Ti $2p_{3/2}$ peak of STO(001) films versus kinetic energy and emission angle α at (θ_i, ϕ_i) . The vertical (horizontal) solid line is profile integrated over the full angle (energy) range. (c) The actual θ and ϕ values of the XPD scan with $\Delta\theta=1^\circ$ and $\Delta\phi=40^\circ$.

projection (Fig. 7.2 (b)). The forward scattering directions (θ scan) for Ti $2p$ of STO along $\phi=0^\circ$ and $\phi=45^\circ$ are also defined in Fig. 7.2 (c).

7.2 Photoelectron Diffraction Simulations: Multiple Scattering Method

The algorithms used here to compute the XPD spectroscopy, which form the MsSpec package, are adopted from Sebilliau *et al.* [213,214] and are based on the multiple scattering theory, which describes how a particle (e.g. an electron) interferes through scattering with the surrounding atoms (see section 3.2.1). This package allows to build a cluster of atoms from the information of the system and Bravais lattice. Both bulk and surfaces can be generated. Then it generates the potential that corresponds to the given cluster and compute the T -matrix elements (T is the transition operator) that are at the centre of the multiple scattering method. We note that this potential does not result from a self-consistent loop. It is produced from a simple superposition of atomic potentials to which an exchange-correlation potential is added. In fact, the algorithms used in the MsSpec package are based on the multiple scattering KKR method, as outlined in the chapter 3. The main difference is that instead of evaluating the MSC path operator τ in the reciprocal space, as it is described in sections 3.2 3.3 for ground states and ARPES calculations, here for the XPD calculations, this quantity is evaluated by real space technique, as it is outlined in the following paragraph.

In order to compute the scattering path operator, i.e. the main ingredient of the present approach to describe spectroscopies, we used two different methods: 1- The multiple scattering series expansion, and 2- the matrix inversion method.

Back to the expression of $T(E)$ (see equation 3.34) that gives an atomic description of the material through standard multiple scattering theory, one can write,

$$\tau_{nm} = T_m \delta_n + \sum_{k \neq m} \tau_{nk} G_0 T_m, \quad (7.1)$$

where τ is the scattering path operator, T_m is the atomic transition operator, and G_0 is the Green's function of unperturbed system.

7.2.1 Multiple scattering series expansion

The first method is based on a perturbation expansion in which the iteration of the τ_{nm} equation is enforced:

$$\tau_{nm} = T_m \delta_n + T_n G_0 T_m + \sum_{k \neq m} T_n G_0 T_k G_0 T_m + \dots \quad (7.2)$$

The convergence of this method is related to the spectral radius described by the operator $G_0 T$ (the convergence is occurred for $r < 1$ [215]). The convergence is also related to the kinetic energies from the practical point of view. In this case, high kinetic energies are required (> 50 eV). As is it expressed in equation 7.2, this method simulates the contribution of every single path the particle (in this case the electron) can take to go from atom m to atom n . The extremely high number of paths leads to a computational blockage, and therefore a maximal number of scattered electrons

has to be defined: this value is called scattering order. Yet, this requirement is not enough to reduce the number of terms that need to be computed. In fact, if we consider the pathway $A=a \rightarrow b \rightarrow c \rightarrow d \rightarrow e$ that contains four scatterers and the absorber a , then the contribution of path A to the scattering path operator is written as:

$$\tau_{L_e L_a}^{ea}(A) = \sum_{L_b, L_c, L_d} T_{l_e} G_{L_e L_d}^{de} T_{l_d} G_{L_d L_c}^{dc} T_{l_c} G_{L_c L_b}^{cb} T_{l_b} G_{L_b L_a}^{ba} T_{l_a}, \quad (7.3)$$

with $L = (l, m)$. This equation. 7.3 is given in a spherical wave representation where the atomic T-matrices are diagonal and the two-site matrix elements of the propagator are given as a function of the Gaunt coefficient defined by

$$G(L_j L | L_i) = \int Y_{L_j}(\mathbf{r}) Y_L(\mathbf{r}) Y_{L_i}^*(\mathbf{r}) d\mathbf{r}. \quad (7.4)$$

It is obvious that the L_i and L_j are connected together through the Gaunt coefficient, and therefore the sums in equation. 7.3 are also one into another and cannot be separated. Note that the number of basis functions used on each atomic site is given by $(l_{max}+1)^2$ with l_{max} assigns the order at which the T-matrix elements are computed. In this case, the contribution of the single path A to the total scattering path operator necessitates the computation of $(l_{1max}+1)^2(l_{2max}+1)^2(l_{3max}+1)^2$ terms, which can be very high for high kinetic energies.

The problem is treated by using the plane wave approximation instead of the spherical waves, as proposed by Rehr and Albers [216]. The contribution of the single path A to the total scattering path operator becomes

$$\tau_{L_e L_a}^{ea}(A) \propto T_{l_e} f(\theta_d) f(\theta_c) f(\theta_b) T_{l_a}, \quad (7.5)$$

where $f(\theta_i)$ is the scattering factor of atom i . Its expression depends on the incoming and outgoing directions, and also of the phase shift induced by the potential of the atom i . The use of the plane wave approximation results in the computation of $(l_{1max}+1)^2 + (l_{2max}+1)^2 + (l_{3max}+1)^2$ terms instead of $(l_{1max}+1)^2(l_{2max}+1)^2(l_{3max}+1)^2$ terms. Further details about this method can be found in Refs. [213–215].

7.2.2 Matrix inversion method

The second method is a full multiple scattering method based on the factorization of the τ_{nm} equation:

$$\tau = (t^{-1} - g_0)^{-1}, \quad (7.6)$$

where t^{-1} is the single-scattering t -matrix operator and g_0 is the structure constant of the underlying system.

Here the multiple scattering matrix $(t^{-1} - g_0)$ is calculated for all the basis functions of the whole cluster, then stored into the computer and finally inverted. From the physical interpretation, this method gives a better description of the system in study, but unfortunately it has some practical limitations: in the case of large clusters or for high kinetic energies (in other words high number of basis functions used for each atomic site), it requires a huge memory storage facilities, hence it is limited to small clusters (of the order of 100 atoms) and low kinetic energy range (<400 eV).

Apart from choosing the physical method to perform multiple scattering (MSC) simulations,

many other parameters can be introduced in the script such as the polarization of the incident light, angular acceptance of the detector, path filtering (this parameter is used to filter the scattering processes by choosing forward scattering and/or backward scattering), temperature, and atomic vibrations. We note that both methods are based on the MTA in which the potential is considered as constant with spherical symmetry within the atomic spheres.

In addition to the electron diffraction simulations, the MsSpec package also allows to compute the scattering factor of an element at a given kinetic energy as a function of the polar and azimuthal angles. It gives information about the scattering paths contributing to the calculation: for high kinetic energies, most of the scattering takes place along a row of atoms due to the strong forward peaking of the scattering factor. For low kinetic energies, backward scattering becomes important and sometimes predominant [217]; therefore both forward and scattering filters must be taken into account. As we are using the plane wave approximation, these calculations give a rough estimation about the importance of paths contributions relatively to each other.

7.3 Results

Our results are presented into three main parts as following: First, for reference, we will investigate the Ti $2p$ XPD pattern of pure STO(001) films at high kinetic energy range $E_{kin}=1.037$ keV, to testify the accuracy of the experimental data, as well as the MSC simulations when forward scattering process dominate. For the given kinetic energy, the calculated mean free path is equal to 17.491 \AA^{-1} equivalent to 4.5 u.c, and the multiple scattering series expansion method is used to compute the T-matrix elements with $l_{max}=21$.

In the second and third parts, XPD measurements from pure STO(100) and STO:Ni_{0.12}(100) respectively, at low kinetic energy range are performed, where forward and backward scattering processes are present. We adjust the photon energy of the different emitters (Ti $2p$, Sr $3d$ and Ni $2p$) to get a fixed kinetic energy equal to 194 ± 3 eV. For this kinetic energy range, the inelastic mean free path is equal to 7.784 \AA^{-1} equivalent to 2 u.c. Here we used the spherical waves multiple scattering-inversion method to compute the T-matrices. For Ti $2p$ and Ni $2p$ the l_{max} is set to 10, and for Sr $3d$ it is set to 14.

7.3.1 High kinetic energy

The results of the Ti $2p_{3/2}$ XPD scans are shown in Fig. 7.3 (a), together with the corresponding simulation using MSC theory (Fig. 7.3 (b)). For the MSC simulation, we used a hemispherical STO cluster of 335 atoms (Sr₆₈Ti₇₆O₁₉₁) and 7 planes. Each layer is composed of two planes (TiO₂ and SrO) with $a=c=3.905 \text{ \AA}$ for the lattice parameters. As the photoelectron kinetic energy is high, the scattering amplitude is mostly directed in the forward direction. We fixed the scattering order to 6 to reduce the total number of paths at each scattering site and filter the forward scattering directions. The absorber (emitter) is positioned at the centre of each plane and the final diffraction intensities are given as the summation of all resulting amplitudes at each plane of the emitter.

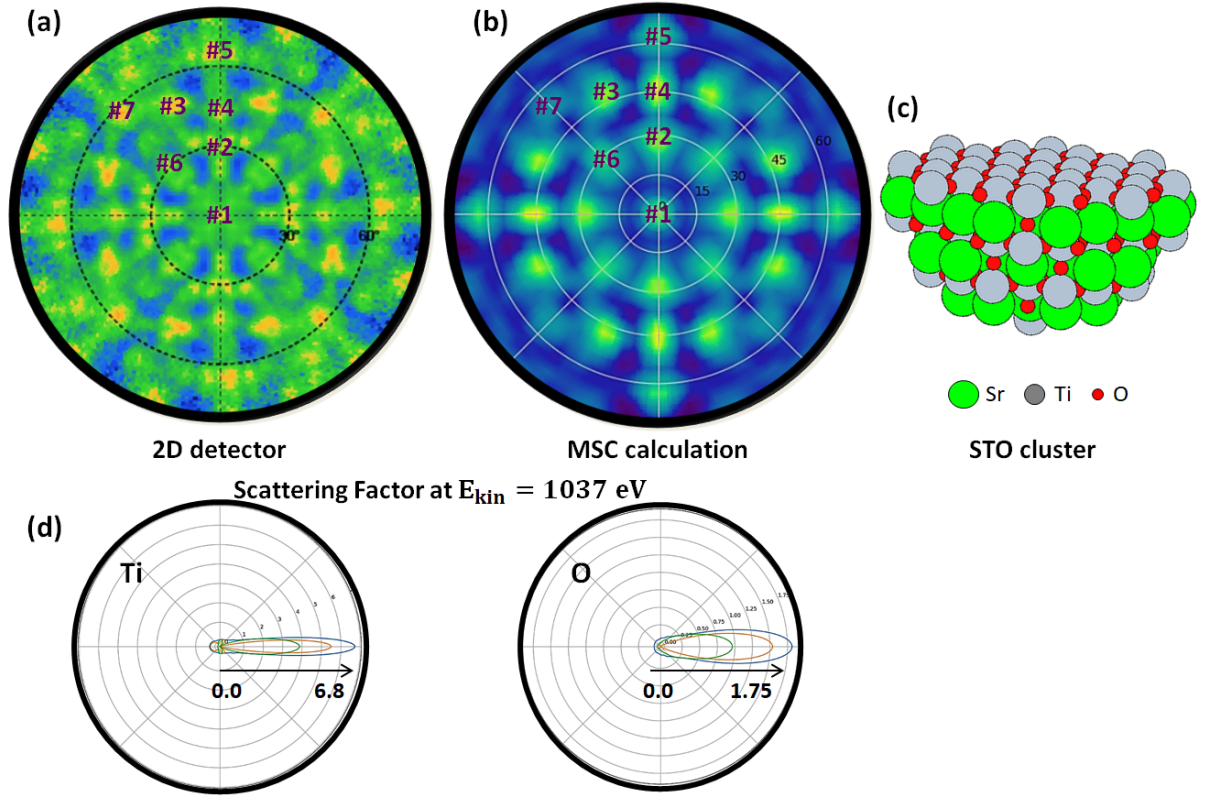


Figure 7.3: (a) Reconstruction of the XPD patterns (Ti $2p_{3/2}$, $h\nu=1500$ eV) from STO(001) thin films (b) Multiple scattering (MSC) calculation of the Ti $2p$ XPD pattern and the atom cluster of the STO(001) surface with TiO_2 termination used for the MSC simulation, respectively. (d) Scattering factors of Ti and O at $E_{kin}=1037$ eV.

The MSC simulation (Fig. 7.3 (b)), shows the result for a perfectly TiO_2 terminated surface of STO. The main diffraction features are labelled #1→#7 and their analogues are tagged in the measured pattern for the comparison. The origin of feature #3 is not completely understood and will not be discussed further, as well as feature #5 because it is located at large θ angle of 70° . For $\phi=0^\circ$, features #1, #2 and #4 represent the scattering of Ti atom (emitter) with another Ti atom (scatterer) as it is shown in Fig. 7.2 (c). The experimental data shows that these features are less pronounced compared to MSC simulation, meaning that the surface has different termination than the expected TiO_2 . Two possible pictures can explain this observation. In the first one, we assume that Ti vacancies are formed at the surface over film deposition, or due to the beam irradiation for long time during the measurements. The second one describes the surface as it is TiO_2 terminated, with the presence of SrO island partially covering the surface. In both cases, the interference of the resulting wavelengths is mitigated by the scattering processes of the emitter atom with the oxygen atoms located at the surface as they have a weak forward scattering factor compared to Ti (see Fig. 7.3 (d))

For $\phi=45^\circ$, features #6 and #7 result from the scattering of the emitter Ti with the scatterer Sr. Feature #6 shows a good agreement between the experimental data and MSC simulation, while feature #7 is more pronounced in the experiments. This means that at the top most layers, the Ti emitter is scattering with another Sr atom resulting in a strong interference. In the case of TiO_2 termination, the Ti emitter at the surface will not scatter and will reduce the outgoing signal as shown in the MSC calculation for a perfect TiO_2 surface termination.

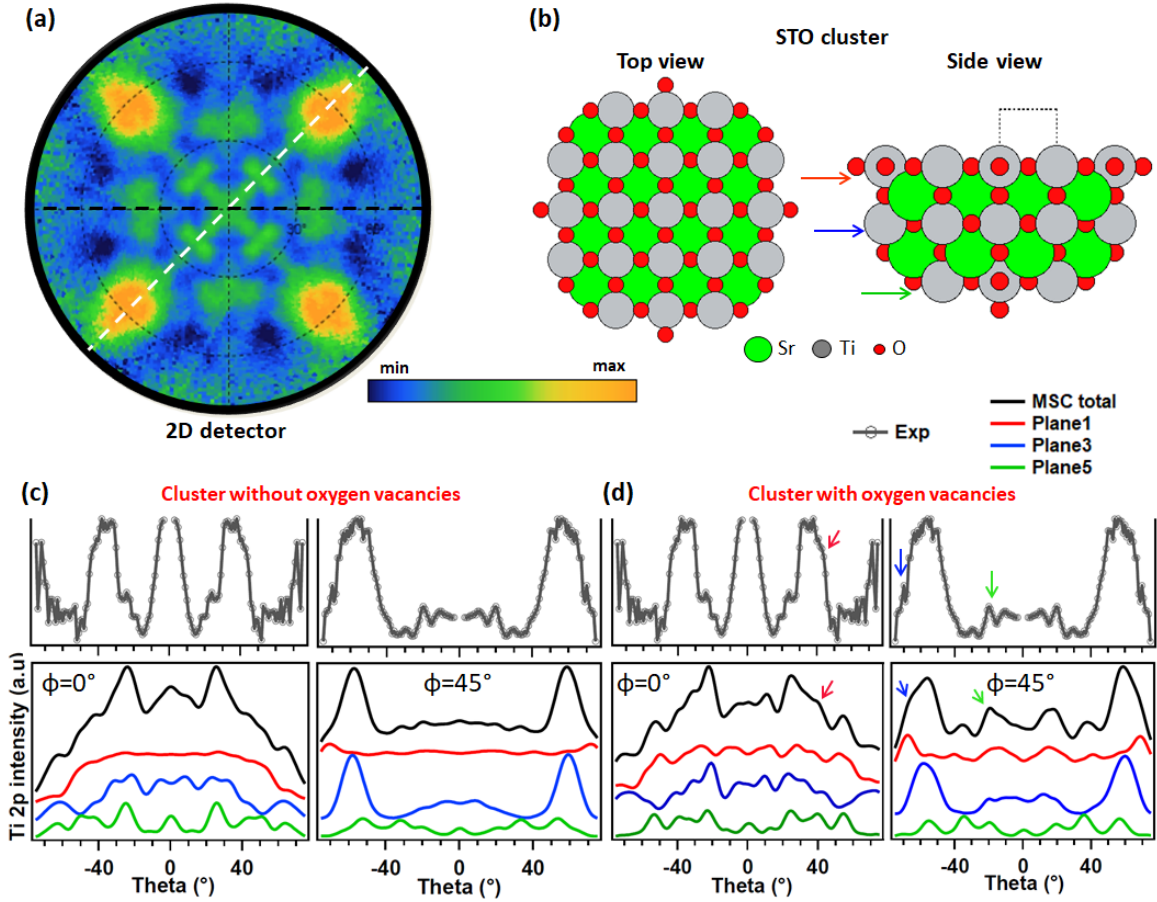


Figure 7.4: (a) Reconstruction of the XPD patterns (Ti $2p_{3/2}$, $h\nu=657$ eV) from STO thin films. (b) The atom cluster of the STO(001) surface with TiO_2 termination used for the MSC simulation. Comparison of the experimental data with the MSC anisotropies as a function of the polar angle θ at azimuthal angle $\phi=0^\circ$ and 45° of the STO cluster (c) without oxygen vacancies, and (d) with oxygen vacancies at the surface. The arrows show the different analogue features (with same colour) observed in experiments and simulations.

7.3.2 Low kinetic energy

In this section, all measurements are performed at low kinetic energy of 194 ± 3 eV where more multiple scattering processes are occurred. First we present the XPD patterns and MSC simulations of Ti $2p$ and Sr $3d$ from STO(100). And then, we show the results from the STO:Ni_{0.12}(100) films and compare them to the pristine films.

STO(100)

In Fig. 7.4 (a), the XPD patterns of the Ti $2p_{3/2}$ is depicted. High anisotropic features with four-fold symmetry are clearly reflected. The diffraction pattern shows the main maxima at $\theta=0^\circ$, and 35° to 45° along the next-nearest-neighbour directions [100], and [010]. It also shows features at $\theta=0^\circ$, 20° and a pronounced spot at $\theta=55^\circ$ along the next-nearest-neighbour directions [110] and $[\bar{1}10]$.

To image how the experimental data can be interpreted, a series of MSC simulations (only polar scans for $\phi=0^\circ$ and 45°) together with the corresponding atomic cluster are presented in Fig. 7.4 (b-d). The hemispherical STO cluster used to perform the simulations contains 94 atoms with 5 planes (TiO_2 termination).

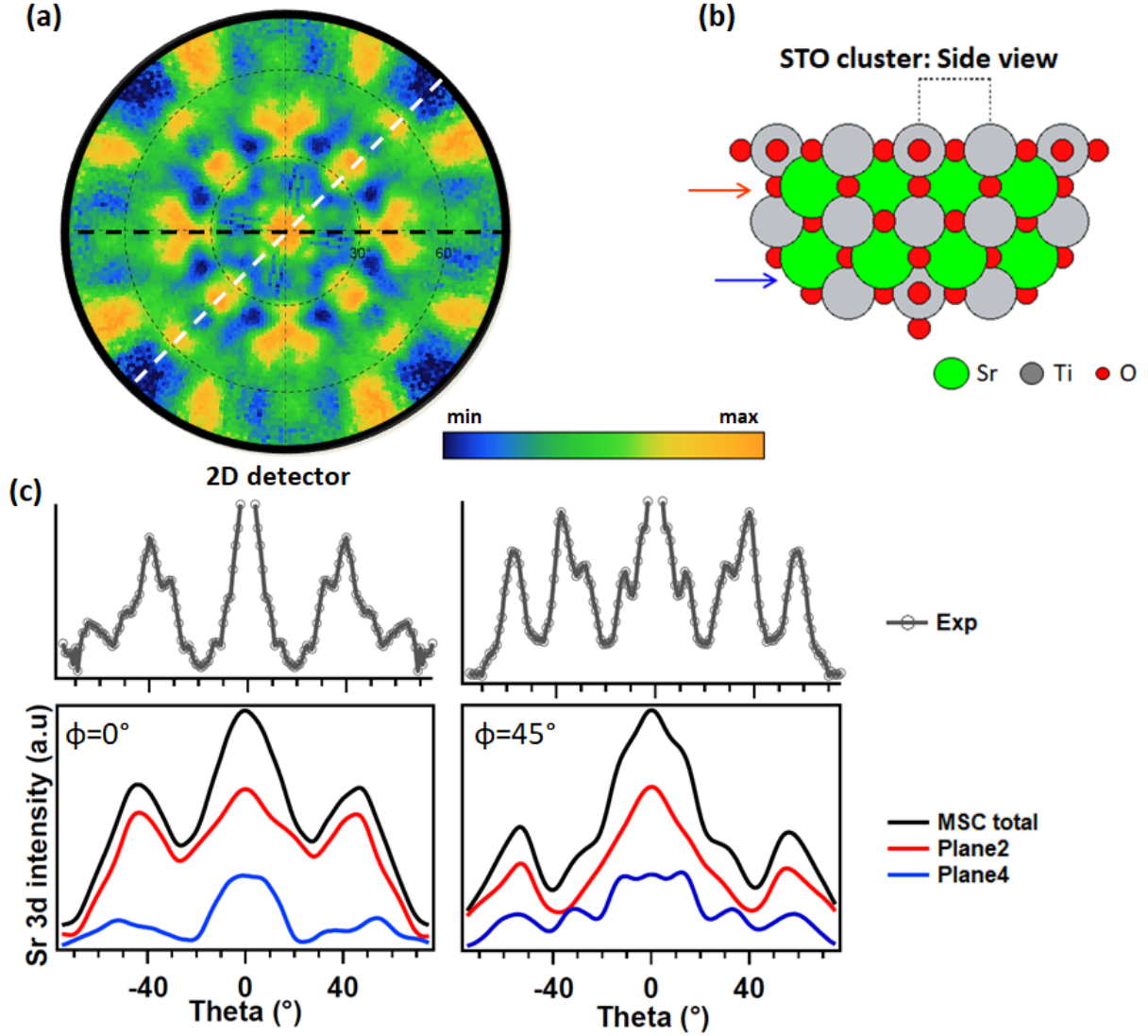


Figure 7.5: (a) Reconstruction of the XPD patterns (Sr $3d_{5/2}$, $h\nu=335$ eV) of STO thin films. (b) The atom cluster of the STO(001) surface with TiO_2 termination used for the MSC simulation. (c) Comparison of the experimental data with the MSC anisotropies in function of the polar angle θ at $\phi=0^\circ$ and 45° .

A comparison of the experimental data with the MSC calculations in the $[100]$ direction ($\phi=0^\circ$, black dashed line in Fig. 7.4 (a)) and the $[110]$ direction $\phi=45^\circ$, white dashed line in Fig. 7.4 (a) is presented in Fig. 7.4 (c) and (d) for a perfect TiO_2 surface termination without oxygen vacancies, and for a surface with low density of oxygen vacancies where one vacancy is set in the oxygen octahedral centred by the emitter Ti, respectively. The resulting MSC diffraction peaks originating from each plane where the absorber is located are also plotted separately. Note that the oxygen vacancies are replaced by empty spheres to get a better estimation of the muffin-tin potential.

The best agreement between simulation (total) and experiment is obtained with a TiO_2 surface termination with oxygen vacancies (see features marked by the coloured arrows). Moreover, the enhancement of the simulated signal is due to the diffraction peaks arising from the surface (plane 1). In the previous paragraph, for measurements at high kinetic energy, we assumed that the surface is TiO_2 terminated by SrO islands. As already mentioned in the theory part, for

electrons from a given core level with high kinetic energies, there are nearly no contribution to the pattern from electrons backscattered from surrounding atoms. Here at low kinetic energies, due to much higher probability for backscattering, more information about the surrounding atoms to the emitter can potentially be extracted. Our present data confirm the TiO_2 termination of the films with oxygen vacancies. An alternative explanation of the results at high kinetic energy can be the ruffled structure at the surface in which the Ti atoms are moved deeper to the bulk compared to oxygen atoms due to surface relaxation [218], which therefore affect the interference process.

The XPD pattern of Sr $3d_{5/2}$ is displayed in Fig. 7.5 (a). The diffraction pattern exhibits strong prominent spots at $\theta=0^\circ$, and 30° to 45° along the $[100]$ and $[010]$ directions, also a broaden maxima around $\theta=0^\circ$, 29° , 40° and 56° along the $[110]$ and $[\bar{1}10]$ directions.

To simulate the Sr $3d_{5/2}$ diffraction peaks, we used a cluster with TiO_2 surface termination, without oxygen vacancies (see Fig. 7.5 (b)). The use of a surface with oxygen vacancies did not seriously affect the results. The comparison between experiment and MSC simulation at $\phi=0^\circ$ and 45° is displayed in Fig. 7.5 (c). At $\phi=0^\circ$, the experimental and simulated data show a good agreement. At $\phi=45^\circ$, the diffraction features at $\theta=0^\circ$, 29° and 56° match with MSC simulation. Yet, the pronounced diffraction peak at $\theta=40^\circ$ (from experiment) is faced with a minima in the MSC simulation. This is mainly caused by the perfect coherence of the MSC data. Moreover, at the surface layer, all Ti and Sr atoms are pushed into the bulk compared to ideal flat surface as we mentioned and lead to surface rumpling that affect the interference.

STO:Ni_{0.12}(100)

Now we tested the reproducibility of the experimental data with MSC simulations, our main goal here is to define the structural position of Ni impurities in the doped STO films if they substitute Ti atoms, Sr atoms and/or occupy interstitial sites. But at first, we start with comparing the XPD patterns of Ti $2p$ from pristine and STO:Ni_{0.12} films.

For the MSC calculations in this section, the hemispherical cluster we used is made of 207 atoms ($\text{Sr}_{28}\text{Ti}_{46}\text{Ni}_6\text{O}_{114}\text{X}_{12}$ with X for empty sphere) and 5 planes with TiO_2 surface termination. Ni atoms here substitute the Ti sites and two empty spheres are located in each Ni related oxygen octahedral (see Fig. 7.6 (b)). The Ti $2p_{3/2}$ diffraction pattern from STO:Ni_{0.12} films is displayed in Fig. 7.6 (a). At the first sight, the anisotropy of the diffraction features looks similar to the one for pure STO. In Fig. 7.6 (c), the polar intensity distribution of the results for pure STO and STO:Ni_{0.12} samples for $\phi=0^\circ$ and 45° are plotted. The comparison shows that, the maxima at $(\theta, \phi)=(38^\circ, 0^\circ)$ in STO is shifted by $+3^\circ$ to $(41^\circ, 0^\circ)$ in STO:Ni_{0.12}. Also at $\phi=45^\circ$, all peaks from the doped sample are shifted by $+5^\circ$ compared to the undoped one. This implies a modification of the lattice parameter, and more specifically a compression in the growth direction (z -axis normal to the surface plane). The polar shifts we observed are equivalent to a ratio of c/a equal to 0.96 obtained from MSC calculations. We believe that this modification is related to Ni-doping. This hypothesis match our conclusion in the previous chapter about the distortion of the oxygen octahedron due to Ni impurities (see section 6.2.2). Also, Ni atoms might not be totally substituting in the lattice and taking other interstitial positions, which leads to more

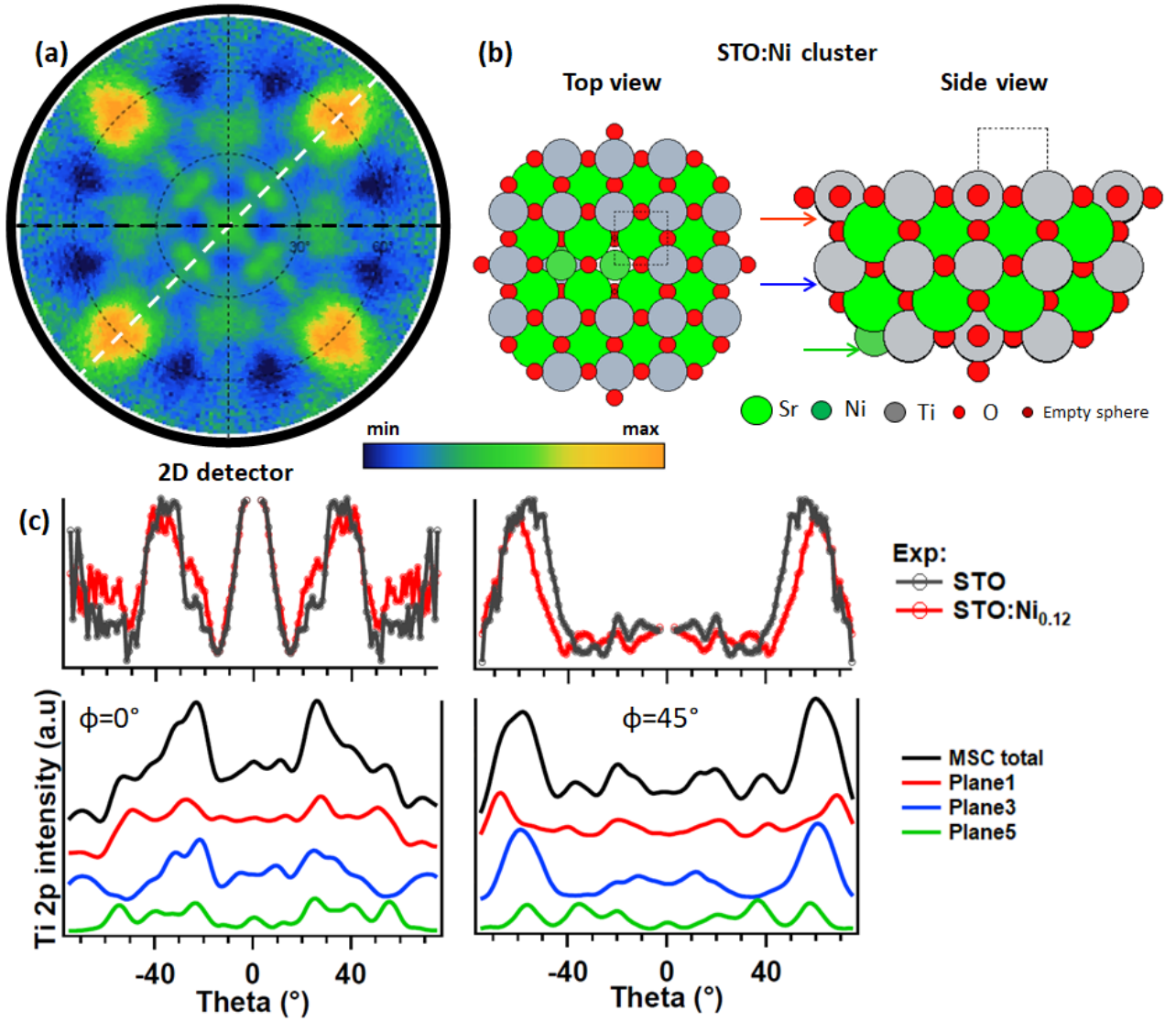


Figure 7.6: (a) Reconstruction of the XPD patterns ($\text{Ti } 2p_{3/2}$, $h\nu=657 \text{ eV}$) from $\text{STO:Ni}_{0.12}$ thin films. (b) The atom cluster of the Ni-doped $\text{STO}(001)$ surface with TiO_2 termination used for the MSC simulation. (c) Comparison of the experimental data of pristine and $\text{STO:Ni}_{0.12}$ films on one side, and the experimental data of $\text{STO:Ni}_{0.12}$ with the corresponding MSC anisotropies on the other side, in function of the polar angle θ at $\phi=0^\circ$ and 45° .

lattice strain and therefore affect the interference of the different scattered waves.

The comparison of the experimental data from $\text{STO:Ni}_{0.12}$ films with the MSC simulations depicted in Fig. 7.6 (c) shows a good agreement. Yet, the maxima observed from experiments at $\theta=0^\circ$ is not present in the results from MSC simulations. If we look at the peaks originating from the different planes in the MSC calculation, we find that this peak results from diffraction of the emitter located in plane 5, and it vanishes with the waves coming from the planes 3 and 1. Meaning that at the surface of our films, the arrangement of the atoms is slightly modified with different lattice relaxation order. This assumption also supports our previous interpretation about the lattice distortion of the oxygen octahedra due to Ni doping.

We will discuss now the $\text{Ni } 2p_{3/2}$ diffraction pattern in Fig. 7.7 (a). The data show a clear 4-fold symmetry attesting the long range ordering of Ni atoms in the hosting lattice. Three main features are observed in the stereographic projection (see the red dashed contours in the pattern):

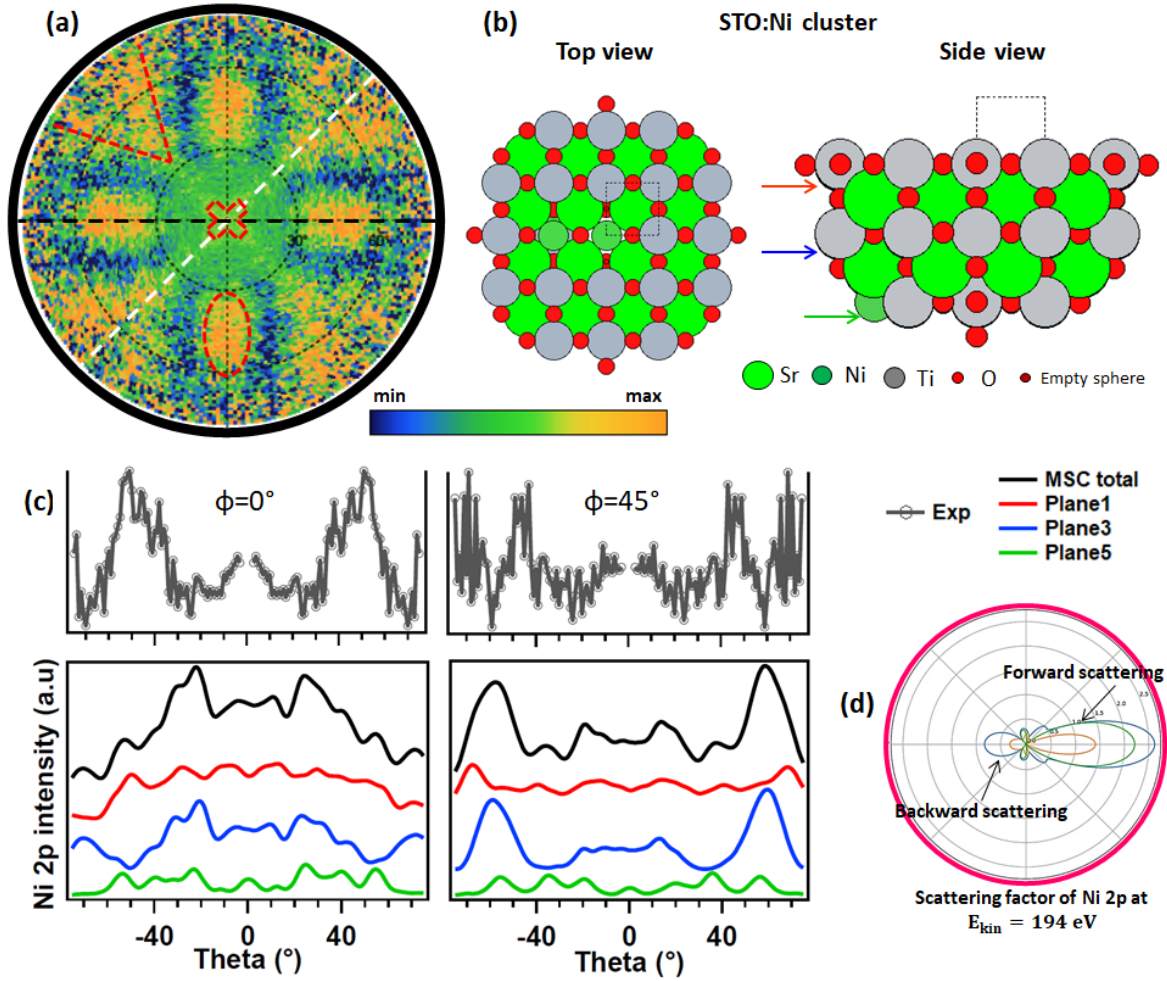


Figure 7.7: (a) Reconstruction of the XPD patterns (Ni $2p_{3/2}$, $h\nu=1053$ eV) from STO:Ni_{0.12} thin films. The diffraction maxima are highlighted by red dashed contours (guide to the eye). (b) The atom cluster of the Ni-doped STO(001) surface with TiO₂ termination used for the MSC simulation. (c) Comparison of the experimental data with the MSC anisotropies in function of the polar angle θ at $\phi=0^\circ$ and 45° . (d) Scattering factor of Ni $2p$ at $E_{kin}=194$ eV showing the forward and backward scattering contributions.

The first one is a weak cross spot located at the centre along the $[110]$ and $[\bar{1}\bar{1}0]$ directions. The second feature is a broad pronounced maxima centred at $\theta=45^\circ$ along the next-nearest-neighbour directions $[100]$ and $[010]$. The last remarkable feature is having a broad V-shape. It is centred along the $[110]$ and $[\bar{1}\bar{1}0]$ directions and located at $\theta=45^\circ$ to 65° .

The comparison with MSC simulation gives rise to globally similar features for $\phi=0^\circ$ and 45° (Fig. 7.7 (c)), attesting the substitution of Ni atoms at Ti sites. The broadening and shift of the diffraction peaks from experiments indicates a modification in the lattice parameter and therefore a distortion of the oxygen octahedral. Note that, at low kinetic energy, the scattering factor of Ni shows an important contribution of the backscattering process (see Fig. 7.7 (d)), resulting in a high sensitivity of the photoelectron diffraction peaks to the surrounding atoms. The interpretation of XPD patterns at low kinetic energies is much less straightforward than in the case of high kinetic energies. The higher complexity of the scattering processes produced demands a more elaborate theoretical treatment starting from the potential of the system in study. The muffin-tin approximation seems to be less accurate for slow electrons, and the surrounding potential in which the photoelectrons are moving is more difficult to compute compared to the

high kinetic energy case.

7.4 Conclusion

In summary, the XPD patterns of Ti $2p_{3/2}$ and Sr $3d_{5/2}$ photoelectron signals in pure STO confirmed the (1×1) surface reconstruction (4-fold symmetry) with TiO_2 termination and low density of oxygen vacancies.

In case of Ni doped STO films, the data showed a shift of the diffraction peaks of 3° in the $[100]$ direction and 5° in the $[110]$ direction, indicating a modification of the lattice parameters with a ration of 0.96. We assume that these shifts are mostly due to lattice strain caused by the doping. The Ni $2p$ diffraction pattern confirms the long range ordering of the Ni impurities in the lattice of STO. It shows as well a 4-fold symmetry demonstrating that the Ni atoms substitute Ti sites.

The Mspec package used to perform XPD simulations by means of multiple scattering theory is a good tool that provides a quantitative description of the local atomic structure and gives information about the atomic surrounding of an emitter. The findings of this work are particularly encouraging in view of the using availability of theoretical tools to get a better understanding of the fundamental phenomena observed in experiments.

Summary

The strongly correlated STO system is as valuable material for photovoltaic applications due to the possibility of broadening its light absorption range through chemical doping by TM elements at the Ti-site. In addition to the optical properties, the electronic structure of such system highly depends on the doping element, growth method, dopant content and surface treatment. Various physical characteristics, as for example the formation of the 2DEG at the surface of STO, adding the correlation effects of the Ti $3d$ and the impurity $3d$ states meet at the same time with an extensive interest in the progress of solid state physics in this field.

The electronic and structural properties of STO doped with several TM elements (Ni, Fe and Cr) has been investigated. All the samples were synthesized as thin films of few nm thickness. The focus is localized on a variety of photoelectron spectroscopy techniques that are primarily efficacious to describe the complicated many body physics. In addition to experimental investigations, first-principle calculations within the KKR-GF framework were also performed to get a better understanding of the different observed fundamental processes.

In the first part of the thesis, Ni-doping effects on STO thin films, grown by magnetron sputtering at RT, were investigated. Using XRD, it was shown that all the as-deposited films have an amorphous-like structure, assigning a lack of long-range order. The crystallinity of the films is induced by annealing them at 500°C , and the mean crystallite size was found to be increasing with temperature from 22.52 nm at 500°C to 28.21 nm at 900°C . Interestingly, the XRD data also showed that for Ni-doped STO films, the crystallite size was increasing and the films microstructure was improving, compared to the non-doped films. Magnetron sputtering method can be useful for industrial sectors: It is inexpensive, relatively fast compared to other film growth methods and does not require complex environment such as high temperature for growth and ultra high vacuum.

To get a better understanding of the modification of the electronic properties due to the doping, high quality of crystalline samples grown by PLD were investigated by means of XPS, ARPES and resPES. We studied pure STO, STO: $\text{Ni}_{0.06}$, STO: $\text{Ni}_{0.12}$, STO: $\text{Fe}_{0.05}$ and STO: $\text{Cr}_{0.05}$ thin films deposited on STO: $\text{Nb}_{0.05}(100)$ substrates with TiO_2 surface termination.

We showed that for Ni-doped STO films, the main line of the Ni $2p_{3/2}$ XPS spectrum contains two peaks separated by 1.9 eV. The main Ni $2p$ peak corresponds to a II oxidation state of Ni, the other peak, located at lower binding energy side from the main line, results from a non-local screening process by an electron that does not come from the oxygen orbitals around the Ni atom with the core hole, but from a neighbouring NiO₆ unit. It also includes the contribution of some surface states, which are resulting from pyramidally coordinated Ni atoms located at the surface and that overlap with the non-local screening structure. For Fe-doped STO films, the Fe $2p_{3/2}$ XPS spectrum reveals the presence of Fe³⁺ ions incorporated in the lattice with an octahedral environment. For Cr-doped STO films, the shape of the Cr $2p_{3/2}$ XPS spectrum demonstrates the presence of Cr³⁺ ions. All in all, the analysis of core level spectra allows to assess the oxidation state of the impurity atoms in the hosting system, and their location in the octahedral environment.

From first principle calculations for ground states (TDOS, PDOS and BSF), and from the resonance photoemission measurements with photon energies around the $3d$ TM L-edge, we could define the distribution of the $3d$ impurity energy levels in the valence band and the band gap of STO. The data showed the formation of the localized defect bands in the band gap at the VBM, which can lead to the improvement of the visible light absorption.

For Ni-doped STO films, the Ni-resonant ARPES measurements revealed the strong correlated nature of Ni $3d$ electrons in STO, where multiplet and satellite structures have an important contribution at the Ni L-edge resonance. These structures are mainly resulting from the strong Coulomb interaction, exchange interaction and crystal field effects. The resonating features resulting from the Ni $3d$ main line and the multiplet structure follow a constant binding energy with the increase of photon energy. Meaning that during the auto-ionization process, the photoelectrons related to these structures are coherently overlapping with the direct photoemission process. The feature resulting from the satellite state and located at 6 eV higher binding energy from the Ni L₃, keeps at a constant binding energy for photon energies around the Ni absorption threshold (853 eV) and then starts to follow a constant kinetic energy line for photon energies away from threshold. This phenomenon is occurred due to the loss of the coherence in the intermediate state, and so the final states of the Auger channel and the direct photoemission channel differ, resulting in an incoherent Auger decay. Another feature located at 1.1 eV in the gap was detected at the Ni-resonance. These states correspond to localized charge carriers trapped in the d -orbitals of Ni ions surrounded by oxygen vacancies, attesting the hybridized nature of the Ni $3d$ and O $2p$ bands in STO.

The resonance behaviour at photon energies around the Fe L₃ absorption edge, showed the enhancement of different features located both in the band gap at binding energies around 2.5 eV, and in the VB. These peaks are related respectively to the main Fe $3d$ states and the Fe related multiplet structure. Another strong background was observed at around 8 eV is originating from the resonance of satellite structure and lead to the emission of an incoherent Auger signal. In case of STO:Cr films, at the Cr ($2p \rightarrow 3d$) resonance, one feature positioned in the gap at $E_B=2$ eV is attributed to the Cr $3d$ bands formed at this binding energy level.

Our DFT (LDA) calculations for the ground states showed only the main $3d$ states of the TM-impurities. The other features related to the multiplet and satellite structures were not observed, as they result from the many-body correlation processes, which are not correctly estimated in LDA.

The band dispersions (ARPES) of STO and $3d$ TM doped STO(100) thin films in a wide binding energy range were presented. From our experimental data, we observed that for the doped films, the bands are shifted toward Fermi level, and the localized $3d$ impurity bands were detected at 2.5 eV in the band gap of STO. The one-step model calculations (LDA) were in a good agreement with the experimental findings when it concerns the dispersion of the bands. However, the position of Fermi level and the bands width did not match. This is due to the approximation we used to perform our calculations, that does not include all correlation effects and does underestimate the Coulomb potential.

The formation of the 2DEG at the surface of STO films doped with Ni was investigated and compared to the findings on pure STO(100) films. Our results showed that the 2DEG states disperse within 1 u.c or 1.5 u.c at the surface. The Γ -point was found at 0.12 \AA^{-1} for STO:Ni_{0.06} and at approximately 0.02 \AA^{-1} for STO:Ni_{0.12} compared to 0.18 \AA^{-1} for STO in literature. The 2D d_{xy} bands were clearly visible at Fermi level at photon energies around the Ti L-edge. Yet, exclusively at photon energies corresponding to the Ti L e_g -edge, the 3D $d_{xz/yz}$ were also observed at few meV from Fermi level, and found to be moving slightly to lower binding energy with Ni-doping content. These findings indicate a modification in the octahedral deformation under lattice strength due to the doping, that leads to different energy splitting of the d -suborbitals.

In the last chapter of this thesis, the local structural properties of the pristine and Ni doped STO(100) films were presented by means of XPD supported with multiple scattering simulations for spectroscopic applications (here photoelectron diffraction). The XPD patterns of all elements in the films confirmed the 4-fold symmetry of the structure with TiO₂ termination and low density of oxygen vacancies at the surface. For Ni-doped films, the data showed a shift of the diffraction peaks which corresponds to a modification of the lattice parameters with a ratio of $c/a=0.96$, due to the doping with Ni. The Ni $2p$ diffraction pattern showed a 4-fold symmetry in which Ni atoms substitute Ti sites in a long range ordering.

Perspective

Back to the last part of chapter 2.1, we presented the ARPES data performed on Ni-doped STO films at $h\nu=124$ eV and RT. We observed a 1D dispersion in the vicinity of Fermi level, and we proposed that these states might be related to Ni impurity atoms differently localized at the surface of the film, due to the light irradiation. A detailed study of this feature is required in order to define their origin.

Our first principle calculations showed that Fe doped STO is a magnetic system with high magnetic order, unlike Ni-doped STO which is a paramagnetic system. Therefore, spin resolved ARPES measurements might lead to more interesting characteristics of this system that can be manipulated. Also, combining barium-doping at the Sr-site with the TM-doping at Ti-site in STO, adds ferroelectricity and other surface properties different from the bulk to the system.

The theoretical findings showed the failure of the LDA to describe the electron-electron correlations and other many-body effects in these compounds. The combination of LDA and DMFT here is required in order to correctly picture the properties of the system.

The transition metal oxides doped with transition metal elements, showed that they can be very interesting compounds, due to the interplay of their lattice, surface, charge, spin and orbital degree of freedom. The interaction of these properties give rise to new mechanisms and new observations that need to be explored. The capacity and phase space to investigate in oxides perovskites are limitless, and only a small part was examined in this thesis, giving a perspective on the scopes that are still undiscovered.

Acknowledgements

Foremost, I would like to express my sincere gratitude to my advisors Prof. Christine Richter, Prof Karol Hricovini and Prof. Ján Minár for the continuous support of my PhD study and research, for their patience, motivation, enthusiasm, and immense knowledge. Their guidance helped me in all the time of research and writing of this thesis. I could not have imagined having better advisors and mentors for my PhD study.

Besides my advisors, I would like to thank the rest of my thesis committee: Dr. Rémi Lazzari, Dr. Andrés Santander-Syro, Dr. Véronique Brouet, Prof. Andreas Honecker, Doc. Šimon Kos and Dr. Ondřej Šipr, for their encouragement, insightful comments, and hard questions.

My sincere thanks also goes to Prof. Ralph Claessen and Prof. Didier Sébilleau, for offering me many opportunities in their groups and leading me working on diverse exciting projects.

I thank my fellow labmates: Laurent Nicolaï, Sunil Dsouza, Saleem Ayaz, Jakub Schusser, Zakaria El-Youbi, Evgeni Boakinov and Phuc Trung, for the stimulating discussions, and for all the fun we have had in the last four years. Also I thank Berengar Leikert in Würzburg University for his remarkable assistance during the PLD growth.

Last but not the least, I would like to thank my family for supporting me spiritually throughout my life.

Bibliography

- [1] A. Zahedi. Solar photovoltaic (PV) energy latest developments in the building integrated and hybrid PV systems. *Renewable Energy*, 31(5):711–718, apr 2006.
- [2] Martin A. Green. Accuracy of analytical expressions for solar cell fill factors. *Solar Cells*, 7(3):337–340, dec 1982.
- [3] A. Shah. Photovoltaic technology: The case for thin-film solar cells. *Science*, 285(5428):692–698, jul 1999.
- [4] Mingzhen Liu, Michael B. Johnston, and Henry J. Snaith. Efficient planar heterojunction perovskite solar cells by vapour deposition. *Nature*, 501(7467):395–398, sep 2013.
- [5] M. M. Lee, J. Teuscher, T. Miyasaka, T. N. Murakami, and H. J. Snaith. Efficient hybrid solar cells based on meso-superstructured organometal halide perovskites. *Science*, 338(6107):643–647, oct 2012.
- [6] Divya Tiwari and Steve Dunn. Photochemistry on a polarisable semi-conductor: what do we understand today? *Journal of Materials Science*, 44(19):5063–5079, oct 2009.
- [7] Yongbo Yuan, Zhengguo Xiao, Bin Yang, and Jinsong Huang. Arising applications of ferroelectric materials in photovoltaic devices. *J. Mater. Chem. A*, 2(17):6027–6041, 2014.
- [8] N. Reyren, S. Thiel, A. D. Caviglia, L. F. Kourkoutis, G. Hammerl, C. Richter, C. W. Schneider, T. Kopp, A.-S. Ruetschi, D. Jaccard, M. Gabay, D. A. Muller, J.-M. Triscone, and J. Mannhart. Superconducting interfaces between insulating oxides. *Science*, 317(5842):1196–1199, aug 2007.
- [9] K. Ueno, S. Nakamura, H. Shimotani, A. Ohtomo, N. Kimura, T. Nojima, H. Aoki, Y. Iwasa, and M. Kawasaki. Electric-field-induced superconductivity in an insulator. *Nature Materials*, 7(11):855–858, oct 2008.
- [10] J. Georg Bednorz and K. Alex Müller. Perovskite-type oxides: The new approach to high-Tc superconductivity. *Reviews of Modern Physics*, 60(3):585–600, jul 1988.

- [11] A. Brinkman, M. Huijben, M. van Zalk, J. Huijben, U. Zeitler, J. C. Maan, W. G. van der Wiel, G. Rijnders, D. H. A. Blank, and H. Hilgenkamp. Magnetic effects at the interface between non-magnetic oxides. *Nature Materials*, 6(7):493–496, jun 2007.
- [12] Madeleine R. Morris, Stephanie R. Pendlebury, Jongin Hong, Steve Dunn, and James R. Durrant. Effect of internal electric fields on charge carrier dynamics in a ferroelectric material for solar energy conversion. *Advanced Materials*, 28(33):7123–7128, jun 2016.
- [13] A. I. Lebedev, I. A. Sluchinskaya, A. Erko, and V. F. Kozlovskii. Direct evidence for off-centering of Mn impurity in SrTiO₃. *JETP Letters*, 89(9):457–460, jul 2009.
- [14] G. Y. Gou, J. W. Bennett, H. Takenaka, and A. M. Rappe. Post density functional theoretical studies of highly polar semiconductive Pb(Ti_{1-x}Ni_x)O₃ solid solutions: Effects of cation arrangement on band gap. *Physical Review B*, 83(20), may 2011.
- [15] A. F. Santander-Syro, O. Copie, T. Kondo, F. Fortuna, S. Pailhès, R. Weht, X. G. Qiu, F. Bertran, A. Nicolaou, A. Taleb-Ibrahimi, P. Le Fèvre, G. Herranz, M. Bibes, N. Reyren, Y. Apertet, P. Lecoeur, A. Barthélémy, and M. J. Rozenberg. Two-dimensional electron gas with universal subbands at the surface of SrTiO₃. *Nature*, 469(7329):189–193, jan 2011.
- [16] W. Meevasana, P. D. C. King, R. H. He, S-K. Mo, M. Hashimoto, A. Tamai, P. Songsiriritthigul, F. Baumberger, and Z-X. Shen. Creation and control of a two-dimensional electron liquid at the bare SrTiO₃ surface. *Nature Materials*, 10(2):114–118, jan 2011.
- [17] Michael Sing, Harald O. Jeschke, Frank Lechermann, Roser Valenti, and Ralph Claessen. Influence of oxygen vacancies on two-dimensional electron systems at SrTiO₃-based interfaces and surfaces. *The European Physical Journal Special Topics*, 226(11):2457–2475, jul 2017.
- [18] Sujuan Wu, Xingsen Gao, Minghui Qin, J.-M. Liu, and Shejun Hu. SrTiO₃ modified TiO₂ electrodes and improved dye-sensitized TiO₂ solar cells. *Applied Physics Letters*, 99(4):042106, jul 2011.
- [19] J.W. Liu, G. Chen, Z.H. Li, and Z.G. Zhang. Electronic structure and visible light photocatalysis water splitting property of chromium-doped SrTiO₃. *Journal of Solid State Chemistry*, 179(12):3704–3708, dec 2006.
- [20] Fei Li, Kai Yu, Lan-Lan Lou, Zhiqian Su, and Shuangxi Liu. Theoretical and experimental study of La/Ni co-doped SrTiO₃ photocatalyst. *Materials Science and Engineering: B*, 172(2):136–141, aug 2010.
- [21] Ryo Niishiro, Hideki Kato, and Akihiko Kudo. Nickel and either tantalum or niobium-codoped TiO₂ and SrTiO₃ photocatalysts with visible-light response for H₂ or O₂ evolution from aqueous solutions. *Physical Chemistry Chemical Physics*, 7(10):2241, 2005.
- [22] H. W. Jang, A. Kumar, S. Denev, M. D. Biegalski, P. Maksymovych, C. W. Bark, C. T. Nelson, C. M. Folkman, S. H. Baek, N. Balke, C. M. Brooks, D. A. Tenne, D. G. Schlom,

- L. Q. Chen, X. Q. Pan, S. V. Kalinin, V. Gopalan, and C. B. Eom. Ferroelectricity in strain-free SrTiO₃ thin films. *Physical Review Letters*, 104(19), may 2010.
- [23] Wei wei Peng, Robert Tétot, Gang Niu, Emilie Amzallag, Bertrand Vilquin, Jean-Blaise Brubach, and Pascale Roy. Room-temperature soft mode and ferroelectric like polarization in SrTiO₃ ultrathin films: Infrared and ab initio study. *Scientific Reports*, 7(1), may 2017.
- [24] M. E. Guzhva, V. V. Lemanov, P. A. Markovin, and W. Kleemann. Critical concentrations in Ba-doped incipient ferroelectric SrTiO₃. *Physics of the Solid State*, 39(4):618–624, apr 1997.
- [25] Ming Liu, Chunrui Ma, Gregory Collins, Jian Liu, Chonglin Chen, Andy D Alemayehu, Guru Subramanyam, Ying Ding, Jianghua Chen, Chao Dai, Yuan Lin, and Melanie W Cole. Ferroelectric BaTiO₃/SrTiO₃ multilayered thin films for room-temperature tunable microwave elements. *Nanoscale Research Letters*, 8(1):338, 2013.
- [26] Xin-Long Dong, Kun-Hua Zhang, and Ming-Xiang Xu. First-principles study of electronic structure and magnetic properties of SrTi_{1-x}M_xO₃ (M = Cr, Mn, Fe, Co, or Ni). *Frontiers of Physics*, 13(5), jul 2018.
- [27] R. Siddheswaran, Pavol Sutta, Petr Novak, Marie Netrvalova, Ales Hendrych, and Ondrej Zivotsky. In-situ x-ray diffraction studies and magneto-optic kerr effect on RF sputtered thin films of BaTiO₃ and Co, Nb co-doped BaTiO₃. *Ceramics International*, 42(3):3882–3887, feb 2016.
- [28] Jürgen Braun, Jan Minar, and Hubert Ebert. Correlation, temperature and disorder: Recent developments in the one-step description of angle-resolved photoemission. *Physics Reports*, 740:1–34, apr 2018.
- [29] Jan Minar. Correlation effects in transition metals and their alloys studied using the fully self-consistent KKR-based LSDA DMFT scheme. *Journal of Physics: Condensed Matter*, 23(25):253201, jun 2011.
- [30] C N R Rao. Transition metal oxides. *Annual Review of Physical Chemistry*, 40(1):291–326, oct 1989.
- [31] H. H. Kung. *Transition Metal Oxides: Surface Chemistry and Catalysis*, volume 45. Elsevier Science, 1st edition edition, 1989.
- [32] Yougui Liao. Practical electron microscopy and database, 2018.
- [33] K. van Benthem, C. Elsässer, and R. H. French. Bulk electronic structure of SrTiO₃: Experiment and theory. *Journal of Applied Physics*, 90(12):6156–6164, dec 2001.
- [34] F. Ann Walker. Magnetic spectroscopic (EPR, ESEEM, mössbauer, MCD and NMR) studies of low-spin ferriheme centers and their corresponding heme proteins. *Coordination Chemistry Reviews*, 185-186:471–534, may 1999.

- [35] V. M. Goldschmidt. Die gesetze der krystallochemie. *Die Naturwissenschaften*, 14(21):477–485, may 1926.
- [36] R. von Helmolt, J. Wecker, B. Holzapfel, L. Schultz, and K. Samwer. Giant negative magnetoresistance in perovskite like $\text{La}_2/3\text{Ba}_1/3\text{MnO}_x$ ferromagnetic films. *Physical Review Letters*, 71(14):2331–2333, oct 1993.
- [37] Myron B. Salamon and Marcelo Jaime. The physics of manganites: Structure and transport. *Reviews of Modern Physics*, 73(3):583–628, aug 2001.
- [38] Silvia Picozzi and Claude Ederer. First principles studies of multiferroic materials. *Journal of Physics: Condensed Matter*, 21(30):303201, jul 2009.
- [39] Fumihiko Fukunaga and Nobuo Tsuda. On the magnetism and electronic conduction of itinerant magnetic system $\text{Ca}_{1-x}\text{Sr}_x\text{RuO}_3$. *Journal of the Physical Society of Japan*, 63(10):3798–3807, oct 1994.
- [40] J. G. Bednorz and K. A. Muller. Possible high T_c superconductivity in the BaLaCuO system. *Zeitschrift fur Physik B Condensed Matter*, 64(2):189–193, jun 1986.
- [41] J. Z. Sun and A. Gupta. Spin-dependent transport and low-field magnetoresistance in doped manganites. *Annual Review of Materials Science*, 28(1):45–78, aug 1998.
- [42] Manuel Bibes and Agns Barthelemy. Oxide spintronics. *IEEE Transactions on Electron Devices*, 54(5):1003–1023, may 2007.
- [43] Tsutomu Miyasaka. Perovskite photovoltaics: Rare functions of organo lead halide in solar cells and optoelectronic devices. *Chemistry Letters*, 44(6):720–729, jun 2015.
- [44] Shan Chen and Gaoquan Shi. Two-dimensional materials for halide perovskite-based optoelectronic devices. *Advanced Materials*, 29(24):1605448, mar 2017.
- [45] Matthias Opel. Spintronic oxides grown by laser-MBE. *Journal of Physics D: Applied Physics*, 45(3):033001, dec 2011.
- [46] Manuel Bibes, Javier E. Villegas, and Agnès Barthélémy. Ultrathin oxide films and interfaces for electronics and spintronics. *Advances in Physics*, 60(1):5–84, feb 2011.
- [47] Huiyuan Zhu, Pengfei Zhang, and Sheng Dai. Recent advances of lanthanum-based perovskite oxides for catalysis. *ACS Catalysis*, 5(11):6370–6385, sep 2015.
- [48] G. Srinivasan, E. T. Rasmussen, B. J. Levin, and R. Hayes. Magnetoelectric effects in bilayers and multilayers of magnetostrictive and piezoelectric perovskite oxides. *Physical Review B*, 65(13), mar 2002.
- [49] Ilya Grinberg, D. Vincent West, Maria Torres, Gaoyang Gou, David M. Stein, Liyan Wu, Guannan Chen, Eric M. Gallo, Andrew R. Akbashev, Peter K. Davies, Jonathan E. Spanier, and Andrew M. Rappe. Perovskite oxides for visible-light-absorbing ferroelectric and photovoltaic materials. *Nature*, 503(7477):509–512, nov 2013.

- [50] Zhengguo Xiao, Yongbo Yuan, Yuchuan Shao, Qi Wang, Qingfeng Dong, Cheng Bi, Pankaj Sharma, Alexei Gruverman, and Jinsong Huang. Giant switchable photovoltaic effect in organometal trihalide perovskite devices. *Nature Materials*, 14(2):193–198, dec 2014.
- [51] Harold H. Kung. *Transition Metal Oxides: Surface Chemistry and Catalysis*. Elsevier science publishers B.V., 1989.
- [52] Ryan B. Comes, Sergey Y. Smolin, Tiffany C. Kaspar, Ran Gao, Brent A. Apgar, Lane W. Martin, Mark E. Bowden, Jason B. Baxter, and Scott A. Chambers. Visible light carrier generation in co-doped epitaxial titanate films. *Applied Physics Letters*, 106(9):092901, mar 2015.
- [53] Nicola A. Hill. Density functional studies of multiferroic magnetoelectrics. *Annual Review of Materials Research*, 32(1):1–37, aug 2002.
- [54] Behmaz Rahmati Kalkhoran. *Microstructural studies on the reoxidation behaviour of Nb-doped SrTiO₃ ceramics*. PhD thesis, Max-planck-Institut für metallforschung Stuttgart, 2004.
- [55] Farrel W. Lytle. X-ray diffractometry of low-temperature phase transformations in strontium titanate. *Journal of Applied Physics*, 35(7):2212–2215, jul 1964.
- [56] K. C. Park and J. H. Cho. Electric field dependence of ferroelectric phase transition in epitaxial SrTiO₃ films on SrRuO₃ and La_{0.5}Sr_{0.5}CoO₃. *Applied Physics Letters*, 77(3):435–437, jul 2000.
- [57] J. H. Haeni, P. Irvin, W. Chang, R. Uecker, P. Reiche, Y. L. Li, S. Choudhury, W. Tian, M. E. Hawley, B. Craigo, A. K. Tagantsev, X. Q. Pan, S. K. Streiffer, L. Q. Chen, S. W. Kirchoefer, J. Levy, and D. G. Schlom. Room-temperature ferroelectricity in strained SrTiO₃. *Nature*, 430(7001):758–761, aug 2004.
- [58] W. D. Rice, P. Ambwani, M. Bombeck, J. D. Thompson, G. Haugstad, C. Leighton, and S. A. Crooker. Persistent optically induced magnetism in oxygen-deficient strontium titanate. *Nature Materials*, 13(5):481–487, mar 2014.
- [59] S. S. Rao, Y. F. Lee, J. T. Prater, A. I. Smirnov, and J. Narayan. Laser annealing induced ferromagnetism in SrTiO₃ single crystal. *Applied Physics Letters*, 105(4):042403, jul 2014.
- [60] Z. Wang, S. McKeown Walker, A. Tamai, Y. Wang, Z. Ristic, F. Y. Bruno, A. de la Torre, S. Riccò, N. C. Plumb, M. Shi, P. Hlawenka, J. Sánchez-Barriga, A. Varykhalov, T. K. Kim, M. Hoesch, P. D. C. King, W. Meevasana, U. Diebold, J. Mesot, B. Moritz, T. P. Devereaux, M. Radovic, and F. Baumberger. Tailoring the nature and strength of electron–phonon interactions in the SrTiO₃(001) 2D electron liquid. *Nature Materials*, 15(8):835–839, apr 2016.
- [61] C. Mitra, C. Lin, J. Robertson, and Alexander A. Demkov. Electronic structure of oxygen vacancies in SrTiO₃ and LaAlO₃. *Physical Review B*, 86(15), oct 2012.

- [62] S. McKeown Walker, A. de la Torre, F. Y. Bruno, A. Tamai, T. K. Kim, M. Hoesch, M. Shi, M. S. Bahramy, P. D. C. King, and F. Baumberger. Control of a two-dimensional electron gas on SrTiO₃(111) by atomic oxygen. *Physical Review Letters*, 113(17), oct 2014.
- [63] Sara Gonzalez, Claire Mathieu, Olivier Copie, Vitaliy Feyer, Claus M. Schneider, and Nicholas Barrett. Room temperature 2D electron gas at the (001)-SrTiO₃ surface. *Applied Physics Letters*, 111(18):181601, oct 2017.
- [64] N. C. Plumb, M. Salluzzo, E. Razzoli, M. Månsson, M. Falub, J. Krempasky, C. E. Matt, J. Chang, M. Schulte, J. Braun, H. Ebert, J. Minár, B. Delley, K.-J. Zhou, T. Schmitt, M. Shi, J. Mesot, L. Patthey, and M. Radović. Mixed dimensionality of confined conducting electrons in the surface region of SrTiO₃. *Physical Review Letters*, 113(8), aug 2014.
- [65] K.W. Blazey and H. Weibel. Optical absorption spectra of reduced transition-metal ion-doped SrTiO₃. *Journal of Physics and Chemistry of Solids*, 45(8-9):917–922, jan 1984.
- [66] I. A. Sluchinskaya, A. I. Lebedev, and A. Erko. Structural position and charge state of nickel in SrTiO₃. *Physics of the Solid State*, 56(3):449–455, mar 2014.
- [67] P. Koidl, K. W. Blazey, W. Berlinger, and K. A. Müller. Photochromism in Ni-doped SrTiO₃. *Physical Review B*, 14(7):2703–2708, oct 1976.
- [68] K. A. Müller, W. Berlinger, and R. S. Rubins. Observation of two charged states of a nickel-oxygen vacancy pair in SrTiO₃ by paramagnetic resonance. *Physical Review*, 186(2):361–371, oct 1969.
- [69] B. W. Faughnan. Photochromism in transition-metal-doped SrTiO₃. *Physical Review B*, 4(10):3623–3636, nov 1971.
- [70] A. I. Lebedev and I. A. Sluchinskaya. On the nature of change in Ni oxidation state in BaTiO₃-SrTiO₃ system. *Ferroelectrics*, 501(1):1–8, sep 2016.
- [71] Andrew M. Beale, Michael Paul, Gopinathan Sankar, Richard J. Oldman, C. Richard A. Catlow, Sam French, and Martin Fowles. Combined experimental and computational modelling studies of the solubility of nickel in strontium titanate. *Journal of Materials Chemistry*, 19(25):4391, 2009.
- [72] Attaphol Karaphun, Sitchai Hunpratub, Sumalin Phokha, Thanin Putjuso, and Ekaphan Swatsitang. Characterization and magnetic properties of SrTi_{1-x}Ni_xO₃ nanoparticles prepared by hydrothermal method. *Physica B: Condensed Matter*, 504:31–38, jan 2017.
- [73] F. J. Morin and J. R. Oliver. Energy levels of iron and aluminum in SrTiO₃. *Physical Review B*, 8(12):5847–5854, dec 1973.
- [74] Rotraut Merkle and Joachim Maier. How is oxygen incorporated into oxides? A comprehensive kinetic study of a simple solid-state reaction with SrTiO₃ as a model material. *Angewandte Chemie International Edition*, 47(21):3874–3894, may 2008.

- [75] Xin Zhou, Jingying Shi, and Can Li. Effect of metal doping on electronic structure and visible light absorption of SrTiO₃ and NaTaO₃ (Metal = Mn, Fe, and Co). *The Journal of Physical Chemistry C*, 115(16):8305–8311, mar 2011.
- [76] V. E. Alexandrov, J. Maier, and R. A. Evarestov. Ab initio study of SrFe_xTi_{1-x}O₃: Jahn-teller distortion and electronic structure. *Physical Review B*, 77(7), feb 2008.
- [77] Evgeny Blokhin, Eugene Kotomin, Alexei Kuzmin, Juris Purans, Robert Evarestov, and Joachim Maier. Theoretical modeling of the complexes of iron impurities and oxygen vacancies in SrTiO₃. *Applied Physics Letters*, 102(11):112913, mar 2013.
- [78] J. Kubacki, D. Kajewski, J. Goraus, K. Szot, A. Koehl, Ch. Lenser, R. Dittmann, and J. Szade. Impact of Fe doping on the electronic structure of SrTiO₃ thin films determined by resonant photoemission. *The Journal of Chemical Physics*, 148(15):154702, apr 2018.
- [79] Ch. Lenser, A. Kuzmin, J. Purans, A. Kalinko, R. Waser, and R. Dittmann. Probing the oxygen vacancy distribution in resistive switching Fe-SrTiO₃ metal-insulator-metal-structures by micro-x ray absorption near-edge structure. *Journal of Applied Physics*, 111(7):076101, apr 2012.
- [80] J. Szade, K. Szot, M. Kulpa, J. Kubacki, Ch. Lenser, R. Dittmann, and R. Waser. Electronic structure of epitaxial Fe-doped SrTiO₃ thin films. *Phase Transitions*, 84(5-6):489–500, may 2011.
- [81] Yiqing Bi, Muhammad Fahad Ehsan, Yan Huang, Jiarui Jin, and Tao He. Synthesis of Cr-doped SrTiO₃ photocatalyst and its application in visible-light-driven transformation of CO₂ into CH₄. *Journal of CO₂ Utilization*, 12:43–48, dec 2015.
- [82] Jiangping Jing, Zhuoyuan Chen, Yuyu Bu, Mengmeng Sun, Wenqiang Zheng, and Weibing Li. Significantly enhanced photoelectrochemical cathodic protection performance of hydrogen treated Cr-doped SrTiO₃ by Cr₆ reduction and oxygen vacancy modification. *Electrochimica Acta*, 304:386–395, may 2019.
- [83] S.F. Alvarado, F. La Mattina, and J.G. Bednorz. Electroluminescence in SrTiO₃:Cr single-crystal nonvolatile memory cells. *Applied Physics A*, 89(1):85–89, jul 2007.
- [84] Agnieszka Łącz, Łukasz Łańcucki, Radosław Lach, Bartosz Kamecki, and Ewa Drożdż. Structural and electrical properties of Cr-doped SrTiO₃ porous materials. *International Journal of Hydrogen Energy*, 43(18):8999–9005, may 2018.
- [85] Tao Wan, Bo Qu, Haiwei Du, Xi Lin, Peiyuan Guan, Qianru Lin, Nan Chen, Thiam Teck Tan, Tao Hang, and Dewei Chu. Tunable resistance switching in solution processed chromium-doped strontium titanate nanoparticles films. *Journal of Colloid and Interface Science*, 494:178–184, may 2017.
- [86] A. Beck, J. G. Bednorz, Ch. Gerber, C. Rossel, and D. Widmer. Reproducible switching effect in thin oxide films for memory applications. *Applied Physics Letters*, 77(1):139–141, jul 2000.

- [87] C. Rossel, G. I. Meijer, D. Brémaud, and D. Widmer. Electrical current distribution across a metal–insulator–metal structure during bistable switching. *Journal of Applied Physics*, 90(6):2892–2898, sep 2001.
- [88] Frank Maldonado, Luz Maza, and Arvids Stashans. Electronic properties of Cr-, B-doped and codoped SrTiO₃. *Journal of Physics and Chemistry of Solids*, 100:1–8, jan 2017.
- [89] Wei Wei, Ying Dai, Meng Guo, Lin Yu, and Baibiao Huang. Density functional characterization of the electronic structure and optical properties of N-doped, La-doped, and N/La-codoped SrTiO₃. *The Journal of Physical Chemistry C*, 113(33):15046–15050, jul 2009.
- [90] Song-Yin Zhang, Yuan-Hua Lin, Ce-Wen Nan, Rongjuan Zhao, and Jinliang He. Magnetic and electrical properties of (Mn, La)-codoped SrTiO₃ thin films. *Journal of the American Ceramic Society*, 91(10):3263–3266, oct 2008.
- [91] E. Earnshaw Earnshaw A Norman Neill Greenwood, Alan Earnshaw. *Chemistry of the Elements*. Butterworth-Heinemann, 1984.
- [92] S. Hüfner. Electronic structure of NiO and related 3d-transition-metal compounds. *Advances in Physics*, 43(2):183–356, apr 1994.
- [93] S. Hüfner and T. Riesterer. Electronic structure of NiO. *Physical Review B*, 33(10):7267–7269, may 1986.
- [94] M. A. van Veenendaal and G. A. Sawatzky. Nonlocal screening effects in 2p x-ray photoemission spectroscopy core-level line shapes of transition metal compounds. *Physical Review Letters*, 70(16):2459–2462, apr 1993.
- [95] Arata Tanaka and Takeo Jo. Resonant 3d, 3p and 3s photoemission in transition metal oxides predicted at 2p threshold. *Journal of the Physical Society of Japan*, 63(7):2788–2807, jul 1994.
- [96] Hufner Stefan. *Photoelectron spectroscopy: principles and applications*. Springer, 2003.
- [97] St Uhlenbrock, C Scharfschwerdt, M Neumann, G Illing, and H J Freund. The influence of defects on the Ni 2p and O 1s XPS of NiO. *Journal of Physics: Condensed Matter*, 4(40):7973–7978, oct 1992.
- [98] L. Soriano, I. Preda, A. Gutiérrez, S. Palacín, M. Abbate, and A. Vollmer. Surface effects in the Ni 2p x-ray photoemission spectra of NiO. *Physical Review B*, 75(23), jun 2007.
- [99] I. Preda, A. Gutiérrez, M. Abbate, F. Yubero, J. Méndez, L. Alvarez, and L. Soriano. Interface effects in the Ni 2p x-ray photoelectron spectra of NiO thin films grown on oxide substrates. *Physical Review B*, 77(7), feb 2008.
- [100] O Tjernberg, S Söderholm, T Rogelet, UO Karlsson, M Qvarford, I Lindau, C-O Almbladh, and LJ Hellbom. Angle resolved photoemission on NiO: on the nature of the valence band. *Vacuum*, 46(8-10):1215–1218, aug 1995.

- [101] O. Tjernberg, S. Söderholm, U. O. Karlsson, G. Chiaia, M. Qvarford, H. Nylén, and I. Lindau. Resonant photoelectron spectroscopy on NiO. *Physical Review B*, 53(15):10372–10376, apr 1996.
- [102] Motohiko Nakamura, Yasutaka Takata, and Nobuhiro Kosugi. Resonant Ni 3p and 3s photoemission for the Ni 2p core-excitation in NiO. *Journal of Electron Spectroscopy and Related Phenomena*, 78:115–118, may 1996.
- [103] G. van der Laan, J. Zaanen, G. A. Sawatzky, R. Karnatak, and J.-M. Esteva. Comparison of x-ray absorption with x-ray photoemission of nickel dihalides and NiO. *Physical Review B*, 33(6):4253–4263, mar 1986.
- [104] J. Minár, J. Braun, and H. Ebert. Correlation effects in magnetic materials: An ab initio investigation on electronic structure and spectroscopy. *Journal of Electron Spectroscopy and Related Phenomena*, 189:129–136, aug 2013.
- [105] Jan Minar. *Multiple Scattering Theory for Spectroscopies, chapter 26*. Springer International Publishing, 2018.
- [106] J. Minár, H. Ebert, and L. Chioncel. A self-consistent, relativistic implementation of the LSDA+DMFT method. *The European Physical Journal Special Topics*, 226(11):2477–2498, jul 2017.
- [107] H. Hertz. Ueber einen einfluss des ultravioletten lichtes auf die electrische entladung. *Annalen der Physik und Chemie*, 267(8):983–1000, 1887.
- [108] A. Einstein. Über einen die erzeugung und verwandlung des lichtes betreffenden heuristischen gesichtspunkt. *Annalen der Physik*, 322(6):132–148, 1905.
- [109] W.E. Spicer C.N. Berglund. *Physical Review*, A 136:1030 and 1044, 1964.
- [110] R.F. Egerton. *Electron Energy-Loss Spectroscopy in the Electron Microscope (The Language of Science)*. Springer, 1996.
- [111] M. P. Seah and W. A. Dench. Quantitative electron spectroscopy of surfaces: A standard data base for electron inelastic mean free paths in solids. *Surface and Interface Analysis*, 1(1):2–11, feb 1979.
- [112] Gabriel Landolt. *Spin-and angle-resolved photoelectron spectroscopy on topological insulators and bulk Rashba systems*. PhD thesis, 2014.
- [113] F. J. Garcia de Abajo, C. S. Fadley, and M. A. Van Hove. Multiatom resonant photoemission: Theory and systematics. *Physical Review Letters*, 82(20):4126–4129, may 1999.
- [114] U. Fano. Effects of configuration interaction on intensities and phase shifts. *Physical Review*, 124(6):1866–1878, dec 1961.
- [115] N. Mårtensson, M. Weinelt, O. Karis, M. Magnuson, N. Wassdahl, A. Nilsson, J. Stöhr, and M. Samant. Coherent and incoherent processes in resonant photoemission. *Applied Physics A: Materials Science & Processing*, 65(2):159–167, aug 1997.

- [116] T. Kashiwakura, S. Suzuki, T. Okane, S. Sato, T. Kinoshita, A. Kakizaki, T. Ishii, Y. Isikawa, H. Yamagami, and A. Hasegawa. Resonant photoemission in CeNi single crystals. *Physical Review B*, 47(12):6885–6897, mar 1993.
- [117] Charles S. Fadley. The study of surface structures by photoelectron diffraction and auger electron diffraction. In *Synchrotron Radiation Research*, pages 421–518. Springer US, 1992.
- [118] D.P. Woodruff. Photoelectron diffraction. In *Reference Module in Materials Science and Materials Engineering*. Elsevier, 2016.
- [119] Didier Sébilleau. Basis-independent multiple-scattering theory for electron spectroscopies: General formalism. *Physical Review B*, 61(20):14167–14178, may 2000.
- [120] Charles S. Fadley. Angle-resolved x-ray photoelectron spectroscopy. *Progress in Surface Science*, 16(3):275–388, jan 1984.
- [121] S. Kono, C. S. Fadley, N. F. T. Hall, and Z. Hussain. Azimuthal anisotropy in deep core-level x-ray photoemission from an adsorbed atom: Oxygen on copper(001). *Physical Review Letters*, 41(2):117–120, jul 1978.
- [122] L. G. Petersson, S. Kono, N. F. T. Hall, C. S. Fadley, and J. B. Pendry. Determination of adsorbate geometries from intramolecular scattering in deep-core-level x-ray photoemission: CO on Ni(001). *Physical Review Letters*, 42(23):1545–1548, jun 1979.
- [123] C.S. Fadley, S. Kono, L.-G. Petersson, S.M. Goldberg, N.F.T. Hall, J.T. Lloyd, and Z. Hussain. Determination of surface geometries from angular distributions of deep-core-level x-ray photoelectrons. *Surface Science*, 89(1-3):52–63, jan 1979.
- [124] Vladimir Strocov. Electron momentum calculations, 2017.
- [125] Matthias Muntwiler, Jun Zhang, Roland Stania, Fumihiko Matsui, Peter Oberta, Uwe Flechsig, Luc Patthey, Christoph Quitmann, Thilo Glatzel, Roland Widmer, Ernst Meyer, Thomas A. Jung, Philipp Aebi, Roman Fasel, and Thomas Greber. Surface science at the PEARL beamline of the swiss light source. *Journal of Synchrotron Radiation*, 24(1):354–366, jan 2017.
- [126] Stephan Muff. *Manipulation of the Two-Dimensional States at Titanates Surfaces studied by ARPES*. PhD thesis, Ecole Polytechnique Federale de Lausanne, 2017.
- [127] Graham K. Hubler Douglas B. Chrisey. *Pulsed Laser Deposition of Thin Films*. Wiley-Interscience, 1994.
- [128] M. Kawasaki, K. Takahashi, T. Maeda, R. Tsuchiya, M. Shinohara, O. Ishiyama, T. Yonezawa, M. Yoshimoto, and H. Koinuma. Atomic control of the SrTiO₃ crystal surface. *Science*, 266(5190):1540–1542, dec 1994.
- [129] Gertjan Koster, Boike L. Kropman, Guus J. H. M. Rijnders, Dave H. A. Blank, and Horst Rogalla. Quasi-ideal strontium titanate crystal surfaces through formation of strontium hydroxide. *Applied Physics Letters*, 73(20):2920–2922, nov 1998.

- [130] C. DAVISSON and L. H. GERMER. The scattering of electrons by a single crystal of nickel. *Nature*, 119(2998):558–560, apr 1927.
- [131] Hans Lüth. *Solid Surfaces, Interfaces and Thin Films*. Springer Berlin Heidelberg, 2010.
- [132] W.N. Unertl. *Physical Structure. Handbook of Surface Science*. North Holland, 1996.
- [133] Bartosz Slomski. *A Spin-and Angle-resolved Photoemission Study of the Rashba-Bychkov Effect in Lead Quantum Well States*. PhD thesis, 2013.
- [134] Wolfgang Braun. *Reflection high-energy electron diffraction studies of semiconductor interfaces during molecular beam epitaxy growth*. PhD thesis, 1996.
- [135] *Horizons of Quantum Chemistry*. Springer Netherlands, 2011.
- [136] P. Geerlings, F. De Proft, and W. Langenaeker. Conceptual density functional theory. *Chemical Reviews*, 103(5):1793–1874, may 2003.
- [137] Giovanni Vignale John F. Dobson and Mukunda P. Das, editors. *Electronic Density Functional Theory: Recent Progress and New Directions*. Springer science, 1996.
- [138] N Papanikolaou, R Zeller, and P H Dederichs. Conceptual improvements of the KKR method. *Journal of Physics: Condensed Matter*, 14(11):2799–2823, mar 2002.
- [139] R. Zeller, P. H. Dederichs, B. Újfalussy, L. Szunyogh, and P. Weinberger. Theory and convergence properties of the screened Korringa-Kohn-Rostoker method. *Physical Review B*, 52(12):8807–8812, sep 1995.
- [140] J. Braun. The theory of angle-resolved ultraviolet photoemission and its applications to ordered materials. *Rep. Prog. Phys*, 59:1267–1338, 1996.
- [141] J. B. Pendry. Low energy electron diffraction. *Surf. Sci.*, 57:679, 1976.
- [142] Andreas Görling. Density-functional theory beyond the Hohenberg-Kohn theorem. *Physical Review A*, 59(5):3359–3374, may 1999.
- [143] Erich Runge and E. K. U. Gross. Density-functional theory for time-dependent systems. *Physical Review Letters*, 52(12):997–1000, mar 1984.
- [144] M. Hussein. N. Assadi and Dorian A. H. Hanaor. Theoretical study on copper’s energetics and magnetism in TiO₂ polymorphs. *Journal of Applied Physics*, 113(23):233913, jun 2013.
- [145] Stefan Grimme. Semiempirical hybrid density functional with perturbative second-order correlation. *The Journal of Chemical Physics*, 124(3):034108, jan 2006.
- [146] Urs Zimmerli, Michele Parrinello, and Petros Koumoutsakos. Dispersion corrections to density functionals for water aromatic interactions. *The Journal of Chemical Physics*, 120(6):2693–2699, feb 2004.

- [147] Stefan Grimme. Accurate description of van der waals complexes by density functional theory including empirical corrections. *Journal of Computational Chemistry*, 25(12):1463–1473, 2004.
- [148] Alexandre Tkatchenko and Matthias Scheffler. Accurate molecular Van Der Waals interactions from ground-state electron density and free-atom reference data. *Physical Review Letters*, 102(7), feb 2009.
- [149] P. Hohenberg and W. Kohn. Inhomogeneous electron gas. *Physical Review*, 136(3B):B864–B871, nov 1964.
- [150] W. Kohn and L. J. Sham. Self-consistent equations including exchange and correlation effects. *Physical Review*, 140(4A):A1133–A1138, nov 1965.
- [151] Kieron Burke and Lucas O. Wagner. Dft in a nutshell. *International Journal of Quantum Chemistry*, 113(2):96–101, jul 2012.
- [152] John P. Perdew, Adrienn Ruzsinszky, Jianmin Tao, Viktor N. Staroverov, Gustavo E. Scuseria, and Gabor I. Csonka. Prescription for the design and selection of density functional approximations: More constraint satisfaction with fewer fits. *The Journal of Chemical Physics*, 123(6):062201, aug 2005.
- [153] Teepanis Chachiyu. Communication: Simple and accurate uniform electron gas correlation energy for the full range of densities. *The Journal of Chemical Physics*, 145(2):021101, jul 2016.
- [154] Richard J. Fitzgerald. A simpler ingredient for a complex calculation. *Physics Today*, 69(9):20–20, sep 2016.
- [155] Ukrit Jitropas and Chung-Hao Hsu. Study of the first-principles correlation functional in the calculation of silicon phonon dispersion curves. *Japanese Journal of Applied Physics*, 56(7):070313, jun 2017.
- [156] Axel D. Becke. Perspective: Fifty years of density-functional theory in chemical physics. *The Journal of Chemical Physics*, 140(18):18A301, may 2014.
- [157] John P. Perdew, J. A. Chevary, S. H. Vosko, Koblar A. Jackson, Mark R. Pederson, D. J. Singh, and Carlos Fiolhais. Atoms, molecules, solids, and surfaces: Applications of the generalized gradient approximation for exchange and correlation. *Physical Review B*, 46(11):6671–6687, sep 1992.
- [158] A. D. Becke. Density-functional exchange-energy approximation with correct asymptotic behavior. *Physical Review A*, 38(6):3098–3100, sep 1988.
- [159] David C. Langreth and M. J. Mehl. Beyond the local-density approximation in calculations of ground-state electronic properties. *Physical Review B*, 28(4):1809–1834, aug 1983.
- [160] J Korrynga. On the calculation of the energy of a bloch wave in a metal. *Physica*, 13(6-7):392–400, aug 1947.

- [161] W. Kohn and N. Rostoker. Solution of the schrödinger equation in periodic lattices with an application to metallic lithium. *Physical Review*, 94(5):1111–1120, jun 1954.
- [162] J. S. Faulkner and G. M. Stocks. Calculating properties with the coherent-potential approximation. *Physical Review B*, 21(8):3222–3244, apr 1980.
- [163] J. Minar, J. Braun, S. Mankovsky, and H. Ebert. Calculation of angle-resolved photo emission spectra within the one-step model of photo emission - recent developments. *Journal of Electron Spectroscopy and Related Phenomena*, 184(3-6):91–99, apr 2011.
- [164] Arthur Ernst. *Multiple-scattering theory: new developments and applications*. PhD thesis, Naturwissenschaftliche Fakultät II Chemie und Physik der Martin-Luther-Universität Halle-Wittenberg, 1968.
- [165] Stanley Raimes. *Many-Electron Theory*. North-Holland Publishing Company Amsterdam-London, 1972.
- [166] Paul Soven. Coherent-potential model of substitutional disordered alloys. *Physical Review*, 156(3):809–813, apr 1967.
- [167] L. Bellaïche and David Vanderbilt. Virtual crystal approximation revisited: Application to dielectric and piezoelectric properties of perovskites. *Physical Review B*, 61(12):7877–7882, mar 2000.
- [168] A. Bansil. Coherent-potential and averaged-matrix approximations for disordered muffin-tin alloys. i. formalism. *Physical Review B*, 20(10):4025–4034, nov 1979.
- [169] J.S. Faulkner. The modern theory of alloys. *Progress in Materials Science*, 27(1-2):1–187, jan 1982.
- [170] Didier Sébilleau, Keisuke Hatada, and Hubert Ebert, editors. *Multiple Scattering Theory for Spectroscopies*. Springer International Publishing, 2018.
- [171] J Minár, S Mankovsky, O Šipr, D Benea, and H Ebert. Correlation effects in fcc-Fe_xNi_{1-x} alloys investigated by means of the KKR-CPA. *Journal of Physics: Condensed Matter*, 26(27):274206, jun 2014.
- [172] J. Minár, L. Chioncel, A. Perlov, H. Ebert, M. I. Katsnelson, and A. I. Lichtenstein. Multiple-scattering formalism for correlated systems: A KKR-DMFT approach. *Physical Review B*, 72(4), jul 2005.
- [173] J. Minar. Theoretical description of ARPES: The one-step model. volume 4. Modeling and simulation, Forschungszentrum Julich, 2014.
- [174] J. M. MacLaren, S. Crampin, D. D. Vvedensky, and J. B. Pendry. Layer korringa-kohn-rostoker technique for surface and interface electronic properties. *Physical Review B*, 40(18):12164–12175, dec 1989.
- [175] G. Borstel. Theoretical aspects of photoemission. *Applied Physics A, Solids and Surfaces*, 38:193–204, 1985.

- [176] J. Braun M. Grass and G. Borstel. New developments in the theory of photoemission. *Prog. Surf. Sci.*, 46:107–122, 1994.
- [177] BA. Movchan and AV. Demchishin. Study of structure and properties of thick vacuum condensates of nickel, titanium, tungsten, aluminium oxide and zirconium dioxide. *PHYSICS OF METALS AND METALLOGRAPHY-USSR*, 28:83, 1969.
- [178] John A. Thornton. Influence of apparatus geometry and deposition conditions on the structure and topography of thick sputtered coatings. *Journal of Vacuum Science and Technology*, 11(4):666–670, jul 1974.
- [179] J. I. Langford. A rapid method for analysing the breadths of diffraction and spectral lines using the voigt function. *Journal of Applied Crystallography*, 11(1):10–14, feb 1978.
- [180] S.R. Stock B.D. Cullity. *Elements of X-Ray Diffraction*. Prentice-Hall, 2001.
- [181] David Ehre, Hagai Cohen, Vera Lyahovitskaya, and Igor Lubomirsky. X-ray photoelectron spectroscopy of amorphous and quasiamorphous phases of BaTiO₃ and SrTiO₃. *Physical Review B*, 77(18), may 2008.
- [182] Andrew P. Grosvenor, Mark C. Biesinger, Roger St.C. Smart, and N. Stewart McIntyre. New interpretations of XPS spectra of nickel metal and oxides. *Surface Science*, 600(9):1771–1779, may 2006.
- [183] M. Hennes, V. Schuler, X. Weng, J. Buchwald, D. Demaille, Y. Zheng, and F. Vidal. Growth of vertically aligned nanowires in metal–oxide nanocomposites: kinetic monte-carlo modeling versus experiments. *Nanoscale*, 10(16):7666–7675, 2018.
- [184] Peter E. Sobol John F. Moulder, William F. Stickle and Kenneth D. Bomben. *Handbook of X-ray Photoelectron Spectroscopy*. Perkin-Elmer Corporation, Physical Electronics Division, 6509 Flying Cloud Drive, Eden Prairie Minnesota 55344, United States of America.
- [185] M. Ghaffari, T. Liu, H. Huang, O.K. Tan, and M. Shannon. Investigation of local structure effect and x-ray absorption characteristics (EXAFS) of Fe (Ti) K-edge on photocatalyst properties of SrTi_(1-x)Fe_xO₃. *Materials Chemistry and Physics*, 136(2-3):347–357, oct 2012.
- [186] A. P. Grosvenor, B. A. Kobe, M. C. Biesinger, and N. S. McIntyre. Investigation of multiplet splitting of fe 2p XPS spectra and bonding in iron compounds. *Surface and Interface Analysis*, 36(12):1564–1574, 2004.
- [187] M. Moukassi, M. Gougeon, P. Steinmetz, B. Dupre, and C. Gleitzer. Hydrogen reduction of wustite single crystals doped with Mg, Mn, Ca, Al, and Si. *Metallurgical Transactions B*, 15(2):383–391, jun 1984.
- [188] M. Aronniemi, J. Sainio, and J. Lahtinen. Chemical state quantification of iron and chromium oxides using XPS: the effect of the background subtraction method. *Surface Science*, 578(1-3):108–123, mar 2005.

- [189] Mark C. Biesinger, Brad P. Payne, Andrew P. Grosvenor, Leo W.M. Lau, Andrea R. Gerson, and Roger St.C. Smart. Resolving surface chemical states in XPS analysis of first row transition metals, oxides and hydroxides: Cr, Mn, Fe, Co and Ni. *Applied Surface Science*, 257(7):2717–2730, jan 2011.
- [190] H Ebert, D Ködderitzsch, and J Minár. Calculating condensed matter properties using the KKR-green's function method—recent developments and applications. *Reports on Progress in Physics*, 74(9):096501, aug 2011.
- [191] B. T. Thole, R. D. Cowan, G. A. Sawatzky, J. Fink, and J. C. Fuggle. New probe for the ground-state electronic structure of narrow-band and impurity systems. *Physical Review B*, 31(10):6856–6858, may 1985.
- [192] S. P. Cramer, F. M. F. DeGroot, Y. Ma, C. T. Chen, F. Sette, C. A. Kipke, D. M. Eichhorn, M. K. Chan, W. H. Armstrong, E. Libby, G. Christou, S. Brooker, V. McKee, O. C. Mullins, and J. C. Fuggle. Ligand field strengths and oxidation states from manganese L-edge spectroscopy. *Journal of the American Chemical Society*, 113(21):7937–7940, oct 1991.
- [193] Piter S. Miedema and Frank M.F. de Groot. The iron l edges: Fe 2p x-ray absorption and electron energy loss spectroscopy. *Journal of Electron Spectroscopy and Related Phenomena*, 187:32–48, apr 2013.
- [194] Yu. S. Dedkov, A. S. Vinogradov, M. Fonin, C. König, D. V. Vyalikh, A. B. Preobrajenski, S. A. Krasnikov, E. Yu. Kleimenov, M. A. Nesterov, U. Rüdiger, S. L. Molodtsov, and G. Güntherodt. Correlations in the electronic structure of half-metallic ferromagnetic CrO₂ films: An x-ray absorption and resonant photoemission spectroscopy study. *Physical Review B*, 72(6), aug 2005.
- [195] C. Theil, J. van Elp, and F. Folkmann. Ligand field parameters obtained from and chemical shifts observed at the Cr L_{2,3}-edges. *Physical Review B*, 59(12):7931–7936, mar 1999.
- [196] J. J. Kim, H. Makino, M. Sakurai, D. C. Oh, T. Hanada, M. W. Cho, T. Yao, S. Emura, and K. Kobayashi. Structure and magnetic properties of Cr-doped GaN. *Journal of Vacuum Science & Technology B: Microelectronics and Nanometer Structures*, 23(3):1308, 2005.
- [197] S. A. Chambers and T. Droubay. Role of oxide ionicity in electronic screening at oxide/metal interfaces. *Physical Review B*, 64(7), jul 2001.
- [198] A. Ikeda, T. Nishimura, T. Morishita, and Y. Kido. Surface relaxation and rumpling of TiO₂-terminated SrTiO₃(001) determined by medium energy ion scattering. *Surface Science*, 433-435:520–524, aug 1999.
- [199] Tokihisa Hikita, Takashi Hanada, Masahiro Kudo, and Maki Kawai. Structure and electronic state of the TiO₂ and SrO terminated SrTiO₃(100) surfaces. *Surface Science*, 287-288:377–381, may 1993.
- [200] Zhi-Qiang Li, Jia-Lin Zhu, C. Q. Wu, Z. Tang, and Yoshiyuki Kawazoe. Relaxations of TiO₂- and SrO-terminated SrTiO₃(001) surfaces. *Physical Review B*, 58(12):8075–8078, sep 1998.

- [201] C. S. Koonce, Marvin L. Cohen, J. F. Schooley, W. R. Hosler, and E. R. Pfeiffer. Superconducting transition temperatures of semiconducting SrTiO₃. *Physical Review*, 163(2):380–390, nov 1967.
- [202] Anderson Janotti, Joel B. Varley, Minseok Choi, and Chris G. Van de Walle. Vacancies and small polarons in SrTiO₃. *Physical Review B*, 90(8), aug 2014.
- [203] Burak Himmetoglu, Andrea Floris, Stefano de Gironcoli, and Matteo Cococcioni. Hubbard-corrected DFT energy functionals: The LDA+U description of correlated systems. *International Journal of Quantum Chemistry*, 114(1):14–49, jul 2013.
- [204] Philipp Scheiderer. *Spectroscopy of Prototypical Thin Film Mott Materials*. PhD thesis, 2019.
- [205] Y Aiura, I Hase, H Bando, T Yasue, T Saitoh, and D.S Dessau. Photoemission study of the metallic state of lightly electron-doped SrTiO₃. *Surface Science*, 515(1):61–74, aug 2002.
- [206] C.M. Yim, M.B. Watkins, M.J. Wolf, C.L. Pang, K. Hermansson, and G. Thornton. Engineering polarons at a metal oxide surface. *Physical Review Letters*, 117(11), sep 2016.
- [207] Chaoyu Chen, José Avila, Emmanouil Frantzeskakis, Anna Levy, and Maria C. Asensio. Observation of a two-dimensional liquid of frohlich polarons at the bare SrTiO₃ surface. *Nature Communications*, 6(1), oct 2015.
- [208] J. B. Mann. ATOMIC STRUCTURE CALCULATIONS. II. HARTREE-FOCK WAVE-FUNCTIONS AND RADIAL EXPECTATION VALUES: HYDROGEN TO LAWRENCIUM. Technical report, jan 1968.
- [209] Jürg Osterwalder, Thomas Greber, Philipp Aebi, Roman Fasel, and Louis Schlapbach. Final-state scattering in angle-resolved ultraviolet photoemission from copper. *Physical Review B*, 53(15):10209–10216, apr 1996.
- [210] T. Greber, O. Raetz, T. J. Kreutz, P. Schwaller, W. Deichmann, E. Wetli, and J. Osterwalder. A photoelectron spectrometer for k-space mapping above the fermi level. *Review of Scientific Instruments*, 68(12):4549–4554, dec 1997.
- [211] M. Muntwiller. Pearl procedures, <https://gitlab.psi.ch/pearl-public/igor-procs>, 2016.
- [212] W. S. Cleveland et al. Software for locally-weighted regression, <http://www.netlib.org/a/dloess>, 1992.
- [213] D Sébilleau, R Gunnella, Z-Y Wu, S Di Matteo, and C R Natoli. Multiple-scattering approach with complex potential in the interpretation of electron and photon spectroscopies. *Journal of Physics: Condensed Matter*, 18(9):R175–R230, feb 2006.
- [214] Didier Sébilleau, Calogero Natoli, George M. Gavaza, Haifeng Zhao, Fabiana Da Pieve, and Keisuke Hatada. MsSpec-1.0: A multiple scattering package for electron spectroscopies in material science. *Computer Physics Communications*, 182(12):2567–2579, dec 2011.

- [215] C. R. Natoli and M. Benfatto. A unifying scheme of interpretation of x-ray absorption spectra based on the multiple scattering theory. *Le Journal de Physique Colloques*, 47(C8):C8-11-C8-23, dec 1986.
- [216] J. J. Rehr and R. C. Albers. Scattering-matrix formulation of curved-wave multiple-scattering theory: Application to x-ray-absorption fine structure. *Physical Review B*, 41(12):8139-8149, apr 1990.
- [217] M.-L. Xu, J. J. Barton, and M. A. Van Hove. Electron scattering by atomic chains: Multiple-scattering effects. *Physical Review B*, 39(12):8275-8283, apr 1989.
- [218] A. Pancotti, N. Barrett, L. F. Zagonel, and G. M. Vanacore. Multiple scattering x-ray photoelectron diffraction study of the SrTiO₃(100) surface. *Journal of Applied Physics*, 106(3):034104, aug 2009.

List of Own Publications

- **F. Alarab**, S. Tricot, B. Leikert, M. Muntwiler, C. Richter, R. Claessen, K. Hricovini, D. Sébilleau, and J. Minár. "Multiple scattering x-ray photoelectron diffraction study on Ni:SrTiO₃ (100) films", Physical Review B (in process).
- **F. Alarab**, K. Hricovini, B. Leikert, L. Nicolai, M. Fanciulli, O. Heckmann, C. Richter, L. Prušáková, Z. Jansa, P. Šutta, J. Rault, P. Lefevre, M. Muntwiler, R. Claessen, and J. Minár. "Photoemission study on pristine and Ni-doped SrTiO₃ thin films". Physical Review B (in process).
- **F. Alarab**, J. Minár, P. Šutta, L. Prušáková, R. Medlín, O. Heckmann, C. Richter, and K. Hricovini. "Study and characterization of SrTiO₃ surface", AIP Conference Proceedings **1996**, 020001 (2018).

List of Public Presentations

- Poster, "Photoemission Studies on SrTiO₃ thin films doped with Ni", 15th Soleil User's Meeting and Thematic Workshop, Paris, January 2020.
- Poster, "ARPES studies on SrTiO₃ thin films doped with Ni", 26th International Workshop on Oxide Electronics (iWOE), Kyoto, September-October 2019.
- Oral presentation, "Controlling fundamental electronic interactions in SrTiO₃ thin films doped with Ni", New Generation in Strongly Correlated Electron Systems (NGSCES), Pescara, September 2019.
- Oral presentation, "SrTiO₃ thin films doped with Ni", Theory Meets Experiment in Low-Dimensional Structures with Correlated Electrons, Prague, July 2019.
- Oral presentation, "ARPES studies on Ni-doped SrTiO₃ (100) thin films", Applied Physics of Condensed Matter (APCOM), Štrbské Pleso, June 2019.
- Oral presentation, "Photoemission Studies on SrTiO₃ thin films doped with transition metal elements", DPG Meeting, Regensburg, April 2019.
- Oral presentation, "Surface characterization of SrTiO₃ thin films", Applied Physics of Condensed Matter (APCOM), Štrbské Pleso, June 2018.
- Oral presentation, "XPS studies on SrTiO₃ thin films doped with transition metal elements", DPG Meeting, Berlin, April 2018.
- Oral presentation, "Characterization of ZnO doped with Ti", School on UV and X-ray Spectroscopies of Correlated Electron Systems (SUCCESS), Les Houches, September 2017.